DIVERSE USE OF IRON OXIDE NANOPARTICLES FOR ANTICANCER THERAPY

by

GAYANI SANDEEPA ABAYAWEERA

B.S., University of Colombo, Sri Lanka, 2008

AN ABSTRACT OF A DISSERTATION

submitted in partial fulfillment of the requirements for the degree

DOCTOR OF PHILOSOPHY

Department of Chemistry
College of Arts and Sciences

KANSAS STATE UNIVERSITY
Manhattan, Kansas

2014

Abstract

Recent development of a variety of superparamagnetic and ferromagnetic iron/iron oxide (Fe/Fe_3O_4) nanoparticles with different surface chemistry have been widely studied for numerous biological applications such as drug delivery, as diagnostics, hyperthermia and magnetic resonance imaging. The wide applications of Fe/Fe_3O_4 nanoparticles are possible since they exhibit favorable properties as high magnetization ability, are smaller than 100 nm in size, they can be coated with several ligands which allow drug delivery at a specific site and are biocompatible. By using Fe/Fe_3O_4 nanoparticles as drug delivery agents treatment costs and side effects can be reduced, however treatment efficacy can be increased. We have demonstrated that Fe/Fe_3O_4 nanoparticles can be utilized in different methods depending on their properties, to be used as therapeutic agents for cancer treatment. In one method we have taken advantage of the Fe/Fe_3O_4 nanoparticles magnetic ability to produce hyperthermia (heat) in cancer cells when subjected to an alternative magnetic field. Here we use the cell based delivery system since the size of the nanoparticles are small they can be taken up by monocyte/ macrophage like cells for systemic transportation to the inflamed cancer cite. The hyperthermia study was conducted in mice with pancreatic cancer. This study demonstrated that the life expectancy of the mice increased by 31%. In the next method we took the advantage of the surface chemistry of the Fe/Fe_3O_4 nanoparticles and changed it with dopamine-peptide and dopamine-thiosemicarbazone ligands. The advantage of the peptide is to deliver the nanoparticle to its target site and the thiosemicarbazone analogue is used as an iron chelator that would initiate apoptosis in cancer cells. This nanoplatform was tested in 4T1 breast cancer cell line and normal fibroblast cell line and demonstrated that it was effective towards the cancer cell line than the normal cell line at a ratio of 5:1 of thiosemicarbazone analogue : dopamine on the nanoparticle. However further studies are needed to be done to clarify the effectiveness of this nanosystem.

DIVERSE USE OF IRON OXIDE NANOPARTICLES FOR ANTICANCER THERAPY

by

GAYANI SANDEEPA ABAYAWEERA

B.S., University of Colombo, Sri Lanka, 2008

A DISSERTATION

submitted in partial fulfillment of the requirements for the degree

DOCTOR OF PHILOSOPHY

Department of Chemistry
College of Arts and Sciences

KANSAS STATE UNIVERSITY
Manhattan, Kansas

2014

Approved by:

Major Professor
Dr. Stefan H. Bossmann

Copyright

GAYANI SANDEEPA ABAYAWEERA

2014

Abstract

Recent development of a variety of superparamagnetic and ferromagnetic iron/iron oxide (Fe/Fe_3O_4) nanoparticles with different surface chemistry have been widely studied for numerous biological applications such as drug delivery, as diagnostics, hyperthermia and magnetic resonance imaging. The wide applications of Fe/Fe_3O_4 nanoparticles are possible since they exhibit favorable properties as high magnetization ability, are smaller than 100 nm in size, they can be coated with several ligands which allow drug delivery at a specific site and are biocompatible. By using Fe/Fe_3O_4 nanoparticles as drug delivery agents treatment costs and side effects can be reduced, however treatment efficacy can be increased. We have demonstrated that Fe/Fe_3O_4 nanoparticles can be utilized in different methods depending on their properties, to be used as therapeutic agents for cancer treatment. In one method we have taken advantage of the Fe/Fe_3O_4 nanoparticles magnetic ability to produce hyperthermia (heat) in cancer cells when subjected to an alternative magnetic field. Here we use the cell based delivery system since the size of the nanoparticles are small they can be taken up by monocyte/ macrophage like cells for systemic transportation to the inflamed cancer cite. The hyperthermia study was conducted in mice with pancreatic cancer. This study demonstrated that the life expectancy of the mice increased by 31%. In the next method we took the advantage of the surface chemistry of the Fe/Fe_3O_4 nanoparticles and changed it with dopamine-peptide and dopamine-thiosemicarbazone ligands. The advantage of the peptide is to deliver the nanoparticle to its target site and the thiosemicarbazone analogue is used as an iron chelator that would initiate apoptosis in cancer cells. This nanoplatform was tested in 4T1 breast cancer cell line and normal fibroblast cell line and demonstrated that it was effective towards the cancer cell line than the normal cell line at a ratio of 5:1 of thiosemicarbazone analogue : dopamine on the nanoparticle. However further studies are needed to be done to clarify the effectiveness of this nanosystem.

Table of Contents

List of Figures

xvii

List of Tables

List of Abbreviations

ABS ---------------------------------- Absorbance

Al   ------------------------------------ Aluminium

AMF ---------------------------------- Alternating Magnetic Field

ATP ----------------------------------Adenosine Triphosphate

BCS ---------------------------------- Body Condition Score

Boc   ---------------------------------- t*ert*-Butyloxycarbonyl

C   ------------------------------------ Carbon

C_e ------------------------------------ Specific heat capacity of the sample

CMP ---------------------------------- Common Myeloid Progenitors

CO_2 ----------------------------- Carbon dioxide

CPPs ---------------------------------- Cell-Penetrating Peptides

Cu   ---------------------------------- -- Copper

D   ------------------------------------ Dextrorotatory

Da   ------------------------------------ Daltons

DCM ---------------------------------- Dichloromethane

DFO ---------------------------------- Desferrioxamine

DIEA ---------------------------------- N,N-Diisopropylethylamine

DLS   ---------------------------------- - Dynamic Light Scattering

DMB ------------------------------------ N, N-Dimethyl-2,3-dihydroxybenzamide

DMEM ----------------------------------- Dulbecco's Modified Eagle's Medium

DMF ------------------------------------ N, N-dimethylformamide

DNA ---------------------------------- Deoxyribonucleic Acid

DOX ------------------------------------ Doxorubicine

DTPA ------------------------------------ Diethylenetriaminepentaacetic Acid

EDC ---------------------------------- 1-Ethyl-3-(3-dimethylaminopropyl)carbodiimide

EDTA ------------------------------------ Ethylenediaminetetraacetic Acid

EPR   ------------------------------------ Electron Paramagnetic Resonance

F   ------------------------------------ Fluorine

FBS   ----------------------------------- Fetal Bovine Serum

Fcc ------------------------------------ Face-centered cubic

Fe ------------------------------------- Iron

$Fe(CO)_5$ --------------------------------- Iron pentacarbonyl

$Fe(NO_3)_3$ -------------------------------- Iron nitrate

Fe/Fe_3O_4 -------------------------------- Iron/iron oxide

Fe^{2+} ------------------------------------- Ferrous ions

Fe^{3+} ------------------------------------- Ferric ions

Fe^{II} -------------------------------------- Ferrous ions

Fe^{III} ------------------------------------- Ferric ions

Fmoc ------------------------------------ Fluorenylmethyloxycarbonyl chloride

FPN -------------------------------------- Ferroportin

G_1 -- Gap 1

Ga -- Galium

GMP ------------------------------------- Granulocyte Macrophage Progenitors

H2NIH ----------------------------------- 2-hydroxy-1-naphthylaldehyde isonicotinoyl hydrazone

H2NT ------------------------------------ 2-hydroxy-1-naphthylaldehyde thiosemicarbazone

H_2O_2 ------------------------------------ ----- Hydrogen peroxide

H_2SO_4 ---------------------------------- Sulfuric acid

HAD·HCl -------------------------------- Hexadecylammonium chloride

HAMP ----------------------------------- Hepcidin

HBTU ---------------- O-benzotriazol-1-yl-N,N,N,N -tetramethyluronium hexafluorophosphate

HCl --------------------------------- Hydrochloric acid

HDp44mT -------------------------- di-2-pyridyl ketone 4,4-dimethyl-3-thiosemicarbazone

HDp4aT --------------------------- di-2-pyridyl ketone-4-allyl-3-thiosemicarbazone

HDp4eT --------------------------- di-2-pyridyl ketone 4-ethyl-3-thiosemicarbazone

HDp4mT -------------------------- di-2-pyridyl ketone 4-methyl-3-thiosemicarbazone

HDp4pT --------------------------- di-2-pyridyl ketone 4-phenyl-3-thiosemicarbazone

HDpT ------------------------------ di-2-pyridyl ketone thiosemicarbazone

$HO^{\bullet}$ ----------------------------------- --- Hydroxyl radicals

HOBT ------------------------------------ Hydroxybenzotriazole

HPKIH ----------------------------- di-2-pyridyl ketone isonicotinoyl hydrazone

HPLC ---------------------------------- High Performance Liquid Chromatography

HSC ------------------------------------ Hematopoietic Stem Cells

HSP ------------------------------------ Heat Shock Proteins

IC_{50} ------------------------------------ Half maximal inhibitory concentration

IRP's ---------------------------------- -- Iron Responsive Proteins

K -- Equilibrium constant

K_{pH} ----------------------------------- Conditional stability constant

L -- Ligand

LIP --------------------------------------- Labile Iron Pool

M --------------------------------------- Metal ion

Ma ------------------------------------- Macrophages

MAP ------------------------------------ Model Amphipathic Peptides

MDP ----------------------------- ----- Monocyte/macrophage Dendritic Cell Progenitors

m_e --------------------------------------- Mass of the sample

M-MDSC ------------------------------ Monocytic -Myeloid-Derived Suppressor Cells

MNP ------------------------------------ Magnetic Nanoparticles

Mo ------------------------------------- Monocytes

Mo-DC ---------------------------------- Monocyte Derived Dendritic Cells

Mo-MΦ --------------------------------- Monocyte-derived Macrophages

MPS ------------------------------------- Mononuclear Phagocyte System

MRI ------------------------------------- Magnetic Resonance Imaging

MS -- Mass Spectrometry

MTS ------------------------------------- Membrane Translocating Sequences

MTT ------------------------- 3-(4, 5-Dimethylthiazol-2-yl)-2,5-diphenyltetrazolium bromide

N --- Nitrogen

NK ----------------------------------- Natural killer cells

NP -------------------------------------Nanoparticle

NPC --------------------------------- ---Nasopharyngeal carcinoma

O ------------------------------------ Oxygen

ODE -------------------------------- Octadecene

P -------------------------------------- Electromagnetic wave power absorbed by the sample

Pbf -------------------------------------- 2,2,4,6,7-Pentamethyldihydrobenzofuran-5-sulfonyl

PBS ------------------------------------- Phosphate buffered saline

PIH -------------------------------------- Pyridoxal isonicotinoyl hydrazone

PTDs ------------------------------------ Protein Transduction Domains

RNA ------------------------------------ Ribonucleic acid

ROS ------------------------------------ Reactive oxygen species

RP-HPLC ----------------------------- Reversed-Phase High Performance Liquid Chromatography

RPMI ------------------------------- Roswell Park Memorial Institute

S ----------------------------------- -Sulfur

SAR ------------------------------------ Specific Absorption Rate

Si ----------------------------------- Silicon

SPIO ----------------------------------- -Superparamagnetic Iron/iron oxide nanoparticles

SPPS ----------------------------------- Solid Phase Peptide Synthesis

TAM ----------------------------------- Tumor-Associated Macrophages

TAT ----------------------------------- Trans-Activator of Transcription

tBu ----------------------------------- *tert*-Butyl

TCPP ----------------------------------- Tetra(4-carboxyphenyl)porphyrin

TEM ---------------------------------- Transmission Electron Microscopy

Tf ------------------------------------ Transferrin

TFA ----------------------------------- Trifluoroacetic acid

TfR ------------------------------------ Transferrin Receptor

THF ----------------------------------- Tetrahydrofuran

TIPS ------------------------------------ Triisopropyl silane

Trt ----------------------------------- Trityl

UV ------------------------------------ Ultraviolet

WBH ---------------------------------- Whole Body Hyperthermia

YS-MΦ ---------------------------- --- Yolk Sac-Derived Macrophages

Zn ------------------------------------ Zinc

β -------------------------------------- Formation constant

Acknowledgements

I would like to thank my major professor Dr. Stefan H. Bossmann for his invaluable guidance and support throughout my research and during my stay at KSU. I am very grateful for the freedom and encouragement he gave me to develop my own ideas.

I would like to thank everyone who helped me with my research, and a big thanks must be given to Dr. Leila Maurmann for helping with the NMR, to Dr. Pin Li for being kind enough to let me use the HPLC, to Mrs. Chammi Attanayake from the department of agronomy for helping me with the ICP experiments and to Mrs. Marla Pyle, Dr. Tej Shrestha and Dr. Matthew Basel, Dr. Sivasai Balivada, Dr. Gwi Moon Seo, from the department of anatomy and physiology for taking their time form their busy schedule to help with the cell culture experiments and animal testing to Dr. Deryl Troyer for letting me work in his lab for the cell culture experiments and to the Center of Biomedical Research Excellence (COBRE) in Protein Structure and Function at the University of Kansas (Dr. Bob Hanzlik) for mass spectra. To Dr. Raj Dani, Dr. Masaaki Tamura, to Dr. Viktor Chikan for assembling of the hyperthermia machine and to Dr. Olga B. Koper from the Nanoscale Corporation, Manhattan, KS for initially providing us with the nanoparticles.

I also greatly appreciate the ideas exchanged between many former and current students and post-docs, especially Dr. Hongwang Wang, Dr. Tej Shrestha, Dr. Thilani Samarakoon, Mr. Sebastian Wendel, Mrs. Harshi Manawadu, Mrs. Aruni Malalasekara.

I would like to thank the non-academic staff; Mr. Jim Hodgson, Mr. Ron Jackson and Mr. Tobe Eggers for helping with preparing equipment for my research.

I would also like to thank my friends for their kindness and support: Miss. Kaushalya Perera, Mrs. Asanka Yapa

I would like to thank my family for their continuous support and encouragement they gave me.

Finally I would like to thank all of my committee members for supervising my work with continuous encouragement: Dr. Deryl Troyer, Dr. Christer Aakeroy, Dr. Viktor Chikan and Dr. Jennifer Anthony.

Dedication

I dedicate my research to my family.

Chapter 1 - Antitumor Activity by Combination of Iron Chelators with Peptide Sequences

1.1 Abstract

In the past few years, the use of iron chelators and therapeutic peptide sequences has been studied for the treatment of cancer. Recent studies have shown that the iron chelators that belong to the thiosemicarbazone group show antitumor activity in the nanomolecular range. Their ability to inhibit tumor growth is understood based on several factors:

1) Tumor cells proliferate much faster than normal cells, therefore they need enhanced Fe concentrations for cell growth.

2) Several enzymes that are needed to catalyze the synthesis of DNA require Fe. Without fast DNA synthesis, the high proliferation rates of virtually all cancers cannot be maintained.

As a tumor proliferates, blood vessels grow with it through angiogenesis. Therefore, inhibition of angiogenesis is a therapeutic strategy that can be used to inhibit tumor growth. We have assembled a nanoplatform for tumor treatment. A thiosemicarbazone analogue and a peptide sequence are attached onto a Fe/Fe_3O_4 nanoparticle. The peptide sequence CGKRK($_D$[KLAKLAKKLAKLAK])PLFAERL comprises of 26 amino acid residues and contains two important sequences, which are the CGKRK peptide, which provides tumor homing ability and $_D$[KLAKLAK]$_2$, which disrupts the mitochondrial cell walls and initiates cell death (apoptosis). The nanoparticle can enhance apoptosis by using hyperthermia. Fe/Fe_3O_4 nanoparticles can also be used for imaging purposes (MRI). Therefore, by combining various therapeutic methods, we can produce a synergistic approach to treat tumors. The efficacy of the nanoplatform has been tested on 4T1 breast cancer cell line and its IC_{50} values have been calculated. Most importantly, the nanoplatform has been optimized to show significantly lower IC_{50} values against 4T1 breast cancer cells than against healthy murine fibroblast cells. This approach has the potential of leading to a new generation of nanoplatforms for cancer treatment with considerably enhanced selectivity towards tumor cells.

1.2 Introduction

Cancer has become one of the leading causes of death worldwide. The most major cause of cancer death in woman is breast cancer.[1] It is said that in a woman's lifetime there is a 1 in 7 in risk of developing breast cancer.[2]

Even though there are several treatment methods for breast cancer such as hormone therapy, aromatase inhibitors and cytotoxins, there is still improvement needed in specifically targeting cancer cells to reduce side effects and toxicity in normal cells.[2] For successful cancer treatment it is essential to deliver chemotherapeutic agents in effective dose into tumor cells minimizing adverse effects into normal healthy cells.[3]

Cancer cells have different growth characteristics than normal cells. In order to supply nutrients for the excessive growth of the cells, leaky blood vessels are formed, due to the absence of pericytes lining the endothelial cells. These blood vessels have pore sizes of 100-600nm, which can be of advantage, allowing nanoparticles to diffuse into tumor cells. Therefore, chemotherapeutic agents coupled onto nanoparticles can be used as successful drug carriers into tumor cells, increasing drug tumor accumulation.[3]

Other than leaky pores on the blood vessels they also express specific endothelial markers, which are not prominent in normal cells. Ligands such as peptides can bind to these vascular markers and when these ligands are bound to drugs they can be concentrated in tumor cells increasing efficacy and reducing adverse effects to normal cells.[3,4]

Peptides play an important role in living organisms. Protein–protein interactions are important in many biological processes such as cell division, to programmed cell death and are also important in regulating these biological processes.[5]

Mimicking these protein-protein interactions can be used as a therapeutic strategy to specifically target and destroy cancer cells.[5]

In our study we have taken advantage of this concept and used two peptide sequences where one is the CGKRK which homes the blood vessels in tumors but not vessels of normal tissues. The other is $_D$[KLAKLAK]$_2$ pro-apototic sequence which disrupts membranes that are of bacterial origin. Therefore, it can disrupt the mitochondrial membrane leading the cancer cells to apoptosis.[4]

Our main goal is to inhibit the growth of tumors by inhibiting the growth of blood vessels. Since when tumors grow their blood vessels grow with them through angiogenesis. An

advantage of using peptides is that they can be conjugated easily together with other compounds. Therefore by conjugating these two peptides together and attaching them onto the surface of an iron/iron oxide (Fe/Fe$_3$O$_4$) nanoparticle we can home the tumors and increase the binding efficiency to the target and lead the cell towards apoptosis.[4]

We have also incorporated an iron chelator onto the Fe/Fe$_3$O$_4$ nanoparticle. Iron is an important element for several cellular processes which are proliferation, DNA synthesis mitochondrial electron transport and is also essential for the activity of iron requiring enzymes such as ribonucleotide reductase which is important for DNA synthesis and repair.[6,7]

The iron chelator that we have used belongs to the thiosemicarbazone group. The mechanism of action by which this thiosemicarbazone analogue would deliver its activity is via several pathways;

1. Since cancer cells have an increased requirement of iron for the rapid proliferation, by using iron chelators we can deprive the cell from iron, thus inhibiting cell proliferation.

2. By chelating iron we can inhibit the activity of ribonucleotide reductase enzyme and inhibit DNA synthesis and repair.

3. Since these chelators form iron complexes that redox cycle they can generate reactive oxygen species (ROS) such as hydroxyl radicals which induce DNA oxidation and mitochondrial damage leading the cells towards apotosis.[6,7]

In our research we have combined the use of tumor homing and pro-apoptotic peptide sequences with iron chelators, which we assume would produce a synergistic effect in cancer treatment.

Here we have assembled a multifunctional Fe/Fe$_3$O$_4$ nanosystem, where the CGKRK peptide will carry the nanoparticle to the tumor vascular cells and into their mitochondria. The $_D$[KLAKLAK]$_2$ sequence will disrupt the mitochondria leading the cell towards apoptosis. The thiosemicarbazone analogue will enhance the cell towards apoptosis by chelating the iron in cancer cells. The Fe/Fe$_3$O$_4$ nanoparticle can be used as a carrier or produce apoptosis via hyperthermia and it can also be used as a diagnostic for MRI (magnetic resonance imaging).

The activity of this nanosystem was tested in 4T1 breast cancer cell line and was compared with normal murine fibroblast cell line. The thiosemicarbazone iron chelator and peptide sequence were successfully coupled to the nanoparticle through a dopamine ligand. The

size of the nanoparticles were in good range for therapeutic use. From the cell culture tests it was determined that the nanosystem containing the 5:1 (thiosemicarbazone analogue: dopamine) ratio is a good system to use for therapeutic use since it showed a difference in cell toxicity in 4T1 breast cancer cell line than the fibroblast normal cell line.

1.3 Literature and Reviews

1.3.1 Cancer Statistics

Currently, cancer is the second major cause of death in USA, shortly behind heart disease. The number of deaths from cancer in 2012 is estimated to 577,150.[1] Although, as Figure 1.1 indicates, the combined cancer death rates in the US are on a slight decline, mortality from cancer during the 2010's is approximately the same than during the 1950's. A more detailed look at cancer mortality by gender in the US from 1975 to 2008 reveals that men have a 16% higher change to die from cancer than women.[8]
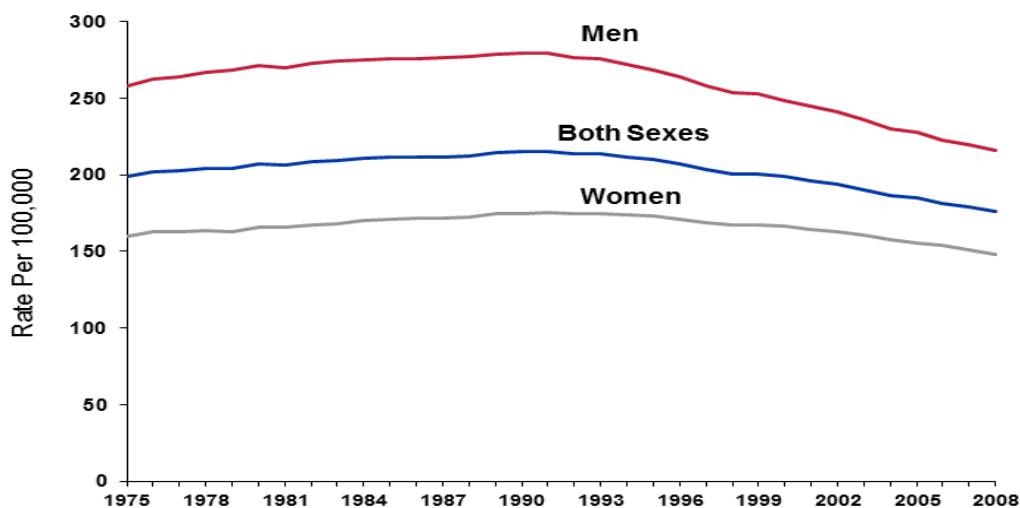
Figure 1.1:- Cancer death rates by gender in USA from 1975 to 2008.
(Taken from: http://www.cancer.org/research/cancerfactsfigures/cancerfactsfigures/cancer-facts-figures-2012).

In our research we would be focusing on treating breast cancer, because breast cancer is the most widespread type of cancer in women (Figure 1.2). Only skin cancer is, statistically speaking, almost as important. Breast cancer has the highest incidence rate in the US. Early stage (stage 0) breast cancer is localized to the breast with no evidence of spread to the lymph nodes (carcinoma in situ).[9] Stage 1 breast cancers are two centimeters or less in size, no spread has been observed. Stage 2A breast cancer has a diameter of up to two centimeters with no lymph node involvement. Stage 2B has lymph node involvement. Metastatic breast cancer results from spreading to the lymph nodes. Stage 3A breast cancer (locally advanced breast cancer) has spread to lymph nodes under the arm, or 4-9 axillary lymph nodes. Stage 3B breast cancer is a tumor of any size that has spread to the skin, chest wall, or internal mammary lymph nodes (located beneath the breast and inside the chest). Stage 3C breast cancer is a tumor of any size that has spread to more than 10 axillary lymph nodes. Final stage is Stage 4 breast cancer. It is defined as a tumor, regardless of size, that has spread to places far away from the breast, such as bones, lungs, liver, brain, or distant lymph nodes. The 5-year relative survival is at 98 percent for stage 1, 83.6 percent at stage 2, and 23.4 percent at stage 3. This clearly indicates that new treatment methods for later stages in breast cancer have to be developed. Since these cases are highly metastatic, they are usually non-operable. Therefore, nanoplatforms have to be developed that are able to target tumors and metastases alike. They should cause apoptosis (programmed cell death) rather than necrosis, because the latter results in massive inflammation.[10]
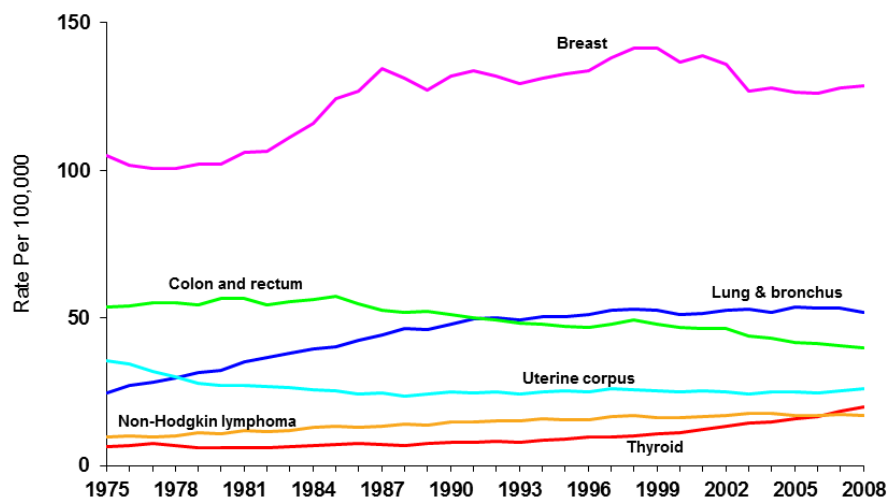
Figure 1.2:- Cancer incidence rates among women in USA from 1975 to 2008
(Taken from: http://www.cancer.org/research/cancerfactsfigures/cancerfactsfigures/cancer-facts-figures-2012).

1.4 Peptides

Peptides are synthesized by amino acids as their building blocks. They are a short sequence containing less than 50 amino acid monomers attached to each other by peptide bonds which is formed through a condensation reaction (Figure 1.3).[11]
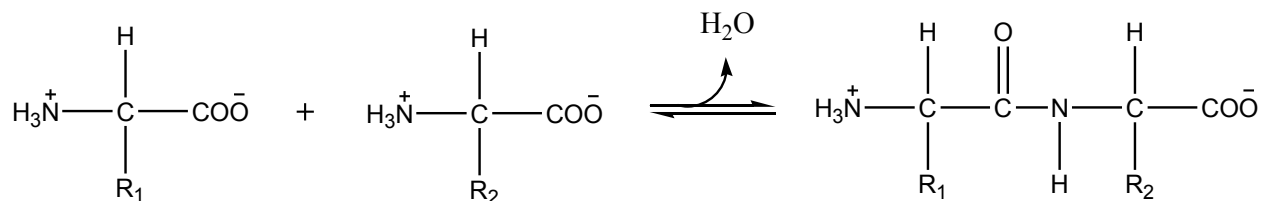
Figure 1.3:- Peptide bond formation through a condensation reaction.

Recently, scientists in various fields such as chemistry, biochemistry, physiology and pharmacology have shown interest in peptides.[12]

Peptides are important due to their biological functions as hormones, enzyme inhibitors, substrates, neurotransmitters and immunomodulators. When bound to their targets, they are able to trigger cell-cell communication, control metabolism, immune defense, sensitivity to pain and electrolyte levels. Therefore, scientists are interested in designing and developing new peptides and study their physiological effects as therapeutic agents.[12]
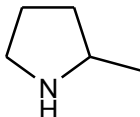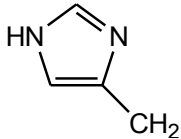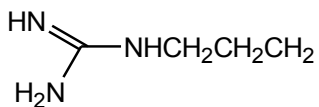
1.4.1 Building Blocks of Peptides
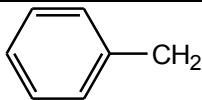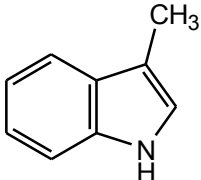
There are 20 standard α- amino acids (Figure 1.4) that can be used to synthesize peptides. They are abbreviated either by a 3 letter or one letter method (Table 1.1). The one letter abbreviation is used to write a peptide sequence.[11]
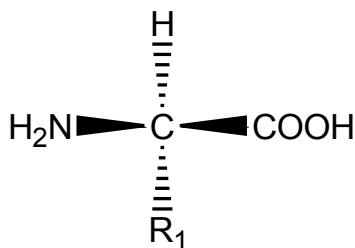
Figure 1.4:- Structure of α- amino acid.

Table 1.1:- Standard amino acids

Amino acid	Three letter code	One letter code	Side chain
Hydrophobic Aliphatic Side Chains			
Glycine	Gly	G	H-
Alanine	Ala	A	CH_3-
Valine	Val	V	$(CH_3)_2CH$-
Leucine	Leu	L	$(CH_3)_2CHCH_2$-
Isoleucine	Ile	I	$CH_3CH_2(CH_3)CH$-
Methionine	Met	M	CH_3-S-CH_2CH_2-
Proline	Pro	P	
Hydrophilic Uncharged Side Chains			
Serine	Ser	S	OH-CH_2-
Threonine	Thr	T	CH_3-CH(OH)-
Cysteine	Cys	C	HS-CH_2-
Asparagine	Asn	N	H_2NOC-CH_2-
Glutamine	Gln	Q	H_2NOC-CH_2CH_2-
Hydrophilic Charged Side Chains			
Lysine	Lys	K	H_2N-$CH_2CH_2CH_2CH_2$-
Aspartic acid	Asp	D	HOOC-CH_2-
Glutamic acid	Glu	E	HOOC-CH_2CH_2-
Histidine	His	H	
Arginine	Arg	R	

Aromatic Side Chains			
Phenylalanine	Phe	F	
Tyrosine	Tyr	Y	
Triptophane	Trp	W	

These α-amino acids differ from each other by their side chains (Figure 1.4). They are divided into hydrophobic aliphatic, hydrophilic uncharged, hydrophilic charged and aromatic groups according to the chemical nature of their side chains (Table 1.1).[11]

Most peptides are synthesized using the L-isomer but the D-isomer can also be used. However they will be toxic since they cannot be degraded by proteolytic enzymes.

1.4.2 Cell-Penetrating Peptides

In the last 10 years Cell-penetrating peptides (CPPs) have opened a new research field due to the finding of the ability of these short peptides to rapidly translocate through plasma membranes in a nonreceptor mediated manner.[11, 13, 14]

It is still a major drawback that drugs cannot translocate cellular membranes and access their intra cellular targets.[13, 15]

There are several types of CPPs: protein transduction domains (PTDs), Trojan peptides, or membrane translocating sequences (MTS), are used for peptide-mediated delivery of bio active molecules. In many examples, the results that were obtained when delivering by means of CPPs were superior to other methods, such as electroporation.[15] Membranes of eukaryotic cells have a barrier that only allows certain substances into the cell and restricts hydrophilic drugs into the cell. The conventional intracellular processes such as transport proteins (carrier proteins, pumps and gated ion channels) regulate the intake of substances through the plasma membrane. They are also energy dependent, which requires adenosine triphosphate (ATP) as their energy

source, which can be saturated. Therefore, limiting the delivery capacity since the number of carriers are fixed in a cell.[13, 14, 15]

New nonphysiological methods such as electroporation and liposomes have been studied and used for gene drug delivery. However, these methods are found to be only effective *in vitro* and are restricted in *in vivo* effectiveness due to toxicity, cell damage lack of tissue and cell specificity. CPPs have appeared to possess rapid translocation in both *in vitro* and *in vivo* of various cargos such as oligonucleotides, peptides, plasmids, liposomes and nanoparticles. Therefore development of CPPs, provide a noninvasive delivery method of hydrophilic and genetic material which can be used as a successful drug delivery method.[11, 13, 14]

This field first emerged with the discovery of the viral protein TAT, translocating through cellular membranes into the cell by Green et al. in 1988.[16] Later in 1994 Alain Prochiantz group discovered a 14 amino acid peptide penetration, which had DNA recognition ability and was able to translocate the whole protein into the cell. Since then hundreds of CPPs have been identified and studied for their therapeutical importance.[11, 15, 17]

1.4.2.1 Cell-Penetrating Peptide Features and Classification

A clear classification of CPPs has not been defined yet. The general features that they present are that they are up to 30 amino acids or less in length and have a net positive charge due to the high content of basic amino acids and are amphipathic in nature.[13, 18]

CPPs can be classified into three classes;[13]

1. Protein derived CPPs

    They contain the minimal effective partial sequence of the parent translocation protein.

    E.g. Penetratin, TAT, pVEC

2. Model CPPs

    These sequences are designed by mimicking structures of known CPPs or aimed to produce amphipathic α-helical structures.

    E.g. Model amphipathic peptides (MAP) , $(Arg)_7$

3. Designed CPPs

    They are chimeric peptides where hydrophilic and hydrophobic parts are coupled from different origin.

    E.g. MPG, transportan

Examples of CPPs are shown in Table 1.2. The above-mentioned CPPs have vastly expanded into numerous analogues.[11]

In our research we have incorporated the use of MAP (D(KLAKLAK)$_2$ sequence) peptide where it is also used as a pro-apoptotic peptide other than a CPP. Its pro-apoptotic activity will be explained in detail later in this chapter.

Table 1.2:- Commonly used Cell-Penetrating Peptides[11, 13]

Name Sequence	Class Source	Applications
Penetratin RQIKIWFQNRRMKWKK	**Protein derived CPP** *Drosophila* Antennapedia homeodomain (amino acids 43-58)	Intracellular delivery of a wide range of bioactive cargos
Tat CGRKKRRQRRRPPQC	**Protein derived CPP** Protein from human immunodeficiency virus 1 (amino acids 48-60)	Intracellular delivery of fused proteins
pVEC LLIILRRRIRKQAHAHSK-amide	**Protein derived CPP** Derived from murine endothelial cadherin	
MAP KLALKLALKALKAALKLA-amide	**Model peptide** Synthetic	
(Arg)$_7$ RRRRRRR	**Model peptide** Synthetic	
MPG GALFLGFLGAAGSTMGAWSQPKSKRKV	**Designed peptide** Peptide derived from fusion sequence of HIV-1 gp41 protein coupled to peptide	Intracellular delivery of a wide range of bioactive cargos

	derived from the nuclear localization sequence of SV40 T-antigen	
Transportan GWTLNSAGYLLGKINLKALAALAKISIL-amide	**Designed peptide** Minimal active part of galanin (amino acids 1-12) coupled to mastoparan via Lys	Intracellular delivery of a wide range of bioactive cargos

1.4.2.2 Mechanism of Membrane Translocation of CPPs

Studies on the uptake of CPPs showed that the translocation mechanism was not affected by depletion of cellular ATP or endocytosis inhibitors and low temperature (+ 4^0C) compared with 37^0C, confirming a non-endocytotic pathway of translocation and an energy independent pathway. Chemical modifications such as retro-, enantio (D isomer) or retroenantio- analogs of the peptide sequences also did not affect the internalization of CPPs. These findings suggests that CPPs translocation occurs through the plasma lipid bilayer of the cell membrane.[15, 18,19]

Many studies have been conducted to postulate a defined mechanism of CPPs translocation, however it is hard to define a particular method since there are various mechanisms that have been suggested.

One method that was suggested was the formation of the inverted micelle model. According to this method the positively charged peptide interact with the negatively charged plasma membrane, next invagination of the peptide takes place with the aid of hydrophobic amino acids forming the inverted micelle. (Figure 1.5).[15, 18, 19]

Recent studies show that an energy dependent process takes place such as extracellular heparane sulfate and various endocytosis pathways such as macropinocytosis, clathrin-dependent, clathrin- independent, caveoal-dependent and caveoal-independent endocytosis to mediate CPP translocation.[11, 15]

Extracellular

Intracellular
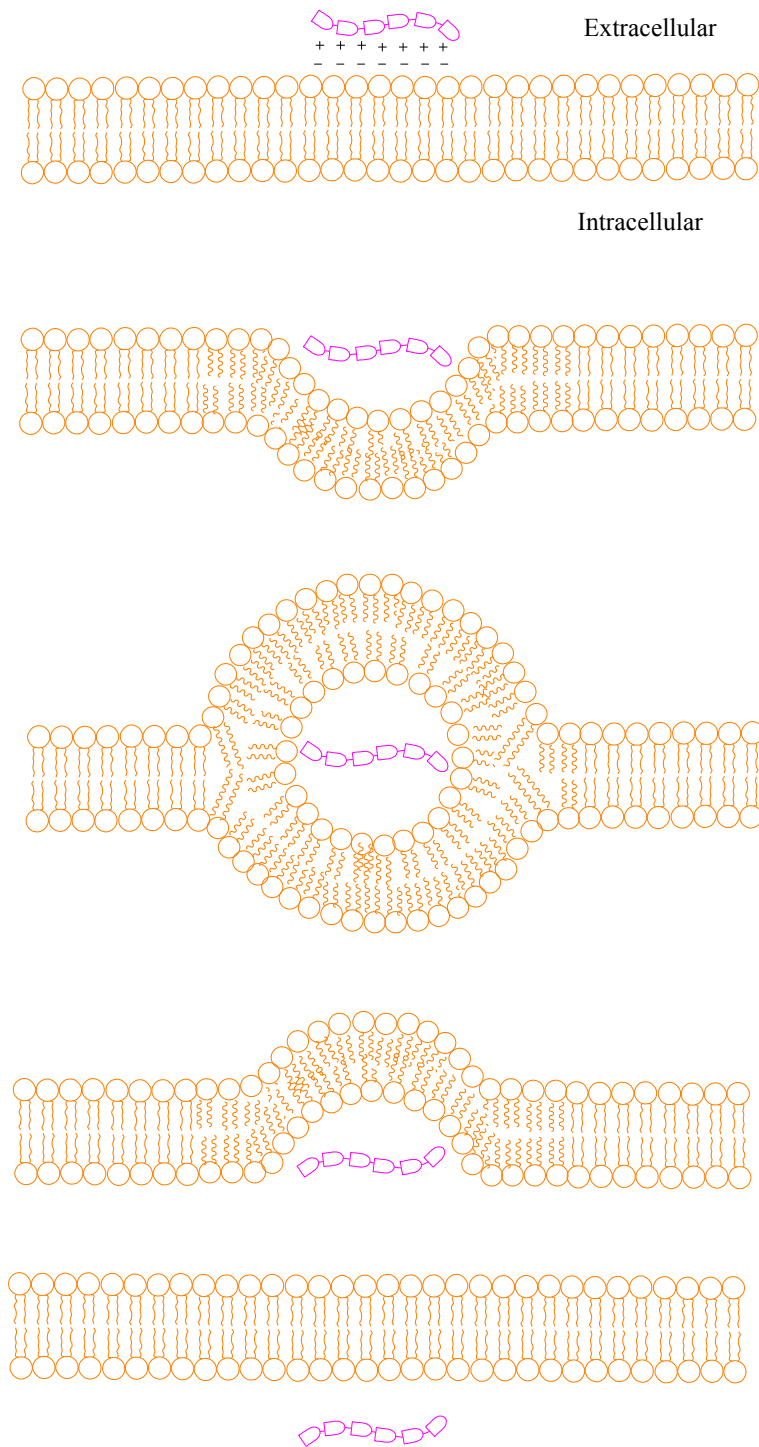
Figure 1.5:- Inverted micelle model.[19]

When CPPs are not attached to any cargo they translocate into cells by the different endocytosis pathways mentioned above. In higher concentrations they can translocate through rapidly by direct penetration. However when CPPs are conjugated to a cargo the endocytotic translocation is prominent (Figure 1.6).[11, 15]

Since it is not clear which pathway peptide mediated membrane translocation takes place, it may occur simultaneously through several different pathways. The process may also depend on the differences in the biophysical properties of the peptide and their cargo.[15]
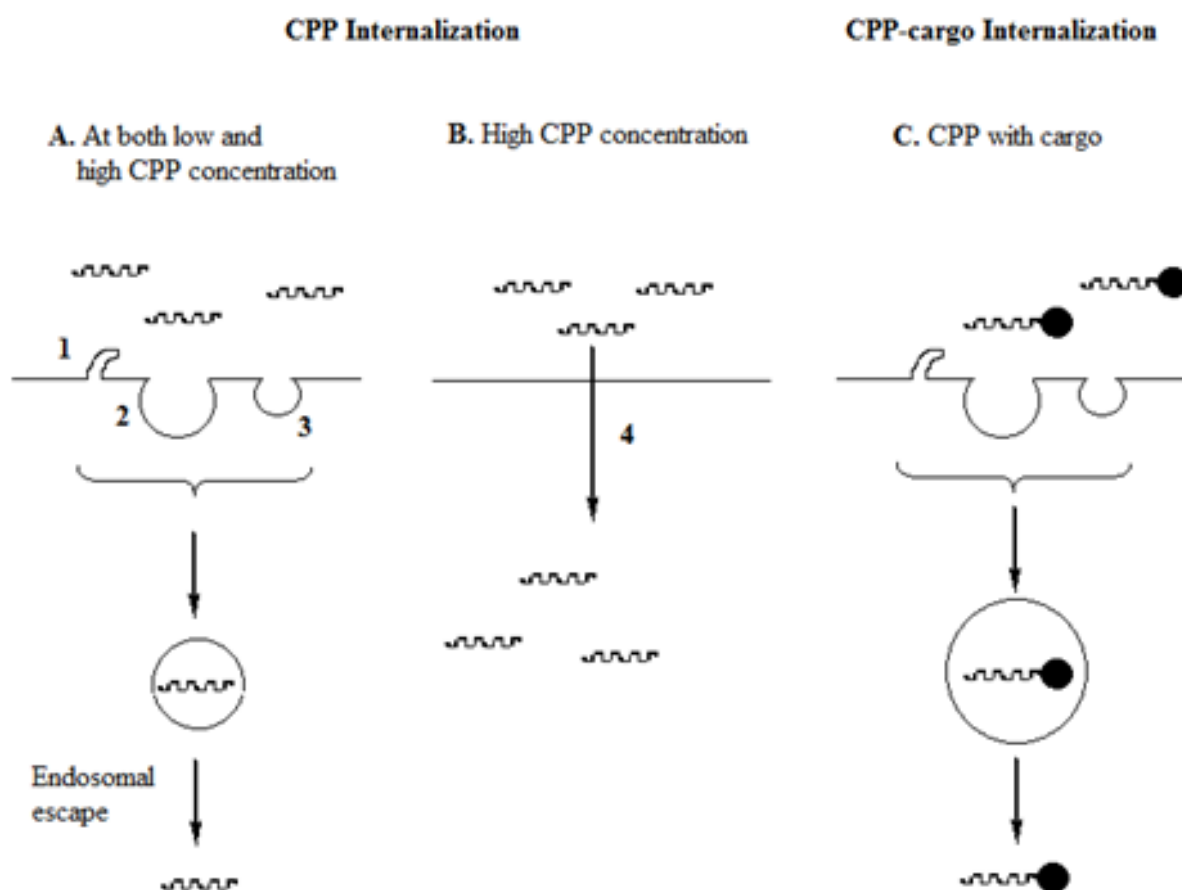
Figure 1.6:- Cellular CPP uptake mechanisms.[11]

A. Endocytotic pathway with combination of macropinocytosis (1), clathrin (2), and caveolin (3) dependent endocytosis. Can occur at low or high CPP concentration.

B. Direct penetration (4) of CPPs at high concentration.

C. Endocytotic pathway of CPPs conjugated with cargo.

1.4.3 Targeting Cancer Cells and Angiogenic Blood Vasculature

In order to deliver the payload successfully to the cancer site it is important to specifically target the site. Most anticancer drugs cannot discriminate between normal and cancer tissues. Therefore it is important to use a targeting drug delivery technique to enhance the drug concentration in the target site and also reduce systemic side effects and toxicity on normal cells.[2, 20]

Tumor cell survival mainly depends on the growth of new blood vessels known as angiogenesis. These newly formed blood vessels provide nutrients and oxygen necessary for the development of cancers. Therefore by inhibiting tumor vasculature using peptides, the blood supply to tumors will be restricted and inhibiting tumor progression.[20]

Cancer cells have different growth characteristics compared to normal cells. Cancer blood vessels express different endothelial surface markers (receptors) which are not expressed in normal vessels or expressed at a lower level.[2,3, 21, 22]

The usage of peptides that recognize these cancer vasculature markers can be used as promising agents to deliver drugs to cancer sites.[20]

These peptides have unique characteristics such as;[20]

- High tissue penetrating ability due to small molecular weight (average ≤ 50 amino acids)
- Low immunogenicity
- High affinity towards target
- Good stability
- Rarely producing drug resistance
- Easily synthesized and can be conjugated with other agents

In our research we used the peptide sequence CGKRK as the tumor homing sequence. This peptide sequence was identified by screening phage peptide libraries, when used to screen for peptides that home epidermal tumors in mice. This peptide sequence specifically recognized tumor vessels but not normal tissue vessels. This peptide sequence specifically recognized tumor vesscular endothelial cells and tumor cells but not normal tissue vessels. A sulfated polysaccharide heparan sulfate is the receptor for CGKRK peptide. This receptor is mainly expressed on the surface of the tumor vascular endothelial cells and tumor cells. Therefore the

CGKRK peptide attached nanoplatform can be internalized into the cell through heparin sulfate receptor mediated manner. [4, 23, 24,]

1.4.3.1 Peptide Screening

Peptide screening is done by using the phage display method, which was introduced by G. Smith in 1985. The main goal of using phage display was to identify peptides with diagnostic or therapeutic value.[25, 26, 27]

A phage library can produce up to 10^{10} different peptides and proteins that can be used for different functions. This can also be used to determine protein- ligand interactions, receptor and antibody binding sites.[26]

Phages are viruses consisting of a single- stranded DNA enclosed in a protein coat that infects gram-negative bacteria. The DNA sequence of interest is inserted into the genome of the filamentous bacteriophage. The protein or peptide that was encoded by the DNA sequence is then expressed on the surface of the filamentous phage. This is a good method to study billions of diverse peptides that can be made simultaneously, rather than genetically engineering proteins or peptides individually and studying them separately.[26, 27]

This filamentous phage, is amplified by transfecting into *Escherichia coli,* and are grown in culture media and the phage particles can be purified. These phage particles which have specific proteins and peptides exposed on its surface, can next be screened by affinity binding to either an antibody or receptor (Figure 1.7).[27, 28]

Identification of important peptides can also be done by in vivo phage peptide screening, which was studied by Ruoslahti in 1996. Here a live animal is used as the target. This method is used since cultured cells do not express certain receptors or may express molecules that are not expressed in vivo.[20, 29]
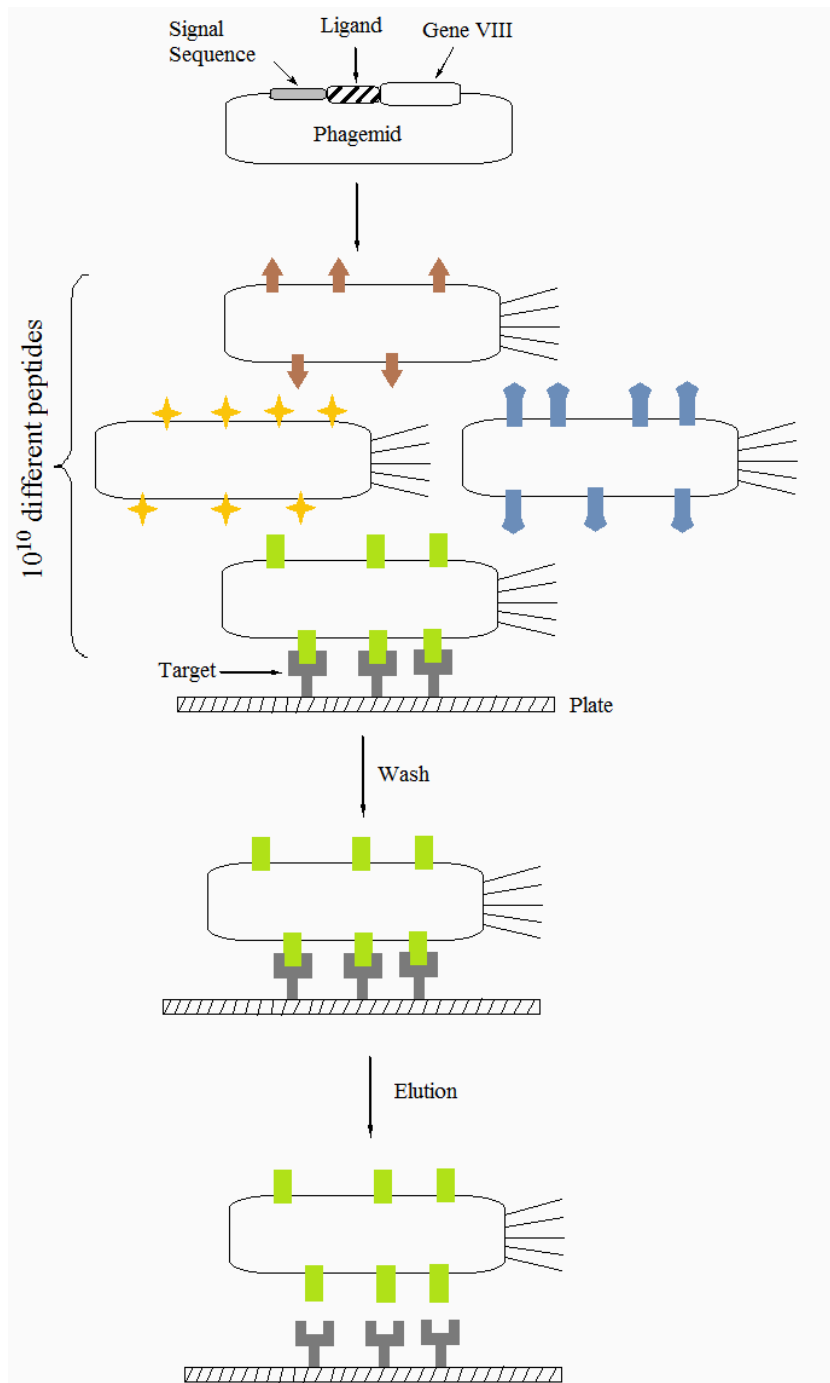
Figure 1.7:- Screening for specific peptides from peptide phage libraries.
The peptide that specifically binds to the target among 10^{10} different peptides that are
incorporated into the filamentous phage are enriched and eluted.[28]

1.4.4 Pro-apoptotic Peptide Sequence

Pro-apototic peptides were originally designed as synthetic antibacterial peptides. They can be either cationic, α-helical or amphipathic in nature. These peptides can disrupt negatively charged membranes by attraction of their cationic amino acids, with the anionic groups of the phospholipids. The electrostatic binding of these peptides disrupt the phospholipid membrane. These peptides are not toxic to eukaryotic cells however prokaryotic membranes and mitochondrial membranes (since they have been originated from bacteria) can be disrupted. This is mainly due to the fact that both prokaryotic and mitochondrial membranes have a higher content of anionic phospholipids and high transmembrane potential than eukaryotic plasma membranes.[4, 30]

Delivering drugs to subcellular organelles such as the nucleus and mitochondria can cause irreversible damage to these organelles leading to cell death. This can be used as a more direct and effective therapeutic method to kill cancer cells and inhibit their growth.[31]

The mitochondria are important organelles in the cell since they control many functions such as regulating calcium, redox signaling and most importantly apoptosis. Therefore apoptosis can be induced in cancer cells by disrupting the mitochondrial membrane. Once the mitochondrial membrane is disrupted it releases caspase activating proteins such as *cytochrome c*. Caspases are responsible for the cascade of reactions involved in apoptosis.[31, 32]

In our research we have used the α-helical amphipathic peptide $_D$[KLAKLAK]$_2$ as the pro-apoptotic peptide sequence. This peptide sequence is synthesized by using the D- enentiomer amino acids and is repeated $_D$(KLAKLAKKLAKLAK). The advantage of using the D- enantiomer is to avoid protease degradation and enhance efficacy.[4, 30, 33]

Therefore by conjugating the homing peptide sequence and pro-apotic peptide sequence we can improve therapeutic efficacy and lower the toxicity in normal cells and cancer treatment can be enhanced.

1.4.5 Peptide Clevage Sequence

Proteases are proteolytic enzymes that cleave proteins at specific sites. Cleavage of proteins is performed to process or degrade proteins in synthesis and maturation of cells or for modifiying the protein for signal transduction. Proteases are important for regulating various biological porcessors. Identifying protease subsrate is important to understand the interaction between the enzyme and the protein. Many screening studies have been done by proteomic methods to identify the protein substrates.[34, 35]

In our research, we have incorporated one of these clevage sequences to facilitate the cleavage of the peptide sequence for its activity. The cleavage sequence we have incorporated is PLFAERL sequence, which is cleaved by the calpain enzyme, which is overexpressed in cancer cells. Calpains are Ca^{2+} dependent cytosolic cysteine proteases that catalyze limited proteolytic activity of target proteins. The physiological role of calpains is that they regulate cellular functions by cleaving various cytoskeletal proteins for cell mobility and cell cycle progression. It has been found that calpain cleaves the PLFAERL sequence at the phenylalanin and alanine bond site, which would release the peptide sequence from the nanoparticle (as shown in Figure 1.8) and carry out its function.[36, 37]
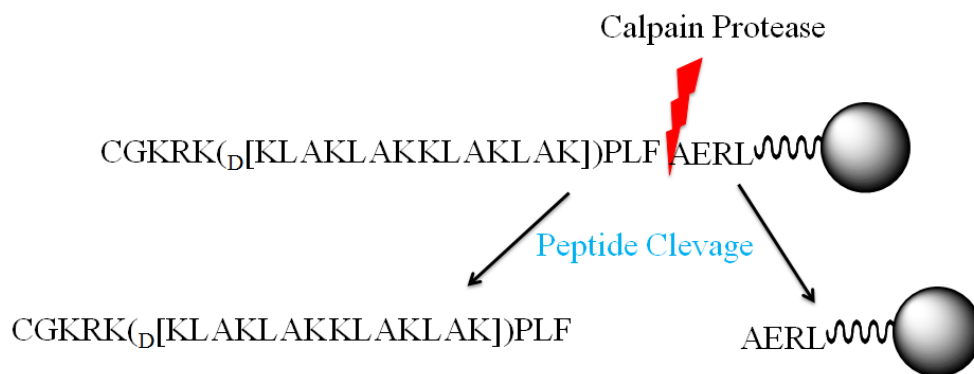
Figure 1.8:- Clevage of CGKRK(D[KLAKLAKKLAKLAK])PLFAERL peptide sequence from the nanoparticle by the Calpain protease.

1.4.6 Peptide Synthesis
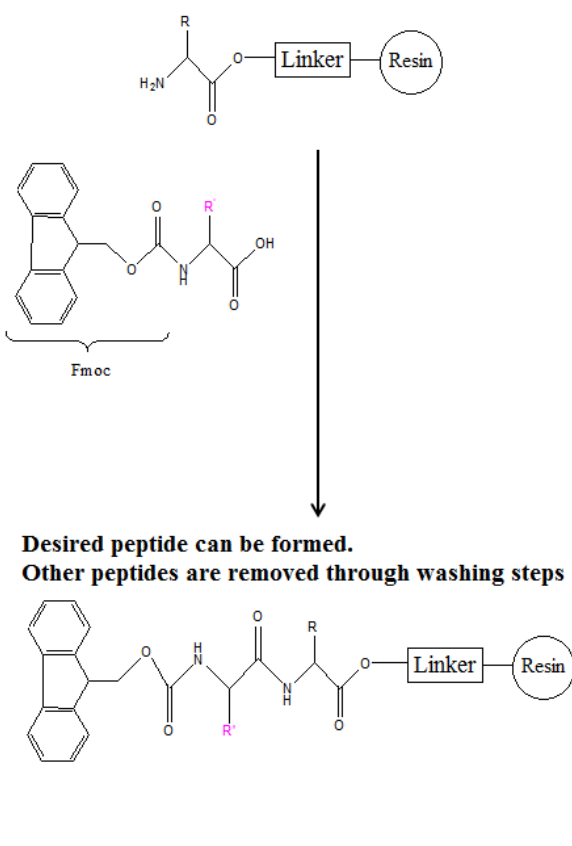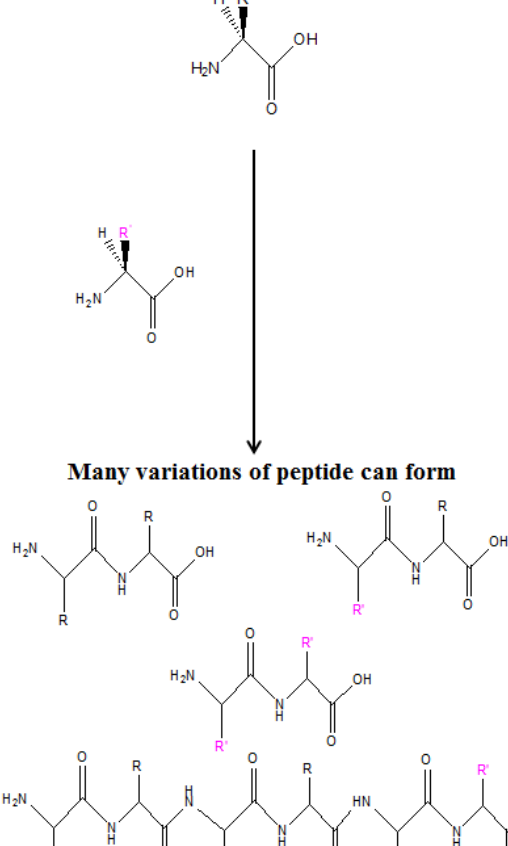
Introducing synthetic methods to synthesize peptide was essential since the conventional biological synthetic methods such as phage display methods were time consuming and tedious. Biological methods had several disadvantages involving extreme conditions that could destroy the phage particles and it was not possible to produce the D- enantio form of the peptides, non-coded peptides or cyclic peptides.[27]

Before the introduction of amino- protecting groups by Emil Fischer in 1903 was successful in coupling two amino acids.[38] However this method was not suitable for producing longer peptides and it was hard to isolate and purify the desired peptide since numerous variations of the peptide could be formed (Table 1.3) when carried out in solution. Which lead to the finding of solid phase peptide synthesis (SPPS) method, which was pioneered by Bruce Merrifield in the early 1960s.[39, 40, 41]

SPPS involves numerous repetitive steps including N deprotection, amino acid coupling, washing and filtration steps. The advantages of using SPPS are that the coupling reactions can be performed more rapidly and to completion without any other variation of the peptide (Table 1.3), by using excess amount of activated amino acids which can be easily separated from the growing peptide during the washing and filtration steps.[40, 41]

Nowadays peptides that range from 30-50 amino acids per peptide can be synthesized manually or by automated systems.[40]

Table 1.3:- Solid phase peptide synthesis Vs. Peptide synthesis in solution.

1.4.6.1 Solid Phase Peptide Synthesis

Matrix polymers are used as the solid support for SPPS. These are often referred to as resins. They are crosslinked polystyrene beads ranging from 100-400 μm in diameter. They have a loading capacity of 0.5-0.8 mmol/g if all the linker sites were accessible. In order to access the buried linker sites the resin should be swelled in DCM (Dichloromethane) and DMF (N, N-dimethylformamide) prior to chemically attaching an amino acid. They contain a linker which allows the anchoring of the N protected C-terminal amino acid moiety (Figure 1.9) to the resin through an ester or amide bond.[41]

There are several different types of resins depending on their linker molecules (Figure 1.10); peptide amides such as Rink amide resin, Pal resin, Sieber resin. Peptide acids,

hydroxymethyl- based resins such as Wang resin, Sasrin resin and HMPB resin. And trityl resins as trityl chloride resin and 2-chlorotrityl chloride resin.[41]

Most of these resins have the first C terminal N-protected amino acids preloaded onto the resin and are commercially available. This is done to avoid the difficult and hazardous methods in linking the first amino acid to the linker for some resins.[40, 41]
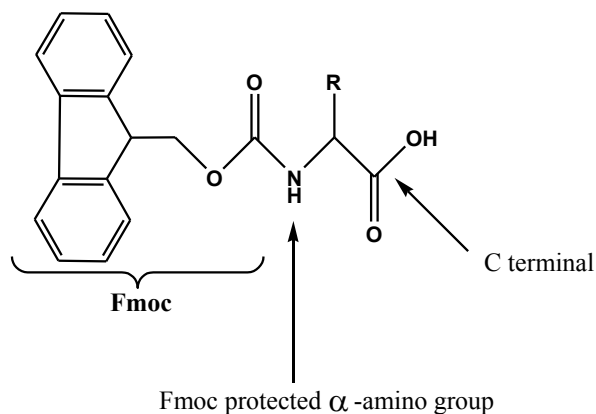
Figure 1.9:- Fmoc protected α- amino C-terminal amino acid.
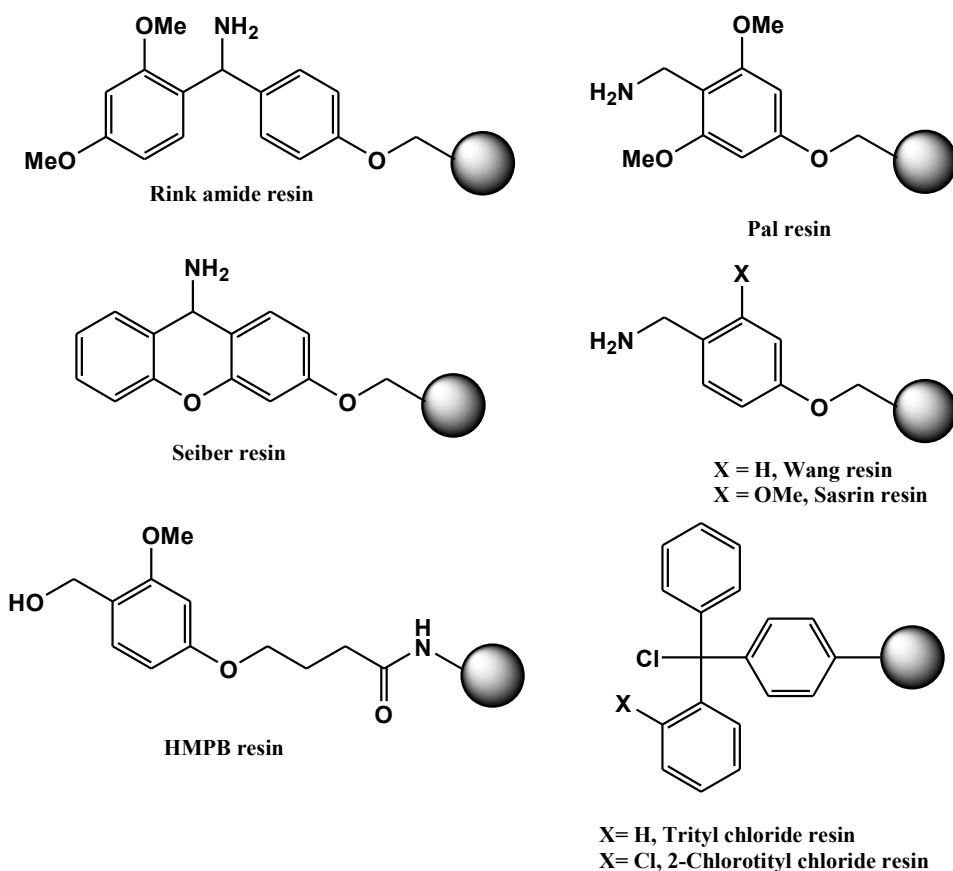
Figure 1.10:- Resins for solid phase peptide synthesis.[41]

1.4.7 Principles of SPPS

SPPS is performed in a glass tube like vessel (Figure 1.11), which has a frit to filter off the solutions by suction filtration. Since the resin beads are fragile mechanical stirring such as magnetic stirring is not preferred. It is necessary to agitate the reaction mixture smoothly to allow the coupling reactions to occur. Here smooth agitation can be performed by rocking, vortexing or swirling by rotary evaporator rotor which is the preferred stirring method.[41]
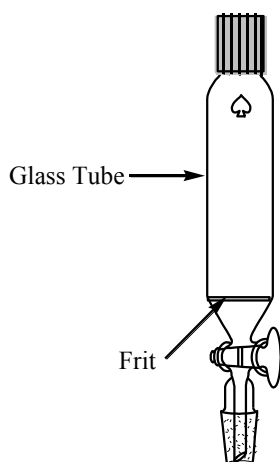
Figure 1.11:- Solid phase peptide synthesis reaction vessel.[41]

The peptide sequence is synthesized from the C-terminus to the N-terminus where the synthesis starts from the opposite direction that the peptide sequence is written in.[41]

The amino acids have protecting groups to avoid side reactions from occurring and to produce the desired peptide sequence accurately. There are two types of protecting groups, which are the temporary protecting groups that protect the α-amino group. This protecting group can be easily removed under mild basic conditions. The Fmoc (9-Fluorenylmethyloxycarbonyl) protecting group is an example for this category of protecting groups. The other type of protecting group is the side chain protecting groups such as Trt (Trityl), Pbf (2,2,4,6,7-Pentamethyldihydrobenzofuran-5-sulfonyl), Boc (*tert*-Butyloxycarbonyl) and tBu (*tert*-Butyl). These groups should be stable during the peptide elongation reaction conditions. These protecting groups are removed in the final step when cleaving the peptide sequence from the resin using TFA (Trifluoroacetic acid).[41]

When coupling an amino acid to the currently synthesizing peptide, an excess of 2-10 times the concentration of amino acid is used compared to the resin. This ensures that the amino acids will attach to all the active sites.[41]

1.4.7.1 Solid Phase Peptide synthesis Protocol

There are many methods to synthesize peptides. In this section the protocol used to synthesize the peptides in our research is described (Figure 1.12).[41]

1. Transfer the amino acid preloaded dry resin into the glass tube.
2. Add DCM into the glass tube to immerse the resin and swirl for 20 min.
3. Remove the DCM by filtration under vacuum.
4. Add DMF into glass tube swirl for 1 min.
5. Remove DMF by filtration under vacuum.
6. Prepare the coupling solution by dissolving 1:3 ratio of resin to amino acid and 1:2.9 ratio of resin to HBTU (O-benzotriazol-1-yl-N,N,N,N -tetramethyluronium hexafluorophosphate) is dissolved in 23:1 ration of DMF: DIEA (N,N-Diisopropylethylamine) coupling solution.
7. Add the coupling solution into the glass tube and swirl for 30 min.
8. Remove coupling solution by filtration under vacuum.
9. Repeat steps 6, 7 and 8.
10. Wash resin 4 times with DMF swirl for 30s each and filter solution each time.
11. Add 20% piperidne in DMF solution to deprotect the Fmoc protected α- amino group swirl for 1 min and filter solution by vacuum.
12. Again add 20% piperidne in DMF solution and swirl for 10 min and filter solution by vacuum.
13. Wash resin 5 times with DMF swirl for 30s each and filter solution each time.
14. Repeat steps 6 to 13 until desired peptide sequence is synthesized.
15. Cleave peptide sequence from resin and side chain protecting groups by adding cleavage cocktail of TFA: TIPS (Triisopropyl silane): water at a ratio of 95:2.5:2.5 per 100mg of resin.
16. Swirl for 3 hrs.
17. Filter peptide solution into cold ether (Peptide will precipitate in cold ether).
18. Centrifuge and decant ether.

19. Add cold ether vortex to wash peptide and centrifuge.

20. Centrifuge and decant ether.

21. Repeat steps 19 and 20.

22. Dry precipitated peptide under argon and store in -20^{0}C freezer for later use.
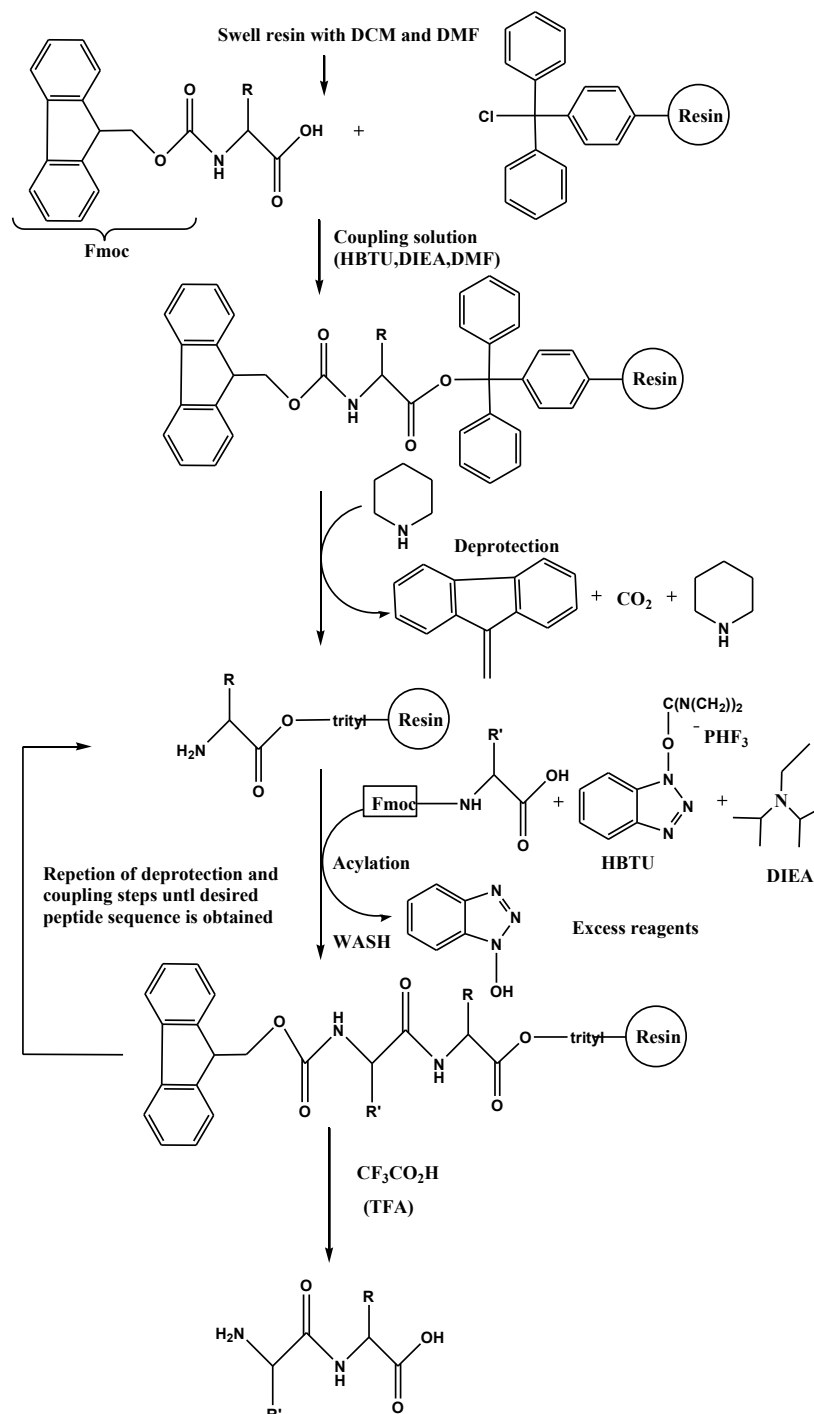
Figure 1.12:- Solid phase peptide synthesis

1.4.8 Peptide Purification and Characterization

A peptide that has been synthesized by SPPS should be purified and isolate from impurities prior to characterization. High performance liquid chromatography (HPLC) is the ideal method to separate peptides, depending on their distribution between the mobile and stationary phase. Subsequently to HPLC, characterization of the purified peptide can be performed by Mass spectrometry.

1.4.8.1 High performance liquid chromatography

The frequently used HPLC methods are size- exclusion HPLC, ion exchange HPLC and reversed-phase HPLC (RP-HPLC). The most preferred choice of HLPC used for peptide separation is RP-HPLC due to its efficiency, speed and excellent resolving ability. Therefore it can separate peptides that are nearly identical in sequence. This method is useful for both analytical and preparative separations.[11, 42, 43]

The separation of peptides is mainly carried out at pH values below pH 3. Here acidic volatile mobile phases such as aqueous TFA and acetonitrile systems are used. Since TFA is volatile it eliminates the desalting step of the peptides. Undesired ionic interaction between positively charged amino acid moieties and unfunctionalized silanol groups of the silica based stationary phase are avoided by the acidity of the mobile phase.[43]

The chromatographic behavior of peptides can be influenced by counter ions. Peptides are charged at most pH values due to their zwitterionic nature. Therefore the anionic counterion TFA$^-$ can neutralize positively charged basic side chains. And cationic counterions such as triethylammonium can be used to neutralize negatively charged acidic side chains. The TFA concentration range that can be used is 0.2- 0.25% to separate peptides. In order to separate hydrophobic peptides a mobile phase with a high ionic strength is used. To achieve this sodium chloride or ammonium sulfate is used in high concentrations of 1-2 mol/l. Here the salts attract water allowing hydrophobic interactions of the peptides and stationary phase to occur.[11, 43]

Next the peptide is eluted by the use of aqueous and nonpolar mobile phase. Nonpolar solvents such as acetonitrile, methanol, ethanol, tetrahydrofuran, 2-propanol can be used. Here the gradient of the nonpolar solvent is gradually increased until the peptide is eluted. The preferred RP-HPLC packing material for the stationary phase is funcionalized silica based supports they are covalently bound to octyl (C_8) or octadecyl (C_{18}) hydrocarbon chains.[11, 43]

The mechanism by which peptides are separated by RP-HPLC involves adsorption and desorption of the peptide between the mobile and stationary phases. Peptides are too bulky to partition into the hydrophobic stationary phase therefore they adsorb onto the hydrophobic surface and remain adsorbed until the organic solvent in the mobile phase reaches a concentration that could desorbs the peptide into the mobile phase and are eluted (Figure 1.13).[44]

Next the eluted peptides are detected by means of ultraviolet (UV) light detection. Peptide bonds absorb UV at the far UV region generally at 210-220 nm. However if the peptide contains tyrosin, phenylalanine or tryptophan amino acid residues they can also absorb in the UV range of 250-290 nm.[43]
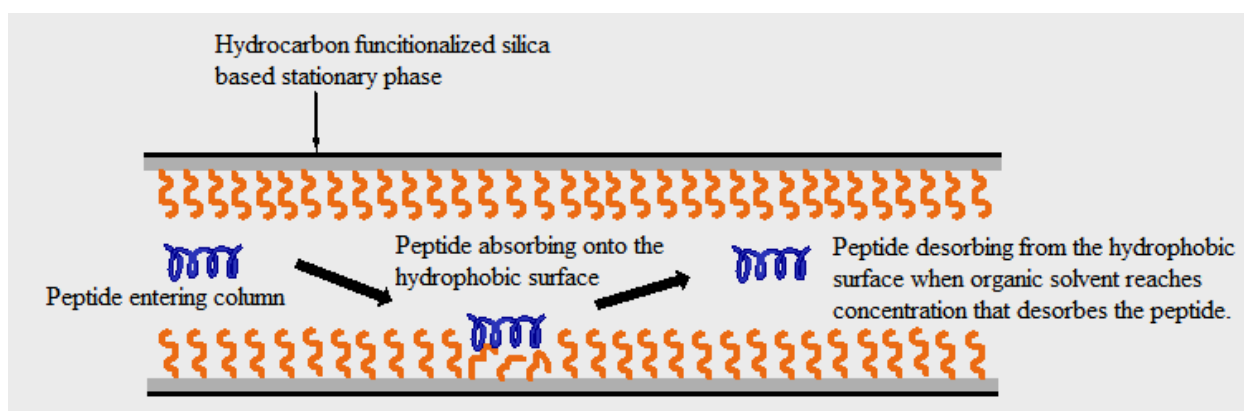
Figure 1.13:- Separation of peptides in RP column by absorption and desorption method.[44]

1.4.8.2 Peptide Characterization by Mass Specrometry

After purifying the peptide sequence by HPLC, it should be characterized to identify the correct peptide sequence. Since there could be peptides that were synthesized half way through or close to the final peptide sequence. The best technique used to analyze peptides is mass spectrometry (MS). The advantages of using MS are that peptides can be analyzed at a low detection limit of 1 pmol. It also provides fast and accurate results of the peptides molecular weight giving rise to instant identification. Nowadays there are instruments containing both HPLC and MS which is much convenient in identifying peptides accurately and quickly (Figure 1.14).[11]

Separation of molecules in MS is based on the size and charge of the molecule. For the analysis to be done the molecules that are in solution or solid phase should be converted into gas phase ions. To achieve this, the capillary that carries the analyte solution is subjected to a voltage difference which creates small charged droplets with many analyte particles in it. The droplets are evaporated until the surface tension of the droplet cannot hold these analytes in due to the charge that builds up on its surface. Therefore the droplets burst releasing bare ions of the analyte (Figure 1.15).[11]
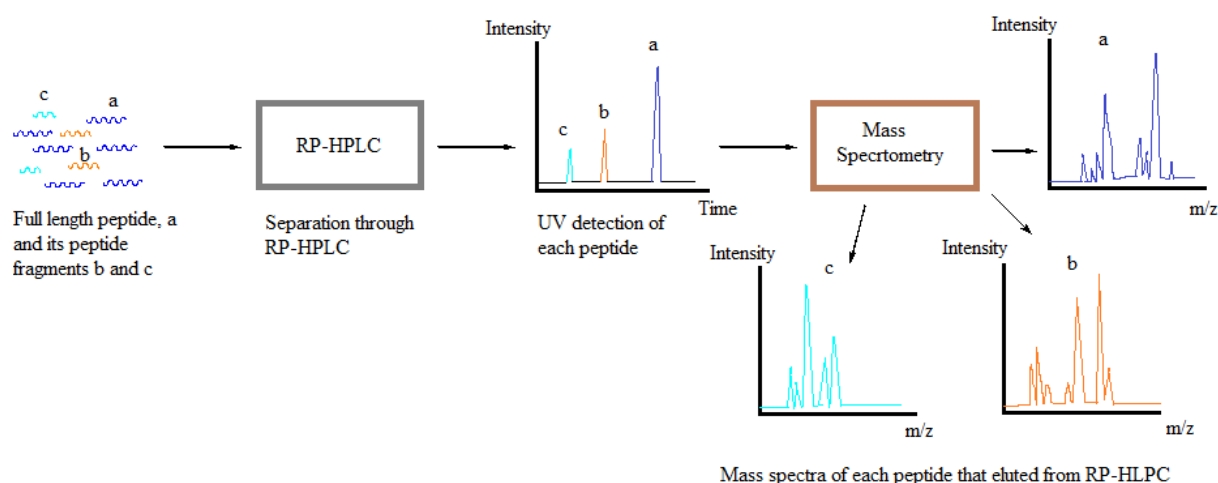
Figure 1.14:- RP-HPLC and MS coupled instrument flow chart.[28]
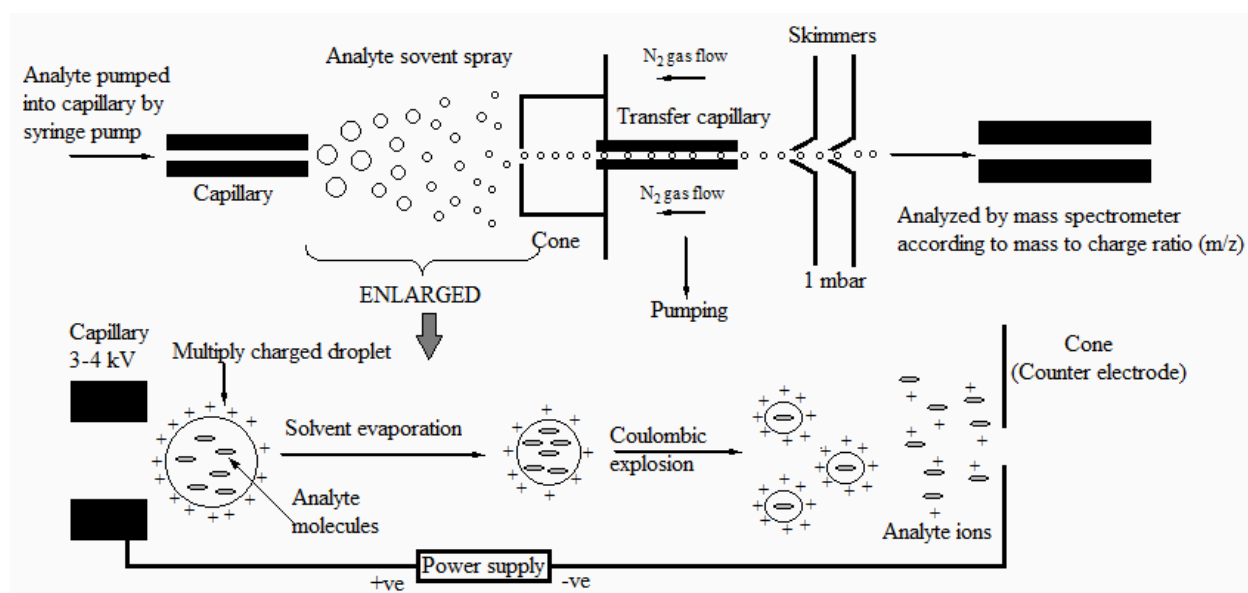
Figure 1.15:- Separation of molecules by mass spectrometry.[11]

Next the ions are separated depending on their mass-to-charge ratio in vacuum using the mass analyzer. These ions are detected by the charge induced or current produced when it hits the detector, which is mainly an electron multiplier. This next produces a mass spectrum of the analyte.[11]

1.4.8.3 Prediction of Peptide Properties

Nowadays peptide properties can be predicted through online software tools. They can calculate the peptides molecular weight, acidic, basic and neutral residue compositions, its hydrophobic nature, isoelectric point, charge and their structure prediction just by entering the peptide sequence in the software. This is a convenient method to get instant information about any peptide.

The properties of the peptide that we have used in our research has been predicted by the peptide property calculator of the Biosyn website; (http://www.biosyn.com/PeptidePropertyCalculator / PeptidePropertyCalculator.aspx) which is supported by a biotechnology company called Bio-synthesis, Inc. The properties predicted are as below;

CGKRK($_D$[KLAKLAKKLAKLAK])PLFAERL include a molecular weight of 2923.87 g/mol and its sequence composition consists of 3.85% acidic residues, 7.69% neutral residues, 38.46 % basic residues and is 50% hydrophobic in nature. It has an isoelectric point of 11.47 and a charge of +9. Its ($_D$[KLAKLAKKLAKLAK]) sequence is an alpha helical structure, its CG part can form turns in the peptide and its PL part can be responsible for forming beta structures (Figure 1.16).
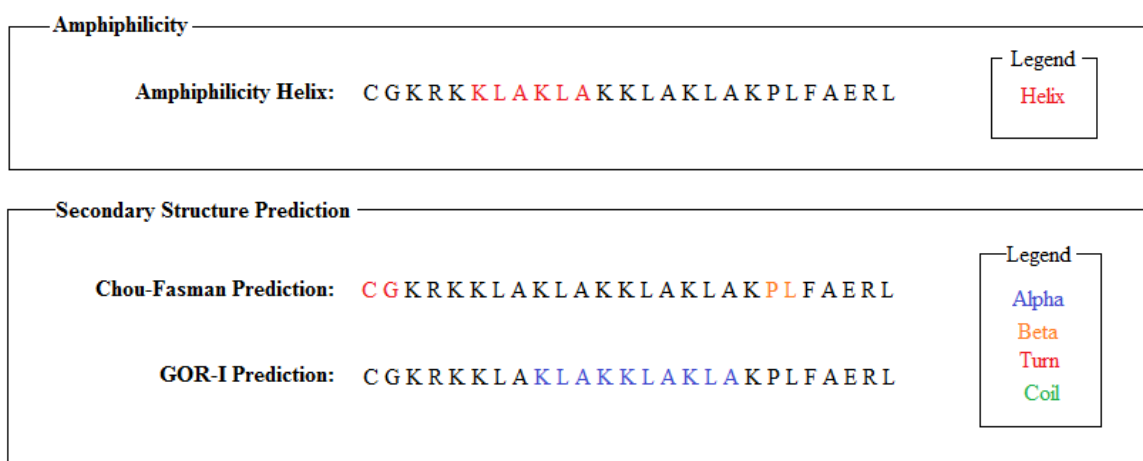
Figure 1.16:- Peptide structure predicted by Bio-synthesis peptide property calculator.[45]

1.5 Iron Chelators

Metal-ion chemistry of transition metal chelators has a wide range of important implications in chemical and biochemical areas.[46] These chelators are polydentate ligands, which from stable complexes with hard Lewis bases as donor atoms such as O, F, or with soft Lewis bases as N and S.[47, 48]

Metal chelators are known to be involved in various metabolic and cellular pathways. Examples can be found in the photosynthesis in plants using chlorophylls (Figure 1.17), respiration in animals using hemoglobin (Figure 1.17) and many enzymes using metals as cofactors in metabolism.[46]
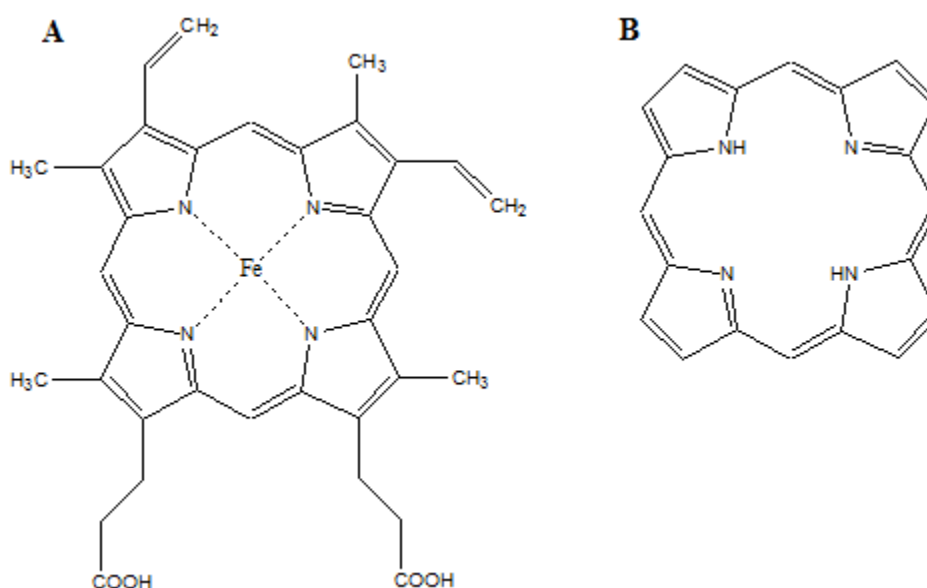
Figure 1.17:- A. Porphyrin of hemoglobin (http://en.wikipedia.org/wiki/File:Heme.svg)[49]

B. Chlorin of chlorophylls (http://en.wikipedia.org/wiki/Chlorin)[50]

Among the diverse group of metal chelators, iron chelators show a wide variety of applications. They have been used against iron overload diseases, as antimicrobial agents, antimalarial agents, anti-inflammatory and anticancer agents. In the past few years great interest has been shown in iron chelators due to their anticancer activity.[51]

Metal selectivity and metal-ligand complex stability are the properties that govern the design of iron chelators in clinical use. Since iron (III) complexes are more stable than iron (II)

complexes the specifications such as metal selectivity, affinity, kinetic stability of the complex and bioavailability and toxicity should be carefully considered in designing iron (III) chelators.[51]

For the proliferation of cancer cells, iron is needed as an essential micro nutrient for its cell cycle progression and DNA synthesis.[52, 53] Therefore depriving cancer cells of iron using iron chelators can be used as a therapeutic approach for against cancer.[54]

1.5.1 Bioinorganic Chemistry of Iron

In the earth's crust iron (Fe) comes fourth after O, Si and Al when the number of atoms are counted. Counting by weight, it is the 2nd most abundant metal, which makes up 6.2 % of the earth's crust.[47]

Iron plays an important role in the metabolism of plants and animals. It is an essential micronutrient for both. However, it is toxic in larger quantities. Iron is the most important transition metal element in biological processes such as;[47]

- As oxygen carrier in blood through hemoglobin.
- For oxygen storage in muscular tissues by myoglobin.
- As an electron carrier in cytochromes and electron transfer in ferredoxins in plants.
- For iron (Fe) storage and transport using ferritin and transferrin (Tf) proteins.
- In various enzymes, such as ribonucleotide reductase, catalase and peroxidase.

The total iron level maintained in a normal human body is 4 g, which is absorbed through food as ferrous ion (Fe^{2+}). Since iron is required in small amounts it is recycled in the body. The iron absorbed is bound to transferrin, which transports Fe to the bone marrow converting it into ferritin. The majority of iron is bound to hemoglobin. About 20-30 % is bound to the iron storing protein ferritin and its lysosomal degradation product hemosiderin. 10 % of iron is present in myoglobin, cytochromes and other iron containing enzymes.[47, 55, 56]

Only 1-3 mg/day of iron is absorbed by humans and about the same amount of iron is lost by cell desquamatation. Cellular iron is tightly controlled by the transferrin receptor (TfR) and ferritin proteins, which are regulated by iron responsive proteins (IRP's) (Figure 1.18).[47, 55]
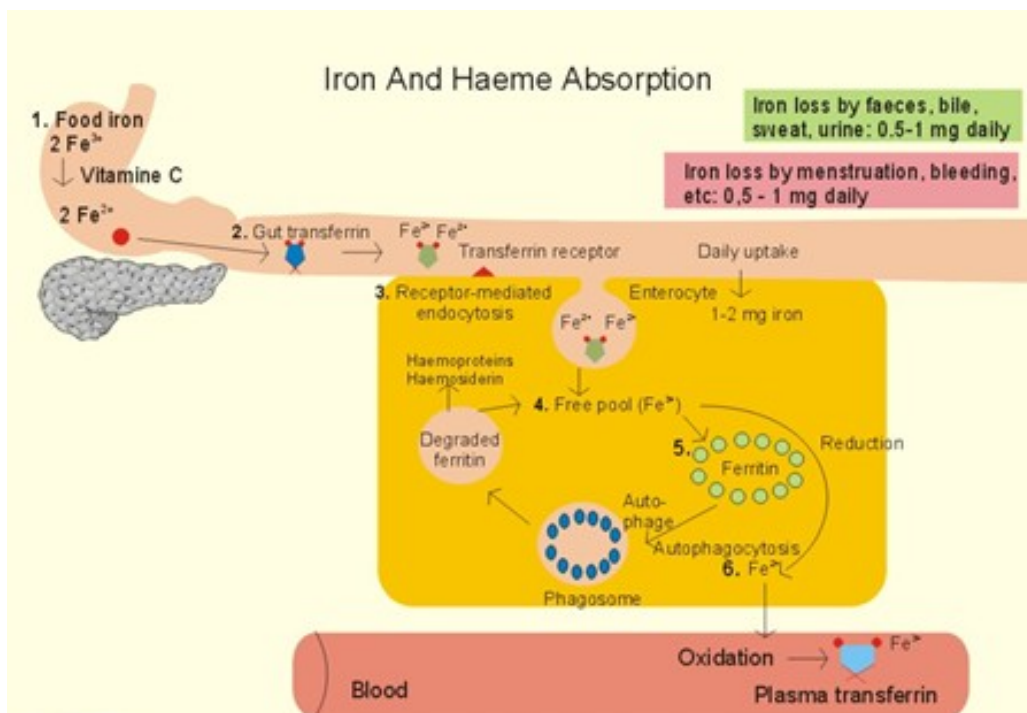
Figure 1.18:- Iron absorption, transportation and storage in the body.

http://www.zuniv.net/physiology/book/chapter22.html[57]

1.5.2 Iron in Cancer

The metabolism of iron in cancer cells is altered. Cancer cells have an increased need for iron to facilitate their high proliferating rate.[32,58] The iron uptake into cancer cells is increased by the elevation of iron regulatory proteins such as transferrin receptors (Figure 1.19).[55]

The need of iron is essential for various cellular processors such as cell proliferation, DNA synthesis and mitochondrial electron transport. Iron is important for the function of ribonucleotide reductase, which is an enzyme that reduces ribonucleotides to deoxyribonucleotides for DNA synthesis and repair. This is the rate-controlling step of DNA biosynthesis. This enzyme is closely correlated with cellular replication in the G_1-S phase of the cell cycle. Since deoxyribonucleoside triphosphates are in low concentrations in cells, it would be a good strategy to inhibit the enzyme, ribonucleotide reductase. This, in turn, causes inhibition of cellular proliferation in cancer cells.[6, 59]

31

Manipulating the iron content in the cancer cells could be a good strategy to destroy cancer cells. This can be done by the use of iron chelators. Iron chelators will have a double impact: Firstly, they will be depleting iron through chelation and inhibiting ribonucleotide reductase, thus inhibiting cell proliferation. The second method is that iron chelators can be used to bind to intrasomal iron to form redox active chelators to produce cytotoxic reactice oxygen species through the Fenton reaction promoting programmed cell death (apoptosis) in cancer cells.[54, 55]
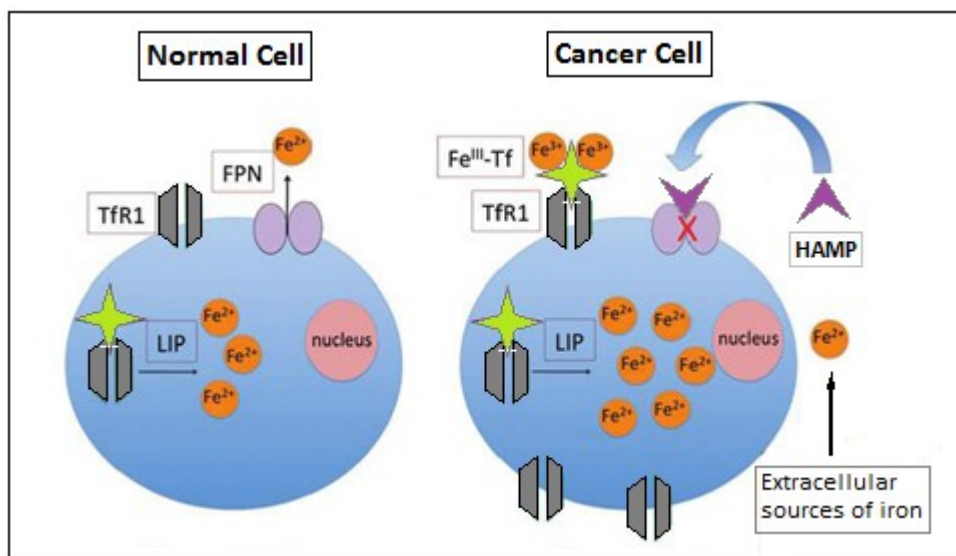
Figure 1.19:- Iron regulation in normal and cancer cells.

The iron regulatory proteins or chemistry involved in cellular metabolism include FeIII-Tf, iron III bound to transferrin; FPN, ferroportin; HAMP, hepcidin; LIP, labile iron pool; and TfR1, transferring receptor. In cancer cells, compared to normal cells LIP is higher; HAMP is higher; FPN is lower; and there are more of TfR1 as well as potential extracellular sources of iron such as macrophages and lipocalins.[55]

1.5.3 Role of Lysosomes and Mitochondria in programmed cell death

In order to find a suitable method to stop the uncontrolled and rapid cellular proliferation of cancer cells, it would be a better strategy to trigger programmed cell death in these cells than to rely on necrosis, because the latter causes massive inflammation.

To understand how to trigger apoptosis in cancer cells the answer may be found by studying normal cellular mechanisms that mediate cell death.[58]

The two main organelles that are involved in apoptosis are the mitochondria and lysosome. It is well known that reactive oxygen species that are produced due to oxidative stress as a byproduct in mitochondrial respiration. Reactive oxygen species (ROS) are toxic to cells and lead to apoptosis.[58, 60, 61]

Resent research shows that the lysosome also plays a major role in apoptosis. Lysosomes are vacuolar organelles, which are acidic and contain hydrolytic enzymes. Their function is to degrade intra- and extra-cellular substrates that have been taken up through autophagy and endocytosis, and to recycle biomolecules, such as sugar, amino acids and fatty acids.[32, 60]

Autophagy of organelles, such as mitochondria and macromolecules (e.g. metalloproteins, cytochromes, hemoglobin, myoglobin, catalase and other enzymes) lead to lysosomes that are concentrated in redox active iron (Figure 1.20).[32, 60]
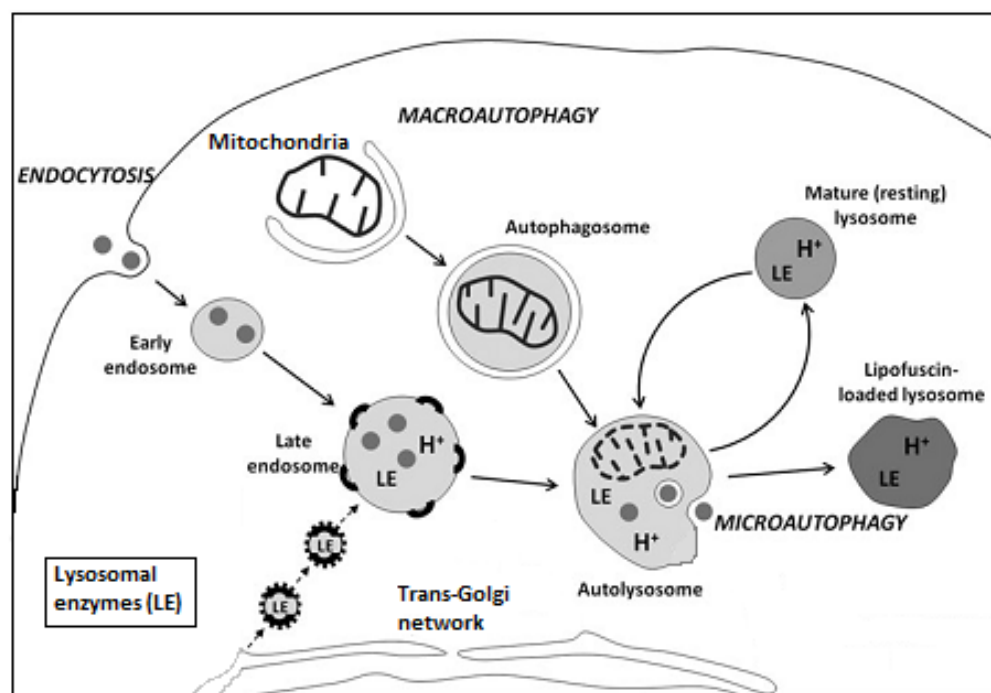
Figure 1.20:- Schematic representation of endocytosis and the different autophagic pathways.[32]

The acidic environment (pH 4.5-5.5) and the presence of reducing agents such as cysteine and glutathione reduce the ferric ion (Fe(III)) to the redox active ferrous ion (Fe(II)) form. Superoxide anion radicals, which are formed in lysosomes due to mitochondrial degradation, can also participate in the formation of Fe (II) ions These processes are commonly described as Haber-Weiss reaction cycle.[32, 60]

The redox active ferrous ion (Fe^{2+}) reacts with hydrogen peroxide (H_2O_2) through the Fenton reaction producing highly toxic hydroxyl radicals ($HO^\bullet$). Here oxidized ferric ion (Fe^{3+}) is reduced back to Ferrous ion via the Haber Weiss reaction with superoxide anion. These toxic reactive species (ROS) can damage biomolecules and DNA, resulting in cell death (Figure 1.21).[32, 55, 61]

$$Fe^{2+} + H_2O_2 \longrightarrow Fe^{3+} + {}^\bullet OH + {}^- OH$$

$$\Downarrow$$

Damages DNA/ other biomolecules
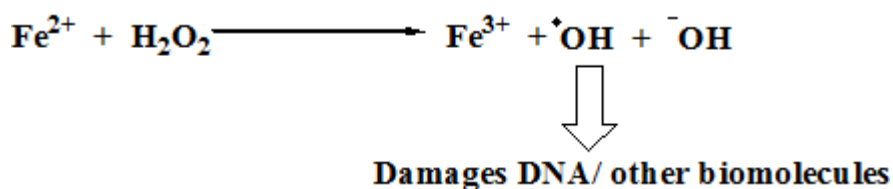
Figure 1.21:- The Fenton reaction.[55]

As a result of higher level of oxidative stress the lysosomal membranes get damaged due to high levels of oxidants or iron overload. As a consequence, lysosomal enzymes are released into the cytosol, triggering apoptosis.[32] ROS can also disrupt electron transfer in mitochondria and cause apoptosis.[61] These two pathways can be activated independent from each other, however, synergy can be observed.

Therefore, by manipulating iron concentrations in the lysosomes of cancer cells, we can trigger apoptosis. Iron chelators form complexes with iron, transforming them into Fe(II)-species with significantly higher redox activity than uncomplexed Fe(II). These redox active Fe(II) complexes can facilitate ROS formation and induce apoptosis in cancer cells (Figure 1.22).[55]

1.5.4 Iron Chelators for Therapy

In chelation therapy the iron concentration in the body should be maintained at normal levels inorder not to deplete the iron in the body. Furthermore, toxicity by chelation or the

chelation agent itself should be avioded. The chelator should be effective at the lowest dose possible.[51]

The iron, which is stored as ferritin or hemosiderin is not readily accessible by chelators at a convinient rate, because it is bound too tightly. Therefore, chelation therapy depends on the weakly bound low-molecular- weight iron, referred to as 'labile iron pool' (LIP). It comprises of both forms of iron (Fe^{2+} and Fe^{3+}) and represents < 5 % of the total iron in the cell (50-100 μM). This accessible iron is bound to various ligands with low affinity.[51]
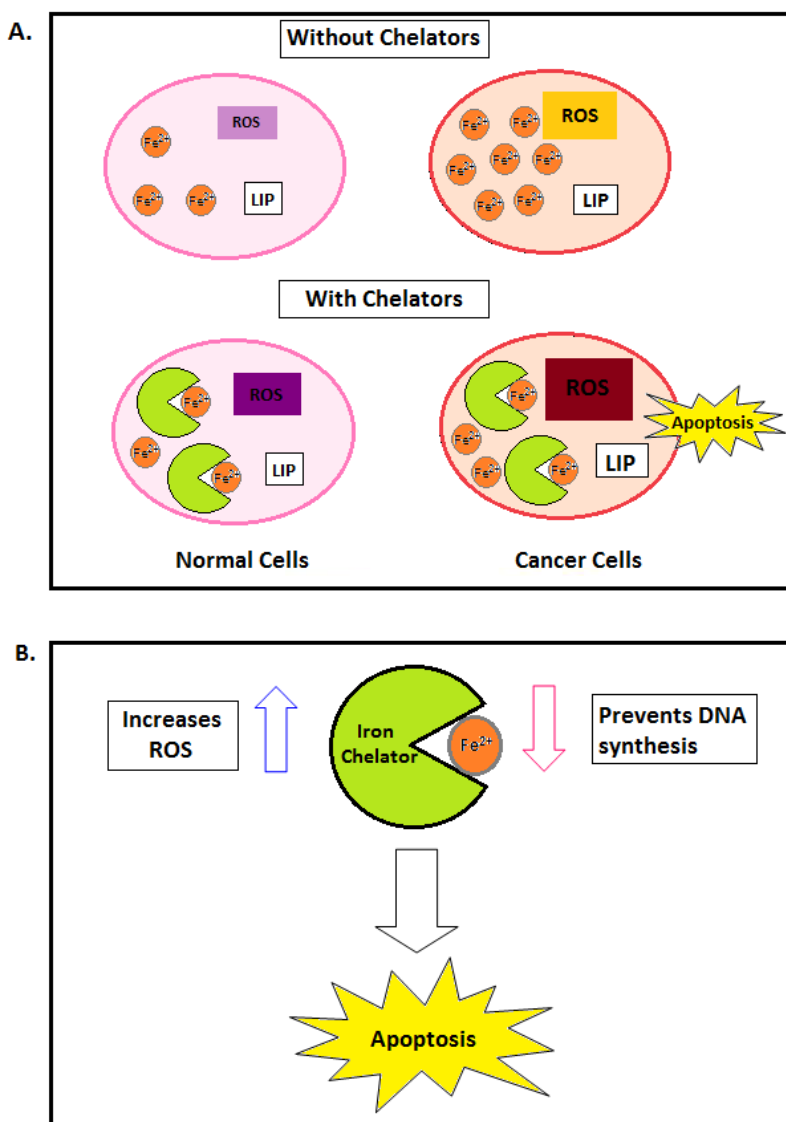
Figure 1.22:- A. Effects of cancer and normal cells treated with iron chelators.
B. Iron chelator effects on cancer cells.[55]

The LIP iron is complexed with low-molecular weight organic chelators such as organic anions (phosphates, carbohydrates and carboxylates), polypeptides, citrate, phospholipids, nucleotides and nucleosides. These LIP's are available for interaction with iron chelators, because the latter bind (usually Fe(II)) more tightly.[51, 62, 63]

Iron chelation therapy was traditionally used to relieve iron overload in patients with diseases such as β thalassemia, sickle cell disease and myelodysplasia, where the patients received multiple blood transfusions as treatment.[64, 65]

However, there is an emerging need for iron chelators for diseases such as cardiovascular diseases, atherosclerosis, neurodegenerative diseases, chronic inflammatory diseases and cancer where oxidative stress plays a major cause.[65]

Naturally synthesized chelators are found in bacteria and fungi called siderophores. They are secreted to scavenge and absorb iron from the environment. Desferrioxamine is an example for one of these natural chelators.[58]

The chelator preference towards Fe^{2+} or Fe^{3+} depend on their chemical properties and binding with iron in iron:chelator ratios of 1:1, 1:2, 1:3. They also have the ability to favor or restrict of binding iron to redox cycle.[58]

1.5.5 Designing Iron Chelators

Iron chelators should be designed by considering the following characteristics; metal selectivity and affinity, kinetic stability of the complex, bioavailability and toxicity. These characteristics are important for clinical use.[51, 64]

1.5.5.1 Metal Selectivity and Affinity

Metal selectivity and ligand-metal complex stability are the major properties that are important in designing iron chelators.[66]

Due to the incompletely filled d- orbital's of iron it has has several valences. Its most common oxidation states in aqueous media are Fe^{2+} and Fe^{3+}.[64] Iron chelators are usually small molecules with molecular mass of approximately 100-900 Da.[58] They can be designed to bind to either Fe^{2+} or Fe^{3+} oxidation states by following the 'hard' and 'soft' acid and base concept.[64, 66]

Chelators containing 'soft' donor atoms such as nitrogen and sulfur such compounds would be 2,2′-bipyridyl (Figure 1.23) and 1,10-phenanthroline (Figure 1.23) prefer the borderline

Lewis acid iron (II). Fe (II) has a high electron density and lower charge density. Which poorly interacts with oxygen donor atom containing compounds. It is also unfavorable to maintain its optimal complex geometry due to low ratio of charge to ionic radius of Fe (II) compared with Fe (III).[48, 64] They can also bind to other biological metals such as copper (II) and zinc (II) ions (Table 1.4). Therefore it is close to impossible to synthesize non-toxic iron (II) selective chelators.[66, 67]

Table 1.4:- Metal affinity constants of ligands with ions[67]

Ligand	Log Cumulative stability Constant					
	Fe (III)	Al(III)	Ga(III)	Cu(III)	Zn(II)	Fe(II)
Desferrioxamine (DFO)	30.6	25.0	27.6	14.1	11.1	7.2
2,2′-bipyridyl	16.3	-	7.7	16.9	13.2	17.2
1,10-phenanthroline	14.1	-	9.2	21.4	17.5	21.0
N, N-Dimethyl-2,3-dihydroxybenzamide (DMB)	40.2	-	-	24.9	13.5	17.5
Acetohydroxamic acid	28.3	21.5	-	7.9	9.6	8.5
Deferiprone	37.2	35.8	32.6	21.7	13.5	12.1
EDTA	25.1	16.5	21.0	18.8	16.5	14.3
DTPA	28.0	18.6	25.5	21.6	18.4	16.5
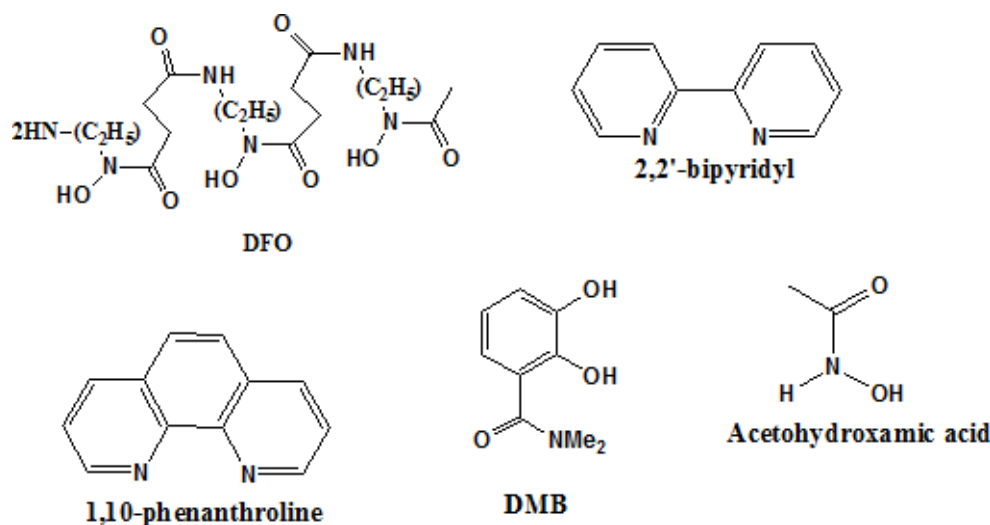
Figure 1.23:- Structures of iron chelators.

Structures of iron chelators continued…………
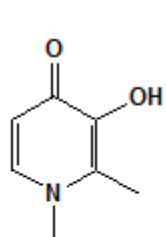
Deferiprone
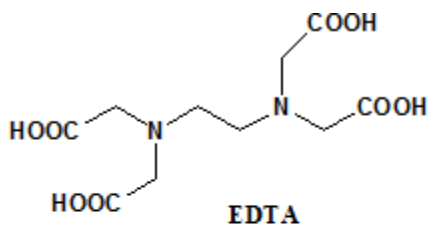
EDTA
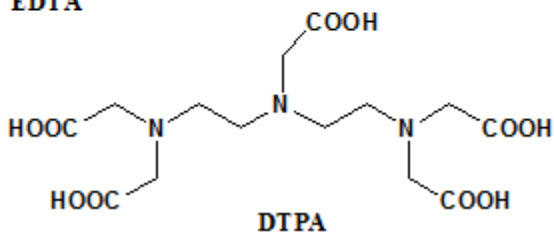
DTPA
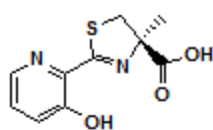
Desferrithiocin
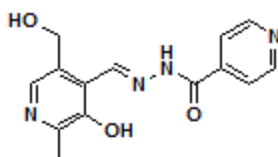
Pyridoxal isonicotinoyl hydrazone (PIH)
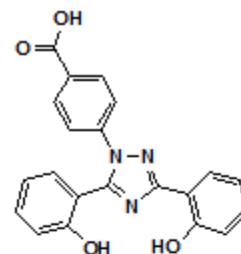
ICL 670A
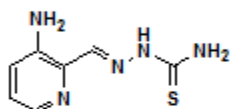
Triapine (3-aminopyridine-2-carboxaldehyde thiosemicarbazone)
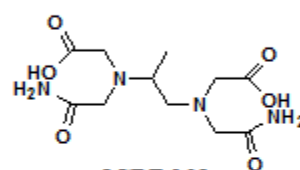
ICRF-198
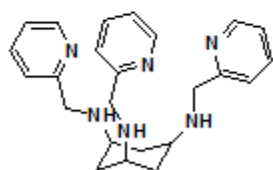
Tachpyridine
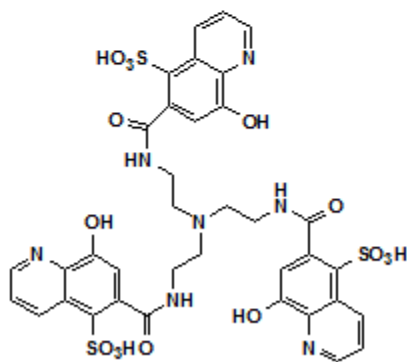
O-Trensox

Structures of iron chelators continued…………
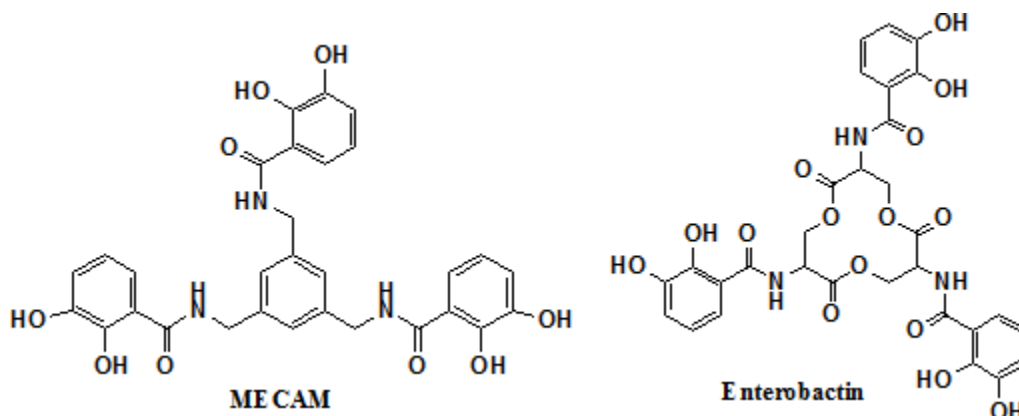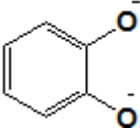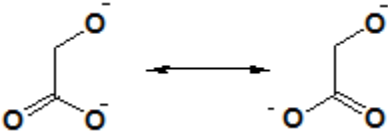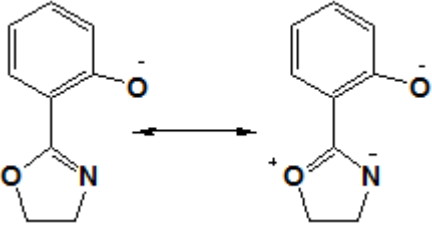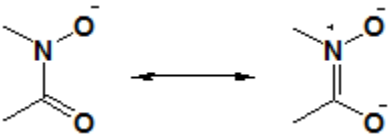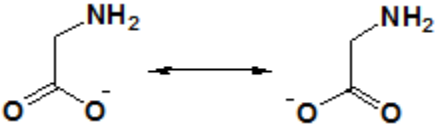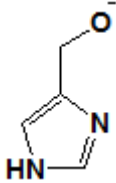
Oxygen containing chelators are more selective to high-spin d^5 configuration of iron (III). It has a radius of $0.65^{\circ}A$ and is a spherically symmetrical tri-fold positive cation with a high charge density. Ligand field stabilization energy is not provided for this configuration, however it is kinetically stable. It also forms strong ionic interactions with weakly polarizable oxygen atoms in ligand such as oxyanions, hydroxamates and catecholates, which prefer tribasic metal cations than dibasic cations.[48, 51, 66]

Furthermore, when the charge on the oxygen atom increases the affinity towards iron (III) also increases. The pKa values of oxygen also affects the affinity towards iron (III). Therefore increasing the affinity, when the pKa value increases (Table 1.5).[47, 68]

Most tribasic ions such as aluminium (III) and gallium (III) are not essential for cells than iron (III). Therefore iron (III) chelators are more suitable for clinical use. High affinity iron (III) chelators can also chelate iron (II) and undergo oxidation in aerobic conditions to form iron (III). Therefore high affinity iron (III) chelators can bind to both iron (II) and iron (III) in physiological conditions.[58, 66, 69]

The common geometry of iron (III) chelators is octahedral where six ligands are arranged around the iron with minimum ligand repulsion. And it favors the thermodynamically stable high- spin iron (III) species. However this octahedral field may be distorted or the incorporation of nitrogen or sulfur donor atoms reduce the affinity for iron (III).[68]

Table 1.5:- Ligand pKa values[68]

Compound	Ionic Structure
Catecholate (9.2, 13.0)	
α-Hydroxycerboxylate (3.0, 14.5)	
Hydroxyphenyloxazolone (9.0)	
Hydroxamate (9.0)	
α-Aminocarboxylate (2.5, 9.5)	
α-hydroxyimidazole (6.0, 14.5)	

1.5.5.2 Thermodynamic Stability of Iron Complexes

In biological environments the iron chelators must compete with biological iron binding ligands. The important factors to consider, when considering them as therepeutic agent, are the affinity of these chelators towards iron and stoichiometry of iron binding.[58]

The classification of ligands is done according to the number of donor atoms available in a ligand. Therefore if a ligand contains 2 donor atoms they are referred to as bidentate ligands and if they contain 3 donor atoms tridentate, likewise 4 atoms tetradentate, 6 atoms hexadentate or in general multidentate ligands.

The number and size of chelate rings formed in the ligand-metal complex is important when determining the thermodynamic stability of the metal complex. Therefore increasing stability can be done by incorporation of all donor atoms into a single ligand creating a hexadentate ligand. By increasing the number of donor atoms in the chelator we can increase the number of chelating rings. Ring sizes of five and six donor atoms are the most favorable. For an example a metal with co-ordination number six forms 3 rings with a bidentate ligand and five ring with a hexadentate ligand (Figure 1.24).[66]

Bidentate Ligand   Tridentate Ligand   Hexadentate Ligand

3:1 Complex   2:1 Complex   1:1 Complex
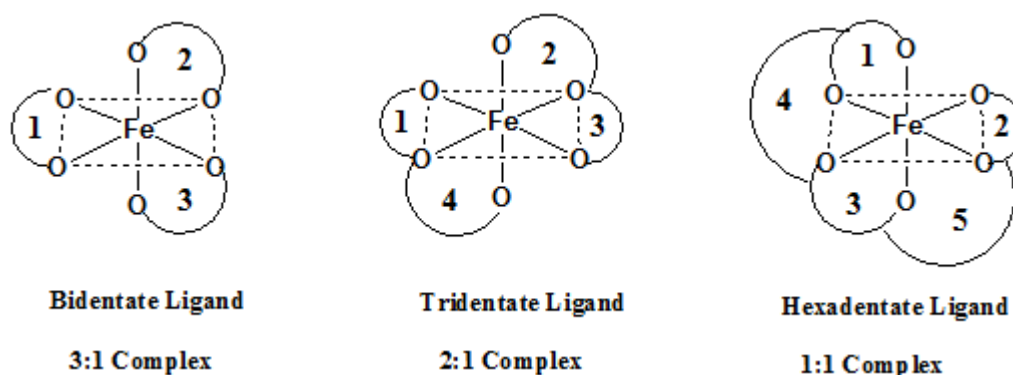
Figure 1.24:- Representation of chelate ring formation in metal-ligand complexes.[66]

The equilibrium between a metal ion (M) and ligand (L) can be expressed in the equation 1.

$$M \quad + \quad xL \quad \rightleftharpoons \quad ML_x \qquad \text{Equation 1}$$

And it's equilibrium constant as equation 2;

$$K \quad = \quad \frac{[ML_x]}{[M]\,[L]^x} \qquad \text{Equation 2}$$

41

When the ligand is completely deprotonated the strength of metal-ligand complex include the parameters overall formation constant (β) which is equal to equilibrium constant K (equation 2). But it is important to consider that the chelators are not fully deprotonated under physiological conditions and it is useful to use the conditional stability constant K_{pH}.[58]

The value pM is most important since it takes into account the stoichiometry of metal complexes formed by different metal complexes. pM is given by the equation 3, at a given pH and specific ligand and metal ion concentration. More effective metal ion binding is shown at higher pM values.[58]

$$\textbf{pM} \ = \ \textbf{-log[M]} \qquad\qquad \text{Equation 3}$$

The ligand metal complex stability increase is due to the entropic changes produced when formation of the ligand metal complex from free ligand and solvated free metal (scheme 1).[66]

Scheme 1:-

$$Fe(H_2O)_6^{3+} + \quad 3L_B \quad \overset{\beta_3}{\rightleftharpoons} \quad Fe(L_B)_3 \ + \ 6H_2O$$

$$Fe(H_2O)_6^{3+} + \quad 2L_T \quad \overset{\beta_2}{\rightleftharpoons} \quad Fe(L_T)_2 \ + \ 6H_2O$$

$$Fe(H_2O)_6^{3+} + \quad L_H \quad \overset{K_1}{\rightleftharpoons} \quad Fe(L_H)_3 \ + \ 6H_2O$$
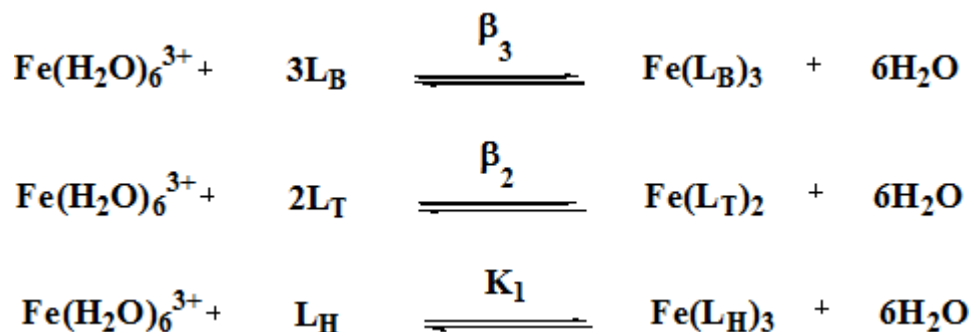
A comparison of pM values of bidentate, tridentate and hexadentate chelators are shown in table 1.6. Here we can see that the ligand concentration can also influence the affinity of metal: ligand complex.[42] For an example 3 log units of stability is observed in the hexadentate ligand MECAM (Figure 1.23) than the bidentate lidgand N,N-dimethyl-2,3-dihydroxybenzamide (DMB) (Figure 1.23) with iron (III). Although this is so there are other hexadentate ligands that bind (III) even more tightly, such as enterobactin (Figure 1.23).[66]

Here the stability of the complex increases when the conformational space of the free ligand is small. The entropy difference decreases when the flexibility of this ligand and its iron complex decreases, this is called "pre-organization".[58,66] The pocket size for iron can be designed precisely in larger ligands. An example is tachpyridine (Figure 1.23) where its closed

conformation favors Fe^{2+} since its donor atom arranges around a space that accommodates Fe^{2+} and is similar to the conformation when Fe^{2+} is inserted.[58]

EDTA (Figure 1.23) can change its conformation since it has several pendant arms but some ligands such as the planar tridentate ligands PIH and ICL670A which are rigid structures can not change their conformations for ligand exchange, providing their kinetic inertness and limits their participation in redox reactions.[58]

Table 1.6:- Affinity of different chelators for iron[58, 66]

$pFe^{3+} = -\log[Fe^{3+}]$ when $[Fe^{3+}]_{total} = 10^{-6}$ M and $[ligand]_{total} = 10^{-5}$ M at pH7.4

Stoichiomerty	pFe^{3+}	Log Stability constant (logK$_{7.4}$)
1:1 Stoichiometry		
DFO	26.6	25.6
O-Trensox	29.5	28.5
ICRF-198	18.8	17.8
DTPA	24.7	23.8
EDTA	23.2	22.2
1:2 Stoichiometry		
PIH	23.2	27.4
Desferithiocine	20.3	24.5
ICL670A	25.4	29.6
1:3 Stoichiometry		
Deferiprone	20.0	29.4
Hydroxyquinoline	22.9	32.4
1,10-Phenanthroline	6.0	14.4
MECAM	28.0	43.0
Enterobactin	-	49.0

The affinity of iron chelator towards Fe^{2+} or Fe^{3+} can also affect the redox reaction. The redox potential (E^0) at pH 7.0 of aquated iron is 110mV (equation 4), which is within the biological range (-320-460mV) accessible to intracellular oxidants and reductants, such as NADPH and thiols. This means that both redox forms are present in biological environment. Therefore due to the chelators affinity of one oxidation state over the other, can lead to changes in th redox equilibrium.[58,70]

$$E = E^0 - 0.059 \log \frac{\beta_{Fe^{3+}} [Fe^{2+}]}{\beta_{Fe^{2+}} [Fe^{3+}]} \qquad \text{Equation 4}$$

Redox potential that are above or below the range accessible by biological systems show the chelators selectivity for one oxidation state of iron as in DFO producing redox-inert complexes.[58]

1.5.5.3 Lipophilicity and Molecular Weight for Clinical Application

For a chelator to perform its biological effect, it should be able to reach its target site in high concentration. Since biological membranes are phospholipid bilayers and are hydrophobic in nature, the iron chelators should be lipophilic. Uncharged compounds are preferred. Appreciable lipid solubility can be obtained by the octanol: water partition coefficient (Log P) ranging from > - 0.7 to < 5 log P values. However, they should not be highly hydrophobic, since they otherwise will be able to penetrate highly regulated barriers, such the blood brain barrier, and placental barriers, thus producing toxic side effects.[66,71]

An iron chelator should have a molecular weight of < 500 Da in order to have >70% penetration into the cells. Most hexadentate ligands have a higher molecular weight, making them less available. An example is DFO having a molecular weight > 500 Da. Smaller molecular weight chelators such as EDTA (292 Da) may be too small, thus causing toxicity. Bidentate and tridentate ligands have lower molecular weight compared to DFO, showing higher absorption.[66]

Another factor that influences the lipophilicity and effectiveness of chelators is the pH. The pFe^{3+} vs. pH plots can be used to compare the effective binding of the chelators with iron (III) at different pH values. Iron (III) forms stable bonds with weakly polarizable atoms, such as oxygen. The affinity of iron binding with chelators containing oxygen atoms depends on the pKa values of the oxygen atoms. The higher the affinity towards iron (III), the higher is the pK_a

value. For example, the high charge density on the oxygen atoms of catechol (Figure 1.23) shows high affinity for protons. Therefore, the binding of catechols to cations is pH sensitive. At pH 7 the complex bears a net charge and cannot permeate membranes. However, catechol can dominate chelation at alkaline pH values (Figure 1.25A).[66]
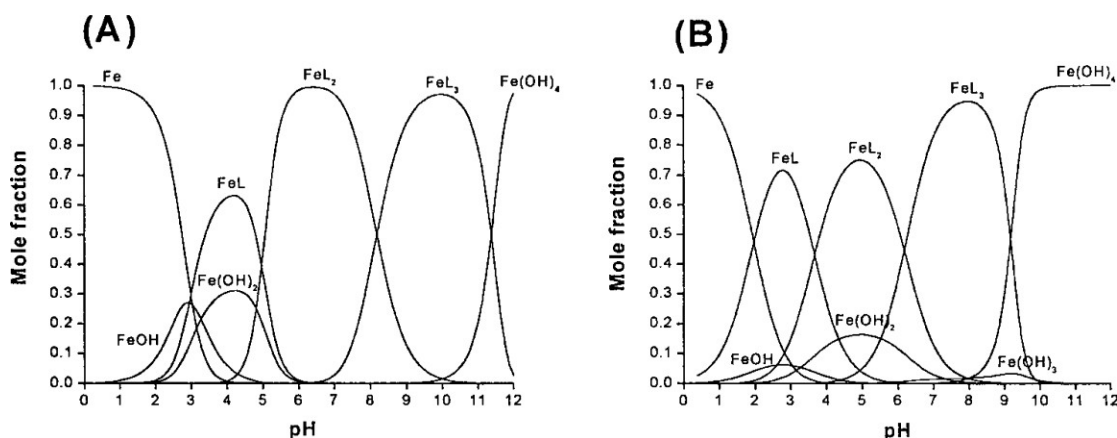
Figure 1.25:- Speciation plot of iron(III) in the presence of;

     (A) N,N-dimethyl-2,3-dihydroxybenzamide

     $[Fe^{3+}]_{total} = 10^{-6}$ M and $[ligand]_{total} = 10^{-5}$ M

     (B) Acetohydroxamic acid , $[Fe^{3+}]_{total} = 10^{-6}$ M and $[ligand]_{total} = 10^{-4}$ M;[66]

In these complexes the iron atom is able to interact with H_2O_2 to form hydroxyl radicals, since it is not completely protected from the solvent.

Hydroxamates have lower affinity towards iron than catechol. They form neutral tris-complexes with iron (III) which can permeate through membranes easily. Since hydroxamates low affinity towards protons there is less H^+ interference at physiological pH (Figure 1.25B).[66]

1.5.5.4 Toxicity

Toxicity by chelators is due to factors such as lack of selectivity of metal ions which lead to deficiency of essential metal ions such as Zn^{2+} and Cu^{2+}. Toxicity can also occur by inhibition of important iron containing metalloenzymes such as ribonucleotide reductase, which is important in DNA synthesis.[66]

1.5.6 Redox Active Iron Complexes Generating Toxic Free Radicals

Chelators with carboxylate and nitrogen have affinity towards both bivalent and trivalent ions. Chelators containing oxygen have a strong affinity towards tribasic cations. For redox activity to occur chelators containing nitrogen have a higher redox potential. These complexes redox cycle under aerobic conditions producing oxygen radicals.[66]

1.5.7 A Suitable Iron Chelator for Cancer Treatment

The factors that would be preferred as an anti-cancer agent in an iron chelator;
- Have considerable lipophilicity
- Capable of generating reactive oxygen species
- Inhibit ribonucleotide reductase activity

The ligands that perfectly fit to these requirements are the thiosemicarbazone compounds (Figure 1.26). They are a set of tridentate ligands which contain nitrogen and sulfur and form 2:1, ligand: iron complexes. They contain aromatic rings with nitrogen such as pyridine or isoquinoline. They bind to divalent ions Cu^{2+}, Zn^{2+}, Mn^{2+}, Fe^{2+} and also trivalent ions. Binding occurs through sulfur and heterocyclic and imine nitrogen donors, which are soft atoms, producing high affinity towards these transition metals.[58]

Among this family of compounds the chelator Dp44mT shows promising anti- cancer activity at nanomolar concentrations.

1.5.8 Experimental Evidence of Anti Cancer activity of Thiosemicarbazones

1.5.8.1 pH Effect

The neutral from of the thiosemicarbazones is preferred since it is important in permeating through the cell membranes.[52]

As in figure 1.27 of the speciation plot for HDp4eT the protonated form is dominant below pH 4 (diamond line) and the deprotonated form is dominant above pH 11 (broken line).

The charge neutral (solid line) form is dominant at physiological pH. This demonstrates that these ligands are in their neutral form in biological systems and can permeate through cell membranes. Therefore showing high biological activity in cells as well as lysosomes.[70]
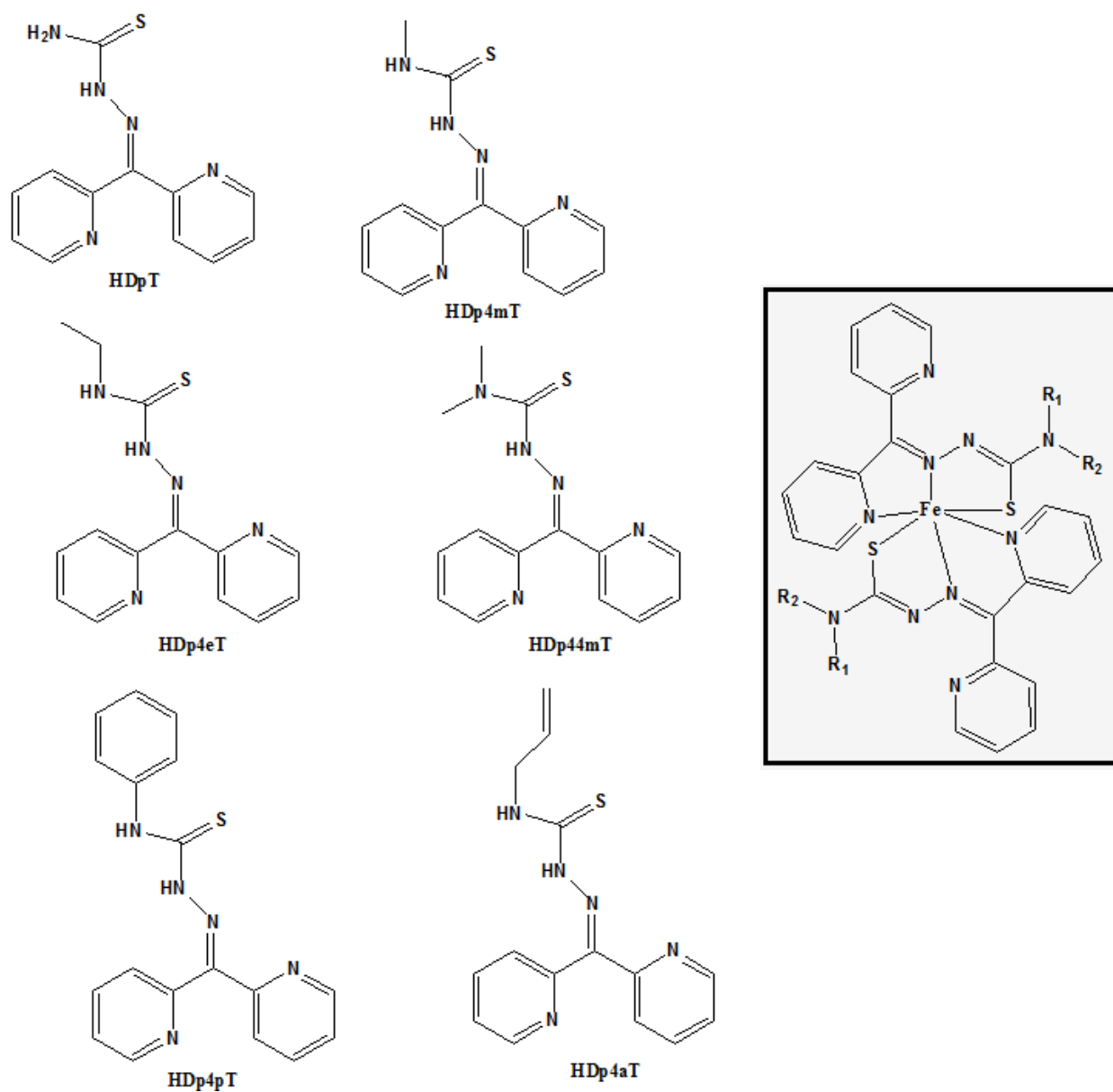
Figure 1.26:- Structural formuas of Pyridoxal isonicotinoyl hydrazone (H2PIH), 2-hydroxy-1-naphthylaldehyde isonicotinoyl hydrazone (H2NIH or 311), 2-hydroxy-1-naphthylaldehyde thiosemicarbazone (H2NT), di-2-pyridyl ketone isonicotinoyl hydrazone (HPKIH), di-2-pyridyl ketone thiosemicarbazone (HDpT), di-2-pyridyl ketone 4-methyl-3-thiosemicarbazone (HDp4mT), di-2-pyridyl ketone 4-ethyl-3-thiosemicarbazone (HDp4eT), di-2-pyridyl ketone 4,4-dimethyl-3-thiosemicarbazone (HDp44mT), di-2-pyridyl ketone 4-phenyl-3-thiosemicarbazone (HDp4pT), di-2-pyridyl ketone-4-allyl-3-thiosemicarbazone (HDp4aT). Schematic representation of a 2:1 Fe complex formed by HDpT analogues.[45]
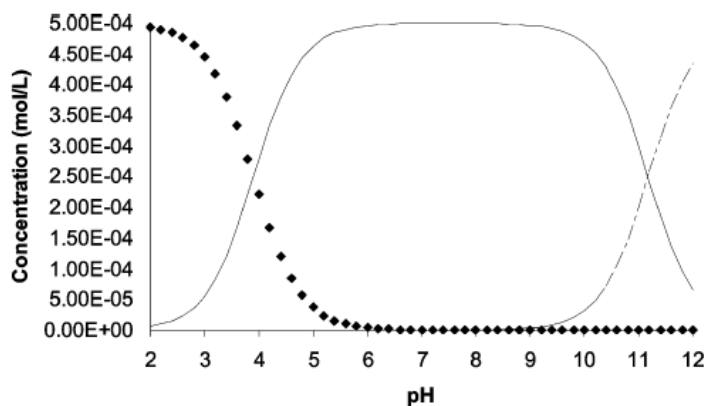
Figure 1.27:- Speciation plot for [H2Dp4eT]+ (diamonds), HDp4eT (solid curve), and [Dp4eT]- (broken curve) as a function of pH.[70]

1.5.8.2 Lipophilicity of the Ligands

The lipophilicity of a chelator is another property of its ability to permeate membranes. This is determined by its partition coefficient of octanol:water (log P) values (Table 1.7).

Table 1.7:- Octanol:water partition coefficient of HDpT analogues[70]

Ligand	Log P
HDpT	0.78
HDp4mT	3.18
HDp4eT	1.23
HDp44mT	2.19
HDp4aT	1.68
HDp4pT	1.96

The compounds with log P values greater than 1.5 are moderately lipophilic. HDpT is mostly hydrophilic since it bears 2 protons on the $S=C-NH_2$. The rest of the other chelators are lipophilic due to presence of 1 or 2 hydrophobic substituents (Figure 1.25). According to the data HDp4mT and HDp44mT are better lipophilic compounds and would show better biological activity.[70]

1.5.8.3 Effects of Antiproliferating Activity

The antiproliferating activity occurs due to inhibition of ribonucleotide reductase enzyme.[45] Ribonucleotide reductase is required for the synthesis of large amounts of DNA that is required in fast-dividing cells, as this is the case in cancer.

Table 1.8:- IC$_{50}$ (µM) values of the complexes ability to inhibit the growth of SK-N-MC cells after 96 h.[70]

Chelator/Complex	IC$_{50}$ (µM)
DFO	8.58 ± 1.65
Fe^{III}DFO	>25
HDpT	5.20 ± 0.44
Fe^{II}(DpT)	> 6.25
[Fe^{III}(DpT)$_2$] ClO$_4$	> 6.25
HDp4mT	0.18 ± 0.02
Fe^{II}(Dp4mT)	1.53 ± 0.21
[Fe^{III}(Dp4mT)$_2$] ClO$_4$	1.02 ± 0.28
HDp4eT	0.05 ± 0.03
Fe^{II}(Dp4eT)	1.21 ± 0.47
[Fe^{III}(Dp4eT)$_2$] ClO$_4$	0.46 ± 0.16
HDp44mT	0.01 ± 0.01
Fe^{II}(Dp44mT)	0.42 ± 0.08
[Fe^{III}(Dp44mT)$_2$] ClO$_4$	0.35 ± 0.02
HDp4aT	0.02 ± 0.01
Fe^{II}(Dp4aT)	0.69 ± 0.24
[Fe^{III}(Dp4aT)$_2$] ClO$_4$	0.68 ± 0.15
HDp4pT	0.01 ± 0.01
Fe^{II}(Dp4pT)	0.21 ± 0.05
[Fe^{III}(Dp4pT)$_2$] ClO$_4$	0.15 ± 0.09

Antiproliferating activity of the iron chelators can be determined by the MTT assay. From the IC_{50} data shown in table 5, the control DFO showed low antiproliferating activity. However, among the HDpT analogues HDpT showed least activity. And Dp4eT, Dp44mT and Dp4pT shows marked efficacy at inhibiting cell proliferation.[70]

Dp44mT was also found to be effective against 28 cancer cells lines with an average IC_{50} of 0.03 ± 0.01 µM concentration (Figure 1.28).[53]
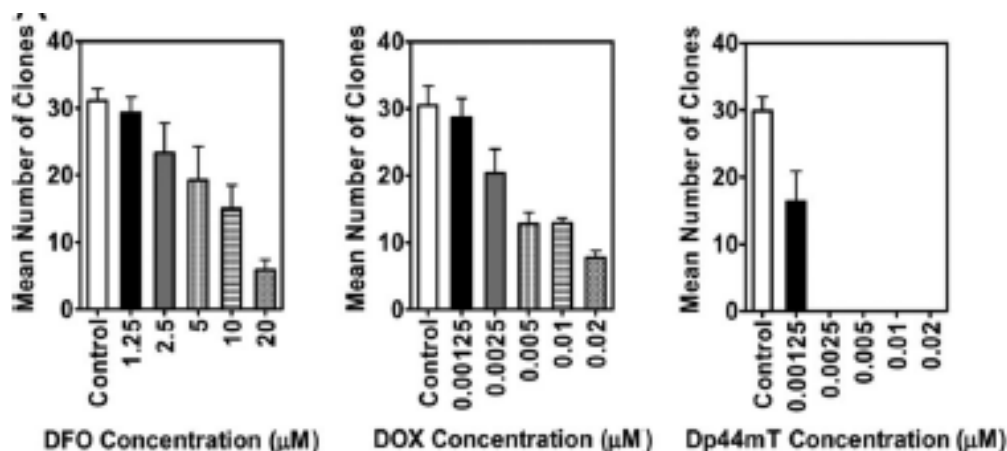
Figure 1.28:- Dp44mT markedly inhibits clonogenic formation [37]

(DFO: desferrioxamine, DOX: doxorubicine)

1.5.8.4 Redox Activity

The redox potentials of HDpT chelators are shown to be 300-400 mV lower than other classes of chelators, which facilitates redox activity (Table 1.9).[70]

Table 1.9:- Electrochemical data of HDpT analogues[70]

Ligand	E^0 (mV)
HDpT	+165
HDp4mT	+153
HDp4eT	+173
HDp44mT	+166
HDp4aT	+170
HDp4pT	+225

From all of these results we can could say that a thiosemicarbazone analogue close in structure to either Dp4eT, Dp44mT or Dp4pT to be a preferentially good candidate as an iron chelator used as an anti caner agent.

1.6 Iron/ Iron Oxide Nanoparticles

The development of nanotechnology has dramatically increased in the last couple of decades. Scientific studies have lead to the understanding of the behavior of the nanoparticles such as stability, control of surfactants, particle size, suitable materials to produce nanoparticles and physical behavior. These studies provide a good insight that will lead to nanoparticles that can be tailored accordingly for biomedical applications and diagnostics.[72, 73]

Iron/iron oxide (Fe/Fe_3O_4) nanoparticles have been used for about 40 years for various medical applications. The physical and chemical properties of these nanoparticles do not contain the characteristics of either the atom or the bulk counterparts and exhibit superparamagnetic properties. These superparamagnetic nanoparticles can be used for several biomedical applications due to their specific mesoscopic physical, chemical, thermal and mechanical properties and with proper surface chemistry. The biomedical applications include;[72, 73]

- Magnetic resonance imaging (MRI)
- Drug delivery
- Hyperthermia
- Tissue repair
- Immunoassays
- Detoxification of biological fluids
- Cell separation
- Magnetofection

In order to achieve these *in vivo* applications they need to have a small particle size smaller that 100 nm, a narrow particle size distribution, they should have a surface coating which is nontoxic and biocompatible and should have high magnetization values.[73]

1.6.1 Magnetic Iron/ Iron Oxide Nanoparticles for Biomedical Applications

There are several types of magnetic Fe/Fe_3O_4 nanoparticles that have been studied and among them are maghemite (γ-Fe_2O_3) and magnetite (Fe_3O_4) that are 5-20 nm in size. Magnetite is mostly used since it is more biocompatible than maghemite. Magnetite forms a fcc closed packing cubic inverse spinel structure. Here the iron cations are occupied at the interstitial tetrahedral and octahedral sites. It is a half- metallic material and has quantum size effects and a large surface area changing its magnetic properties into superparamagnetic properties since a particle is considered as a single magnetic domain.[72, 74]

The synthesis of nanoparticles is challenging in producing nanoparticles with specific size and shape. There are many methods to synthesize nanoparticles such as Ostwald ripening, water-in-oil microemulsion method. In the synthesis of nanoparticles there are two stages involved where first when the concentration of the species reaches its critical supersaturation a short burst of nucleation occurs, next, a slow growth of nuclei occurs by the diffusion of solutes to the surface of the crystal. Continuous nucleation should be avoided in order to produce monodispersed nanoparticles.[73]

The size and shape of the nanoparticles can be controlled by adjusting the pH, ionic strength, temperature, and nature of salts (halogens, nitrates, perchlorates) and the concentration of Fe^{II}/ Fe^{III} ratio used in the reaction. The use of surface modifiers is crucial to stabilize the Fe/Fe_3O_4 nanoparticles from aggregation in both biological medium and magnetic field. This can be achieved by using electrostatic or steric repulsion (Figure 1.29).[72, 73]

Stabilizers that can be used are;[72, 73]

- Carboxylates, phosphates which are known to bind to the surface of magnetites.
- Inorganic material such as silica or gold can be used to coat the nanoparticles. They can also help in binding other biological ligands.
- Polymer stabilizers such as dextran, polyethylene glycol, polyvinyl alcohol and chitosan.
- Long chain surfactants such as oleic acid, stearic acid.

To prevent the Fe/Fe_3O_4 nanoparticles from oxidation and agglomeration an inert gas such as argon or nitrogen can be bubbled through the reaction solution during the synthesis. It not only protects from oxidation but can also further help in reducing the particle size.[72]
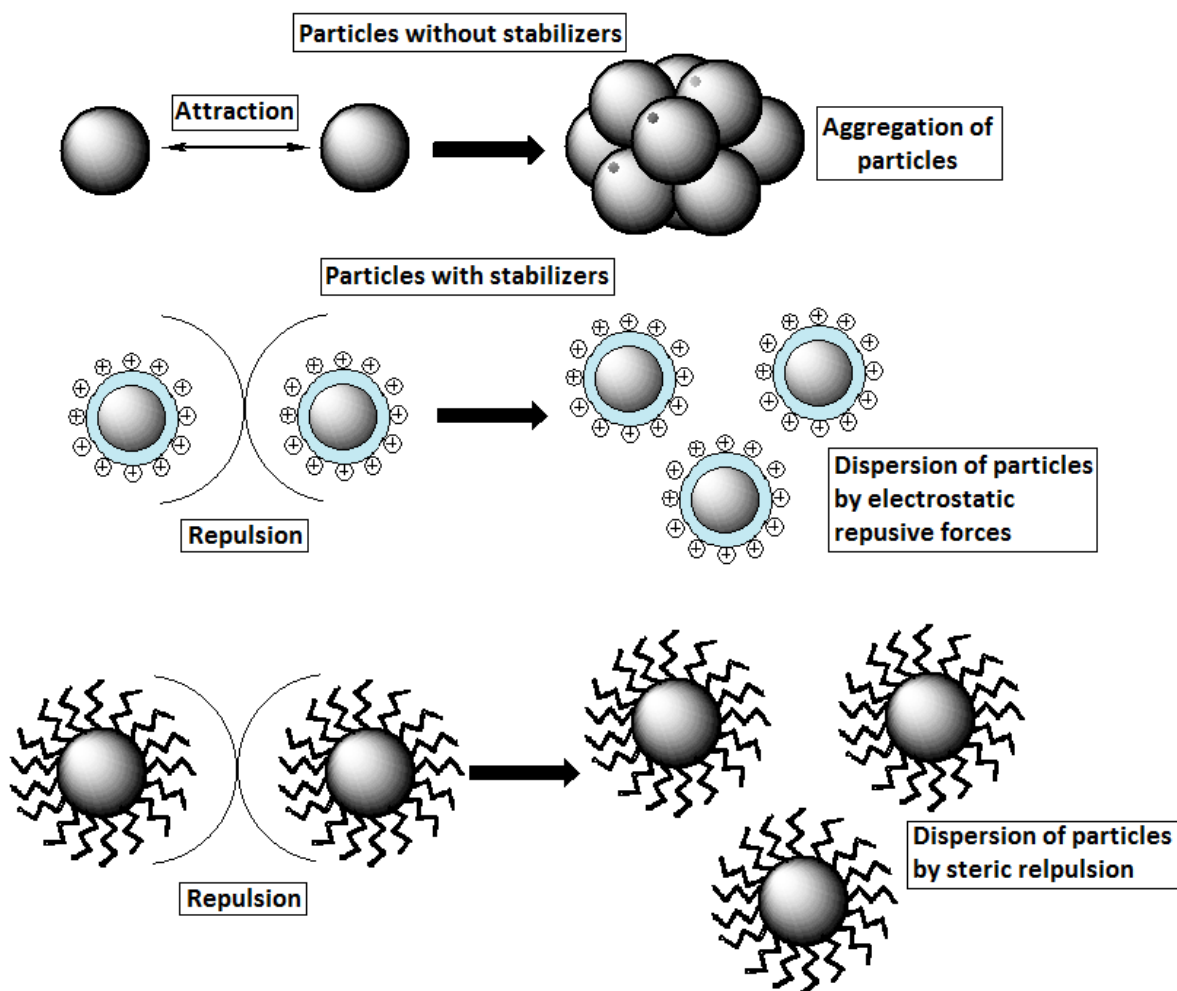
Figure 1.29:- Stabilization of Iron/ Iron oxide nanoparticles coated with stabilizers.[73]

1.6.1.1 Drug Delivery

Magnetic nanoparticles show promising applications in drug delivery. The surface of the nanoparticles can be modified with drugs and various biological ligands (e.g. tumor targeting peptides, proapoptotic peptides, DNA, RNA and antibodies), which target tumors or specific organs. These surface modified nanoparticles are able to reduce drug doses and side effects to normal cells, as well as the costs associated with drug treatment. This is most important in cancer treatment since therapeutic nanoplatforms would specifically target the cancer cells and release their payload into the cells as discussed in topic 1.4.2 and 1.4.3.[72, 73]

Fe/Fe$_3$O$_4$ nanoparticles that are not surface modified have a short blood half-life of several minutes and are mainly used for imaging of liver, spleen and gastrointestinal tract. However surface modified Fe/Fe$_3$O$_4$ nanoparticles have long blood circulating times of hours (48 hrs) and are useful for imaging vascular compartment (magnetic resonance angiography), lymph nodes, perfusion imaging, receptor imaging and target specific imaging.[72]

These magnetic nanoparticles can be magnetically controlled in the vascular by an external magnetic field. Therefore, they can be magnetically guided and can be retained into a specific location. For instance, magnetic nanoparticles can be retained at the tumor site, where it can release its payload and carry out its activity.[72]

The internalization of nanoparticles into cells depends on their size. Nanoparticles administered which range from 10 nm to 100 nm are the ideal size for intravenous injection. They show long circulation times and are small enough to avoid rapid clearance by the reticuloendothelial system. They can also penetrate through capillaries prior to systemic clearance and are the most effective particle size for biological application. Particles larger than 200 nm in diameter are removed by the spleen by mechanical filtration and are ultimately removed by phagocyte system reducing its blood circulation time. Particles with diameters less than 10 nm are rapidly removed by extravasation and renal clearance. These effects greatly reduce their blood circulation time.[72, 73]

Since cancer cells proliferate at a higher ratio than normal cells they need to meet the high demand of nutrients. Therefore, new blood vessels have to be formed when the cancer grows. This process is called angiogenesis. These blood vessels are leaky with average pore size of 100-600 nm. The leaky pores can facilitate nanoparticles to diffuse into the cancer tissues thereby making it a good carrier for drugs into cancer cells.[3]

1.6.1.2 Magnetic Resonance Imaging (MRI)

The use of superparamagnetic Fe/Fe$_3$O$_4$ nanoparticles (SPIO) as contrasting agents play an important role for MRI. SPIO tagged with certain specific homing peptides or antibodies allows early detection of pathological tissues, such as the differentiation of cancerous tissues form normal healthy tissues (Figure 1.30). MRI can also be used to track cells in the body that have been tagged with SPIO and can also be used to detect apoptosis where the MR image contrast changes when morphological changes occur during apoptosis such as cell shrinkage and membrane blebbing.[72, 73]
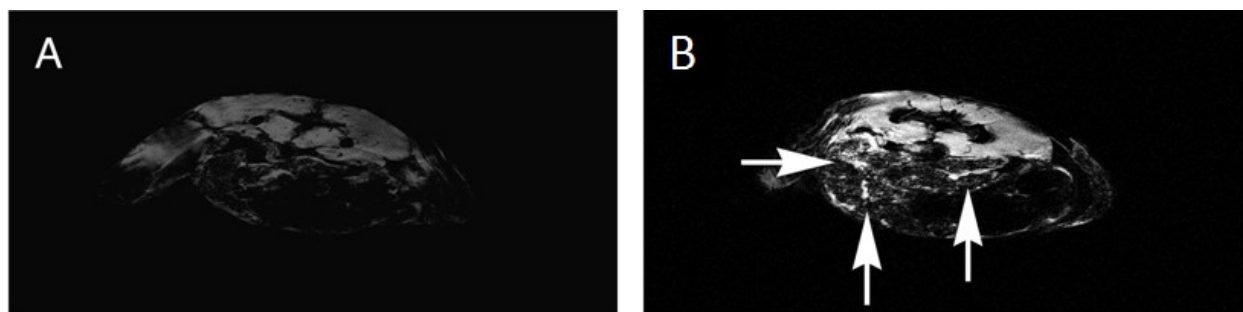
Figure 1.30:- MRI Using Fe/Fe$_3$O$_4$-NPs, Delivered by NPC cells, B16F10 Lung Tumors in Black Mice.

       A: Control

       B: Accumulation of the Fe/Fe$_3$O$_4$/stealth nanoparticles in lung melanomas

All results were obtained in an 400MHz at the Oklahoma Medical Research Foundation Nuclear Magnetic Resonance Core. These figures were adopted form Dr. Thilani Samarakoon's thesis, Kansas State University, 2010

The contrasting ability of SPIO is due to their high transverse relaxivity. In a magnetic fluid, ferromagnetic particles dispersed in a liquid, which forms a colloid. Each crystal in the colloid suspension is small in size and is fully magnetized forming nanomagnets and is composed of single domains. When a SPIO is subjected to an external magnetic field, the entire crystal aligns with the applied field due to the single crystal nature, which enhances the magnetic flux. Changes in MRI signal are produced through disturbances caused in the local magnetic field induced by large magnetic moments causing rapid dephasing of surrounding protons.[72, 73, 75]

The MRI contrast relies on the relaxation of these crystals back to equilibrium. There are two relaxation processors involved, which are commonly described as Néel relaxation and Brownian relaxation (Figure 1.31).

The Néel relaxation occurs in sufficiently small nanoparticles and is defined as the time taken for the particles to return back to equilibrium after perturbation. Brownian relaxation is detected in larger particles and characterizes the viscous rotation of the entire particle. Therefore, the total relaxation rate is the sum of both Néel relaxation and Brownian relaxation rates (Equation 5).[73, 75]

$$\frac{1}{\tau} = \frac{1}{\tau_N} + \frac{1}{\tau_B} \qquad \text{Equation 5}$$
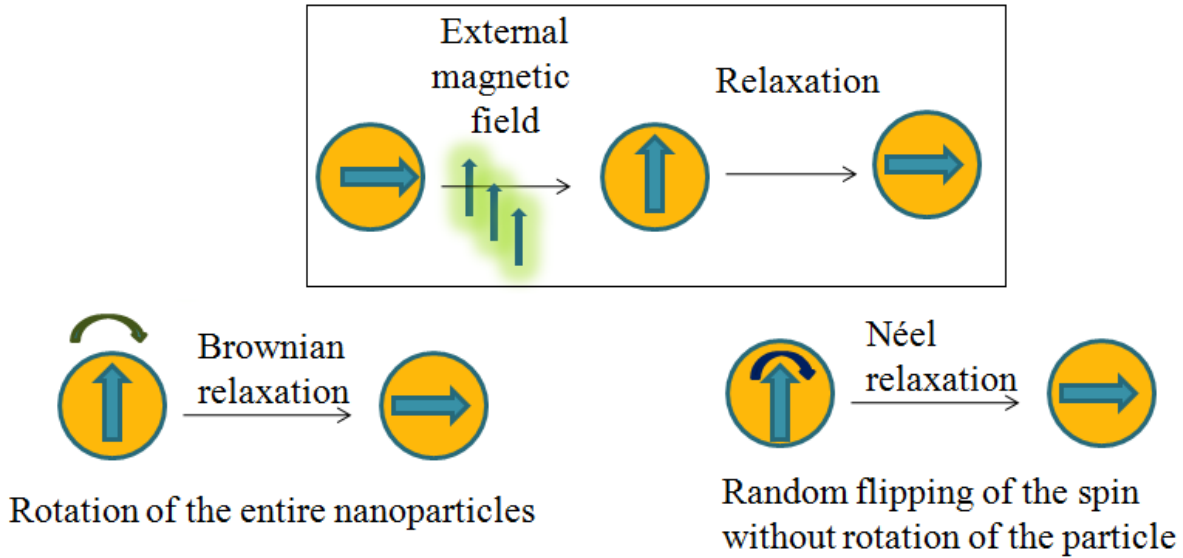
Figure 1.31:- Illustration of Néel relaxation and Brownian relaxation.[73]

1.6.1.3 Hyperthermia

The use of heat (hyperthermia) as a treatment method for tumors has been practiced for centuries. It is known that tumor cells are more sensitive to heat than normal healthy cells. When the temperature is increased more than 43^0C tumor cells are destroyed. However normal cells survive at higher temperatures. Therefore by exposing tumor cells to increased temperatures the tumor tissue can be destroyed by hyperthermia. Heating methods that were used to destroy tumors included the use of a hot water bath, pyrogens (bacterial toxins), perfusion heating, high frequency radiation and magnetic fluid hyperthermia.[72, 73]

Ferrofluids of superparamagnetic Fe/Fe_3O_4 nanoparticles when subjected to an alternating magnetic field they start to spin (Figure 1.32), generating heat. Therefore, by embedding magnetic particles into the tumor site and exposing it to an alternating magnetic field (AMF) heat will be generated depending on magnetic properties of the material, the strength of the magnetic field applied, frequency of oscillations, and cooling capacity of the blood in the tumor site.[72, 73]
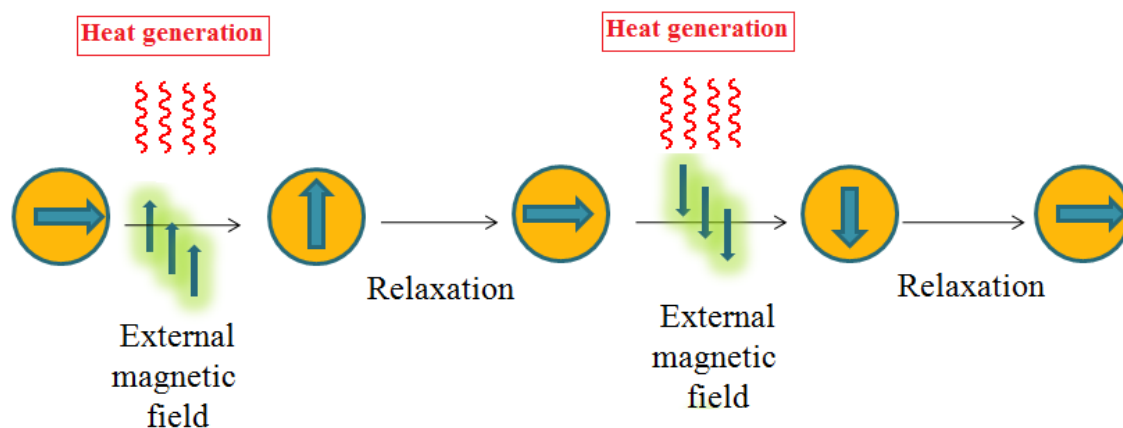
Figure 1.32:- Heat generation by superparamagnetic and/or ferromagnetic Fe/Fe$_3$O$_4$ nanoparticles when subjected to an alternating magnetic field.

The magnetic energy of the nanoparticles shows a synoidal wave when subjected to an alternative magnetic field (figure 1.33). This synoidal effect depends on the direction of the external magnetic field.[73]
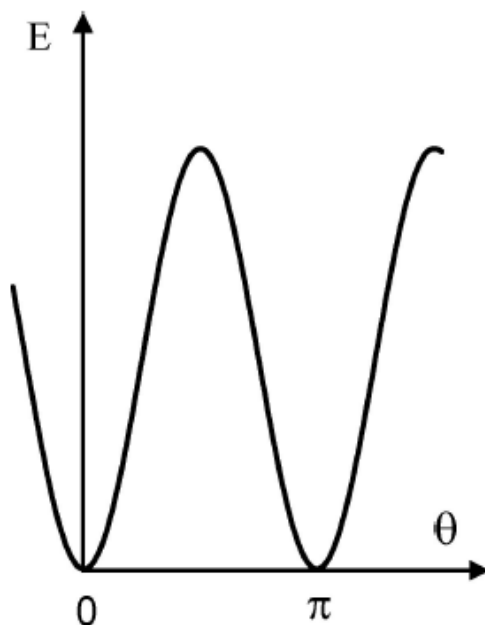
Figure 1.33:- Magnetic energy change when the nanoparticle is subjected to an alternating magnetic field.[73]

The specific absorption rate (SAR) is the parameter that determines heating of the tissues. It is defined as; "The rate of which electromagnetic energy is absorbed by a unit mass of biological material". Its units are in calories per kilogram. SAR is proportional to the increase in temperature ($\Delta T / \Delta t$) and is calculated by the equation below (Equation 6).

$$SAR = 4.1868 \; \frac{P}{m_e} = C_e \frac{\Delta T}{\Delta t} \qquad \text{Equation 6}$$

Where;

P = Electromagnetic wave power absorbed by the sample

m_e = Mass of the sample

C_e = Specific heat capacity of the sample

The use of low-frequency magnetic wave ranging around 100 kHz to 400 kHz is appropriate to be exposed to tissues containing ferrofluids. This specific range is used to control the energy released into the tissue, if not inhomogeneous heating will occur.[73]

1.7 Methods

1.7.1 Synthesis of the Thiosemicarbazone Analogue

Potassium hydroxide (8.36 g, 0.14 mol) was dissolved in 90% ethanol (30 ml) this mixture was cooled in an ice bath. To this mixture cold hydrazine hydrate (7.29 ml, 0.14 mol) was added slowly while stirring. Next cold carbon disulfide (9 ml, 0.14 mol) was added drop wise with vigorous stirring. The temperature of the reaction mixture was not allowed to rise above 6 ^{0}C during the period of carbon disulfide addition. This reaction mixture was reacted for 2 hrs. To the same reaction mixture cold methyl iodide (9.27 ml, 0.14 mol) was added slowly and further reacted for 30 min. The resultant white product (hydrazinecarbodithioc acid methyl ester) was filtered and washed with cold water and dried (70 % yield). This product was next recrystallized in hot ethanol and the NMR was taken (Appendix B Figure B.1). This intermediate methyl ester product was then refluxed in the presence of di-2-pyridyl ketone at an equivalence of 3:1 respectively. Di-2-pyridyl ketone (3.01g, 0.016 mol) was dissolved in 15 ml of ethanol to this a catalytic amount of HCl (2.8 ml) was added. Next the methyl ester dissolved in 15 ml of ethanol was added to this mixture and refluxed at 100 ^{0}C for 3 hrs. After 3 hrs cold distilled water was added and a yellow color precipitate formed. This precipitate was filtered and washed with cold water and was dried. This resulting product was recrystalized by hot ethanol and the resulting yellow colored needle shaped crystals were filtered by suction and washed with cold ethanol (80 % yield).[76] The ^{1}H-NMR of this product was taken (Appendix B Figure B.2). The reaction scheme can be found in Appendix A Figure A.1.

1.7.2 Synthesis of the Peptide

The peptide sequence CGKRK($_D$[KLAKLAKKLAKLAK])PLFAERL was synthesized according to the protocol discussed in topic 1.4.6.1.

The peptide was synthesized on a leucine preloaded trityl resin (H-Leu-2-ClTrt-resin) and through many repeating cycles of N-deprotection using piperidine and subsequent amino acid coupling with the coupling solution. Amino acid by amino acid the peptide sequence was synthesized from the C-terminus to the N-terminus (Figure 1.12). Dried and stored the peptide on resin for future use.

1.7.3 HPLC Purification of the Peptide

The peptide sequence CGKRK(D[KLAKLAKKLAKLAK])PLFAERL was purified using the Waters 1525- Binary HPLC pump instrument and Kinetex 5 µ XB- C18 100 A size 250 * 4.6 mm reverse phase column. The peptide (2.5 mg) was dissolved in equal amounts of 0.2 % TFA (125 µl) and acetonitrile (125 µl) and 40 µl was injected into the machine. The peptide was purified using 0.2 % TFA as the aqueous solvent and acetonitrile as the organic solvent (table 1.10).[43] The purification was achieved through a gradient of aqueous and organic solvent as shown below; The HLPC can be found in Appendix B Figure B.6.

Table 1.10:- Solvent gradient of aqueous and organic solvents.

Time (min)	Flow	A$_{(aq)}$	B$_{(org)}$	Flow rate A %	Flow rate B %
0	1	99	1	0.99	0.01
60.00	1	60	40	0.60	0.40
60.01	0	60	40	-	-

1.7.4 Synthesis of the Dopamine Peptide Ligand

First the resin with the peptide (150 mg, 0.075 mmol) was swelled in 5 ml of DCM and was swirled for 20 mins. The DCM was filtered and the resin was swirled with 2.5 ml of DMF for 1 min and was filtered off. Next the peptide sequence was deprotected by reacting with 4 ml of 20% piperidine: DMF solution for 1 min and was filtered, this step was repeated and was swirled for 10 mins and filtered. The resin was washed 5 times with 2.5 ml of DMF and was filtered. The resin with peptide sequence was next reacted with glutaric anhydride (25.67 mg, 0.225 mmol) for 3 hrs at an equivalence of 1:3 respectively. This step was repeated two more times. This was next reacted with dopamine hydrochloride (14.22 mg, 0.075 mmol) at an equivalence of 1:1 and HBTU (82.40 mg, 0.217 mmol) at an equivalence of 1:2.9 in 6 ml of the DIEA: DMF coupling solution for 30 mins and was filtered off. This step was repeated. The resin was washed 4 times with 2.5 ml of DMF for 30 s each and was filtered off. It was next washed 5 times with 2.5 ml of DCM for 30 s each and was filtered off.[77] Next the dopamine peptide ligand was cleaved from the resin using 2 ml of the cocktail of 1.9 ml TFA, 0.05 ml TIPS and 0.05 ml distilled water and was swirled for 3 hrs. The cleaved dopamine peptide ligand was

precipitated in 15 ml of cold ether and was centrifuged. The precipitated ligand was washed two more times with 15 ml of cold ether and the ligand was centrifuged the supernatant was decanted and the ligand was dried and stored under argon in a -20 ^{0}C freezer for later use. The reaction scheme is found in Appendix A Figure A.2.

1.7.5 Synthesis of Core/Shell Fe/Fe$_3$O$_4$ Magnetic Nanoparticles (MNPs) and Characterization

Fe/Fe$_3$O$_4$ nanoparticles were synthesized by a modified seeded growth procedure, which was originally published by Sun et al.[78] Iron pentacarbonyl (Fe(CO)$_5$) (10.5 ml) is initially thermally decomposed at 200°C in octadecene (ODE) (300 ml). This reaction produces Fe(0) atoms, which aggregate to form the initial sub-nanometer clusters. The reaction temperature is then lowered to 180°C. The Fe(0) clusters are capable of catalyzing the thermal decomposition of Fe(CO)$_5$. In the presence of the binary ligand system oleylamine (4.5 ml) and hexadecylammonium chloride (HAD·HCl) (4.15 g) this process leads to the controlled growth of iron(0) nanoparticles (the reaction scheme can be found in Appendix A Figure A.3). Depending on the iron pentacarbonyl concentration, initial reaction time and temperature, as well as the duration and temperature of the subsequent ripening procedure, near monodisperse (polydispersity < 1.03) nanoparticles possessing diameters between 5nm and 100nm can be prepared.[79] The second step in nanoparticle synthesis consists in the defined oxidation of the surface Fe(0) to Fe$_3$O$_4$. Dr. Wang has optimized this procedure in the Bossmann group by bubbling O$_2$/N$_2$ mixtures through a dispersion of the initially prepared nanoparticles at room temperature. By selecting the duration of air oxidation, various chain thicknesses can be achieved. As this is shown in TEM (Appendix B Figure B.8), the typical thickness of the outer Fe$_3$O$_4$ layer in the nanoparticles that I have synthesized in my thesis (d = 28+/-2 nm) was 2nm.

This synthetic procedure was scaled up to 100g batches in 2013 in the Bossmann group. Kansas State University Research Foundation (KSURF) in collaboration with Kansas State University's Institute for Commercialization (KSU-IC) is currently pursuing a combined patent with Battelle Memorial Institute, Columbus, OH.

The resulting nanoparticles were characterized by means of XRD, TEM and XPS.

1.7.6 Powder X-ray diffraction (XRD) of the Fe/Fe₃O₄ Magnetic Nanoparticles

Powder X-ray diffraction (XRD) patterns were obtained on a Bruker D8 X-ray diffractometer with Cu Kα radiation.[77]

1.7.7 X-ray photoelectron spectroscopy (XPS) of the Fe/Fe₃O₄ Magnetic Nanoparticles

X-ray photoelectron spectroscopy (XPS) data[80] was recorded with a Perkin–Elmer PHI 5400 electron spectrometer using acrochromatic Al Kα radiation (1486.6 eV). Analysis was carried out under vacuum less than 5×10^{-9} Torr and heated to 120 $^{\circ}$C to remove any adsorbed molecules on the surface. The XPS binding energies were measured with a precision of 0.025 eV. The analyzer pass energy was set to 17.9 eV, the contact time was 50 ms, and the area scanned was 4 mm^2.

1.7.8 Ligand exchange of Fe/Fe₃O₄ Nanoparticles with the Dopamine Peptide Sequence and Free Dopamine

The oleylamine and octadecyl coated Fe/Fe₃O₄ nanoparticles (500 mg) were reacted with the dopamine peptide ligand (50 mg) at a ratio of 10:1 respectively. They were reacted in 10 ml of THF (Tetrahydrofuran) under argon overnight. The reaction mixture was centrifuged and the supernatant was removed. Next the nanoparticles were reacted with an excess amount of dopamine hydrochloride (150 mg) in 10 ml of THF under argon overnight. The reaction mixture was centrifuged and the supernatant was removed. The nanoparticles were washed 5 times with 5 ml of DCM.[77] And the naoparticles were stored in DCM for future use. The reaction scheme can be found in Appendix A Figure A.4.

Another batch of nanoparticles was synthesized with just dopamine as their ligand, following, principally, the same procedure.

1.7.9 Coupling of the Thiosemicarbazone Analogue to the Free Dopamine on the Fe/Fe₃O₄ nanoparticles

Coupling was done in different ratios of the iron chelator thiosemicarbazone analogue: free dopamine, dopamine peptide coated Fe/Fe₃O₄ nanoparticles at ratios of 1: 10, 1: 5, 1: 1, 5: 1 and 10:1 respectively (Table 1.11). The reaction was done in DMF with two equivalence each of EDC, HOBT and 2.5 equivalence of DIEA.[77] The reaction solution was reacted for four days under argon. The reaction scheme is found in (Appendix A Figure A.5).

The same reaction procedure was done for the nanoparticle coated with just dopamine.

Table 1.11:- Coupling ratios.

Thiosemicarbazone analogue	Dopamine
1	10
1	5
1	1
5	1
10	1

An example for the calculation involved to prepare the different ratios are as below;

Surface are of a Fe/Fe_3O_4 nanoparticles with a diameter of 20 nm

$$= 4\pi r^2$$
$$= 4 * 22/7 * 10^2 \text{ nm}$$
$$= 1257.14 \text{ nm}^2$$

Space demand of dopamine linker $= 1.094 \text{ nm}^2$

Number of dopamine per nanoparticle $= 1257.14 \text{ nm}^2/ 1.094 \text{ nm}^2$
$$= 1149.12$$

Volume of Fe/Fe_3O_4 nanoparticles in 30 mg $= d = m/ v$
$$= v = m/ d$$
$$= (30 * 10^{-3})g / 7.84 \text{ gml}^{-1}$$
$$= 3.826 * 10^{-3} \text{ ml}$$
$$= 3.826 * 10^{-9} \text{ m}^3$$

Volume of a Fe/Fe_3O_4 nanoparticle $= 4/3 *22/7* (10* 10^{-9})^3 \text{ m}^3$
$$= 4.190 * 10^{-24} \text{ m}^3$$

Number of Fe/Fe_3O_4 nanoparticles in the given volume $= (3.826*10^{-9}) \text{ m}^3/(4.190 *10^{-24}) \text{ m}^3$
$$= 9.132 * 10^{14}$$

Number of dopamine in the Fe/Fe_3O_4 nanoparticles $= (9.132 * 10^{14}) * 1149.12$
$$= 1.049 * 10^{18}$$

Moles of dopamine in 30 mg of Fe/Fe_3O_4 nanoparticles $= (1/ (6.023 * 10^{23})) * (1.049 * 10^{18})$
$$= 1.742 * 10^{-6} \text{ mols}$$

Reaction of thiosemicarbazone analogue 1: 10 dopamine and dopamine peptide coated nanoparticle:

Moles of thiosemicarbazone to be added $= ((1.742 * 10^{-6})$ mols/ 10) * 1

$$= 1.742 * 10^{-7} \text{ mols}$$

Moles of EDC needed to be added $= ((1.742 * 10^{-7})$ mols)/ 1) * 2

$$= 3.454 * 10^{-7} \text{ mols}$$

Moles of HOBT needed to be added $= ((1.742 * 10^{-7})$ mols)/ 1) * 2

$$= 3.454 * 10^{-7} \text{ mols}$$

Moles of DIEA needed to be added $= ((1.742 * 10^{-7})$ mols)/ 1) * 2.5

$$= 4.355 * 10^{-7} \text{ mols}$$

1.7.10 UV Measurements of Thiosemicarbazone Analogue Coupling with the Dopamine on the Nanoparticle

UV measurements were taken at UV range from 200- 500 nm. UV measurements were taken at different stages of the reaction;

1. Thiosemicarbazone analogue alone in DMF.
2. Thiosemicarbazone analogue, EDC, HOBT and DIEA in DMF.
3. Supernatant of the reaction mixture after adding the nanoparticles.
4. Supernatant of the reaction mixture after 4 days of reaction. (the nanoparticles were centrifuged to take the supernatant).
5. Reaction mixture of the control after 4 days. The reaction done without nanoparticles. (Thiosemicarbazone analogue, EDC, HOBT, DIEA).

The measurements were taken for both batches of nanoparticles at the different reaction ratios of 1: 10, 1: 5, 1: 1, 5: 1 and 10:1 as mentioned in section 1.7.7;

- For nanoparticles coated with both dopamine and dopamine peptide ligands.
- For nanoparticles coated with just dopamine ligands.

From the UV measurements the amount of thiosemicarbazone analogue reacted was calculated.

1.7.11 Dynamic Light Scattering (DLS) and Zetapotential measurments

A weight of 1 mg of nanoparticles were sonicated for 15 min in 1 ml of distilled water. A volume of 75 µl of this solution was diluted in 3 ml of distilled water. DLS and zetapotential measurements were taken for this solution.

1.7.12 ICP (Inductively coupled plasma) Measurements to Determine the Iron Content in the Nanoparticles and Sulfur Content on the Nanoparticles due to Thiosemicarbazone Coupling

Some assumptions were done to calculate the iron content in the Fe/Fe_3O_4 nanoparticle; We assumed the 1 mg of ligand coated Fe/Fe_3O_4 nanoparticle contains 1 mg of iron.

ICP measurements were taken of the dopamine nanoparticle, dopamine peptide nanoparticle and all the different coupling ratios of thiosemicarbazone on to the nanoparticles (1:10, 1:5, 1:1, 5:1 and 10:1). To determine the iron content approximately 2 mg of the nanosystem was weighed and digested in 1 ml of 10 % HCl. Since the concentration was high a dilution was done by taking 100 µl of concentrated sample and diluted to 5 ml with 10 % HCl. To determine the sulfur content approximately 6 mg of the nanosystem was weighed and digested in 3 ml of 10 % HCl. A standard concentration series of iron and sulfur were prepared using iron nitrate ($Fe(NO_3)_3$ 1000 mg/L) and sulfuric acid (H_2SO_4 1000 mg/ L) in 10 % HCl (Table 1.12);

Table 1.12:- Standard concentration series of iron and sulfur.

Iron concentration ppm (mg /L)	Sulfur concentration ppm (mg /L)
0	0
10	5
20	10
40	15
60	20

The iron content was measured at a wavelength of 259.94 nm and the sulfur content was measured at a wavelength of 181.97 nm.

1.7.13 FTIR Identification of Dopamine and Thiosemicarbazone on the Nanoparticle

FTIR was performed to identify the Dopamine and Thiosemicarbazone attached to the nanoparticle.

FTIR was conducted using the Thermo Scientific Smart Performer Nicolet 380 FT-IR using the ZnSe crystal wavelength range of 500-4000 cm^{-1}. When performing the FTIR on the nanoparticles some spectra were obtained with low noise (190 scans). However, most of the nanoparticles generated noise, either due to the scattering effect of the Fe/Fe_3O_4 nanoparticles, or insufficient sample concentration. (Appendix B Figure B.36-42). FTIR was also recorded for pure dopamine hydrochloride and thiosemicarbazone analogue for comparison (Figures 1.36, 1.38, 1.39).

Therefore, FTIR was also carried out employing a 4 cm^{-1} resolution diffuse reflectance FT-IR spectrometer (Cary 630 FTIR) with a wavelength range of 500-4000 nm to reduce the scattering produced by the nanoparticles. First, the background measurement was taken from a gold standard block. Next, the sample was prepared by grinding the nanoparticles (1 mg) with potassium bromide (100 mg). This mixture was packed into the sample plate holder for IR measurements. 200 scans were taken for each sample (Figure 1.40 and Appendix B Figure B.30-35).

1.7.14 Extracting Thiosemicarbazone Analogue from the Nanoparticle and Detection from HPLC

Extraction of thiosemicarbazone was carried out by digesting 3 mg of the nanoparticle in 1 ml of 10 % HCl. Next, the organic compounds, such as thiosemicarbazone, were extracted into 1 ml of methylene chloride. The methylene chloride layer was neutralized by 1 ml of 10 % sodium bicarbonate. The sample was concentrated by evaporating the solvent.

A pure sample of thiosemicarbazone analogue (0.5 mg), diluted in 400 µl of acetonitrile, and was used as the standard to determine at which retention time the thiosemicarbazone peak is detected. A volume of 3 µl was injected into the HPLC machine for detection.

HPLC was carried out using the LC-6AD Shimadzu liquid chromatography instrument with a SPD-20 A UV/Visible detector and Kinetex 5 µ XB- C18 100 A size 250 * 4.6 mm reverse phase column. A volume 20 µl of the extracted solvent was injected into the machine.

The HPLC was conducted using HLPC grade water as the aqueous solvent and acetonitrile as the organic solvent. The HLPC was achieved through a gradient of aqueous and organic solvent as shown below (Table 1.13); The HLPC can be found in section 1.8.11 in Figures 41-43.

Table 1.13:- Solvent gradient of aqueous and organic solvents for the detection of thiosemicarbazone.

Time (min)	Flow	A_(aq)	B_(org)	Flow rate A %	Flow rate B %
0	1	70	1	0.70	0.30
30.00	1	20	80	0.20	0.80
30.01	0	20	80	-	-

1.7.15 Transmission Electron Microscopy (TEM)

The size of the nanoparticles were determined by TEM, which was performed in the Microscopy and Analytical Imaging Laboratory of the University of Kansas. Sample preparation and data collection are similarly described in the literature.[81] Samples were prepared by suspending the nonoparticles in methylene chloride and agitating in an ultrasonic bath for 15 minutes. The sample was placed onto copper mesh grid with lacey carbon film. The wet grids were allowed to air-dry for several minutes prior to being examined under TEM. The nanoparticle size and morphology were examined by bright-field and dark-field transmission electron microscopy (TEM) using an FEI Technai G_2 transmission electron microscope at an electron acceleration voltage of 200 kV. High resolution images were captured using a standardized, normative electron dose and a constant defocus value from the carbon-coated surfaces.

1.7.16 Cell Viability Test Measured by MTT Assay

Cell viability was tested on both the 4T1 murine breast cancer cell line and a normal (healthy) murine fibroblast cell line for the dopamine nanoparticle, dopamine peptide nanoparticle and all the different coupling ratios of thiosemicarbazone on to the nanoparticles (1:10, 1:5, 1:1, 5:1 and 10:1). The test was done in a 96 well plate. The plate was divided into three columns of 4 replicas each for the control, 24 h and 48 h cell viability were tested for concentrations of 0 µg/ ml (control), 10 µg/ ml, 50 µg/ ml, 100 µg/ ml for all the nanoparticle

ratios (Appendix A Figure A.6). The nanoparticle concentrations were made in the growth media.

The 4T1 murine breast cancer cells were cultured in RPMI (Roswell Park Memorial Institute) with 10% FBS (Fetal bovine serum) and 1X penicillin-streptomycin in a 37 °C humidified incubator with 5% CO_2. After 24 hrs the growth media was removed and 75 µl of fresh media was added to the wells. To the 24 h cells 7.5 µl of MTT reagent (3-(4, 5-Dimethylthiazol-2-yl)-2,5-diphenyltetrazolium bromide) was added and incubated for 4 hrs. After 4hrs 75 µl of MTT buffer solution was added to the 24 h wells to dissolve the formazan crystals and was incubated overnight. After 48 hrs the same procedure was carried out for the 48 h wells. The solubilizing reagent was added to the control wells at the time it was added to the 48 h wells. After incubating overnight the UV was measured at a wavelength range from 550 nm to 690 nm.

The same procedure was carried out for the fibroblast cell line except the growth media was DMEM (Dulbecco's Modified Eagle's Medium).

1.7.17 Test for Cell Uptake of Nanoparticles by Prussian Blue Staining

Form the results obtained from the cell viability test the cell uptake test was done in only the dopamine nanoparticle, dopamine peptide nanoparticle and coupling ratio 5:1 of thiosemicarbazone on both the nanopaticles batches with the dopamine ligand and dopamine peptide ligand. Nanoparticle dispersions were prepared in the growth media and the concentrations tested; 0 µg/ml (control) 5 µg/ ml, 10 µg/ml (Appendix A Figure A.7).

Murine breast cancer cells 4T1, were grown in a 24 well plate. The cells were grown in RPMI with 10% FBS and 1X penicillin-streptomycin in a 37 °C humidified incubator with 5% CO_2 for 24 hrs. After 24 hrs the media was removed and 500 µl of the nanoparticle solution was added and for the control 500 µl RPMI media was added and was incubated for 24 hrs.

After 24 hrs the staining procedure was carried out. The cells were washed twice with 500 µl RPMI and twice with 1 x PBS (Phosphate buffered saline). Next, 500 µl of 10 % NBF (neutral buffered formalin) was added and was allowed to stand for 10 min for fixation to occur. The cells were washed three times with 500 µl of 1 x PBS. Next, equal amounts of 4 % potassium ferrocyanide and 4 % HCl (500 µl each) were added to the wells. Again, 10 min for reaction were allowed. This step was repeated again and the wells were rinsed three times with

500 µl distilled water. Next, the cells were stained with 200 µl of nuclear fast red for 5 min and washed four times with 500 µl distilled water. The cells were stored in 500 µl PBS and were observed under the microscope.

1.8 Results

1.8.1 NMR Characterization of Thiosemicarbazone Analogue

The NMR studies were performed in an Inova NMR Spectrometer, which operates at 400MHz frequency (9.7 Tesla).

1.8.1.1 ^1H NMR of Hydrazinecarbodithioic acid methylester

^{1}H NMR (CDCl$_3$-d, δ ppm) 2.66 (s, 3H, CH$_3$), 4.15(s, 2H, NH$_3^+$ (protonated nitrogen) D$_2$O exchangeable) 4.66 (s, 2H, NH$_2$, D$_2$O exchangeable), 8.11 (s, H, NH$_2^+$CS (protonated nitrogen), D$_2$O exchangeable), 8.53 (s, H, NHCS, D$_2$O exchangeable). Appendix B Figure B.1 and Figure B.2.

Melting point of the compound is 79-81^{0}C

1.8.1.2 ^1H NMR and ^{13}C NMR of N´-(Di-pyridin-2yl-methylene)-hydrazinecarbodithioic acid methylester

^{1}H NMR (CDCl$_3$-d, δ ppm) 2.67 (s, 3H, CH$_3$); 7.52 (s, H, NH); 8.81 (d, H3), 8.62 (d, H8), 8.06 (d, H6), 7.84 (m, H5 & 8), 7.73 (d, H7), 7.42 (m, H4), 7.37 (m, H9) of the Ar-H. The ^{1}H NMR can be found in Appendix B Figure B.3 and B.4.

^{13}C NMR (CDCl$_{3-d}$, δ ppm, J, Hz): 17.70 (CH$_3$); 124.08 (C10), 124.46 (C5), 124.69 (C12), 127.56 (C7), 137.33 (C6 & 11), 142.55 (C13), 148.30 (C8), 148.62 (C9), 151.31 (C4) of the Ar-C; 155.68 (C=N); 202.44 (C=S). The ^{13}C NMR can be found in Appendix B Figure B.5.

Melting point of the compound is 150-153^{0}C

1.8.2 Characterization of the Peptide by HPLC purification and MS

At time 51.62 mins the peptide was detected and shows ~ 90% purity. The HPLC can be found in Appendix B Figure B.6.

The Mass spectrum was taken by Voyager DE STR High performance matrix-assisted laser desorption time-of-flight mass spectrometer (MALDI-TOFMS) equipped with a nitrogen laser (337nm). The calculated molecular weight of the oligopeptide (CGKRK($_D$[KLAKLAKKLAKLAK])PLFAERL) is 2923.87 gmol^{-1}. The mass spectrometry data shows peaks at 2921.77, 2922.77, 2923.77, 2924.77 gmol^{-1}. The most abundant peak 2922.77 gmol^{-1} is due to a removal of a hydrogen atom. The second most abundant peak is due to the

molecular weight of the peptide. The third most abundant peak 2921.77 gmol^{-1} is due to removal of 2 hydrogen's from the peptide. And the least abundant peak 2924.77 gmol^{-1} is due to an addition of a hydrogen to the peptide. The mass spectrum can be found in Appendix B Figure B.7.

1.8.3 TEM Images of the Coated Nanoparticles

The size of the nanoparticles were determined to be 25-35 nm in size (Appendix B Figure B.8). The core/shell structure of Fe/Fe$_3$O$_4$ is clearly discernible. From the TEM it can be observed that the bulk Fe(0) phase is crystalline. However, the nanoparticles are not composed of a single crystal. The Fe$_3$O$_4$ layer, formed by O$_2$ oxidation after nanoparticle synthesis, however it can passivate in aqueous buffers and under air.

1.8.4 Powder X-ray diffraction (XRD) of the Fe/Fe$_3$O$_4$ Magnetic Nanoparticles

The XRD pattern is indicative of the presence of bcc Fe(0) as bulk phase (Figure 1.34). Other XRD peaks were not detected when characterizing dopamine-coated Fe/Fe$_3$O$_4$ nanoparticles (d = 28 +/-2nm). It must be noted that the presence of a surface layer of Fe$_3$O$_4$ would not be detected by means of XRD, which is sensitive to the chemical composition of the bulk phase.[77]
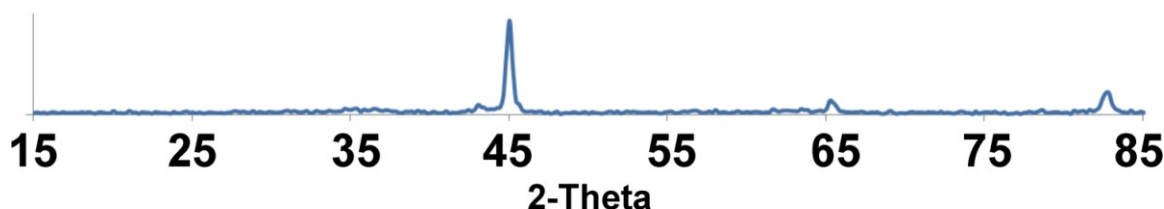
Figure 1.34:- XRD pattern of the synthesized Fe/Fe$_3$O$_4$ nanoparticles after ligand exchange oleylamine/ hexadecylamine$^.$ HCl vs. dopamine.

1.8.5 X-ray photoelectron spectroscopy (XPS) of the Fe/Fe₃O₄ Magnetic Nanoparticles

XPS is able to reveal the chemical surface composition of the nanoparticles. Typically, it can analyze nanoparticles to a depth of 5-10nm. Therefore, it is unable to discern the bulk composition. The XPS measurements shown in Figure 1.35 were performed by Dr. Myles Ikenberry in the group of Prof. Dr. Keith Hohn, Department of Chemical Engineering, Kansas State University. Shown is the surface composition after nanoparticle synthesis and after exchange of oleylamine/ hexadecylamine. HCl against dopamine. XPS clearly indicates the presence of Fe_3O_4 at the nanoparticles' surface, as a comparison with literature findings.[82]
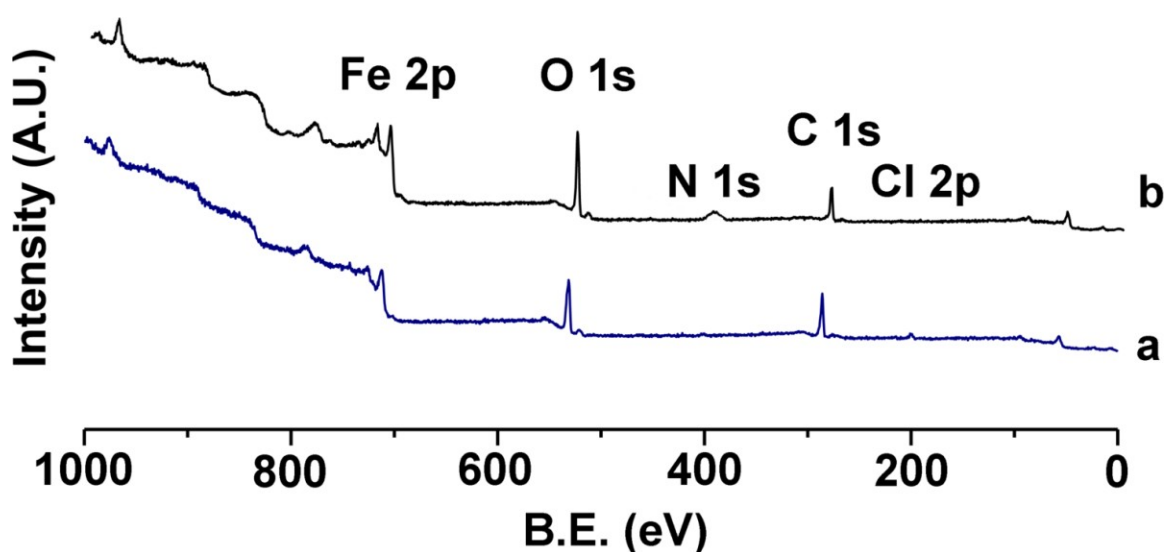
Figure 1.35:- X-ray photoelectron spectroscopy of the Fe/Fe₃O₄ nanoparticles.

Table 1.14:- Iron, oxygen, nitrogen, carbon and chloride content at the catalyst surface, as determined by XPS.

a) Freshly synthesized Fe/Fe_3O_4 nanoparticles (after air oxidation).

b) Fe/Fe_3O_4 nanoparticles after ligand exchange with dopamine.

Sample	Fe	O	N	C	Cl
a) Fe/Fe_3O_4 featuring oleylamine/ hexadecylamine·HCl at the surface	3.4	30.0	2.5	60.8	3.3
b) dopamine exchanged Fe/Fe_3O_4 nanoparticles	4.5	35.7	10.2	49.3	0.3

In both nanoparticles, the inorganic surface consisted of Fe_3O_4. The observed increase in nitrogen and oxygen content, together with a decrease in carbon and chlorine content at the surface indicates exchange of oleylamine/ hexadecylamine.HCl against dopamine. Unfortunately, XPS is only a semiquantitative analysis method.

1.8.6 UV Measurements of Thiosemicarbazone Analogue Coupling with the Dopamine on the Nanoparticle

Thiosemicarbazones in DMF exhibit two absorption peaks. The absorption that occurs at 289-313 nm are due to the $\pi \rightarrow \pi^*$ transitions from the aromatic rings. Absorptions at wavelengths around 356-396 nm are due to n→π* transitions from the azomethine (C=N) and thioamide (C=S) functions overlapped in the same envelope.[83]

When looking at the thiosemicarbazone analogue that we have incorporated in our research, it also shows two peaks around 282-285 nm and 359-371 nm wavelengths.

After reacting with the nanoparticles for four days for the coupling of the thiosemicarbazone analogue to the dopamine on either dopamine coated nanoparticles or dopamine and dopamine peptide coated nanoparticles the 359-371 nm peak would decrease and the 282-285 nm peak would increase. The reason for the decrease in the 359-371 nm peak is that after the reaction most of the thiosemicarbazone analogue is coupled with the dopamine and is removed when centrifuging the nanoparticles, giving evidence that the thiosemicarbazone has

coupled successfully with the dopamine. The increase in the 282-285 nm peak is due to the absorption of the Fe/Fe$_3$O$_4$ nanoparticles. Appendix B Figure B.9-13.

The concentration of thiosemicarbazone that reacted with the nanoparticles were calculated as below (Table 1.15);

Reaction of thiosemicarbazone analogue 1: 10 dopamine and dopamine peptide coated nanoparticle:

Concentration used $=\ 2.4889 * 10^{-5}$ mol/L

Diluted concentration used for UV

measurements (in reaction mixture $=C_1V_1 = C_2V_2$

without nanoparticles) $= (2.4889 * 10^{-5})$ mol/L $* 0.5$ ml $= C_2 * 2.5$ ml

                                     $= 4.9778 * 10^{-6}$ mol/L

Used the highest absorbance (A) $= 0.432474136$

(371 nm) $= A = \mathcal{E}Cl$

                                     $= \mathcal{E} = A/\ Cl$

                                          $= 0.432474136 / ((4.9778 * 10^{-6}$mol/L)$* 1$ cm)

                                          $= 86880.5769$ Lmol^{-1}cm^{-1}

Remaining concentration of $=\ \ C = A/\ \mathcal{E}l$

thiosemicarbazone analogue $= 0.347630501 / (86880.5769$ Lmol^{-1}cm^{-1})$* 1$ cm

in the reaction mixture $= 0.4001245 * 10^{-5}$ mol/ L

with nanoparticles at 371 nm

Reacted concentration of $=\ (2.4889 * 10^{-5})$ mol/L $- (0.4001245 * 10^{-5})$ mol/ L

Thiosemicarbazone $= 2.0887 * 10^{-5}$ mol/L

Percentage of thiosemicarbazone $= ((2.0887 * 10^{-5})$ mol/L $/ (2.4889 * 10^{-5})$ mol/L)$* 100\%$

reacted $=\ 83.92\ \%$

Table 1.15:- Concentration and percentage to thiosemicarbazone reacted with dopamine in dopamine and dopamine peptide coated nanoparticle.

Reaction Ratio	Starting concentration of thiosemicarbazone analogue (mol/L)	Reacted concentration of thiosemicarbazone analogue (mol/L)	Reacted percentage
1:10	$2.489*10^{-5}$	$2.088*10^{-5}$	84 %
1:5	$4.978*10^{-5}$	$0.593*10^{-5}$	11 %
1:1	$2.489*10^{-4}$	$1.792*10^{-4}$	72 %
5:1	$1.244*10^{-3}$	$0.480*10^{-3}$	38 %
10:1	$2.489*10^{-3}$	$0.6707*10^{-3}$	27 %

1.8.7 DLS Results

The mean diameters of the nanoparticles were found as stated below (Table 1.16); (the original data are found in Appendix B Figure B.14-21.

Table 1.16:- Mean diameters of the nanoparticles.

Reaction Ratio	Mean Diameter of nanoparticles (nm)
Dopamine-NP	475.6/ 17 = 28
Peptide-Dopamine-NP-Dopamine	599.0/ 17 = 35
Peptide-Dopamine NP-Dopamine Thiosemicarbazone (1:10)	505.5/ 17 = 30
Peptide-Dopamine NP-Dopamine Thiosemicarbazone (1:5)	426.9/ 17 = 25
Peptide-Dopamine -NP-Dopamine Thiosemicarbazone (1:1)	532.1/ 17 = 31
Peptide-Dopamine -NP-Dopamine Thiosemicarbazone (5:1)	422.9/ 17 = 25
Peptide-Dopamine -NP-Dopamine Thiosemicarbazone (10:1)	451.7/ 17 = 27

1.8.8 Zeta Potential Results

Zeta potential is the measurement of electrical potential or surface charge of particles. For small particles higher zeta potential will give more stability and reduce aggregation. Therefore particles with high negative or positive zeta potentials ($\pm$ 40-60 mV) are stable and would not aggregate however particles with low zeta potentials would aggregate or would have moderate stability ($\pm$ 0-40 mV).[84, 85] Since the nanoparticles we made have many N atoms in the ligands they should give positive zetapotentials. And since they range from 14 – 38 mV they show moderate stability and are expected to show some aggregation.

The zeta potential data of the nanoparticles are as below (Table 1.17); (data can be found in Appendix B Figure B.22-29).

Table 1.17:- Zeta potentials of the nanoparticles

Reaction Ratio	Zeta potential (mV)
Dopamine-NP	30.85
Dopamine-peptide-NP-Dopamine	35.37
Peptide-Dopamine NP-Dopamine Thiosemicarbazone (1:10)	24.37
Peptide-Dopamine -NP-Dopamine Thiosemicarbazone (1:5)	14.82
Peptide-Dopamine -NP-Dopamine Thiosemicarbazone (1:1)	37.13
Peptide-Dopamine NP-Dopamine Thiosemicarbazone (5:1)	38.70
Peptide-Dopamine -NP-Dopamine Thiosemicarbazone (10:1)	32.08

1.8.9 ICP (Inductively coupled plasma) Measurements to Determine the Iron Content in the Nanoparticles and Sulfur Content on the Nanoparticles due to Thiosemicarbazone Coupling

From the ICP measurements obtained from the different ratios of the nanoparticles the iron content for the nanoparticles ranged from 60-73 %. There was no sulfur detected in the nanoparticle coated with dopamine. Sulfur was detected in the nanoparticle that was coated with dopamine-peptide ligand due to the sulfur present in the cysteine moiety in the peptide sequence, confirming the coupling of the peptide to the dopamine. Sulfur was detected in the different ratios of the Dopamine-peptide-NP-Dopamine-Thiosemicarbazone and NP Thiosemicarbazone-

Dopamine-NP confirming the coupling of the thiosemicarbazone analogue to the dopamine on the nanoparticle. The results obtained are as below (Table 1.18);

Table 1.18:- Iron and sulfur content in the nanoparticles.

Nanoparticle (NP) system	Iron content per 1mg of NP (mg)	Iron percentage per 1mg of NP	Sulfur content per 1mg of NP (mol)	Sulfur percentage per 1mg of NP
Dop-NP	0.6109	61 %	-	-
Dop-Peptide-NP	0.6542	65.42%	$6.503 * 10^{-6}$	9.68 %
Dop-Peptide-NP-Dop-Thio (1:10)	0.7063	70.63 %	$0.082 * 10^{-6}$	0.26 %
Dop-Peptide-NP-Dop-Thio (1:5)	0.7265	72.65 %	$0.104 * 10^{-6}$	0.33 %
Dop-Peptide-NP-Dop-Thio (1:1)	0.7276	72.76 %	$0.300 * 10^{-6}$	0.94 %
Dop-Peptide-NP-Dop-Thio (5:1)	0.7285	72.85 %	$0.240 * 10^{-6}$	0.77 %
Dop-Peptide-NP-Dop-Thio (10:1)	0.7195	71.95 %	$0.096 * 10^{-6}$	0.31 %
Thio-Dop-NP (1:10)	0.7581	75.81 %	$0.139 * 10^{-6}$	0.44 %
Thio-Dop-NP (1:5)	0.6961	69.61 %	$0.156 * 10^{-6}$	0.50 %
Thio-Dop-NP (1:1)	0.7841	78.41 %	$0.161 * 10^{-6}$	0.52 %
Thio-Dop-NP (5:1)	0.8390	83.90 %	$0.096 * 10^{-6}$	0.31 %
Thio-Dop-NP (10:1)	0.8160	81.60 %	$0.094 * 10^{-6}$	0.30 %

Dop-NP denotes Dopamine-NP, Peptide-Dop-NP denotes Peptide-Dopamine -NP,

Thio-Dop-NP denotes Thiosemicarbazone-Dopamine-NP, NP denotes nanoparticles.

Calculations to determine the iron and sulfur content in the nanosytems.

Iron concentration detected by ICP $= 31.29 \text{ mgL}^{-1}$

Original concentration before dilution $= C_1V_1 = C_2V_2$

$= C_1 * 0.1 \text{ ml} = 31.29 \text{ mgL}^{-1} * 5 \text{ ml}$

$= C_1 = 1564.5 \text{ mgL}^{-1}$

Weight of iron in 2.15 mg of NP $= (1564.5 \text{ mg}/ 10^3 \text{ ml}) * 1 \text{ ml}$

$= 1.565 \text{ mg}$

Weight of iron in 1 mg of NP $= (1.565 \text{ mg}/ 2.15 \text{ mg}) * 1 \text{ mg}$

$= 0.7276 \text{ mg}$

Percentage of iron $= (0.7276 \text{ mg}/ 1 \text{ mg}) * 100 \%$

$= 72.76 \%$

Sulfur content detected by ICP $= 19.53 \text{ mgL}^{-1}$

Weight in 3 ml of the solution $= (19.53 \text{ mg}/ 10^3 \text{ ml}) * 3 \text{ ml}$

$= 0.05859 \text{ mg}$

Weight of sulfur in 1 mg of NP $= (0.05859 \text{ mg}/ 6.10 \text{ mg}) * 1 \text{ mg}$

$= 0.009604 \text{ mg}$

Percentage of sulfur $= (0.009604 \text{ mg}/ 1 \text{ mg}) * 100 \%$

$= 0.96 \%$

Moles of sulfur in 1 mg of NP $= (0.009604 * 10^{-3}) \text{ g}/ 32 \text{ gmol}^{-1}$

$= 0.300 * 10^{-6} \text{ mol}$

1.8.10 FTIR Identification of Dopamine and Thiosemicarbazone on the Nanoparticle

FTIR signals for aromatic C-C stretching peaks occur between 1335- 1250 cm^{-1}. Pure dopamine is featuring these peaks at 1344.89 cm^{-1} and 1288.96 cm^{-1}. Peaks ranging from 1400-1650 cm^{-1} are due to C=C for dopamine. They are seen at 1495.01 cm^{-1}, 1465.58 cm^{-1} for symmetric stretching, and 1577.43 cm^{-1}, 1615.70 cm^{-1} for asymmetric stretching. Aromatic C-H stretching is between 3000-3120 cm^{-1}. This peak is at 3072.77 cm^{-1} for dopamine. The alcoholic O-H symmetric and asymmetric stretching vibrations are between 3670-3580 cm^{-1}; for dopamine they occur at 3340.64 cm^{-1}. Alcoholic C-O stretching vibrations are between1200-1000 cm^{-1} for dopamine. They are seen at 1077.02-1062.31 cm^{-1}. Alphatic C-H symmetric stretching vibrations

are between 2975-2840 cm^{-1}. For dopamine this peak is seen at 2931.48 cm^{-1}. N-H stretching is at 3300-3500 cm^{-1}. In dopamine it is seen at 3322.98 cm^{-1}. And scissoring of N-H is seen at 1550-1650 cm^{-1}. For dopamine it is seen at 1598.04 cm^{-1}. C-O-H symmetric bending and asymmetric bending occur at 1261 cm^{-1} and 1320 cm^{-1}, respectively. For dopamine they are at 1259.53 cm^{-1} and 1318.96 cm^{-1}, respectively. The spectrum is seen in figure 1.36. The FTIR for the dopamine coated on the nanoparticle show similar peaks (Figure 1.37). Therefore, we can determine that dopamine has been successfully incorporated onto the Fe/Fe$_3$O$_4$ nanoparticle.[86, 87]
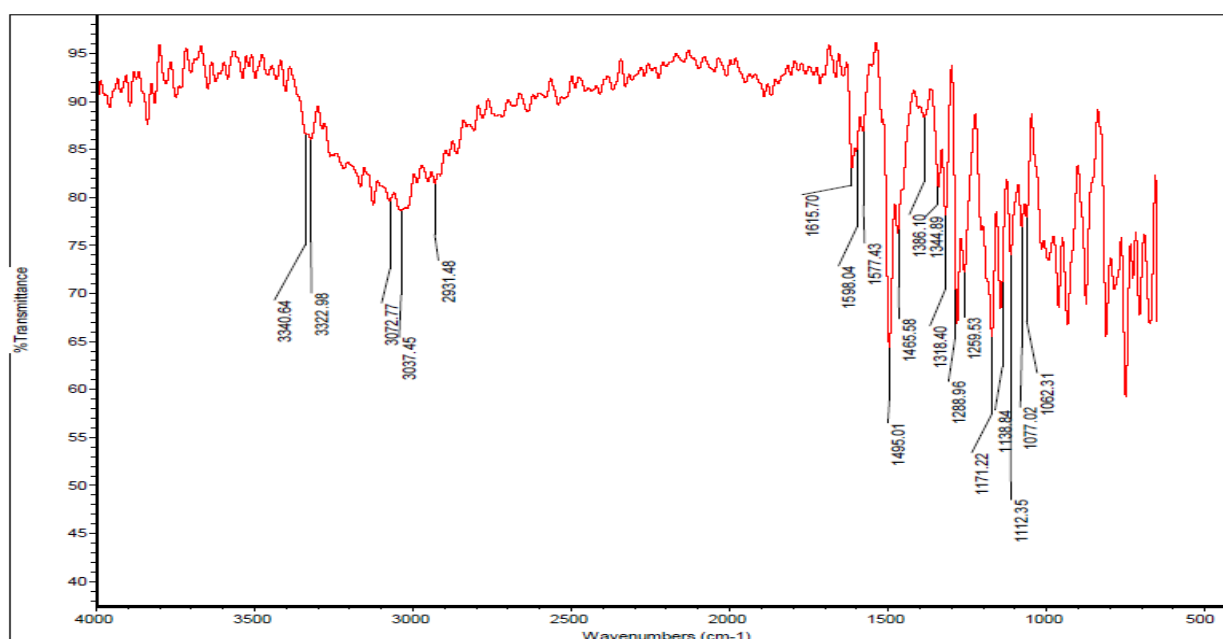
Figure 1.36:- FTIR of dopamine.
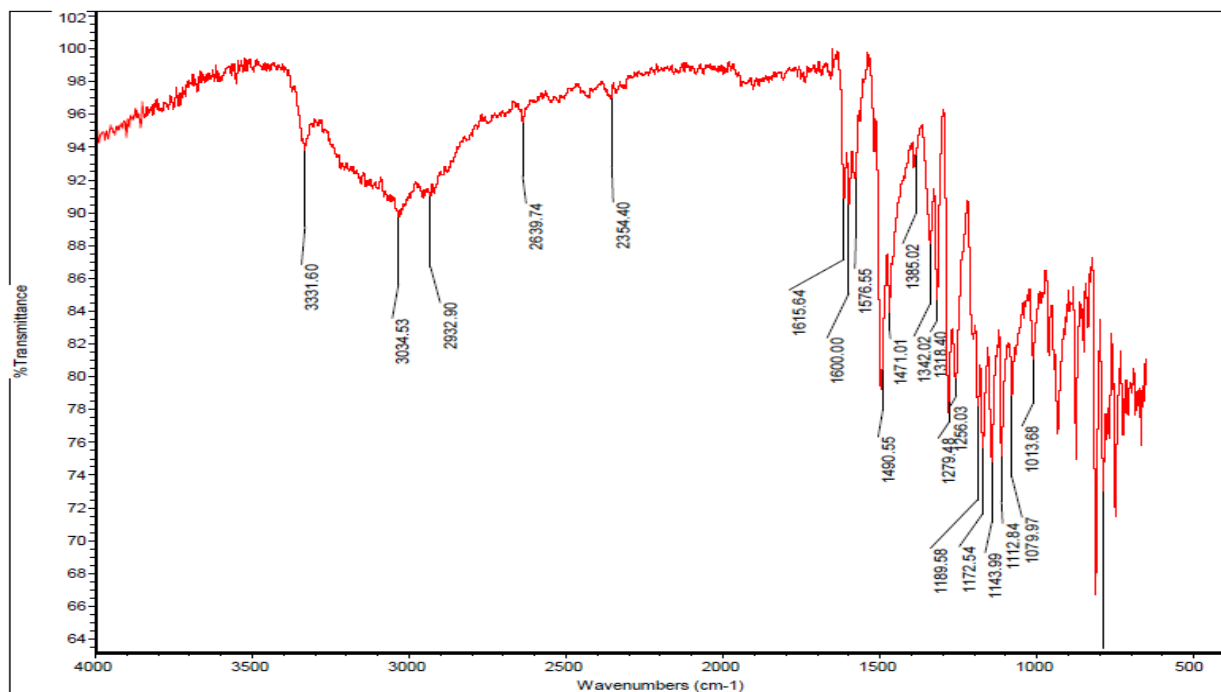
Figure 1.37:- FTIR of dopamine coated Fe/Fe$_3$O$_4$-nanoparticles.

The characteristic FTIR peaks for the thiosemicarbazone analogue are the bands in the 1636 and 1588 cm^{-1} region that may be assigned to the symmetric or asymmetric (C=N) vibrations. A peak at 1636.30 cm^{-1} in the thiosemicabazone analogue corresponds to the C=N bond. A strong band at 1030-1275 cm^{-1} corresponds to the C=S bond in the thiosemicarbazone analogue. It is seen at 1275.57 cm^{-1}. The bands that appear in the 1410-1435 cm^{-1} region are due to the coupled vibrations of C=S and N-H. There is a peak present due to these vibrations at 1412.38 cm^{-1}. The band for C=N, which ranges from 3300-3500 cm^{-1}, is observed at 3487.82 cm^{-1}. A band for the C-N stretching vibration, which ranges from 1020-1250 cm^{-1}, is seen at 1235.98 cm^{-1}. Aromatic C-H stretching is observed at 3037.45 cm^{-1}. Alphatic C-H symmetric stretching for the methylene group is seen at 2850.81-2979.80 cm^{-1}.[88,89] The FTIR for thiosemicabazone is shown in figure 1.38.
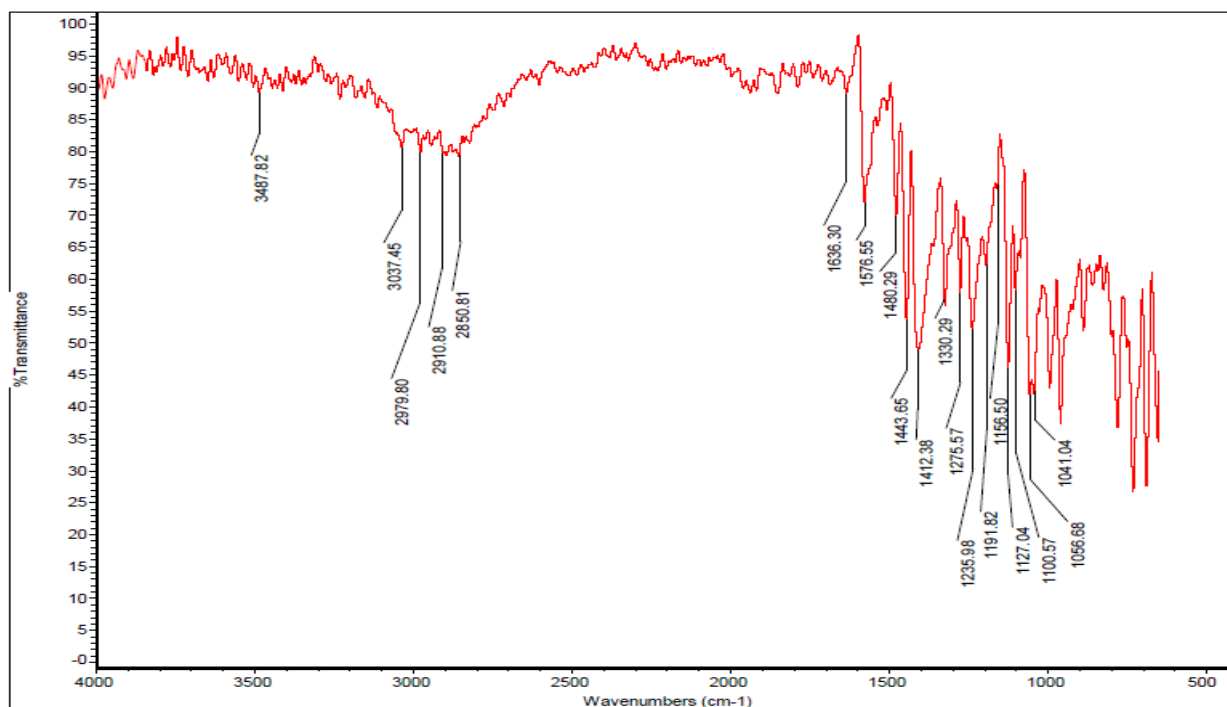
Figure 1.38:- FTIR of Thiosemicarbazone analogue.

A comparison of dopamine HCl, dopamine coated Fe/Fe$_3$O$_4$-nanoparticles, thiosemicarbazone analogue, and the thiosemicarbazone-dopamine coated Fe/Fe$_3$O$_4$-nanoparticles was performed, which is shown in figure 1.39. Here we can see similar peaks of dopamine and thiosemicarbazone, in comparison with dopamine and thiosemicarbazone-dopamine coated nanoparticles. Therefore, we can determine that the thiosemicarbazone was successfully coupled to the nanoparticle.

For the peptide-dopamine and thiosemicarbazone-dopamine coated nanoparticle, other than the IR peaks for dopamine and thiosemicarbazone, additional peaks for C=O stretching are seen around 1700-1600 cm^{-1} and C=N vibrations are seen around 1636-1588 cm^{-1}. These peaks are much more intense (Figure 1.40).[90] Therefore, we could determine that the both the peptide and thiosemicarbazone analogue were succsessfuly coupled to the dopamine on the nanoparticle.
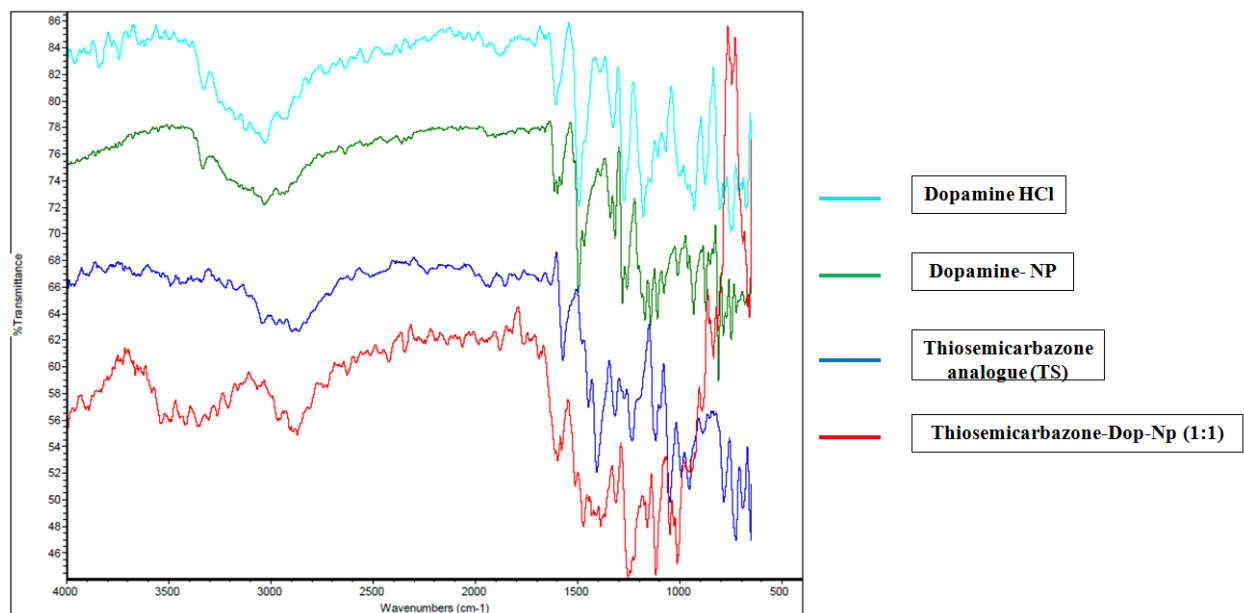
Figure 1.39:- FTIR comparison for Thiosemicarbazone-Dopamine-NP.
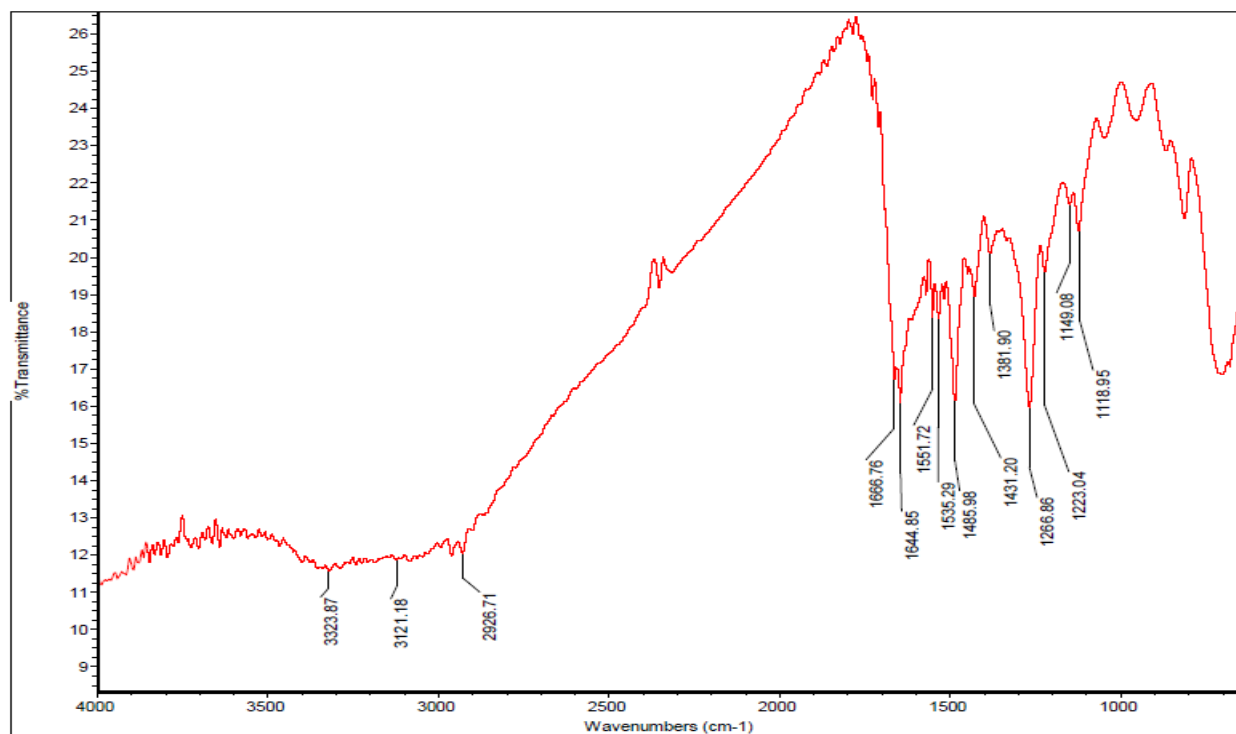
Figure 1.40:- FTIR of Peptide –Dopamine-NP-Dopamine-Thiosemicarbazone 1:1.

1.8.11 Extracting Thiosemicarbazone Analogue from the Nanoparticle and Detection from HPLC

From the HPLC data we were able to detect the pure thiosemicarbazone analogue at 13.60 mins (Figure 1.41). The peak area was 84 rel.% as shown in table 1.19.
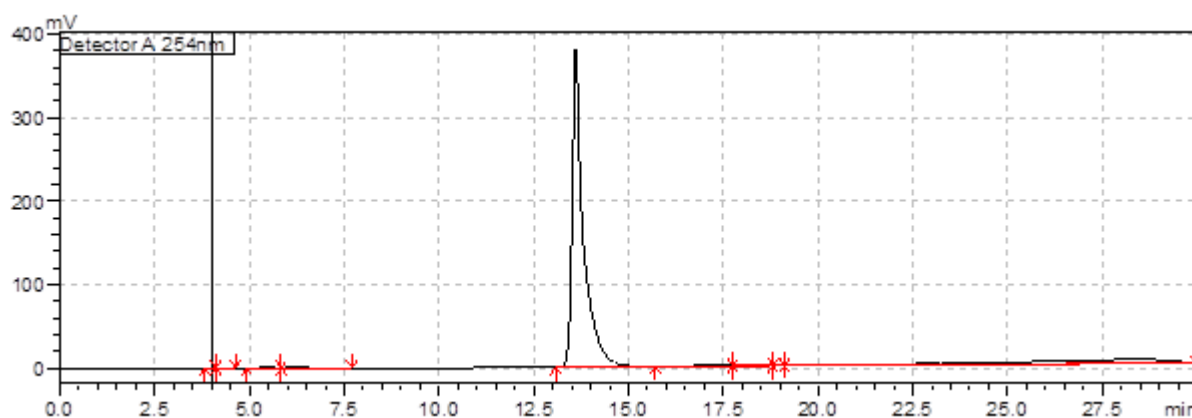
Figure 1.41:- HPLC of Thiosemicarbazone analogue.

Table 1.19:- HPLC data for Thiosemicarbazone analogue.

Peak number	Retention Time	Area	Height	Area%
1	4.002	1281	118	0.014
2	4.239	2194	142	0.023
3	5.378	21827	1063	0.232
4	6.149	40615	1553	0.432
5	13.606	7966059	380985	84.752
6	17.631	32156	772	0.342
7	18.156	52770	1957	0.561
8	18.983	4152	231	0.044
9	28.424	1278163	4663	13.599

Similarly, detection of the thiosemicarbazone peak was observed in the HPLC of the extractions of peptide-dopamine-NP-dopamin-thiosemicarbazone analogue (1:1) at 13.45mins (Figure 1.42) and area of 0.07 % (Table1.20) and thiosemicarbazone-dopamine-NP (1:1) also observed at 13.10 mins (Figure 1.43) and an area of 0.079 % (Table1.21).

The detection times were slightly less than that of the pure thiosemicarbazone analogue. This may be because that the concentrations of the thiosemicarbazone was low, or their might have been some chemical modification of the analogue, which is less likely, according to the FTIR results. The peak areas were also low since concentration of thiosemicarbazone was low.
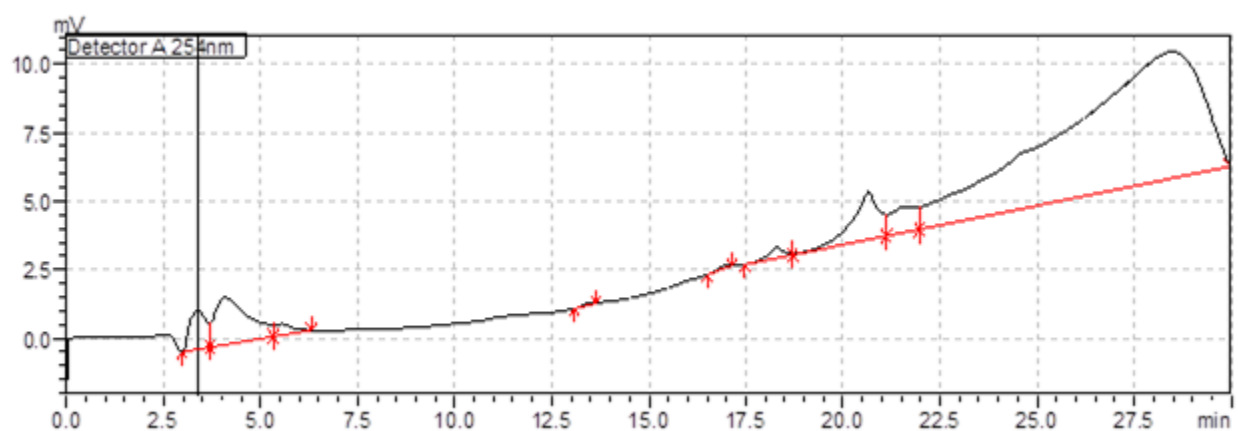
Figure 1.42:- HPLC of Peptide-Dopamine-NP-Dopamin-Thiosemicarbazone analogue (1:1) extract.

Table 1.20:- HPLC data for Peptide-Dopamine-NP-Dopamin-Thiosemicarbazone analogue (1:1) extract.

Peak Number	Retension Time	Area	Height	Area%
1	3.388	41579	1402	2.776
2	4.07	102848	1722	6.865
3	5.558	13170	409	0.879
4	13.45	1042	52	0.07
5	17.001	1996	97	0.133
6	18.322	10597	386	0.707
7	20.66	83323	1749	5.562
8	21.725	44029	897	2.939
9	28.472	1199477	4616	80.069
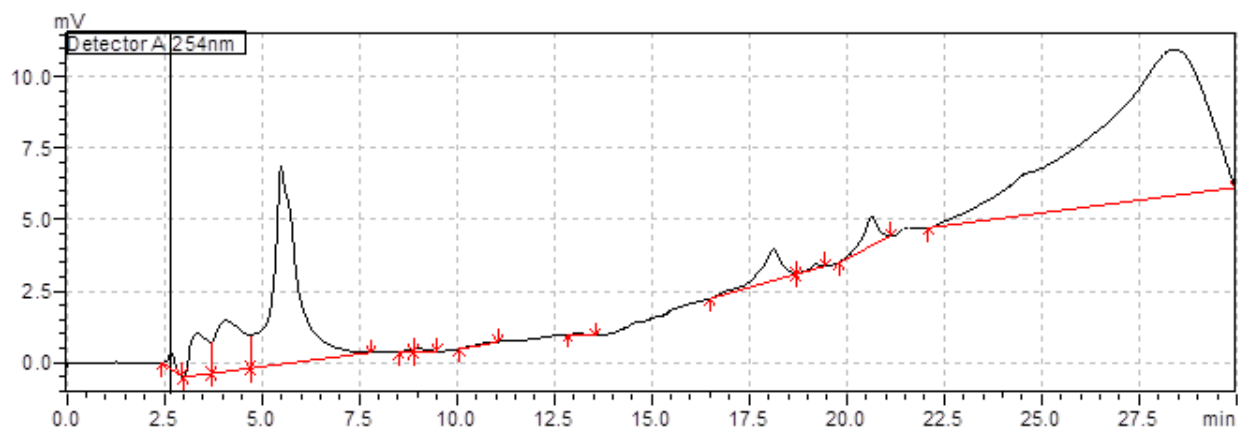
Figure 1.43:- HPLC of Thiosemicarbazone-Dopamine-NP (1:1) extract.

Table 1.21:- HPLC data for Thiosemicarbazone-Dopamine-NP (1:1) extract.

Peak Number	Retension Time	Area	Height	Area%
1	2.677	6804	562	0.414
2	3.361	45598	1462	2.777
3	4.055	88210	1790	5.372
4	5.489	308545	6958	18.79
5	8.8	1165	87	0.071
6	9.016	2238	110	0.136
7	10.842	1556	31	0.095
8	13.1	1593	64	0.079
9	18.129	43148	1118	2.628
10	19.234	2702	144	0.165
11	20.649	28016	1046	1.706
12	28.405	1044928	5127	63.634

1.8.12 Calculation of the Amount of Thiosemicarbazone Analogue coupled to the Dopamine on the Nanoparticle

The average size of the nanoparticles used for the delivery of the thiosemocarbazone analogue and the therapeutic peptide sequence is 28 +/- 2nm. Furthermore, the average thickness of the passivating Fe_3O_4 layer is 2nm.

Therefore, the core of one typical nanoparticles has a diameter of 24nm. This corresponds to a volume of 7.2411×10^{-24} m^3. The density of elemental Fe is 7873 kg m^{-3}.[91] Therefore, weight of the Fe(0) core of one Fe/Fe_3O_4 core/shell nanoparticle with 24 nm core diameter is 5.6987×10^{-20} kg.

The Fe_3O_4 shell has a volume of 4.2529×10^{-24} m^3, which is calculated from the volume of a nanoparticle with 28 nm in diameter (1.1494×10^{-23} m^3), minus a nanoparticle with 24nm in diameter (7.2411×10^{-24} m^3). The density of Fe_3O_4 is 5100 kg m^{-3},[92] leading to a weight of the Fe_3O_4 shell of 2.1689×10^{-20} kg.

The total weight of a Fe/Fe_3O_4 core/shell nanoparticle is 7.8691×10^{-20} kg. This means that in one kg of the material are 1.2798×10^{19} nanoparticles or 2.1099×10^{-5} mol nanoparticles.

What is the maximum number of dopamine at the surface of Fe/Fe_3O_4 core/shell nanoparticles with a diameter of 28nm?

The surface area of the nanoparticle is 2.4630×10^{-15} m^2.

The space demand of one dopamine linker is 1.094×10^{-18} m^2, as calculated from its Connolly solvent excluded volume of 1.075×10^{-28} m^3.[93] This data is available from the program package Chemdraw 3D (Cambridge Soft Corporation, 1999). The space demand was calculated by assuming a sphere for dopamine. This permitted the calculation the area of the circle with the same diameter than the sphere. According to this approximation, the surface of a Fe/Fe_3O_4 nanoparticle of 28nm in diameter is covered with maximally 2251 dopamine ligands.

Assuming that each of the 2251 ligands would be capable of reacting with one thiocarbazone precursor (see Appendix A Figure A.5), we would add either 2251 sulfur atoms to the outer layer, because each thiocarbazone molecule reacts with the terminal amino group of dopamine. The weight of one S atom is 5.3247×10^{-26} kg. The weight of 2251 sulfur atoms is 1.199×10^{-22} kg. The weight of the dopamine layer is 4.56×10^{-22} kg, assuming that 2251 dopamine molecules are present in the outer organic layer. Therefore, the weight of one dopamine-coated nanoparticle increases to 7.9147×10^{-20} kg.

The weight of the chemisorbed sulfur (1.199 x 10^{-22} kg), divided by the weight of one nanoparticle (7.9147 x 10^{-20} kg.), yields the factor of 0.0015. This means that coverage with a complete layer of thiocarbazone analogues will lead to only 0.15 percent sulfur by weight. The sulfur content may increase to 0.24 percent, if the methyl sulfide that is formed as a by-product of the coupling reaction, is chemisorbed as well. This calculation also indicates that in the case of Dop-Peptide-NP with a sulfur content of 9.68% we have multiple physisorbed layers of peptide sequence (CGKRK($_D$[KLAKLAKKLAKLAK])PLFAERL) around the nanoparticle.

Based on this estimate, it is evident that the sulfur content that was determined by ICP (see Table 1.18), is slightly too high, by a factor of two to three. This is indicative that byproducts of the coupling reactions were trapped by the reactive iron oxide surface during the coupling reaction. In conclusion, measuring the sulfur content of the nanoparticles cannot be regarded as a feasible strategy to determine the loading degree of the nanoparticles with the thiosemicarbazone analogue. It is noteworthy that the coupling efficacy of the thiosemicarbazone analogue to dopamine-coated Fe/Fe_3O_4 core/shell nanoparticles was determined by UV/Vis-measurements, and the chemical identity of the thiosemicarbazone analogue was confirmed by using HPLC. Therefore, the principal composition of these nanoplatforms for drug delivery is not in question.

1.8.13 Cell Viability Test Measured by MTT Assay

The cell toxicity of both the 4T1 murine breast cancer cell line and normal murine fibroblast cell line of individual nanosystems were incorporated into one graph to determine if there was a significant difference in cell toxicity towards the cancer cell line than the normal cell line. The data can also show if the nanosystem is able to specifically target the cancer cells vs. the normal cells (Table 1.22). The data are found in Appendix B Figure B.41-52.

The cell toxicity data were analyzed and plotted as below;
1. For each well the UV690 values were subtracted from the UV540 values.
2. The mean UV values were calculated for every test sample concentration.
3. The mean UV values of the blanks were calculated.
4. The sample and solvent control UV's were corrected as below:

Mean UV$_{abs}$ of samples/controls – mean UV$_{abs}$ of blanks

5. Relative inhibition activity is expressed as percent of solvent control:

$$\% \text{ inhibition} = 100 - \left(\frac{\text{Corrected mean UV}_{abs} \text{ sample x 100}}{\text{Corrected mean UV}_{abs} \text{ solvent controls)}} \right)$$

6. The % inhibition of activity against the test compound concentration was plotted to obtain the cell toxicity curve.

Notable difference in toxicity can be seen in the 5:1 ratio of both the dopamine-peptide-NP-dopamine-thiosemicarbazone and NP-dopamne-thiosemicarbazone nanoparticle systems. From this observation we can say that the ratio of thiosemicarbazone incorporated in the nanosystem is of importance when considering therapeutic activity.

Most of the other nanosystems showed close or similar toxicity in both cell lines. In some ratios the 48 h cell toxicity would be more in the cancer cell line.

The IC_{50} values were calculated by the equation below;

Log (% inhibition / (100 -% inhibition)) vs. Concentration

The IC_{50} values were obtained from the intercept on the x-axis (Appendix B Figure B.53-64).

Table 1.22:- IC$_{50}$ values for 4T1 cell line and fibroblast cell line.

Nanoparticle (NP) system	IC$_{50}$ Values for 4T1 cell line (ug/ml)	IC$_{50}$ Values for Fibroblast cell line (healthy cells) (ug/ml)
Dop-NP	71 ($\pm$ 0.02)	50 ($\pm$ 0.02)
Dop-Peptide-NP	37 ($\pm$ 0.05)	17 ($\pm$ 0.11)
Peptide-Dop--NP-Dop-Thio (1:10)	50 ($\pm$ 0.06)	82.5 ($\pm$ 0.02)
Peptide-Dop-NP-Dop-Thio (1:5)	45 ($\pm$ 0.02)	~
Peptide-Dop-NP-Dop-Thio (1:1)	44 ($\pm$ 0.06)	47 ($\pm$ 0.03)
Peptide-Dop--NP-Dop-Thio (5:1)	36 ($\pm$ 0.03)	80 ($\pm$ 0.03)
Peptide-Dop-NP-Dop-Thio (10:1)	37 ($\pm$ 0.01)	43 ($\pm$ 0.01)
Thio-Dop-NP (1:10)	70 ($\pm$ 0.05)	92 ($\pm$ 0.01)
Thio-Dop-NP (1:5)	80 ($\pm$ 0.02)	~
Thio-Dop-NP (1:1)	80 ($\pm$ 0.06)	~
Thio-Dop-NP (5:1)	32.5 ($\pm$ 0.06)	~
Thio-Dop-NP (10:1)	67 ($\pm$ 0.03)	80 ($\pm$ 0.02)

IC$_{50}$ values given with standard errors.

~ denotes that the IC$_{50}$ is more than 100 µg/ml.

Dop-NP denotes Dopamine-NP, Peptide-Dop-NP denotes Peptide-Dopamine -NP-Dopamine,

Thio-Dop-NP denotes Thiosemicarbazone-Dopamine-NP, NP denotes nanoparticles.

1.8.14 Cell Uptake of Nanoparticles by Prussian Blue Staining

According to the cell toxicity experiment only the nanoparticle systems;

1. Dopamine-NP
2. Peptide-Dopamine-NP-Dopamine
3. Peptide-Dopamine -NP-Dopamine-Thiosemicarbazone (5:1)
4. Thiosemicarbazone-Dopamine-NP (5:1)

Were tested for the cell uptake experiment.

All nanosystems showed cell uptake. The nanoparticles, which are blue in color after staining, have surrounded the nucleus confirming that the nanoparticles are taken up by endocytosis. Images of cells can be found in Appendix B Figure B.65-73.

1.9 Discussion

We were successful in exchanging the dopamine-peptide ligand onto the nanoparticles and this was confirmed by the sulfur content obtained by the ICP experiments, which is due to the cysteine moiety in the peptide sequence. The usual method to attach ligands onto the nanoparticle is by first synthesizing the ligand and next exchanging the ligand with the existing ligands on the nanoparticle. However we used a non-conventional method where we have coupled thiosemicarbazone analogue onto the free dopamine on the nanoparticle, where the free dopamine ligand has already been exchanged to the nanoparticle. This method was done since it was impossible to synthesize the dopamine-thiosemicarbazone analogue in the required purity, in spite of attempting numerous synthetic methods and purification methods. The result was, principally, always the same: the yield would be low and the compound was impossible to purify. In sharp contrast, coupling of the thiosemicarbazone analogue with the dopamine on the nanoparticle was confirmed by the detection of sulfur content obtained by the ICP experiments, therefore by using the unconventional method we were successful in coupling the thiosemicarbazone iron chelator onto the nanoparticle. One would assume that the sulfur content of the nanoparticles containing both the peptide and thiosemicarbazone analogue would be higher than the nanoparticle with just the peptide sequence. However, after coupling with thiosemicarbazone, the sulfur content was lower than that of the nanoparticle with just the peptide sequence. This may be due the fact that physisorption of the dopamine peptide ligand had occurred instead of chemisorption. Therefore, when the coupling reaction with the thiosemicarbazone is performed, the physisorbed peptide is competitively removed. Another possibility is the degradation of the peptide during the reaction, although we have not obtained experimental evidence in favor of this assumption.

According to the DLS and zeta potential experiments we can see that the nanosystems are of preferable size needed for therapeutic activity. From the cell toxicity experiments we were able to determine that the ratio at which thiosemicarbazone was coupled, was of importance since only the 5:1 ratio was successful in obtaining a significant difference in the toxicity of the 4T1 cancer cells than the normal fibroblast cells. The other nanosystems showed very similar toxicity to the cancer cells and their control group. From the IC_{50} values we can see that all the nanosystems with thiosemicarbazone show lower IC_{50} values for the 4T1 cell line than the

fibroblast cell line. This shows that the nanosystem is more effective in the cancer cell line than the healthy cell line. Furthermore the lowest IC_{50} values are shown in both the 5:1 ratio nanosystems further demonstrating that this ratio is ideal for therapeutic use. From the prussian blue staining experiment we were able to determine that the nanosystem were successfully taken up by the 4T1 cells confirming the that the endocytic pathway is the main uptake pathway.

According to our calculations (see chapter 1.8.12), the weight of one dopamine-coated Fe/Fe_3O_4 core/shell nanoparticles of 28 nm in diameter is 7.8691×10^{-20} kg. Considering that the molecular mass of the thiosemicarbazone analogue is 276 g/mol, the weight of one molecule is 4.6329×10^{-25} kg. This leads to a weight ratio of thiosemicarbazone analogue and nanoparticle of approx. 1 to 169,853.

The nanoplatform showed the highest efficacy against 4T1 cells when reacting with 5 thiosemicarbazone analogue per surface dopamine. We have determined by means of UV/Vis-measurements (see 1.8.6) that 38 percent of the thiocarbazone precursor has reacted. This means that we have complete surface coverage, plus a second layer of physisorbed thiocarbazone. This surface coverage showed the highest efficacy in killing highly metastatic cancer cells (IC_{50}= 36 μg/mol), while being significantly less toxic against the healthy control cell line (fibroblast cell line, IC_{50}= 80 μg/mol). At an attempted loading of 10:1 (27% conversion), we have a complete chemisorbed layer and a larger physisorbed layer, consisting of approx. 1.7 times the amount of thiocarbazone that was bound to dopamine. This higher loading caused toxicity against cancer cells and healthy cells alike. Therefore, it is our conclusion that synthesizing a monolayer of thiosemicarbazone analogue around the thiosemicarbazone analogue is most favorable with respect to minimizing the collateral damage to healthy cells. At this optimal ratio (monolayer), the IC_{50} Value for 4T1 cell line is 36 (± 0.03) μg/ mol. However, the required mass of the therapeutic nanoplatform contains the Fe/Fe_3O_4 iron core. With respect to the thiosemicarbazone analogue, is at by a factor of 30 lower, considering that the drug is only surface bound. This means that the thiosemicarbazone analogue synthesized at the surface of the Fe/Fe_3O_4 nanoparticles is active in the low micromolar range.

The results we obtained do not justify our original hypothesis that the combination of both peptide sequence and iron chelators would cause a synergistic effect increasing the cytotoxicity when treating cancer. However, they lead the way towards a novel strategy in increasing the toxicity of nanoformulations towards cancer cells and decrease their toxicity for

normal cells. This is of great importance, because only approx. 10 percent of a nanoparticle-based drug is able to reach the tumor.

Future work will be performed to clarify our hypothesis by synthesizing the nanosystem in the reverse manner, by first coupling the thiosemicarbazone analogue to the dopamine coated nanoparticle and then exchanging ligands with the dopamine-peptide ligand. Other studies can be performed to determine the redox activity and ROS activity of the nanosystem by conducting EPR (Electron paramagnetic resonance) experiments.

1.10 References

1. Report of American cancer society.

2. Myrberg H.; Zhang L.; Mäe M.; Langel U.; Design of a Tumor-Homing Cell-Penetrating Peptide, *Bioconjugate Chemistry*, 2008, *Vol. 19,* 70–75.

3. Li Y.; Lei Y.; Wagner E.; Xie C. et.al; Potent Retro-Inverso D‑Peptide for Simultaneous Targeting of Angiogenic Blood Vasculature and Tumor Cells, *Bioconjugate Chemistry*, 2013, *Vol. 24*, 133−143.

4. Agemy L.; Morvinski D. F.; Kotamraju R.V.; Roth L.; Sugahara K.N.; Girard O.M.; Mattrey R.F.; Verma I.M.; Ruoslahti E.; Targeted nanoparticle enhanced proapoptotic peptide as potential therapy for glioblastoma, *PNAS*, 2011, *Vol. 108*, 17450-17455.

5. Denicourt C.; Dowdy S. F.; Targeting Apoptotic Pathways in Cancer Cells, *Science*, 2004, *Vol. 305*, 1411-1413.

6. Rao V A.; Klein S R.; Agama K K.; Toyoda E.; Adachi N.; Pommier Y.; Shacter E B.; The Iron Chelator Dp44mT Causes DNA Damage and Selective Inhibition of Topoisomerase IIA in Breast Cancer, Cells*American Association of Cancer Research*, 2009, *Vol. 69*, 948-957.

7. Kalinowski D S.; Yu Y.; Sharpe P C.; Islam M; Liao Y T.; Lovejoy D B.; Kumar N.; Bernhardt P V.; Richardson D R.; Design, Synthesis, and Characterization of Novel Iron Chelators: Structure-Activity Relationships of the 2-Benzoylpyridine Thiosemicarbazone Series and Their 3-Nitrobenzoyl Analogues as Potent Antitumor Agents, *J. Med. Chem.*, 2007, *Vol. 50,* 3716-3729.

8. http://www.cancer.org/research/cancerfactsfigures/cancerfactsfigures/cancer-facts-figures-2012.

9. http://www.cancer.gov/cancertopics/factsheet/Detection/staging.

10. Balivada S.; Rachakatla R. S.; Wang H.; Samarakoon T. N.; et.al; *BMC Cancer*, 2010, *Vol. 10*, 119.

11. Langel U.; Cravatt B. F.; Gräslund A; Heijne G. V.; et.al; *Introduction to Peptides and Proteins*, 2010, 5-7, 18,152-154,195-197, 373,374.

12. Goodman M.; Shao H.; Peptidomimetic building blocks for drug discovery: An overview, *Pure and Appl. Chem.*, 1996, *Vol. 68*, 1303-1305.

13. Zorko M.; Langel U.; Cell-penetrating peptides: mechanism and kinetics of cargo delivery, *Advanced Drug Delivery Reviews*, 2005, *Vol. 57,* 529-545.

14. Langel U.; Cell-Penetrating Peptides Processes and Applications, 2002, v-vi.

15. Järver P.; Langel U.; Cell-penetrating peptides—A brief introduction, *Biochimica et Biophysica Acta*, 2006, *Vol. 1758*, 260-263.

16. Green M.; Loewenstein P.M.; Autonomous functional domains of chemically synthesized human immunodeficiency virus tat trans-activator protein, *Cell 55*, 1988, 1179–1188.

17. Derossi D.; Joliot A.H.; Chassaing G.; Prochiantz A.; The third helix of the Antennapedia homeodomain translocates through biological membranes, *J. Biol. Chem, Vol. 269*, 1994, 10444–10450.

18. Lundberg P.; Langel U.; A brief introduction to cell-penetrating peptides, *J. Mol. Recognition*, 2003, *Vol.16*, 227-233.

19. Derossi D.; Calvet S.; Trembleau A.; Brunissen A.; Chassaing G.; Prochiantz A.; Cell internalization of the third helix of the Antennapedia homeodomain is receptor-independent, *J. Biol. Chem., Vol. 271*, 1996, 18188–18193.

20. Li Z. J.; Cho C. H.; Peptides as targeting probes against tumor vasculature for diagnosis and drug delivery, *Journal of Translational Medicine*, 2012, *Vol. 10.*

21. Rajotte D.; Arap W.; Hagedorn M.; Koivunen E.; Pasqualini R. and Ruoslahti E. J.; Molecular heterogeneity of the vascular endothelium revealed by in vivo phage display,*Clin. Invest., Vol. 102*, 1998, 430−437.

22. Ruoslahti E.; Bhatia S. N.; Sailor M. J.; Targeting of drugs and nanoparticles to tumors, *J Cell Biol., Vol. 188*, 2010, 759–768.

23. Hu Q.; Gao X.; Kang T.; Feng X.; Jiang D.; et.al; CGKRK-modified nanoparticles for dual-targeting drug delivery to tumor cells and angiogenic blood vessels, *Biomaterials*, *Vol. 34*, 2013, 9496-9508.

24. Yao X. Y.; Yoshioka Y.; Ruan G. X.; Chen Y. Z.; Mizuguchi H.; et.al.; Optimization and Internalization Mechanisms of PEGylated Adenovirus Vector with Targeting Peptide for Cancer Gene Therapy, *Biomacromolecules, Vol. 13*, 2012, 2402−2409.

25. Smith G. P.; Filamentous fusion phage: novel expression vectors that display cloned antigens on the virion surface, *Science*, *Vol. 228*, 1985, 1315–7.

26. Azzazy H. M. E.; Highsmith W. E.; Phage display technology: clinical applications and recent innovations, *Clinical Biochemistry,* 2002, *Vol. 35,* 425–445.

27. Birnbaum S.; Mosbach K.; Peptide screening, *Current Opinion in Biotechnology*, 1992, *Vol. 3*, 49-54.

28. Sidhu S. S.; Lowman H. B.; Cunningham B. C.; Wells J. A.; Phage display for selection of novel binding peptides, *Methods in Enzymology,* 1994, *Vol. 328*, 333- 363.

29. Pasqualini R.; Ruoslahti E,; Organ targeting in vivo using phage display peptide libraries, *Nature*, *Vol. 380*, 1996, 364-366.

30. Ellerby H. M.; Arap W.; Ellerby L. M.; Kain R.; et.al; Anti-cancer activity of targeted pro-apoptotic peptides, *Nature Medicine*,1999, *Vol. 5*, 1032-1038.

31. Chen W. H.; Chen J. X.; Cheng H.; Chen C. H.; et.al; A new anti-cancer strategy of damaging mitochondria by pro-apoptotic peptide functionalized gold nanoparticles, *Chem. Commun.,* 2013, *Vol. 49*, 6403-6405.

32. Terman A.; Kurz T.; Lysosomal Iron, Iron Chelation, and Cell Death, *Anitoxidants & Redox Signaling*; 2012.

33. Javadpour MM, et al., De novo antimicrobial peptides with low mammalian cell toxicity*, J Med Chem*, *Vol. 39*, 1996, 3107–3113.

34. Schilling O.; Overall C. M.; Proteomic discovery of protease substrates,*Current Opinion in Chemical Biology*, *Vol. 11*, 2007,36–45.

35. Klingler D.; Hardt M.; Profiling protease activities with dynamic proteomics workflows, *Proteomics*., *Vol.12*, 2012, 587–596.

36. Cuerrier D.; Moldoveanu T.; Davies P. L.;Enzyme Catalysis and Regulation:INTERACTIONS IMPORTANCE OF PRIMED SIDELibrary-based Approach: The Specificity for m-Calpain by a Peptide Determination of Peptide Substrate, *J. Biol. Chem., Vol. 280,* 2005, 40632-40641.

37. Zhao J.; Redell j. B.; Moore A. N.; Dash P, K.; A novel strategy to activate cytoprotective genes in the injured brain, *Biochemical and Biophysical Research Communications*, *Vol. 407,* 2011, 501–506.

38. Fischer E.; Otto E.; Synthesis of the derivatives of some dipeptides. Ber. Deutsch, *Chem. Ges.*, *Vol.36*, 1903, 2106–2116.

39. Merrifield R.B.; Solid phase peptide synthesis. 1. Synthesis of a tetrapeptide, *J. Am. Chem. Soc.*, *Vol. 85*, 1963, 2149–2154.

40. Coin I.; Beyermann M.; Bienert M.; Solid-phase peptide synthesis: from standard procedures to the synthesis of difficult sequences, *Nature Protocols*, 2007, 3247-3256.

41. Amblard M.; Fehertz J.A.; Martineze J.; Subra G.; and Protocols of Modern Solid Phase Peptide Synthesis, *Molecular Biotechnology*, 2006, *Vol. 33*, 239-254.

42. Chen Y.; Mant C. T.; Hodges R. S.; Methods Preparative reversed-phase high-performance liquid chromatography collection efficiency for an antimicrobial peptide on columns of varying diameters (1 mm to 9.4 mm I.D.), *J Chromatogr A.*, 2007, 1140-1157.

43. Fields G.; Methods in Molecular Biology, 2007, Vol. 386, 3-55.

44. Vydac G.; The Handbook of Analysis and Purification of Peptides and Proteins by Reverse-Phase HPLC,3rd Edition, 2002, 2,4,30.

45. http://www.biosyn.com/PeptidePropertyCalculator/PeptidePropertyCalculator.aspx

46. Lindoy L. F.; The Chemistry of Macrocyclic Ligand Complexes, 1986, 1, 2.

47. Lee J. D.; Concise Inorganic Chemistry, 5th Edition, 778.

48. Miethke M.; Marahiel M.A.; Siderophore-Based Iron Acquisition and Pathogen Control, *Microbiology and Molecular Biology Reviews*, 2007, *Vol. 71*, 413-451.

49. http://en.wikipedia.org/wiki/File:Heme.svg

50. http://en.wikipedia.org/wiki/Chlorin

51. Anderson G. J.; McLaren G. D.; *Iron Physiology and Pathophysiology in Humans*, 2012, 597, 568-571.

52. Yu Y.; Rahmanto Y S.; Hawkins C L.; Richardson D R.; The Potent and Novel Thiosemicarbazone Chelators Di-2-pyridylketone-4,4-dimethyl-3-thiosemicarbazone and 2-Benzoylpyridine-4,4-dimethyl-3-thiosemicarbazone Affect Crucial Thiol Systems Required for Ribonucleotide Reductase Activity, *Molecular Pharmacology*, 2011, *Vol. 79*, 921-931.

53. Whitnall M.; Howard J.; Ponk P.; Richardson D R.; A class of iron chelators with a wide spectrum of potent antitumor activity that overcomes resistance to chemotherapeutics, *PANS,* 2006, *Vol. 103*, 14901-149067.

54. Foy S. P.; Labhasetwar V.; Oh the Irony: Iron as a Cancer Cause or Cure?, *Biomaterialsm*, 2011, *Vol. 32*, 9155–9158.

55. Bystrom L M.; Guzman M L.; Rivella S.; Iron and Reactive Oxygen Species: Friends or Foes of Cancer Cells?, A*ntioxidants and Redox Signaling*, 2013.

56. Galey J. B.; Recent Advances in the Design of Iron Chelators Against Oxidative Damage, *Mini Reviews in Medicinal Chemistry,* 2001*, Vol. 1,* 233-242.

57. http://www.zuniv.net/physiology/book/chapter22.html

58. Buss J. L.; Torti F. M.; Torti S. V.; The Role of Iron Chelation in Cancer Therapy, *Current Medicinal Chemistry*, 2003, *Vol. 10*, 1021-1034.

59. Liu M.C.; Lin T. S.; Sartorelli A. C.; Synthesis and Antitumor Activity of Amino Derivatives of Pyridine-2-carboxaldehyde Thiosemicarbazone, *Journal of Medicinal Chemistry* 1992, *Vol. 35*, 3672-3677.

60. Terman A.; Gustaffson B.; Brunk U. T.; The lysosomal-mitochondrial axis theory of post mitotic aging and cell death, *Chemico-Biological Interactions*, 2006, *Vol. 163*, 29-37.

61. Castino R.; Fiorentino I.; Cagnin M.; Giovia A.; Isidoro C.; Chelation of Lysosomal Iron Protects Dopaminergic SH-SY5Y Neuroblastoma Cells from Hydrogen Peroxide Toxicity by Precluding Autophagy and Akt Dephosphorylation, *Toxicological Sciences*, 201, *Vol.123(2)*, 523–541.

62. Kakhlon O.; Cabantchik Z. I.; The labile iron pool: characterization, measurement and participation in cellular processes, *Free Radical Biology and Medicine*, 2002, *Vol. 33*, 1037-1046.

63. Kruszewski M.; Labile iron pool: the main determinant of cellular response to oxidative stress, *Mutation Research*, 2003, *Vol. 531*, 81-92.

64. Liu Z. D.; Hider R. C.; Design of iron chelators with therapeutic application, *Coordination Chemistry Reviews*, 2002, *Vol. 232*, 151-171.

65. Hatcher H. C.; Singh R. N.; Torti F. M.; Torti S. V.; Synthetic and natural iron chelators: therapeutic potential and clinical use, *Future Medicinal Chemistry*, 2009, *Vol. 1*, 1643-1670.

66. Liu Z. D.; Hider R. C. Design of Clinically Useful Iron(III)-Selective Chelators, *Medicinal Research Reviews*, 2002, *Vol. 22*, No. 1, 26-64.

67. Martell A. E.; Smith R. M.; Critical stability constant, *Vols. 1–6. London: Plenum Press*; 1974–1989.

68. Hider R. C.; Kong X.; Chemistry and biology of siderophores, *Natural Product Reports*, 2010, *Vol .27,* 637–657.

69. Harris D.C.; Aisen P.; Facilitation of Fe(II) autoxidation by Fe(III) complexing agents, *Biochim Biophys Acta*, *Vol. 329*, 1973, 156–158.

70. Richardson D R.; Sharpe P C.; Lovejoy D B.; Senaratne D.; Kalinowski D S.; Islam M.; Bernhardt P V.; Dipyridyl Thiosemicarbazone Chelators with Potent and Selective Antitumor Activity Form Iron Complexes with Redox Activity, *Journal of Medicinal Chemistry*, 2006, *Vol. 49*, 6510-6521.

71. Liu D. Y.; Liu Z. D.; Hider R. C.; Oral iron chelators- development and applications, *Best Practice And Research Clinical Haematology*, 2002, *Vol. 15, No2*, 369-384.

72. Gupta A. K.; Gupta M.; Synthesis and surface engineering of iron oxide nanoparticles for biomedical applications, *Biomaterials*, 2005, *Vol. 26*, 3995–4021.

73. Laurent S.; Forge D.; Port M.; Roch A.; Magnetic Iron Oxide Nanoparticles: Synthesis, Stabilization, Vectorization, *Chem. Rev.* 2008, *Vol. 108,* 2064–2110.

74. Schwertmann U.; Cornell R. M.; Iron oxides in the laboratory: preparation and characterization. Weinheim, Cambridge: VCH; 1991.

75. Thorek D. L. J.; Chen A. K.; Czupryna J.; Tsourkas A.; Superparamagnetic Iron Oxide Nanoparticle Probes for Molecular Imaging, *Annals of Biomedical Engineering*, 2006, *Vol. 34*, 23–38.

76. Hu K.; Yang Z.H.; Pan S.S.; Xu H. J.; Ren J.; Synthesis and antitumor activity of liquiritigenin thiosemicarbazone derivatives, *European Journal of Medicinal Chemistry*, *Vol. 45, Issue 8*, 2010, 3453–3458.

77. Wang H.; Shrestha T. B.; Basel M. T.; Dani R. K.; Chikan V.; Troyer D. L.; Bossmann S. H.; et.al.; Magnetic-Fe/Fe3O4-nanoparticle-bound SN38 as carboxylesterase-cleavable prodrug for the delivery to tumors within monocytes/macrophages, *Beilstein J. Nanotechnol.*, *Vol.3*, 2012, 444-455.

78. Lacroix L.M.; Huls F. N.; Ho D.; Sun X.; Cheng K.; Sun S.; Stable Single-Crystalline Body Centered Cubic Fe Nanoparticles, *Nano Lett., Vol 11*, 2011, 1641-1645.

79. Perera A. S.; Wang H.W.; Yapa A. S.; Bossmann S. H.; Final Report to Battelle Memorial Institute, Columbus/OH "Upscaling of core/shell magnetic nanoparticles for catalytical applications", 2013.

80. Ikenberry M.; Pena L.; Wei D.; Wang H.; Bossmann S. H.; Wilke T.; Wang D.; Komreddy V. R.; Rillema D. P.; Hohn K. L.; Acid monolayer functionalized iron oxide nanoparticles as catalysts for carbohydrate hydrolysis, *Green Chem.*, *Vol. 16*, 2014, 836-843.

81. Wang, H.; Udukala D. N.; Samarakoon T. N.; Basel M. T.; Kalita M.; Troyer D. L.; Bossmann S. H.; et.al.; Nanoplatforms for highly sensitive fluorescence detection of cancer-related proteases, *Photochem. Photobiol. Sci.*, *Vol 13*, 2014, 231-240.

82. Wilson D.; Langell M. A.; XPS analysis of oleylamine/oleic acid capped Fe_3O_4 nanoparticles as a function of temperature, *Appl. Surf. Sci.*, *Vol. 303*, 2014, 6-13.

83. Da Silva J. G.; Despaigne A. A. R.; Louro S. R. W.; Bandeira C. C.; et. al.; Cytotoxic activity, albumin and DNA binding of new copper (II) complexes with chalcone-derived thiosemicarbazones,*European Journal of Medicinal Chemistry*, 2013, *Vol 65*, 415-426.

84. Greenwood R.; Kendall K.; *Journal of the European Ceramic Society*, 1999, *Vol 19*, 479–488.

85. Hanaor D.A.H.; Michelazzi M.; Leonelli C.; Sorrell C.C.; The effects of carboxylic acids on the aqueous dispersion and electrophoretic deposition of ZrO_2, *Journal of the European Ceramic Society*, 2012, *Vol 32*, 235–244.

86. Mehta V.N.; Kumar M.A.; Kailasa s.K.; Colorimetric Detection of Copper in Water Samples Using Dopamine Dithiocarbamate-Functionalized Au Nanoparticles, *Ind. Eng. Chem. Res.*, *Vol 52*, 2013, 4414−4420.

87. Gunasekaran S.; Thilak R. T.;Ponnusamy S.; Vibrational spectra and normal coordinate analysis of adrenaline and dopamine, *Indian Journal of Pure and Applied Physics, Vol 45*, 2007, 884-892.

88. Kumari P.Y.A.S.J.; Chandra1 J. S.; Rao Bs.; Sunandamma Y.; Synthesis, characterization and antibacterial activity of Alloxanthiosemicarbazone Au(III) complexes, *Journal of Current Pharmaceutical Research*, *Vol 10*, 2012, 28-33.

89. Sulekh Chandra S.; Gupta L.K.; EPR, mass, IR, electronic, and magnetic studies on copper(II) complexes of semicarbazones and thiosemicarbazones, *Spectrochimica Acta Part A 61*, 2005 269–275.

90. Kong J.; Yu S.; Fourier Transform Infrared Spectroscopic Analysis of Protein Secondary Structures, *Acta Biochimica et Biophysica Sinica*, *Vol 39*, 2007, 549–559.

91. http://www.rsc.org/periodic-table/element/26/iron

92. Kalambur V. S.; Longmire E. K.; Bischof J. C.; Cellular Level Loading and Heating of Superparamagnetic Iron Oxide Nanoparticles, *Langmuir*, *Vol 23*, 2007, 12329–12336.

93. Connolly M. L.; "The molecular surface package", *J Mol Graphicsi,* Vol 11, 1993, 139–141.

Chapter 2 - Using Cell Delivered Nanoparticles to Cause Local Hyperthermia and Increasing Survival in a Murine Metastatic Pancreatic Cancer Model

2.1 Abstract

Localized hyperthermia using magnetic nanoparticles to absorb alternating magnetic field (AMF) energy has been shown to be a potential cancer treatment. Here, we demonstrate a system that uses tumor homing cells to actively carry iron/iron oxide nanoparticles into tumor tissue for AMF treatment. Paramagnetic iron/iron oxide nanoparticles were synthesized and loaded into RAW264.7 cells (mouse monocyte/macrophage like cells, Mo/Ma), that we have shown to be tumor homing cells. A murine model of disseminated peritoneal pancreatic cancer was then generated by intraperitoneal (i.p.) injection of Pan02 cells. After tumor development, Mo/Ma loaded with iron/iron oxide nanoparticles were injected i.p. and allowed to migrate into the tumor. Three days after injection, mice were exposed to an alternating magnetic field for twenty minutes to cause the cell-delivered nanoparticles to generate heat. This treatment regimen was repeated three times. A survival study demonstrated that this system can significantly increase survival in a murine pancreatic cancer model, with an average post-tumor insertion life expectancy increase of 31%. This system has the potential to become a useful method for specifically and actively delivering nanoparticles for local hyperthermia treatment of cancer. (This work has already been published in; *International Journal of Nanomedicine ,2012, Vol 7, 297–306*.)

2.2 Introduction

Pancreatic cancer is known to be one of the most lethal forms of cancer, with five year survival rates of less than 5%.[1] Discovering new methods for successfully treating pancreatic cancer is a virtual necessity for combating this disease.

Hyperthermia has been a cancer therapy method for decades. Tumors have shown increased susceptibility to thermal toxicity versus healthy tissue due to their increased rate of cell cycling, increased hypoxia, poor fluid exchange and increased acidity.[2, 3] Whole body hyperthermia is an easy way to take advantage of this differential toxicity to treat cancer. Unfortunately, 'extreme' whole body hyperthermia (>41.5°C), which elevates core temperatures to the level where direct thermal toxicity is observed, can cause severe side effects, which may limit its usefulness.[4-8] Fever-level whole body hyperthermia (~39-41°C) can mitigate many of these side effects and has potential to be an effective cancer treatment, but this lower heat level is thought, primarily, to stimulate the immune system and the benefits of direct thermal toxicity are reduced.[9,10]

Generating localized 'extreme' hyperthermia at the cancer site could alleviate many of the side effects associated with whole body hyperthermia while still taking advantage of the thermal susceptibility of tumors. One particularly promising method for generating localized hyperthermia is using magnetic nanoparticles (MNP) to absorb energy from alternating magnetic fields (AMF) and turn this energy into heat. This method is promising because the body is extremely permeable to AMF, which produce no known effects in the body. Fe/Fe_3O_4 MNP also have been shown to be very safe with very little interaction in the body. Only at the location of the MNP is the AMF energy absorbed and converted to heat. By specifically delivering the MNP to the tumor site, localized hyperthermia can be created.[11-13]

Using MNP for generating localized hyperthermia has proven successful; there are several clinical trials using injectable MNP combined with AMF for tumor treatment. Current methods of delivering MNP for localized hyperthermia depend on direct injection of milligram amounts of MNP into the tumor site.[14-23]

Although practical for easily accessible, primary tumors, this limits the usefulness of MNP-generated localized hyperthermia for deep tumors, locally or systemically metastatic tumors, and other diffuse tumors. A recent method for targeting cancer therapy is using

cytotherapy.   Cytotherapy utilizes delivery cells, such as stem cells or other cells, to carry a payload into the tumor site.[24-32]

Cytotherapy-directed hyperthermia has been successfully demonstrated to attenuate mouse melanomas. Monocytes and macrophages are known to infiltrate tumor sites and thus could act as cytotherapeutic drug delivery vehicles.[33-35] Several recent studies have demonstrated the feasibility of delivering therapy to tumors using monocytes or macrophages, including targeting liposomes containing fluorescent markers to gastric tumor[36], targeting adenovirus to prostate tumors[37], and targeting gold nanoshells to gliomas[38].

Here we demonstrate a system that uses monocyte-like tumor homing cells to deliver MNP directly into the tumor tissue. We have demonstrated that RAW264.7 cells (monocyte/macrophage-like cells, Mo/Ma, ATCC TIB-71) specifically infiltrate pancreatic tumors when injected intraperitoneally (i.p.) without infiltrating other organs. These cells were loaded with MNP in order to deliver the MNP specifically to the tumor for localized hyperthermia. To test this system, a murine model of disseminated peritoneal carcinomatosis of the pancreas was generated by injecting Pan02 cells i.p. into C57BL/6 mice.[39] MNP loaded Mo/Ma were then injected and allowed to infiltrate the tumor tissue. Three days after Mo/Ma injection, mice were treated with AMF. This treatment system significantly increased the survival time of mice bearing i.p. pancreatic tumors, with an average lifespan increase post tumor injection of 31%.

2.3 Literature

2.3.1 Iron/ Iron Oxide Nanoparticles

The development of nanotechnology has dramatically increased in the last couple of decades. Scientific studies have lead to the understanding of the behavior of the nanoparticles such as stability, control of surfactants, particle size, suitable materials to produce nanoparticles and physical behavior. These studies provide a good insight that will lead to nanoparticles that can be tailored accordingly for biomedical applications and diagnostics.[40, 41]

Iron/iron oxide (Fe/Fe_3O_4) nanoparticles have been used for about 40 years for various medical applications. The physical and chemical properties of these nanoparticles do not contain the characteristics of either the atom or the bulk counterparts and exhibit superpaprmagnetic properties. These superparamagnetic or ferromagnetic nanoparticles can be used for several biomedical applications due to their specific mesoscopic physical, chemical, thermal and mechanical properties and with proper surface chemistry. The biomedical applications include;[40,41]

- Magnetic resonance imaging (MRI)
- Drug delivery
- Hyperthermia
- Tissue repair
- Immunoassays
- Detoxification of biological fluids
- Cell separation
- Magnetofection

In order to achieve these *in vivo* applications they need to have a small particle size smaller that 100 nm, a narrow particle size distribution, they should have a surface coating which is nontoxic and biocompatible and should have high magnetization values.[41]

2.3.2 Magnetic Iron/ Iron Oxide Nanoparticles for Biomedical Applications

There are several types of magnetic Fe/Fe_3O_4 nanoparticles that have been studied and among them are maghemite (γ-Fe_2O_3) and magnetite (Fe_3O_4) that are 5-20 nm in size. Magnetite

is mostly used since it is more biocompatible than maghemite. Magnetite forms a fcc closed packing cubic inverse spinel structure. Here the iron cations are occupied at the interstitial tetrahedral and octahedral sites. It is a half- metallic material and has quantum size effects and a large surface area changing its magnetic properties into superparamagnetic properties since a particle is considered as a single magnetic domain.[40, 42]

The synthesis of nanoparticles is challenging in producing nanoparticles with specific size and shape. There are many methods to synthesize nanoparticles such as Ostwald ripening, water-in-oil microemulsion method. In the synthesis of nanoparticles, there are two stages involved where first when the concentration of the species reaches its critical supersaturation a short burst of nucleation occurs, next, a slow growth of nuclei occurs by the diffusion of solutes to the surface of the crystal. Continuous nucleation should be avoided in order to produce monodispersed nanoparticles.[41]

The size and shape of the nanoparticles can be controlled by adjusting the pH, ionic strength, temperature, and nature of salts (halogens, nitrates, perchlorates) and the concentration of Fe^{II}/ Fe^{III} ratio used in the reaction. The use of surface modifiers is crucial to stabilize the Fe/Fe_3O_4 nanoparticles from aggregation in both biological medium and magnetic field. This can be achieved by using electrostatic or steric repulsion (Figure 2.1).[40, 41]

Stabilizers that can be used are;[40, 41]

- Carboxylates, phosphates, which are known to bind to the surface of magnetites.
- Inorganic material such as silica or gold can be used to coat the nanoparticles. They can also help in binding other biological ligands.
- Polymer stabilizers such as dextran, polyethylene glycol, polyvinyl alcohol and chitosan.
- Long chain surfactants such as oleic acid, stearic acid.

To prevent the Fe/Fe_3O_4 nanoparticles from oxidation and agglomeration and inert gas such as argon or nitrogen can be bubbled through the reaction solution during the synthesis. It not only protects from oxidation but can also further help in reducing the particle size.[40]
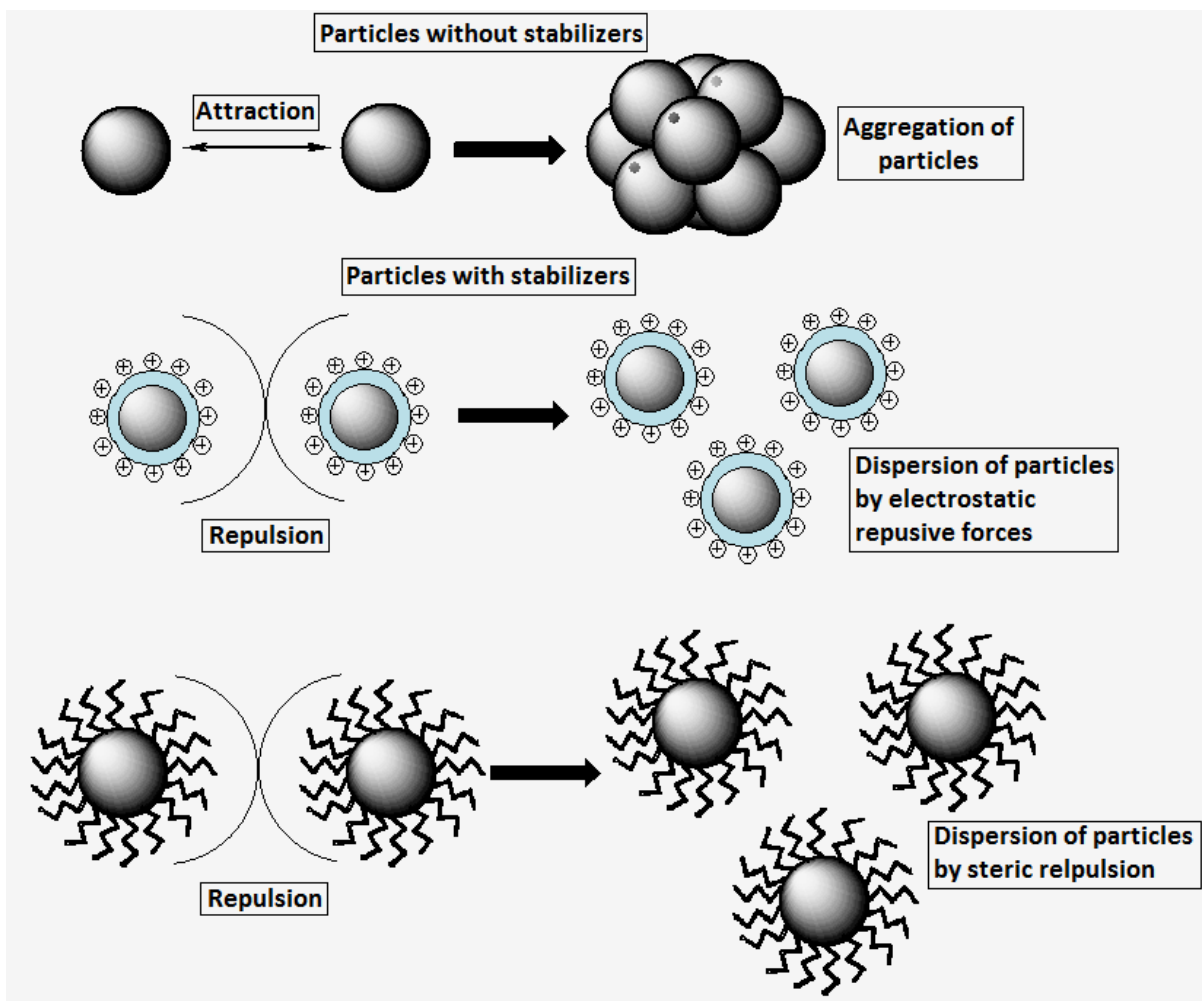
Figure 2.1:- Stabilization of Iron/ Iron oxide nanoparticles coated with stabilizers.[40]

2.3.2.1 Drug Delivery

Magnetic nanoparticles show promising applications in drug delivery. The surface or the nanoparticles can be modified such that drugs and various biological ligands (e.g. tumor targeting peptides, proapoptotic peptides, DNA, RNA and antibodies), which target tumors or specific organs. These surface modified nanoparticles are able to reduce drug doses and side effects to normal cells, as well as the costs associated with drug treatment. This is most important in cancer treatment since therapeutic nanoplatforms would specifically target the cancer cells and release their payload into the cells.[40,41]

Fe/Fe$_3$O$_4$ nanoparticles that are not surface modified have a short blood half-life of several minutes and are mainly used for imaging of liver, spleen and gastrointestinal tract.

However surface modified Fe/Fe_3O_4 nanoparticles have long blood of hours (48 hrs) circulating times and are useful for imaging vascular compartment (magnetic resonance angiography), lymph nodes, perfusion imaging, receptor imaging and target specific imaging.[40]

These magnetic nanoparticles can be magnetically controlled in the vascular by an external magnetic field. Therefore, they can be magnetically guided and can be retained into a specific location. For instance, magnetic nanoparticles were retained at the tumor site, where it can release its payload and carry out its activity.[40]

The internalization of nanoparticles into cells depends on their size. Nanoparticles administered which range from 10 nm to 100 nm are the ideal size for intravenous injection. They show long circulation times and are small enough to avoid rapid clearance by the reticuloendothelial system. They can also penetrate through capillaries prior to systemic clearance and are the most effective particle size for biological application. Particles larger than 200 nm in diameter are removed by the spleen by mechanical filtration and are ultimately removed by phagocyte system reducing its blood circulation time. Particles with diameters less than 10 nm are rapidly removed by extravasation and renal clearance. . These effects greatly reduce their blood circulation time.[40, 41]

Since cancer cells proliferate at a higher ratio than normal cells they need to meet the high demand of nutrients. Therefore, new blood vessels have to be formed when the cancer grows. This process is called angiogenesis. These blood vessels are leaky with average pore size of 100-600 nm. The leaky pores can facilitate nanoparticles to diffuse into the cancer tissues thereby making it a good carrier for drugs into cancer cells.[43]

2.3.2.2 Magnetic Resonance Imaging (MRI)

The use of superparamagnetic Fe/Fe_3O_4 nanoparticles (SPIO) as contrasting agents play an important role for MRI. SPIO tagged with certain specific homing peptides or antibodies allows early detection of pathological tissues, such as the differentiation of cancerous tissues form normal healthy tissues (Figure 2.2). MRI can also be used to track cells in the body that have been tagged with SPIO and can also be used to detect apoptosis where the MR image contrast changes when morphological changes occur during apoptosis such as cell shrinkage and membrane blebbing.[40, 41]
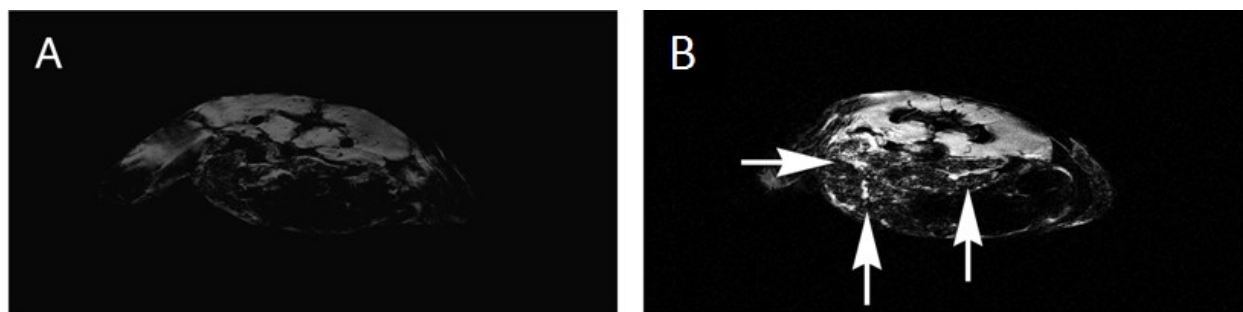
Figure 2.2:- MRI Using Fe/Fe$_3$O$_4$-NPs, Delivered by NPC cells, B16F10 Lung Tumors in Black Mice.

   A: Control

   B: Accumulation of the Fe/Fe$_3$O$_4$/stealth nanoparticles in lung melanomas

All results were obtained in an 400MHz at the Oklahoma Medical Research Foundation Nuclear Magnetic Resonance Core. These figures were adopted form Dr. Thilani Samarakoon's thesis, Kansas State University, 2010

   The contrasting ability of SPIO is due to their high transverse relaxivity. In a magnetic fluid, ferromagnetic particles dispersed in a liquid, which forms a colloid. Each crystal in the colloid suspension is small in size and is fully magnetized forming nanomagnets and is composed of single domains. When a SPIO is subjected to an external magnetic field, the entire crystal aligns with the applied field due to the single crystal nature, which enhances the magnetic flux. Changes in MRI signal are produced through disturbances caused in the local magnetic field induced by large magnetic moments causing rapid dephasing of surrounding protons.[40, 41, 44]

   The MRI contrast relies on the relaxation of these crystals back to equilibrium. There are two relaxation processors involved, which are commonly described as Néel relaxation and Brownian relaxation (Figure 2.3).

   The Néel relaxation occurs in sufficiently small nanoparticles and is defined as the time taken for the particles to return back to equilibrium after perturbation. Brownian relaxation is detected in larger particles and characterizes the viscous rotation of the entire particle. Therefore the total relaxation rate is the sum of both Néel relaxation and Brownian relaxation rates (Equation 5).[41, 44]

$$\frac{1}{\tau} = \frac{1}{\tau_N} + \frac{1}{\tau_B} \qquad \text{Equation 5}$$
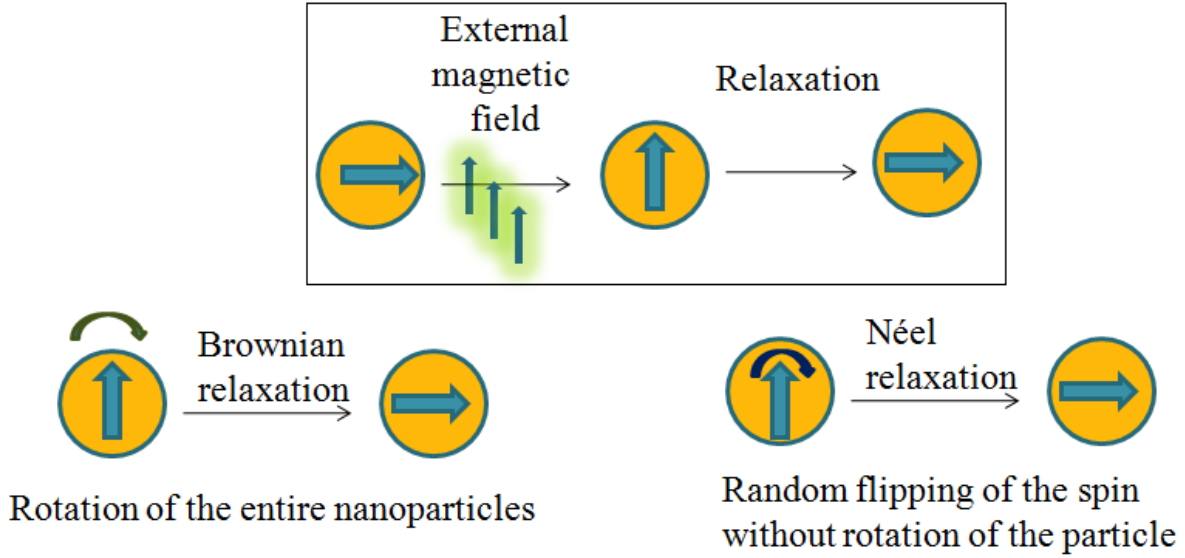
Figure 2.3:- Illustration of Néel relaxation and Brownian relaxation.[41]

2.4 Hyperthermia

The use of heat (hyperthermia) is a therapeutic procedure to increase the temperature of a particular area of the body with cancer. This treatment method has been practiced for centuries. Heating methods that were used to destroy tumors included hot irons which was stated by Hippocrate (460-370 BC), later methods included the use of a hot water bath, pyrogens (bacterial toxins), perfusion heating and more recently high frequency radiation and magnetic fluid hyperthermia. [40, 41, 45, 46,]

It is known that tumor cells are more sensitive to heat than normal healthy cells. When the temperature is increased more than 43^0C tumor cells are destroyed. However normal cells survive at higher temperatures. Therefore by exposing tumor cells to increased temperatures the tumor tissue can be destroyed by hyperthermia. [40, 41]

The rationale behind this theory is that the microenvironment of cancers are chaotic where reduction of blood vessel density and blood flow is seen resulting in hypoxia and acidic

conditions which is not seen in normal cells. Therefore, making cancer cells more sensitive to hyperthermia.[46, 2]

The effectiveness of hyperthermia depends on the temperature and the exposure time used. The exposure time can be halved with each 1^0C increase at temperatures above 42.5-43^0C. Normal cells exposed to temperatures up to 44^0C for 1 h are undamaged however, the nervous system can be irreversibly damaged at treatment exposure times of 40-60 min at 42-42.5^0C temperatures. The main mechanism of cancer cell death is due to protein denaturing at temperatures more than 40^0C. The various cellular damages that occur through hyperthermia are the membranes, cytoskeleton, synthesis of macromolecules and DNA repair.[45, 46]

After the cells are exposed to heat they undergo a phenomenon called thermo resistance (thermotolerance) for about 24-48 hrs. This occurs due to upregulation of certain proteins such as heat- shock proteins (HSP). These HSPs are a heterogeneous group of molecular chaperones and are subdivided into HSP 60, HSP 70, HSP 90 and HSP 100. They prevent the interaction of denatured proteins with other proteins, which would have caused loss of function in the other proteins. HSPs are involved in protecting cells against heat damage when exposed to hyperthermia.[2, 45]

2.4.1 Methods to induce hyperthermia

Currently in clinical applications of hyperthermia the optimum temperature distribution is still not known. It is challenging to increase temperatures above the systemic temperature 37.5^0C. Temperature increase ranges around 39.5 ^{0}C to 40.5 ^{0}C and limited homogeneity is observed due to the physical and physiological characteristics such as electrical tissue boundaries, local perfusion variations and perfusion regulations. It is observed that a temperature of at least 42^0C can be reached at one measurement point and 50% of the deep tumors will reach this tempaerature.[45]

There are three main methods that are used to maintain hyperthermia;

1. Local hyperthermia
2. Regional hyperthermia
3. Whole body Hyperthermia

2.4.1.1 Local hyperthermia

This method is aimed to be used for superficial tumors. The types of methods that local hyperthermia can be applied are external, intraluminal or interstitial methods. Heating is done by the use of antennas or applicators, which emit electromagnetic energy such as microwaves or radio waves or ultrasound energy. This method of heating system has several components (Figure 2.4) as a water bolus to ensure the electromagnetic coupling of the applicator to the tissue. The temperature of the tumor can be controlled by the output of the power generator or by changing the position of the applicator. The therapeutic depth reaches only several centimeters and is limited in areas such as the head and neck due to the irregular surface. There are some applicators that are commercially available that have a frequency of 150- 430 MHz having an emitting diameter of 15 cm and show about 3 cm of therapeutic depth.[45, 46]

2.4.1.2 Regional hyperthermia

This method of hyperthermia is done for deep-seated tumors such as tumors in the abdomen or pelvic area. Regional hyperthermia system uses several antennas. One of the mostly used regional hyperthermia applicators is the Sigma-60 applicator (Figure 2.5) it has 4 dipole antenna pairs that are situated around the patient for heating. Each pair of antennas can be controlled by changing the phase and amplitude of the energy used. However monitoring of heating should be done to ensure proper specific absorption rate (SAR) distribution.[45]

2.4.1.3 Whole body hyperthermia

This method of heating is done for patients with metastatic cancer. Whole body hyperthermia (WBH) is done under strong analgesics and sedation or general anesthesia. It is known to achieve a maximum heating temperature of 42^0C for 1 h with acceptable side effects. The basal metabolic rate can be doubled at a temperature of 42^0C in a patient weighing 70 kg (basal metabolic rate is 85W at 37 ^0C). It would take 180 min to reach 42 ^0C from 37.5 ^0C of body temperature. The current WBH systems (Figure 2.6) that are clinically used have heating times of 60-90 min. A heating system that is currently used is the Aquatherm system (Figure 2.6) which has an isolated- moisture- saturated chamber containing tubes with water that flows at a temperature of $50-60^0C$ in the interior of the system where the patient lies. Long wavelength infrared waves are also emitted at the same time. The systemic toxicity seen include cardiac

disorders, changes in the coagulation system, permeability of the capillary endothelium. Fluid substitution is necessary due to the fall in peripheral resistance and hypovolaemia.[45]
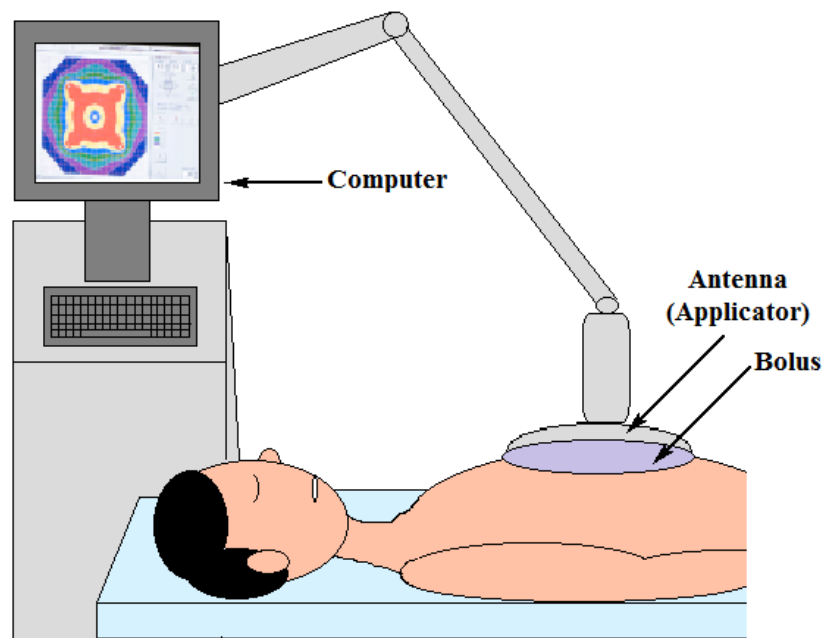
Figure 2.4:- Scheme for a local hyperthermia system.[45]
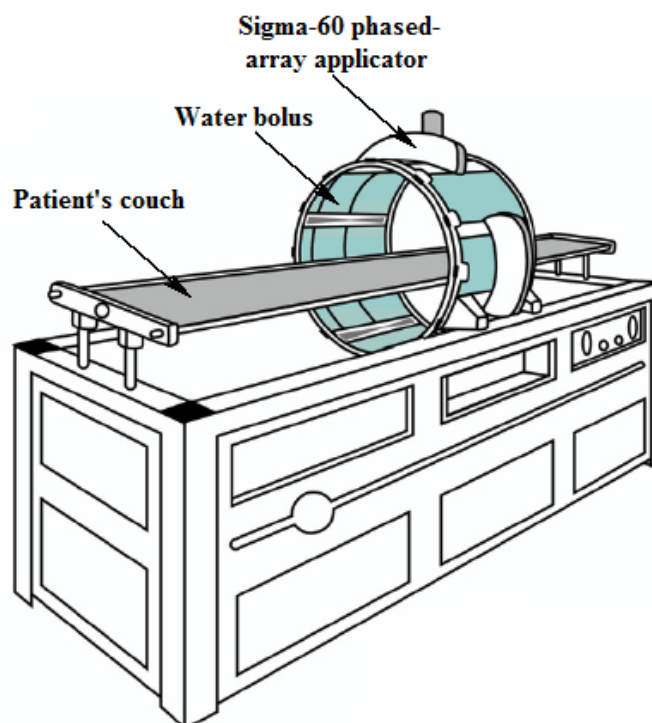
Figure 2.5:- Commercially available Sigma-60 applicator for regional hyperthermia.[2]
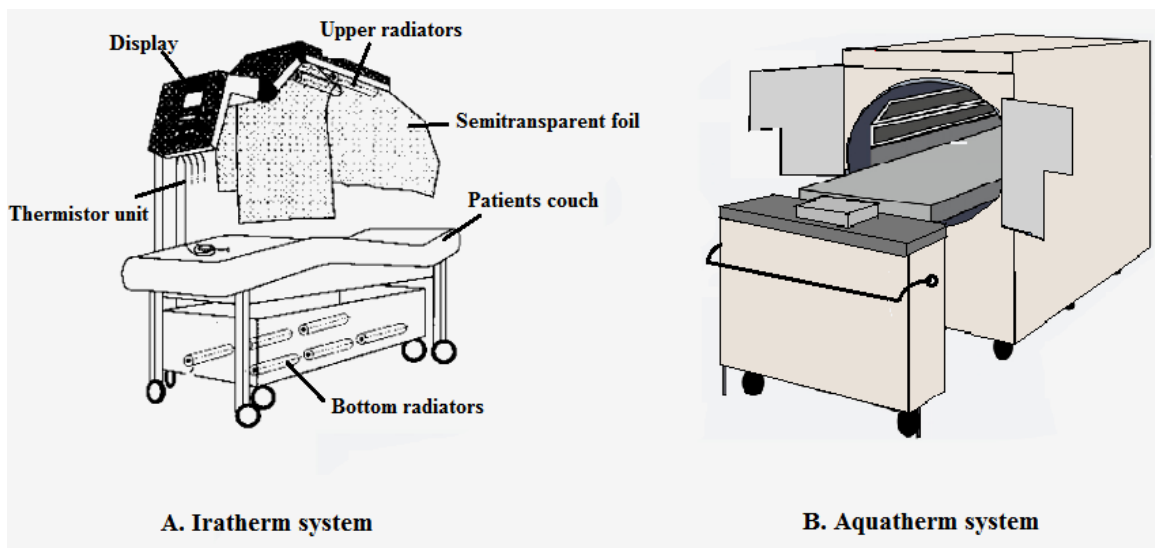
Figure 2.6:- Whole body hyperthermia systems

      A. Iratherm system **B.** Aquatherm system.[2, 45]

2.4.1.4 Heating by magnetic nanoparticles

A much more recent approach to induce interstitial hyperthermia in tumors can be done by injecting a ferrofluid (fluid containing Fe/Fe_3O_4 nanoparticles) into the tumor and expose it to an alternating magnetic field. This is a method that can be used to have better control over hyperthermia at the tumor location.[46]

Ferrofluids of superparamagnetic or ferromagnetic Fe/Fe_3O_4 nanoparticles when subjected to an alternating magnetic field they start to spin (Figure 2.7), generating heat. Therefore, by embedding magnetic particles into the tumor site and exposing it to and alternating magnetic field heat will be generated depending on magnetic properties of the material, the strength of the magnetic field applied, frequency of oscillations, and cooling capacity of the blood in the tumor site.[40, 41]
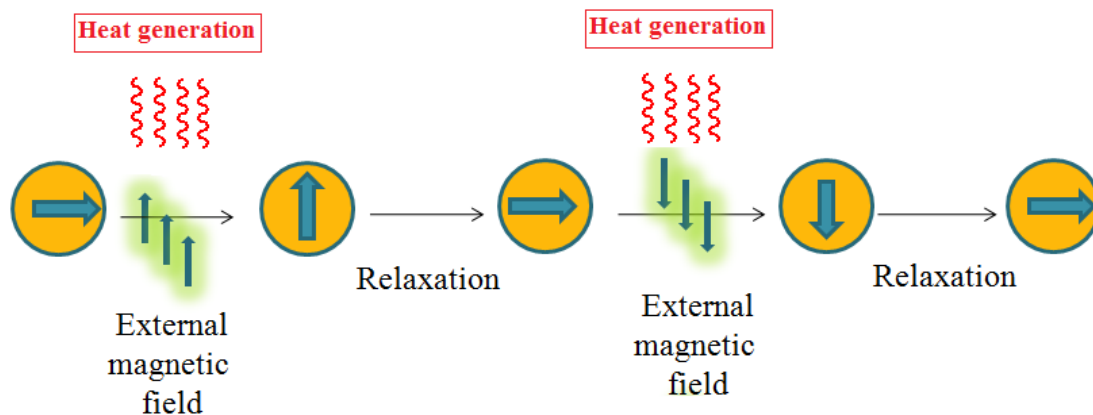
Figure 2.7:- Heat generation by superparamagnetic Fe/Fe$_3$O$_4$ nanoparticles when subjected to an alternating magnetic field.

The magnetic energy of the nanoparticles shows a synoidal wave when subjected to an alternative magnetic field (figure 2.8). This synoidal effect depends on the direction of the external magnetic field.[41]
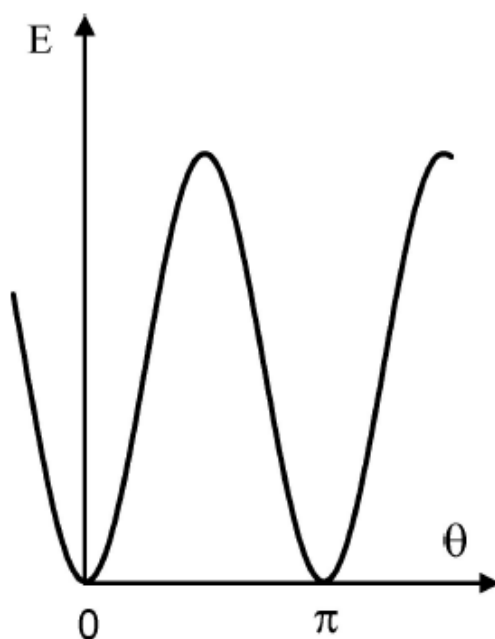
Figure 2.8:- Magnetic energy change when the nanoparticle is subjected to an alternating magnetic field.[41]

The specific absorption rate (SAR) is the parameter that determines heating of the tissues. It is defined as; "The rate of which electromagnetic energy is absorbed by a unit mass of biological material". Its units are in calories per kilogram. SAR is proportional to the increase in temperature ($\Delta T / \Delta t$) and is calculated by the equation below (Equation 6).

$$SAR = 4.1868 \; \frac{P}{m_e} = C_e \frac{\Delta T}{\Delta t} \qquad \text{Equation 6}$$

Where;

    P = Electromagnetic wave power absorbed by the sample

  m_e = Mass of the sample

  C_e = Specific heat capacity of the sample

The use of low-frequency magnetic wave ranging around 100 kHz to 400 kHz is appropriate to be exposed to tissues containing ferrofluids. This specific range is used to control the energy released into the tissue, if not inhomogeneous heating will occur.[41]

2.4.1.4.1 Magnetic heating apparatus used in our study

A heating apparatus was constructed by converting a 10 kW commercial inductive heater into an AMF generating apparatus (Figure 2.8). Here a copper coil was used to produce 145 kHz of alternating magnetic field. The mice were placed through the copper coil for heating.

Figure 2.9:- Induction heating machine for producing an alternating magnetic field.

2.5 Monocyte/ Macrophage like Cells as a Drug Delivery Vehicle

Monocytes and macrophages are mononuclear phagocytic cells that represent the mononuclear phagocyte system (MPS) and are derived from the bone marrow and yolk sac progenitors (Figure 2.10). They are also synthesized by the extra-medullary hematopoiesis in the spleen and its levels are found to increase in inflammatory diseases such as atherosclerosis and cancer. [47, 48]

Monocytes and macrophages are essential for innate immune functions, support of adaptive immunity and tissue homeostasis. It is known that monocytes are recruited to site of inflammation for pathogen clearance, tissue repair and wound healing that restores homeostasis. It is now understood that chronic inflammation may be the underlying cause of cancer. At these inflammated sites monocytes are recruited and differentiated into mature inflammatory macrophages which intern produces chemokines and cytokines. These chemokines and cytokines are receptors expressed on the monocytes, which lead to further recruitment of monocytes and macrophages and enhances the inflammation in the cancer site. There are several surface markers and receptors or so called as receptor ligand pairs that recruit monocytes and macrophages into tumors and they are CD62L/ CD62L ligands, CX3CR1/ CX3CL1, CCR2/ CCL2 and VEGFR1/ VEGF-A.[47, 49]
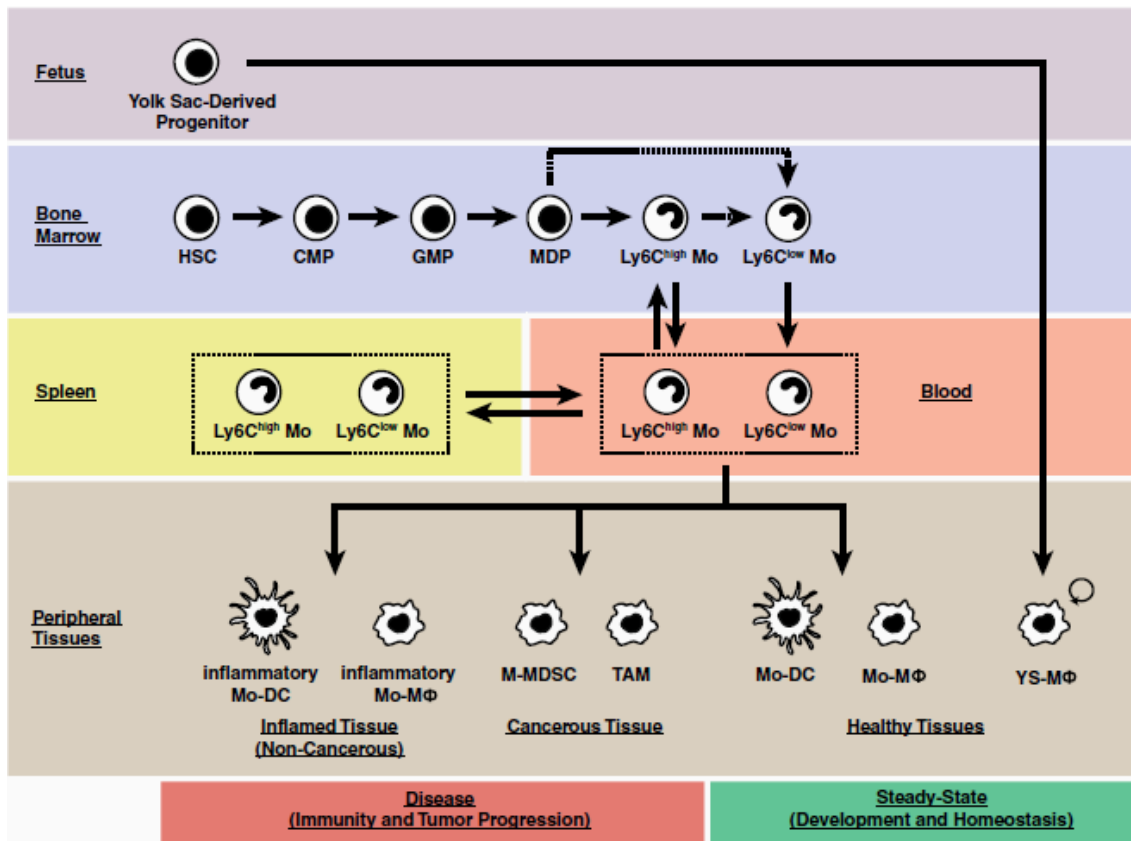
Figure 2.10:- Origin of monocytes and macrophages in steady-state and disease conditions.

Monocytes (Mo), hematopoietic stem cells (HSC), common myeloid progenitors (CMP), granulocyte macrophage progenitors (GMP), monocyte/macrophage dendritic cell progenitors (MDP), "classical" Ly6Chigh and "non-classical" Ly6Clow monocytes, monocyte-derived macrophages (Mo-MΦ), monocyte derived dendritic cells (Mo-DCs), yolk sac-derived macrophages (YS-MΦ), monocytic -myeloid-derived suppressor cells (M-MDSCs), immunosuppressive tumor-associated macrophages (TAMs).[47]

The method by which monocytes are infiltrated into tumor tissue is first by the interaction of monocytes CD62L receptor on the monocyte to its ligand expressed on the inflamed endothelial cells. The CD62L is highly efficient in tethering monocytes that are flowing in the blood stream onto the inflamed endothelial cells (Figure 2.11).[49]
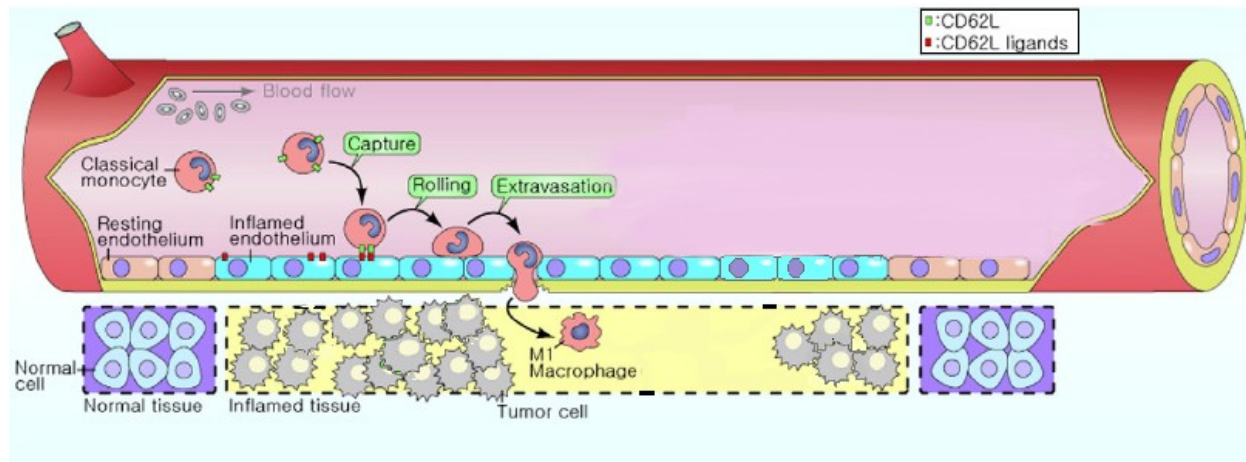
Figure 2.11:- Mechanism of monocyte recruitment and exravasation.[49]

Drugs can be delivered to inflamed site in cancer by taking advantage of the monocytes ability to migrate to site of inflammation. Monocytes and macrophages can be used as vehicles to transport superparamagnetic Fe/Fe_3O_4 nanoparticles to cancer sites and facilitate the uptake of the nanoparticle to achieve their therapeutic effect. The mechanism by which the nanoparticles are incorporated into the monocytes and macrophages is by their ability to uptake or in other words to be able to phagocyte foreign particles through opsonization. Opsonization is the process where foreign bodies are marked by antigens, which allows the recognition for the monocytes or macrophages to facilitate phagocytosis. It is found that charged particles are taken up more than neutral particle and among the positively charged particles are able to accumulate more than negative particles. Due to the small size and stable nature of nanoparticles they can be packed within monocytes and macrophages for drug transport.[48-51]

This monocyte / macrophage mamoparticle delivery system offers several advantages such as improved targeted drug transport to inflamed site, prolong plasma half life and increase in therapeutic efficacy, the dose amount can be reduced and reduction in drug immunogenicity and cytoxicity profiles can be achieved. There are some factors that are needed to be considered when cells are used as carriers for drugs, which are, that the loaded drug should not be released before it reaches its target site, but should be able to be released at its target site continuously, the

119

cell carriers loaded with the drugs should not diminish its ability to migrate to the target site and the drug loaded in should be safe for both the cell carrier and the organism.[50, 51]

2.6 Methods

2.6.1 Cell Culture

RAW264.7 cells were cultured in RPMI medium containing 10% FBS, with 100 μg/mL G418 and 100 μg/ml hygromycin in a 37°C humidified incubator with 5% CO_2. Pan02 cells were cultured in RPMI with 10% FBS and 1X penicillin-streptomycin in a 37 °C humidified incubator with 5% CO_2.

2.6.2 Synthesis of Nanoparticles

The ligand 3-(3,4-dihydroxyphenethylcarbamoyl)propanoic acid tetraethylene glycol ester (ligand1) (Appendix A Figure A.8 A) was synthesized from 3-(3,4-dihydroxyphenethyl carbamoyl)propanoic acid, (3-(3,4-dihydroxyphenethylcarbamoyl)propanoic acid was synthesized by multi-step protection and de-protection of dopamine hydrochloride, followed by reacting with succinic anhydride), EDC coupling with tetraethylene glycol and Pd/C catalyzed hydrogenation de-protecting benzyl group according to published methods.[52, 53, 54] 50 mg of ligand 1 was dissolved in 10 mL THF, and 20 mg Fe/Fe_3O_4 nanoparticles (NanoScale) were added. After sonicating for 60 minutes, the nanoparticles were precipitated by centrifugation (10000 rpm) and washed with 3.0 mL of THF for 10 washing-centrifugation/re-dispersion cycles. After drying in high vacuum, 18 mg of surface-modified nanoparticles were obtained. TEM imaging showed that the resulting nanoparticles were rod-like in shape (Appendix A Figure A.8 B, C, D).

The following procedures were adopted from Beistein J. Nanotechnology, Wang et al.

2.6.2.1 Synthesis of Boc Protected Dopamine
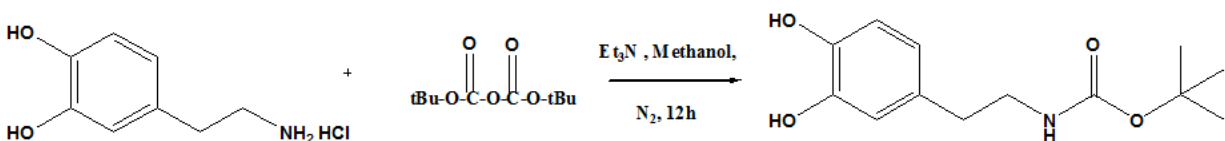
Dopamine (310 mg, 1.63 mmol) was stirred in methanol (8 mL) under N2 for 5 minutes. After 5 minutes TEA (1.8 mmol) was added followed by Boc-anhydride (393 mg, 1.8 mmol).

The reaction was carried out for 12 hrs under N2. Next the solvent was removed under reduced pressure. The product was dissolved in 40 mL CH2Cl2 and washed with 1 N HCl (3×5 mL) and brine (5 mL). The organic layer was dried with anhydrous Na2SO4. The organic phase was filtered and was kept at −5 °C for 3 hours. The Boc protected dopamine precipitated out as a white product and was collected by filtration. (98% yield).

2.6.2.2 Synthesis of Benzyl Protected Boc-Dopamine
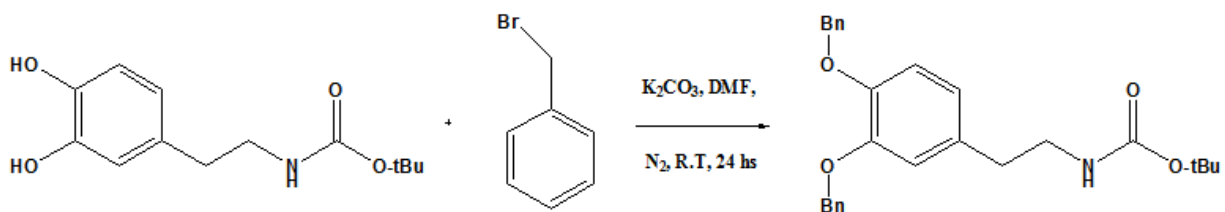
Boc-protected dopamine (3.47 g) was dissolved in 100 mL DMF. To this solution K_2CO_3 (12.6 g) was added and was reacted under N_2. Next benzyl bromide (4.69 g, 2 eq.) was added drop wise. The reaction was reacted in dark conditions at room temperature for 24 hours. Filtration of the solid was done through a short pad of celite and the filter-cake was washed with ether (3×100 mL). The filtrate was washed with ice-water (3×50 mL) and brine (15 mL). The organic layer was dried with anhydrous Na_2SO_4 and concentrated to 150 mL. The product was formed after setting at −5 °C for 5 hours. The white precipitate was collected by vacuum filtration. (93% yield).

2.6.2.3 Deprotection of the Boc Protectiong Group

122
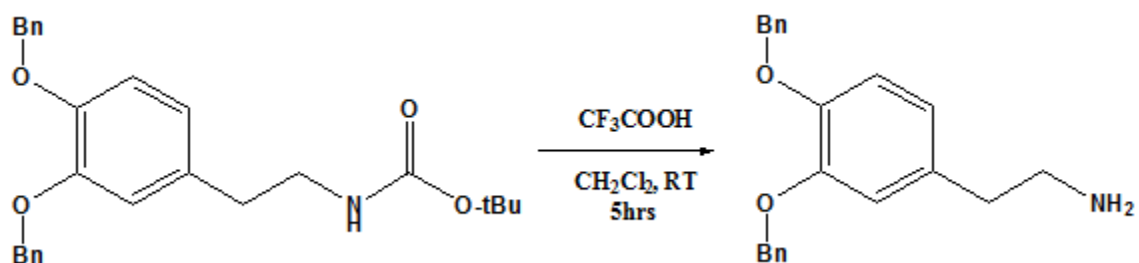
Benzyl and Boc protected-dopamine (4.3g) was stirred in 150 mL 5% TFA CH$_2$Cl$_2$ solution and at room temperature for 5 hours. The clear oily product was obtained by removing the solvent by vacuum. (100% yield).

2.6.2.4 Coupling of Succinic Anhydride
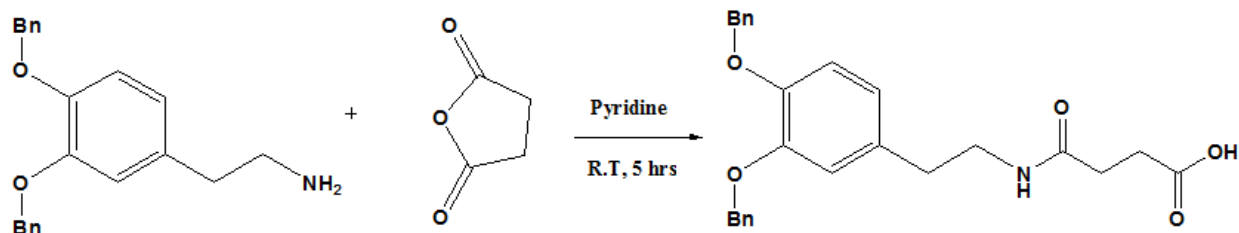
Benzyl protected dopamine (1.43 g) was reacted with 0.43 g succinic anhydride in 6 mL pyridine and stirred at room temperature for 5 hours. Co-evaporation with toluene (toluene 5×5 ml) was done to remove the solvent. The white solid was washed with CH$_2$Cl$_2$ for 3 times and was drydried in vacuum, 1.4 g of the product was obtained. (89% yield).

2.6.2.5 Coupling of Tetraethylene glycol to the Benzyle Protected Dopamine
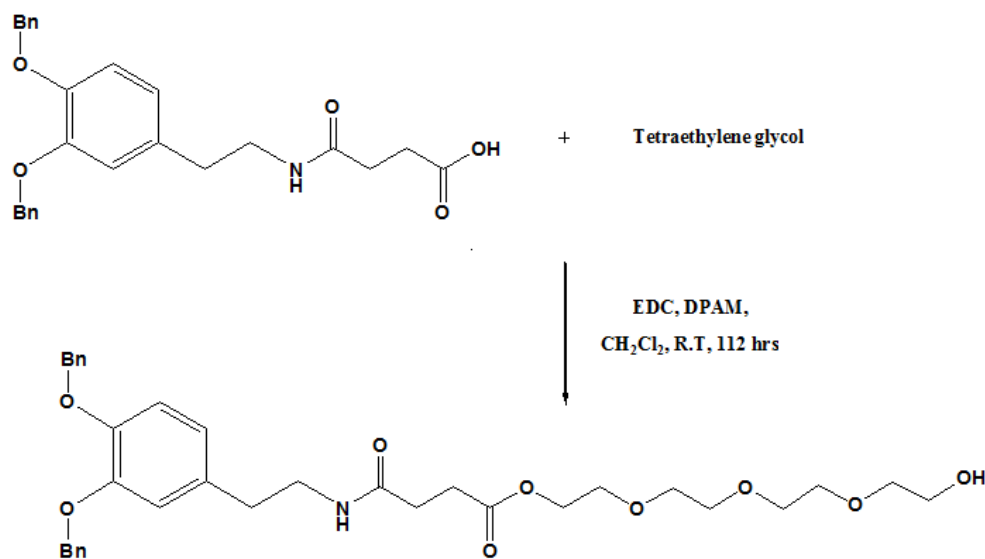
Benzyl protected dopamine-based carboxylic acid (0.964 g) and 0.426g EDC was and stirred in 100 mL CH_2Cl_2 at room temperature for 10 minutes. Next 0.433 g tetraethylene glycol was added followed by 5 mg DMAP and was stirring for 12 hours at room temperature. The organic phase was washed with 10% H_3PO_4 solution (3×10 mL), water (3×10 mL) and brine (10 mL) and was dried with anhydrous $MgSO_4$. The solvent was removed by vacuum. A weight of 0.77g of the product was purified by column chromatography. The solvent system used was 1:1 acetone:methylene chloride. (79% yield).

2.6.2.6 Deprotection of Dopamine-tetraethylene glycol
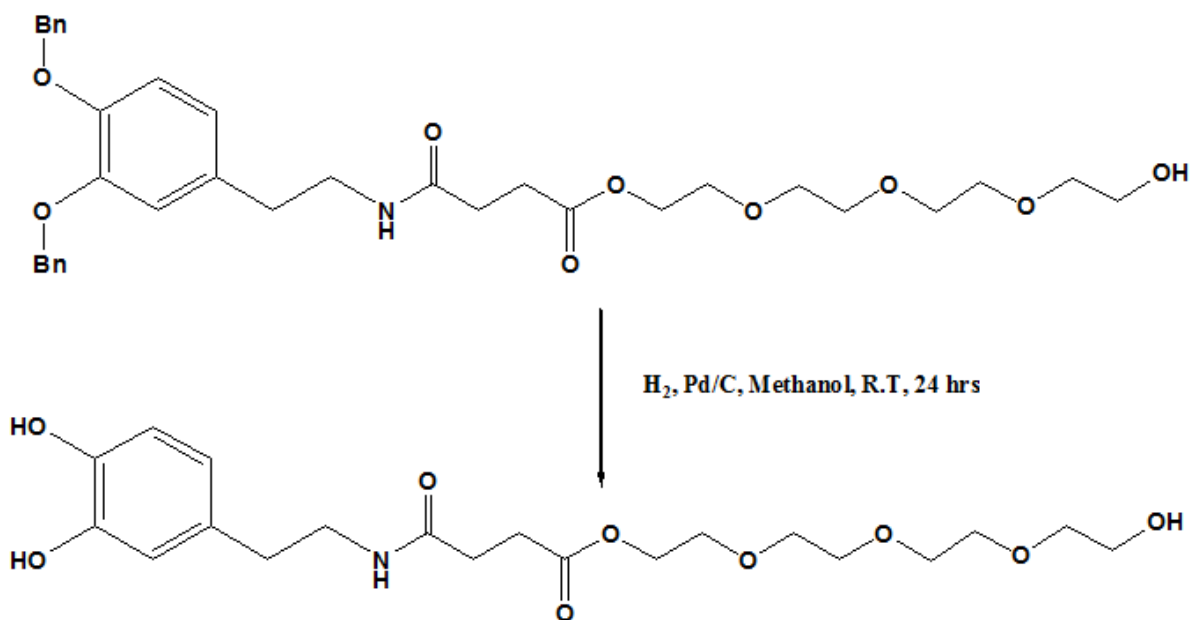
Benzyl protected dopamine tetraethylene glycol (0.34 g) was dissolved in 50 mL methanol and was reacted with Pd/C (77 mg) under N_2. Next 1 atm. H_2 was applied and the mixture was stirred for 24 hours at room temperature. The catalyst was removed by filtering through a short pad of celite and the solvent was removed by vacuum. A weight of 0.23 g of product was obtained. (100% yield).

2.6.3 Measuring the Heat Generation of Fe/Fe$_3$O$_4$ Nanoparticles by an alternating magnetic field

For the measurement of the heating effect, an induction heater (Superior Induction Company, Pasadena, CA) was used. The heater is one inch in diameter and is a copper coil, with four turns, and is continuously cooled with cold water. The heater was operated with 5 kA/m field amplitude and 366 kHz frequency. The Fe/Fe$_3$O$_4$ nanoparticles were dispersed in water, and were subjected to the alternating magnetic field for 5 min. The temperature change was measured by a fiber optic probe (Neoptix, Quebec, Canada).

2.6.4 Loading Mo/Ma with Nanoparticles and Determination of Iron Loading Concentration

To determine the optimal concentration for nanoparticle loading, Mo/Ma were plated in 24 well plates and allowed to come to 70% confluency. Medium was removed from the cells and fresh medium was added containing from 0 to 200 µg/mL iron from the nanoparticles. Sixteen hours later the medium was removed, the cells were washed with PBS, and fresh medium was added. Loading confirmation and concentration were obtained by lifting the cells and running a ferrozine assay for iron content. The percent of cells loaded was measured using flow cytometry. Cytotoxicity was measured using the MTT assay (Flow Chart 1).

For injections, Mo/Ma were cultured to 70% confluency in T75 flasks. Sixteen hours before using the cells, cells for groups 3 and 5 (see below) were given nanoparticles consisting of 373µg (37.3 µg/mL) of iron added to the media in 100 µL of PBS and mixed well.   At the same time, cells for groups 1, 2, and 4 were given 100 µL of PBS. The next morning, the medium was removed, the cells were washed with PBS, and fresh medium was added. The cells were lifted by scraping and counted in a hemocytometer. The correct cell density was attained by spinning the cells in 15 mL conical tubes at 1000 RPM for 5 minutes and resuspending in the correct volume of PBS to give 2,000,000 cells in 100 µL.
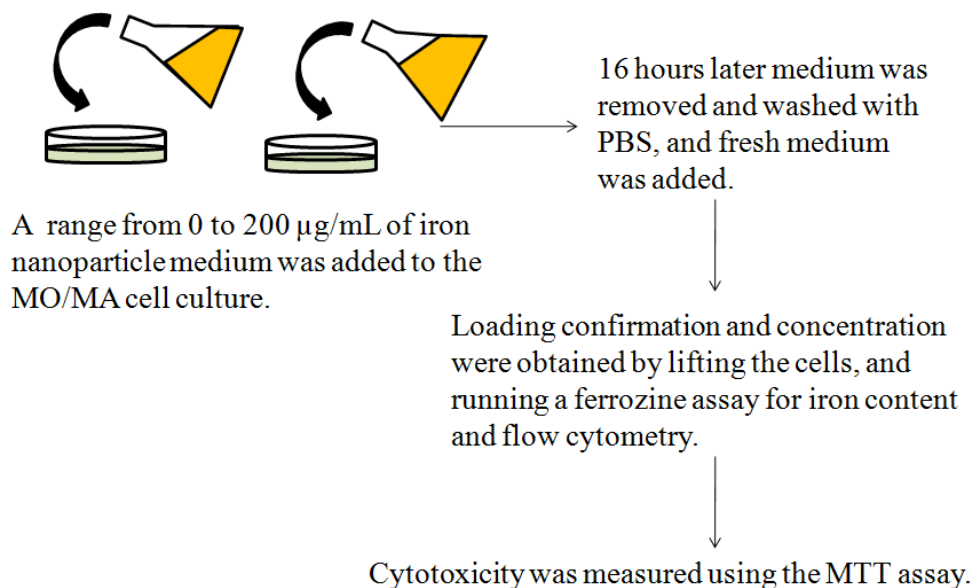
Flow Chart 1:- Loading Mo/Ma with Nanoparticles and Determination of Iron Loading Concentration.

2.6.5 Ferrozine Assay

To determine the iron content of the nanoparticle solutions and the nanoparticle loaded cells, a ferrozine assay for iron was carried out. Ferrozine reagent was prepared by dissolving 9.7g ammonium acetate and 8.8g of ascorbic acid in 10 mL of water. 80mg of ferrozine and 80mg of neocuprine were added to the solution and water was added to bring the total volume to 25 mL. The sample to be measured (either cell suspension or nanoparticle solution) was diluted to appropriate concentrations in deionized water. For cell suspension samples, the cells were counted on a hemocytometer using trypan blue before dilution. 2 mL of the diluted sample was then placed in a test tube and 0.5 mL of 1.2 M HCl and 0.2 mL of 2M ascorbic acid was added. The sample was then vortexed and incubated at 70°C for 1 hour. 0.2 mL of the ferrozine reagent was then added to the test tube and the sample was incubated at room temperature for 30 min. A standard curve was also prepared with 0, 0.1, 0.2, 0.5, 1, 2, and 5 μg/mL iron and treated in the same way. After the second incubation, the absorbance at 562 nm of the standard curve and the

samples was measured (Flow Chart 2). The ABS_{562} *versus* iron concentration was plotted for the standard curve and the sample concentration was determined.

2 ml of cell suspension

0.5 ml 1.2 M HCl,
0.2 ml 2M ascorbic acid

Sample was vortexed and incubated at 70^0C for 1 hr

Ferrozine reagent

Incubated the sample at room temperature for 60 min

Absorbance was measured at 562 nm

- A standard curve was also prepared with 0, 0.1, 0.2, 0.5, 1, 2, and 5 mg/mL iron and treated in the same way.
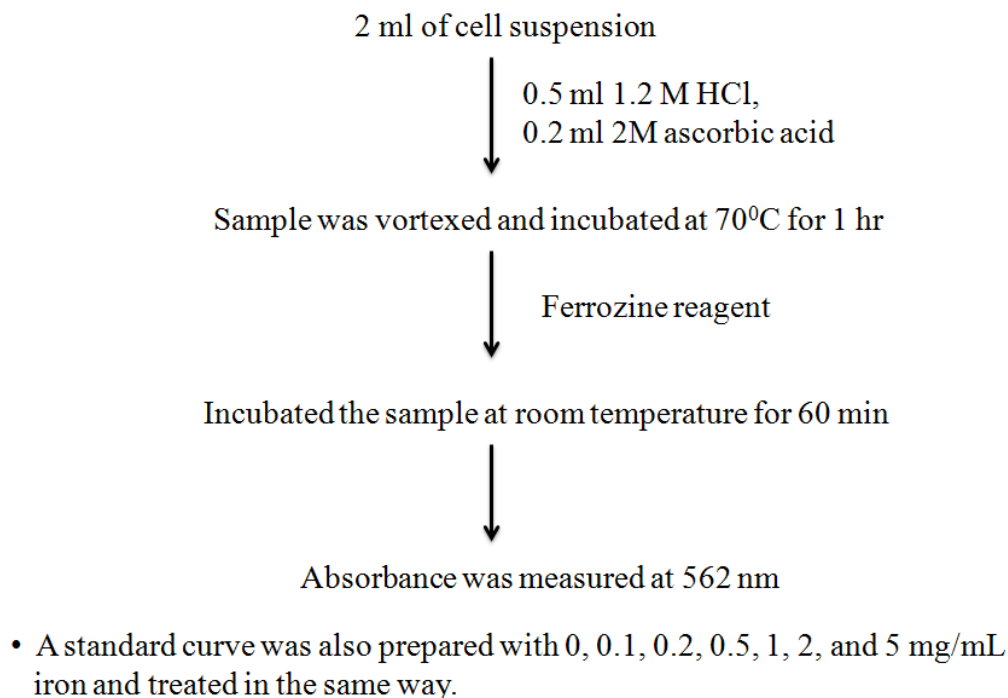
Flow Chart 2:- Determining Iron Content by Ferrozine Assay.

2.6.6 Flow Cytometry

To find the percent of MNP loaded Mo/Ma, cells were treated with nanoparticles consisting of 5,10,15,20,or 25 µg/mL Fe. The cells were incubated overnight and were washed twice with 1x PBS and analyzed by flow cytometry (Guava Easycyte Plus System, Millipore Corporation, MA). Side scatter was measured and was used as a marker for nanoparticles; cells with increased side scatter compared to control cells were counted as MNP loaded cells. Experiment was conducted in triplicate and 10,000 cells were analyzed for each replicate. Data were analyzed by using Cytosoft software (Guava Easycyte Plus System, Millipore Corporation, MA).

2.6.7 MTT Assay

Thiazolyl blue was dissolved in PBS at 5 mg/mL to give the reagent solution. MTT buffer solution was prepared as 10% (w/v) sodium dodecylsulfate and 0.1 M HCl in water. To assay cell viability the reagent solution was added 1:10 to the cell medium and the cells were placed back into the incubator. After four hours, the MTT buffer solution was added 1:1 to the medium and the plates were placed back into the incubator overnight. After incubating, the absorbance at 550 nm and 690 nm was recorded. The quantity $ABS_{550} - ABS_{690}$ was calculated, and the control value was scaled to 100% cell viability.

2.6.8 Tumor Homing

To test the homing ability of Mo/Ma cells on Pan02 tumors, $7x10^5$ Pan02 cells were injected i.p. to two mice on day 0. On day 4, $1x10^6$ PKH26 red fluorescent dye labeled Mo/Ma cells were injected i.p. (manufacturer's instructions were followed for PKH26 labeling). Mice were euthanized on day 7 and 10, and tissues (mesentery/tumor, kidney, liver, spleen, lung) collected and fixed in buffered neutral formalin. Twenty-four hours after fixation, tissues were incubated in sucrose gradient and snap frozen. 5-8 micron sections were made and stained with Hoechst for nuclear counter-staining; serial sections were stained with hematoxylin and eosin (H&E).

To verify that Mo/Ma cells were in Pan02 tumors, $7x10^5$ Pan02-fluc cells (which express firefly luciferase intracellularly) were injected i.p. to five mice on day 0. On day 13, $1x10^6$ Hoescht labeled Mo/Ma cells were loaded with MNP and were injected i.p. Mice were euthanized on day 17 and tissues were snap frozen. 5-8 micron sections were made and stained with rabbit α-firefly luciferase antibody and DyLite649 conjugated sheep α-rabbit Igg antibody.

2.6.9 Magnetic Heating Apparatus to generate AMF

The AMF was generated by a converted 10 kW commercial inductive heater. In these experiments, only 1.5 kW power was used to produce 145 kHz sinusoidal alternating magnetic field in a copper coil. The magnetic field intensity has been calculated to be approximately 0.05 Tesla. The 4 turn 1" diameter coil is coated with silver and water cooled to eliminate residual

heating effects from the resistive loss. The diameter of the coil was chosen to facilitate the complete inclusion of mice studies in the experiments including a perforated plastic tube. .

2.6.10 Intratumoral Nanoparticle Heat Generation

Six C57BL/6 mice (11 weeks old) were injected with 700,000 Pan02 cells in 100 µL PBS subcutaneously. To create a model for intratumoral heat generation by the loaded Mo/Ma, 21 days later, when tumors were palpable, 1,000,000 Mo/Ma loaded with nanoparticles were injected in 10 µL PBS intratumorally to three of the mice. The other three mice received 1,000,000 unloaded Mo/Ma in 10 µL PBS intratumorally. After injections, the mice were euthanized and the tumors were removed. The temperature of the tumors was recorded using an infrared camera. The tumors were then exposed to AMF for 15 min and the temperature of the tumors was again measured using the infrared camera. The difference in temperature before and after AMF was calculated and the loaded and unloaded monocyte groups were compared (Flow Chart 3).

Six C57BL/6 mice (11 weeks old) were injected with 700,000 Pan02 cells in 100 µL PBS subcutaneously. → After 21 days later, when tumors were palpable

3 mice were injected with 1,000,000 Mo/Ma loaded with nanoparticles in 10 µL PBS intratumorally.

3 mice were injected with 1,000,000 Mo/Ma in 10 µL PBS intratumorally.

After injections, the mice were euthanized and the tumors were removed.

The temperature of the tumors was recorded using an infrared camera.

Before exposing to AMF

After exposing to AMF for 15 min

The temperature difference before and after AMF was calculated and the;
Loaded and unloaded monocyte groups were compared.

Flow Chart 3:- Intratumoral Nanoparticle Heat Generation.

130

2.6.11 In Vivo Experiment

C57BL/6 mice (11 weeks old) were injected with 700,000 Pan02 cells in 100 μL PBS intraperitoneally (i.p.) on day 0 to generate a murine model of disseminated pancreatic cancer. These mice were then randomly divided into five groups as follows: (1) tumor control; (2) Mo/Ma control; (3) nanoparticle control; (4) AMF control; and (5) AMF treatment.

On day 5, 2,000,000 Mo/Ma loaded with the nanoparticles were injected in 100 μL PBS i.p. to groups 3 (nanoparticle control) and 5 (AMF treatment). Groups 2 (Mo/Ma control) and 4 (AMF control) also received 2,000,000 Mo/Ma, which were not loaded. Group 1 (tumor control) received 100 μL PBS i.p. This procedure was repeated on days 9 and 13. On day 8, mice from groups 4 (AMF control) and 5 (AMF treatment) were anesthetized with isofluorane and exposed to an AMF for 20 minutes. This procedure was repeated on days 12 and 16 (Flow Chart 4) (Appendix A Figure A.9).

After three rounds of treatments, the mice were closely observed and allowed to continue until they displayed signs of clinical symptoms of cancer, at which point they were euthanized using CO_2, and the tumors were collected and weighed.
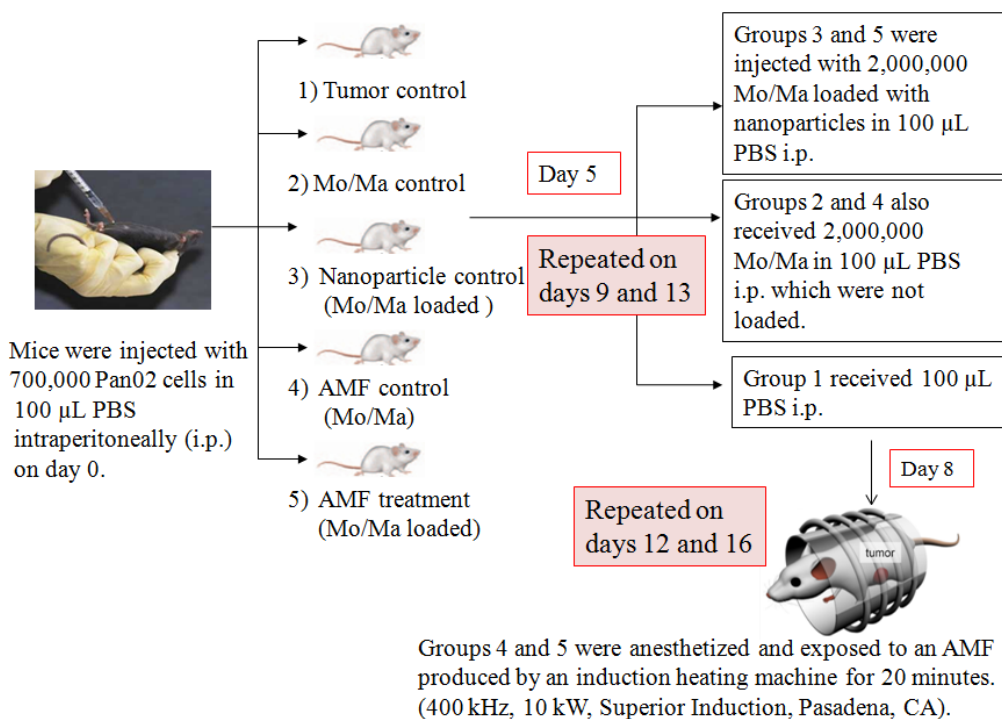
Flow Chart 4:- In Vivo Experiment Procedure.

2.6.12 Duration to Clinical Symptoms

The measured outcome for this study was mouse survival. To minimize potential pain and distress of the mice, however, a system was developed that allowed the euthanasia of the mice shortly before they died. The mice were scored numerically 1 - 5 based on the body condition of the mice (primarily the spine and dorsal pelvic bone prominence) with a score of 3 indicative of a healthy mouse. This initial score was then modified by the presence of extreme lethargy, dehydration, ataxia, head tilt, severe hunching, limb dragging, severe raised hair, Harderian gland secretions, ascites, labored breathing, or bloody tail. If pronounced, these symptoms led to a subtraction of 1 point from the BCS score while mild cases led to the addition of a 'minus symbol' to the score (e.g. 3-). The mice were scored by this system every 12 hours and any mouse that scored a 2 or less was euthanized and the day/time was recorded. The euthanasia day/time data were then treated like survival data and modeled using Kaplan-Meier statistics to determine the statistical significance of the data.

2.7 Results

2.7.1 ^{1}H NMR data of the Compounds

2.7.1.1 Boc-protected Dopamine

^{1}H NMR (DMSO-*d*6) δ: 1.73 (s, 9H); 2.48 (t, 2H); 3.02 (q, 2H); 6.40 (d, 1H); 6.54 (s, 1H); 6.61 (d, 1H); 6.83 (t, 1H); 6.85 (s, 1H); 6.76 (s, 1H). (Appendix B Figure B.74).

2.7.1.2 Benzyl-protected Boc-dopamine

^{1}H NMR (CDCl3) δ: 1.45 (s, 9H); 2.70 (t, 2H); 3.31 (q, 2H); 4.49 (s, 1H); 5.15 (d, 4H); 6.71 (d, 1H); 6.80 (s, 1H); 6.88 (d, 1H); 7.32 (t, 2H); 7.37 (t, 4H); 7.45 (d, 4H). (Appendix B Figure B.75).

2.7.1.3 Benzyl-protected dopamine

^{1}H NMR (CDCl3) δ: 2.79 (t, 2H); 3.08 (m, 2H); 5.11 (s, 4H); 6.68 (d, 1H); 6.75 (s, 1H); 6.90 (d, 1H); 7.32 (t, 2H); 7.35 (t, 4H); 7.42 (d, 4H). (Appendix B Figure B.76).

2.7.1.4 Succinic anhydride coupled Benzyl-protected dopamine

^{1}H NMR (DMSO-*d*6) δ: 2.29 (t, 2H); 2.42 (t, 2H); 2.60 (t, 2H); 3.21 (q, 2H); 5.09 (d, 4H); 6.71 (d, 1H); 6.94 (s, 1H); 6.96 (d, 1H); 7.32 (t, 2H); 7.38 (d, 4H); 7.45 (t, 4H); 7.90 (t, 1H); 12.08 (s, 1H). (Appendix B Figure B.77).

2.7.1.5 Tetraethylene glycol coupled Benzyl-protected dopamine

^{1}H NMR (CDCl3) δ: 2.39 (t, 2H); 2.57 (t, 1H); 2.70 (q, 4H); 3.44 (q, 2H); 3.60 (t, 2H); 3.65 (broad 12H); 4.24 (t, 2H); 5.15 (d, 4H); 5.74 (t, 1H); 6.71 (d, 1H); 6.81 (s, 1H); 6.89 (d, 1H); 7.31 (t, 2H); 7.37 (t, 4H); 7.46 (d, 4H). (Appendix B Figure B.78).

2.7.1.6 Tetraethylene glycol coupled dopamine

^{1}H NMR (DMSO-*d*6) δ: 2.33 (t, 2H); 2.48 (q, 2H); 3.15 (broad multiplet, 4H); 3.41 (t, 2H); 3.49 (t, 2H); 3.51 (broad multiplet, 8H); 3.59 (t, 2H); 4.11 (t, 2H); 6.41 (d, 1H); 6.55 (s, 1H); 6.61 (d, 1H). (Appendix B Figure B.79).

2.7.2 Measuring the Heat Generation of Fe/Fe₃O₄ Nanoparticles by an alternating magnetic field

More than 30 °C temperature increase was achieved when exposing a dispersion of 2.0 mg nanoparticles in 2.0 mL of water to the alternating magnetic field for five minutes.The specific absorption rate (SAR) is calculated to be 522 ± 40 W/g.

2.7.3 Toxicity and Loading of Nanoparticles

The nanoparticles did not show any toxicity at concentrations less than 100 μg/mL Fe, although some slight toxicity was shown at 100 and 200 μg/mL Fe (Appendix B Figure B.80 A). Mo/Ma took up the nanoparticles in a manner proportional to the iron concentration (Appendix B Figure B.80 B). The percentage of cells containing nanoparticles (defined as cells that exhibit increased side scatter after loading) also increased in a manner proportional to the iron concentration (Appendix B Figure B.80 C). Based on these results, to prevent undesired toxicity while maximizing the amount of iron loaded, nanoparticles were loaded at 37.5 μg/mL Fe for the *in vivo* experiment. To determine the exact amount of iron loaded in the cells for the *in vivo* experiment, when Mo/Ma were lifted for the *in vivo* experiment, excess cells were collected and iron content was measured using the ferrozine assay. The iron content of Mo/Ma injected was 2.12 +/- 0.37 pg Fe/cell or 4.25 +/- 0.74 μg Fe/2,000,000 cells.

2.7.4 Tumor Homing Studies

To determine if monocyte-like cells would home to Pan02 tumors, two mice bearing i.p. Pan02 tumors were injected i.p. with PKH26 labeled Mo/Ma. Three days after injection, the first mouse was euthanized. Tissue imaging showed that the monocyte-like cells effectively homed to the tumor, but did not infiltrate other organs, including the pancreas, spleen, liver, and kidney (Appendix B Figure B 81). At six days, the second mouse was sacrificed and tissue imaging showed again that the monocyte-like cells penetrated tumor tissue but not healthy tissue (Appendix B Figure B 81).

H&E staining of serial sections demonstrate that the tissue that the Mo/Ma home to is highly disorganized, indicative of tumor tissue (Appendix B Figure B.82 A,B). To further verify that the monocyte-like cells were, in fact, in tumor tissue, five mice bearing i.p. Pan02 tumors

expressing firefly luciferase were injected i.p. with Hoechst labeled Mo/Ma which were loaded with MNP. Four days after injection, the mice were euthanized. Antibody staining for firefly luciferase demonstrated that the Mo/Ma were in tumor tissue (Appendix B Figure B.82 C).

2.7.5 Nanoparticle Heating of Tumors

To verify that the cell-delivered nanoparticles could cause significant heating of the tumor, a subcutaneous Pan02 model was generated. (The subcutaneous model was used to give more accessible tumors for measurement purposes). The temperature change caused by AMF induced hyperthermia using the nanoparticle loaded Mo/Ma was 4.0+/-0.7°C after 15 min of AMF exposure, or moderate hyperthermia. As a comparison, the temperature change using the unloaded Mo/Ma was 1.0+/-0.5°C (Appendix B Figure B.83, p value = 0.0056).

2.7.6 Mouse Survival

To determine the effectiveness of the treatment, Pan02 tumors were given i.p. to C57BL/6 mice and the mice were treated as described in the methods section. The euthanasia data were collected and modeled using Kaplan-Meier survival statistics. The data are reported as days subsequent to tumor injection (day 0) (Appendix B Figure B.84). The Kaplan-Meier test showed that the survival curves were significantly different ($p < 0.005$). All of the mice from the tumor control group were euthanized due to clinical symptoms (hereafter referred to as 'succumbed') by day 23. Similarly all of the Mo/Ma control mice succumbed by day 25, all of the nanoparticle control mice succumbed by day 26 and all of the AMF control mice succumbed by day 25. Modeling with Kaplan-Meier statistics showed no significant difference between any of these groups. The AMF treatment mice survived substantially longer, with mice lasting until 33.5 days. The survival of the AMF treatment group was shown to be significant against all control groups ($p < 0.005$ for all comparisons). The average increase in survival *versus* tumor control for the nanoparticle treatment group was 7 days, a 31% increase in life expectancy post tumor insertion.

2.8 Discussion

Here we have shown for the first time that tumor-homing cells can specifically deliver MNP for AMF therapy, and this treatment can significantly prolong the lives of mice bearing deep and disseminated intraperitoneal pancreatic tumors. Core/shell iron/iron oxide MNP were synthesized that are superparamagnetic. Clusters of these nanoparticles are ferromagnetic. These MNP were loaded into Mo/Ma cells, which we demonstrated to be tumor homing cells. The Mo/Ma cells were injected i.p. into tumor bearing mice and trafficked specifically to the tumor. Three days later, the mice were exposed to AMF, which caused the nanoparticles to generate heat, leading to localized hyperthermia.

We found that the mouse monocytes homed effectively to the pancreatic tumors after i.p. administration. This is not surprising because monocytes and/or macrophages are often found as tumor-associated cells. Rat monocytes were shown to efficiently invade rat glioma spheroids *in vitro*, and peritoneal macrophages specifically migrated to rat gliomas after intravenous or intracarotid administration.[34, 35] Interestingly, in this case, the mouse monocytes physically migrated only to the tumors within the peritoneal cavity, while normal tissues did not contain monocytes.

Classically, hyperthermia kills tumor tissue by heating proteins and other macromolecules to the point of denaturing faster than the cell can renature them. Since the system demonstrated here was substantially effective with only 4 μg of iron injected into the mouse per treatment cycle, other mechanisms of action may be present. The nanoparticle control group demonstrates that the nanoparticles themselves do not have any treatment value; similarly, the AMF control group demonstrates that AMF treatment does not have any stand-alone value. The Mo/Ma control group demonstrates that the Mo/Ma neither increase nor decrease tumor growth. Thus, AMF activation of the MNP is primarily responsible for the effect. Low grade hyperthermia has been shown to recruit various immune cells including dendritic cells, natural killer (NK) cells, neutrophils, and cytotoxic T cells.[55-62] Although future studies need to be done, this or another similar mechanism may have greatly increased the effectiveness of the treatment and could explain why such a low dose of MNP can effect such a large survival advantage.

We have described the development of a localized hyperthermia treatment using tumor-tropic cells, monocyte/macrophage-like cells, to deliver MNP for AMF activation (Appendix B

Figure B.85). The system we describe here holds potential for further development as a specific delivery method for MNP-generated localized hyperthermia for targeted therapy of pancreatic and other types of cancer.

2.9 References

1. Philip P. A.; Mooney M.; Jaffe D.; Eckhardt G.; et al.; Consensus report of the national cancer institute clinical trials planning meeting on pancreas cancer treatment, *J Clin Oncol*, 2009, *Vol.* 27, 5660-5669.

2. Hildebrandt B.; Wust P.; Ahlers O.; Dieing A.; et al.; The cellular and molecular basis of hyperthermia, *Crit Rev Oncol Hematol*, 2002, *Vol. 43*, 33-56.

3. Shecterle L. M.; St Cyr J. A.; Whole body hyperthermia as a potential therapeutic option, *Cancer Biother*, 1995, *Vol. 10,* 253-256.

4. Habash R. W.; Bansal R.; Krewski D.; Alhafid H. T.; Thermal therapy, part 2: hyperthermia techniques, *Crit Rev Biomed Eng*, 2006, *Vol. 34,* 491-542.

5. Sminia P.; van der Zee J.; Wondergem J.; Haveman J.; Effect of hyperthermia on the central nervous system, *Int J Hyperthermia*, 1994, *Vol.* 10, 1-30.

6. Vertree R. A.; Leeth A.; Girouard M.; Roach J. D..; Zwischenberger J. B.; Whole-body hyperthermia: a review of theory, design and application, *Perfusion*, 2002, *Vol.* 17, 279-290.

7. Hildebrandt B.; Hegewisch-Becker S.; Kerner T.; Nierhaus A.; et al.; Current status of radiant whole-body hyperthermia at temperatures >41.5 degrees C and practical guidelines for the treatment of adults. The German 'Interdisciplinary Working Group on Hyperthermia', *Int J Hyperthermia*, 2005, *Vol. 21*, 169-183.

8. Jia D.; Liu J.; Current devices for high-performance whole-body hyperthermia therapy, *Expert Rev Med Devices*, 2010, *Vol.* 7, 407-423.

9. Kraybill W. G.; Olenki T.; Evans S. S.; Ostberg J. R.; et al.; A phase I study of fever-range whole body hyperthermia (FR-WBH) in patients with advanced solid tumours: correlation with mouse models, *Int J Hyperthermia*, 2002, *Vol.* 18, 253-266.

10. Jia D.; Rao W.; Wang C.; Jin C.; et al.; Inhibition of B16 murine melanoma metastasis and enhancement of immunity by fever-range whole body hyperthermia, *Int J Hyperthermia*, 2011, *Vol.* 27, 275-285.

11. Koetitz R.; Fannin P. C.; Trahms L.; Time domain study of Brownian and Neel relaxation in ferrofluids, *J Magn Magn Mater*, 1995, *Vol. 149*, 42-46.

12. Pakhomov A. B.; Bao Y.; Krishnan K .M.; Effects of surfactant friction on Brownian magnetic relaxation in nanoparticle ferrofluids, *J Appl Phys*, 2005, *Vol. 97,* 10Q305/1-10Q305/3.

13. Shapiro M. G.; Atanasijevic T.; Faas H.; Westmeyer G. G.; Jasanoff A.; Dynamic imaging with MRI contrast agents: quantitative considerations, *Magn Reson Imaging*, 2006, *Vol.* 24, 449-462.

14. Shinkai M.; Yanase M,; Suzuki M.; Honda H.; et al.; Intracellular hyperthermia for cancer using magnetite cationic liposomes, *J Magn Magn Mater*, 1999, *Vol. 194*, 176-184.

15. Le B.; Shinkai M.; Kitade T.; Honda H.; et al.; Preparation of tumor-specific magnetoliposomes and their application for hyperthermia, *J Chem Eng Jp*, 2001, *Vol. 34*, 66-72.

16. Ito A.; Shinkai M.; Honda H.; Yoshikawa K.; et al.; Heat shock protein 70 expression induces antitumor immunity during intracellular hyperthermia using magnetite nanoparticles, *Cancer Immunol Immunother*, 2003, *Vol. 52*, 80-88.

17. Jordan A.; Scholz R.; Maier-Hauff K.; van Landeghem F. K.; et al.; The effect of thermotherapy using magnetic nanoparticles on rat malignant glioma, *J Neurooncol*, 2006, *Vol. 78*, 7-14.

18. Jordan A.; Scholz R.; Wust P.; Fahling H.; et al.; Effects of magnetic fluid hyperthermia (MFH) on C3H mammary carcinoma in vivo, *Int J Hyperthermia*, 1997, *Vol. 13*, 587-605.

19. Jordan A.; Scholz R.; Wust P.; Schirra H.; et al.; Endocytosis of dextran and silan-coated magnetite nanoparticles and the effect of intracellular hyperthermia on human mammary carcinoma cells in vitro, *J Magn Magn Mater*, 1999, *Vol. 194*, 185-196.

20. Hilger I.; Andra W.; Hergt R.; Hiergeist R.; Schubert H.; Kaiser W. A.; Electromagnetic heating of breast tumors in interventional radiology: in vitro and in vivo studies in human cadavers and mice, *Radiology*, 2001, *Vol. 218*, 570-575.

21. Johannsen M.; Thiesen B.; Jordan A.; Taymoorian K.; et al.; Magnetic fluid hyperthermia (MFH) reduces prostate cancer growth in the orthotopic Dunning R3327 rat model, *Prostate*, 2005, *Vol. 64*, 283-292.

22. Ohno T.; Wakabayashi T.; Takemura A.; Yoshida J.; et al.; Effective solitary hyperthermia treatment of malignant glioma using stick type CMC-magnetite. In vivo study, *J Neurooncol*, 2002, *Vol. 56*, 233-239.

23. Kawai N.; Futakuchi M.; Yoshida T.; Ito A.; et al.; Effect of heat therapy using magnetic nanoparticles conjugated with cationic liposomes on prostate tumor in bone, *Prostate*, 2008, *Vol. 68*, 784-792.

24. Aboody K. S.; Brown A.; Rainov N. G.; Bower K. A.; et al.; Neural stem cells display extensive tropism for pathology in adult brain: evidence from intracranial gliomas, *Proc Natl Acad Sci U S A*, 2000, *Vol. 97*, 12846-12851.

25. Arbab A. S.; Pandit S. D.; Anderson S. A.; Yocum G. T.; et al.; Magnetic resonance imaging and confocal microscopy studies of magnetically labeled endothelial progenitor cells trafficking to sites of tumor angiogenesis, *Stem Cells*, 2006, *Vol. 24*, 671-678.

26. De Palma M.; Mazzieri R.; Politi L. S.; Pucci F.; et al.; Tumor-targeted interferon-alpha delivery by Tie2-expressing monocytes inhibits tumor growth and metastasis, *Cancer Cell*, 2008, *Vol. 14*, 299-311.

27. Ganta C.; Chiyo D.; Ayuzawa R.; Rachakatla R.; et al.; Rat umbilical cord stem cells completely abolish rat mammary carcinomas with no evidence of metastasis or recurrence 100 days post-tumor cell inoculation, *Cancer Res*, 2009, *Vol. 69*, 1815-1820.

28. Nakamizo A.; Marini F.; Amano T.; Khan A.; et al.; Human bone marrow-derived mesenchymal stem cells in the treatment of gliomas, *Cancer Res*, 2005, *Vol. 65*, 3307-3318.

29. Rachakatla R. S.; Marini F.; Weiss M. L.; Tamura M.; Troyer D.; Development of human umbilical cord matrix stem cell-based gene therapy for experimental lung tumors, *Cancer Gene Ther*, 2007, *Vol. 14*, 828-835.

30. Rachakatla R. S.; Pyle M. M.; Ayuzawa R.; Edwards S. M.; et al.; Combination treatment of human umbilical cord matrix stem cell-based interferon-beta gene therapy and 5-fluorouracil significantly reduces growth of metastatic human breast cancer in SCID mouse lungs, *Cancer Invest*, 2008, *Vol. 26*, 662-670.

31. Studeny M.; Marini F. C.; Champlin R. E.; Zompetta C.; Fidler I. J.; Andreeff M.; Bone marrow-derived mesenchymal stem cells as vehicles for interferon-beta delivery into tumors, *Cancer Res*, 2002, *Vol. 62*, 3603-3608.

32. Studeny M.; Marini F. C.; Dembinski J. L.; Zompetta C.; et al.; Mesenchymal stem cells: potential precursors for tumor stroma and targeted-delivery vehicles for anticancer agents, *J Natl Cancer Inst*, 2004, *Vol. 96*, 1593-1603.

33. Rachakatla R.; Balivada S.; Seo G.; Myers C. B.; Wang H.; Samarkoon T.; et al. ; Attenuation of Mouse Melanoma by A/C Magnetic Field after Delivery of Bi-Magnetic Nanoparticles by Neural Progenitor Cells, *ACS Nano*, 2010, *Vol. 4*, 7093-7104.

34. Solinas G.; Germano G.; Mantovani A.; Allavena P.; Tumor-associated macrophages (TAM) as major players of the cancer-related inflammation, *J Leukoc Biol*, 2009, *Vol. 86*, 1065-1073.

35. Strik H. M.; Hulper P.; Erdlenbruch B.; Meier J.; et al.; Models of monocytic invasion into glioma cell aggregates, *Anticancer Res*, 2006, *Vol. 26*, 865-871.

36. Matsui M.; Shimizu Y.; Kodera Y.; Kondo E.; Ikehara Y.; Nakanishi H.; Targeted delivery of oligomannose-coated liposome to the omental micrometastasis by peritoneal macrophages from patients with gastric cancer, *Cancer Sci*, 2010, *Vol. 101*, 1670-1677.

37. Muthana M.; Giannoudis A.; Scott S. D.; Fang H.; et al.; Use of Macrophages to Target Therapeutic Adenovirus to Human Prostate Tumors, *Cancer Res*, 2011, *Vol. 71*, 1805-1815.

38. Baek S.; Makkouk A. R.; Krasieva T.; Sun C.; et al.; Treatment of glioma; an in vitro study of macrophage-mediated delivery of gold nanoshells, *J Neurooncol*, 2011, EPub.

39. Doi C.; Maurya D. K.; Pyle M. M.; Troyer D.; Tamura M.; Cytotherapy with naive rat umbilical cord matrix stem cells significantly attenuates growth of murine pancreatic cancer cells and increases survival in syngeneic mice, *Cytotherapy*, 2010, *Vol. 12*, 408-417.

40. Gupta A. K.; Gupta M.; Synthesis and surface engineering of iron oxide nanoparticles for biomedical applications, *Biomaterials*, 2005, *Vol. 26*, 3995–4021.

41. Laurent S.; Forge D.; Port M.; Roch A.; Magnetic Iron Oxide Nanoparticles: Synthesis, Stabilization, Vectorization, Physicochemical Characterizations, and Biological Applications *Chem. Rev.* 2008, *Vol. 108,* 2064–2110.

42. Schwertmann U.; Cornell R. M.; Iron oxides in the laboratory: preparation and characterization. Weinheim, Cambridge: VCH; 1991.

43. Li Y.; Lei Y.; Wagner E.; Xie C. et.al; *Bioconjugate Chemistry*, 2013, *Vol. 24*, 133−143.

44. Thorek D. L. J.; Chen A. K.; Czupryna J.; Tsourkas A.; Superparamagnetic Iron Oxide Nanoparticle Probes for Molecular Imaging, *Annals of Biomedical Engineering*, 2006, *Vol. 34*, 23–38.

45. Wust P.; Hildebrandt B.; Sreenivasa G.; Rau B.; et. al.; Hyperthermia in combined treatment of cancer, *Lancet Oncol*, 2002, *Vol. 3,* 487–97.

46. Van der Zee J.; Heating the patient: a promising approach?, *Annals of Oncology*, 2002, *Vol. 13*, 1173-1184.

47. Richards D. M.; Hettinger J.; Feuerer M.; Monocytes and Macrophages in Cancer: Development and Functions, *Cancer Microenvironment*, 2013, *Vol. 6,* 179–191.

48. Beduneau A.; Ma Z.; Grotepas C. B.; Kabanov A.; et. al.; Facilitated Monocyte-Macrophage Uptake and Tissue Distribution of Superparmagnetic Iron-Oxide Nanoparticles, *PLoS ONE*, 2009, *Vol. 4*, e4343. doi:10.1371/journal.pone.0004343.

49. Lee H. W.; Choi H. J.; Ha S. J.; Lee K. T.; Kwon Y. G.; Recruitment of monocytes/macrophages in different tumor microenvironments, *Biochimica et Biophysica Acta*, 2013, *Vol.* 1835, 170–179.

50. Dou H.; Destache C. J.; Morehead J. R.; Mosley R. L.; Development of a macrophage-based nanoparticle platform for antiretroviral drug delivery, *Blood*, 2006, *Vol. 108*, 2827-2835.

51. Batrakova E. V.; Gendelman H. E.; Kabanov A. V.; Cell-Mediated Drugs Delivery, *Expert Opin Drug Deliv*, 2011, *Vol. 8*. 415–433.

52. Mefford O. T.; Saville S.; Qi B.; Controlled surface functionalization of iron-oxide nanoparticles for field responsive biomedical applications, *PMSE*, 2009, *Vol 101*,1569.

53. Hong R.; Fischer N. O.; Emrick T.; Rotello V. M.; Surface PEGylation and Ligand Exchange Chemistry of FePt Nanoparticles for Biological Applications, *Chem Mater,* 2005, *Vol.* 17, 4617-4621.

54. Wang H.; Shrestha T. B.; Basel M. T.; Dani R. K.; Chikan V.; Troyer D. L.; Bossmann S. H.; et.al.; Magnetic-Fe/Fe3O4-nanoparticle-bound SN38 as carboxylesterase-cleavable prodrug for the delivery to tumors within monocytes/macrophages, *Beilstein J. Nanotechnol.*, *Vol.3*, 2012, 444-455.

55. Appenheimer M. M.; Chen Q.; Girard R. A.; Wang W. C.; Evans S. S.; Impact of fever-range thermal stress on lymphocyte-endothelial adhesion and lymphocyte trafficking, *Immunol Invest*, 2005, *Vol.* 34, 295-323.

56. Calderwood S. K.; Theriault J. R.; Gong J.; How is the immune response affected by hyperthermia and heat shock proteins? *Int J Hyperthermia*, 2005, *Vol.* 21, 713-716.

57. Chen T.; Guo J.; Yang M.; Zhu X.; Cao X.; Chemokine-containing exosomes are released from heat-stressed tumor cells via lipid raft-dependent pathway and act as efficient tumor vaccine, *J Immunol*, 2011, *Vol.* 186, 2219-2228.

58. Fuggetta M. P.; Alvino E.; Tricarico M.; D'Atri S.; et al.; In vitro effect of hyperthermia on natural cell-mediated cytotoxicity, *Anticancer Res*, 2000, *Vol.* 20, 1667-1672.

59. Ito A.; Honda H.; Kobayashi T.; Cancer immunotherapy based on intracellular hyperthermia using magnetite nanoparticles: a novel concept of "heat-controlled necrosis" with heat shock protein expression, *Cancer Immunol Immunother*, 2006, *Vol. 55*, 320-328.

60. Manjili M. H.; Wang X. Y.; Park J.; Macdonald I. J.; et al.; Cancer immunotherapy: stress proteins and hyperthermia, *Int J Hyperthermia*, 2002, *Vol. 18*, 506-520.

61. Milani V.; Noessner E.; Effects of thermal stress on tumor antigenicity and recognition by immune effector cells, *Cancer Immunol Immunother*, 2006, *Vol.* 55, 312-319.

62. Segal B. H.; Wang X. Y.; Dennis C. G.; Youn R.; et al.; Heat shock proteins as vaccine adjuvants in infections and cancer, *Drug Discov Today*, 2006, *Vol. 11*, 534-540.

Appendix A - Figures for Methods
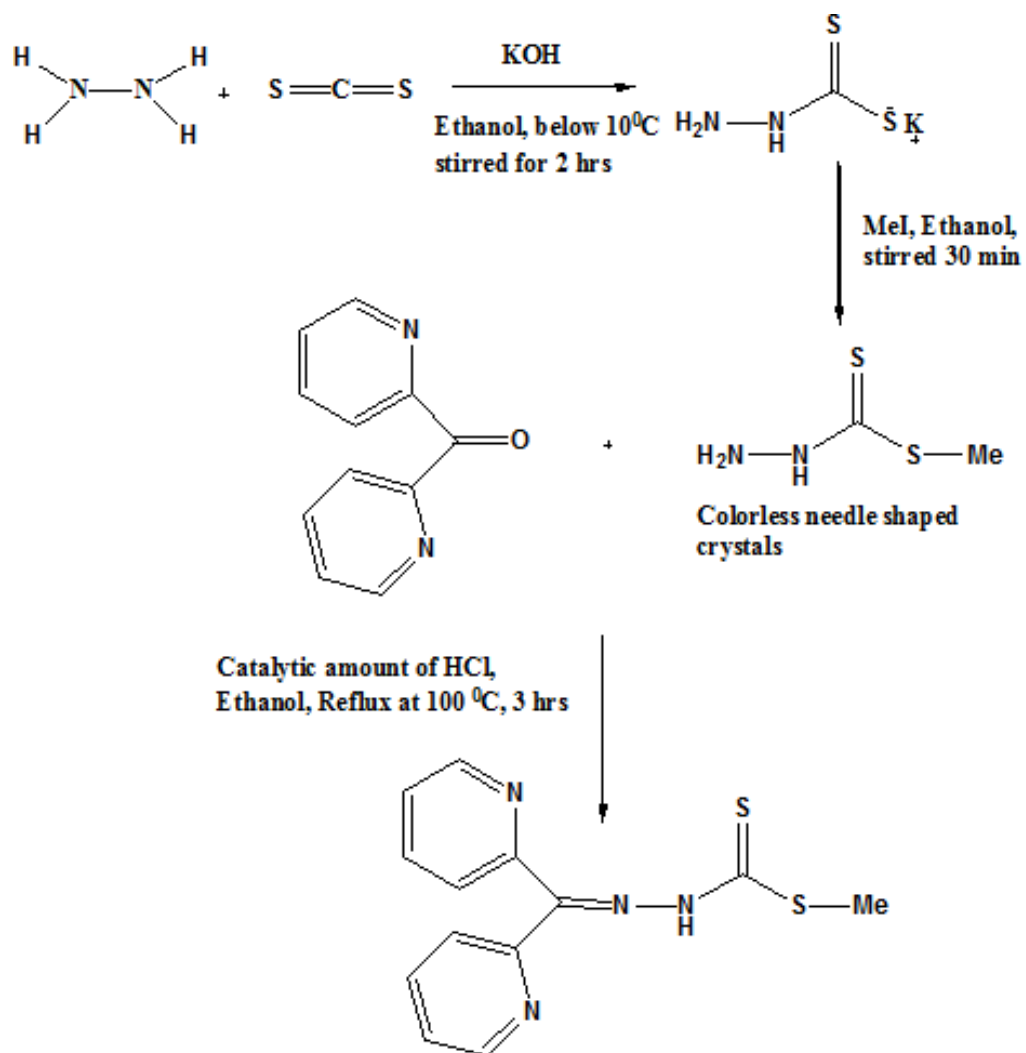
Figure A.1:- Synthetic scheme of the thiosemicarbazone iron chelator, N'-(Di-pyridin-2-yl-methylene)-hydrazinecarbodithioic acid methylester
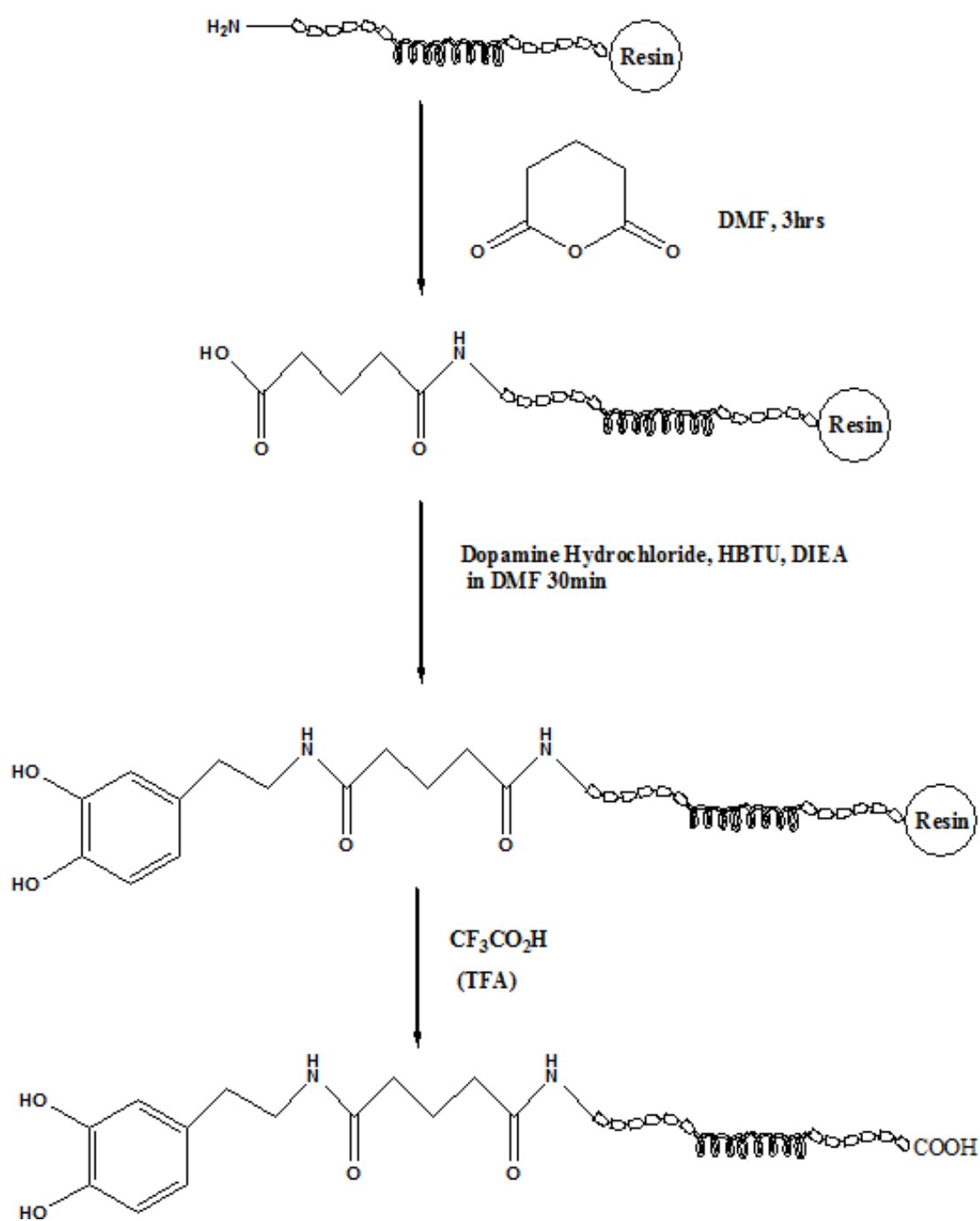
Figure A.2:- Synthetic scheme of the dopamine-peptide ligand.
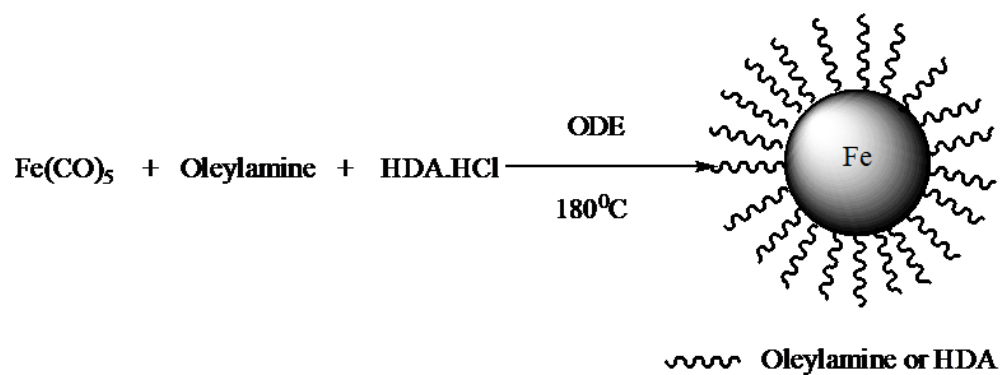
Figure A.3:- Preparation of core/shell Fe/Fe3O4 magnetic nanoparticles (MNPs).
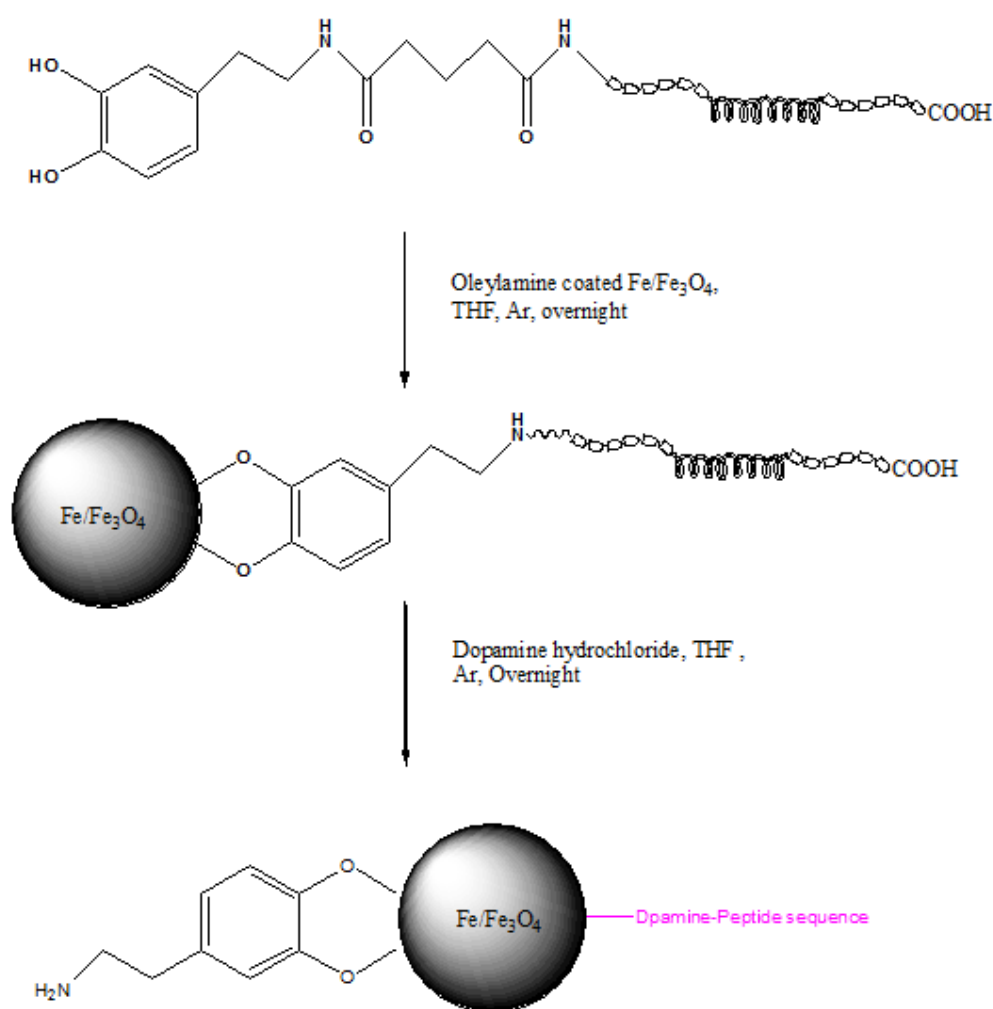
Figure A.4:- Ligand exchange of the Fe/Fe3O4 magnetic nanoparticles with Dopamine-peptide ligand.
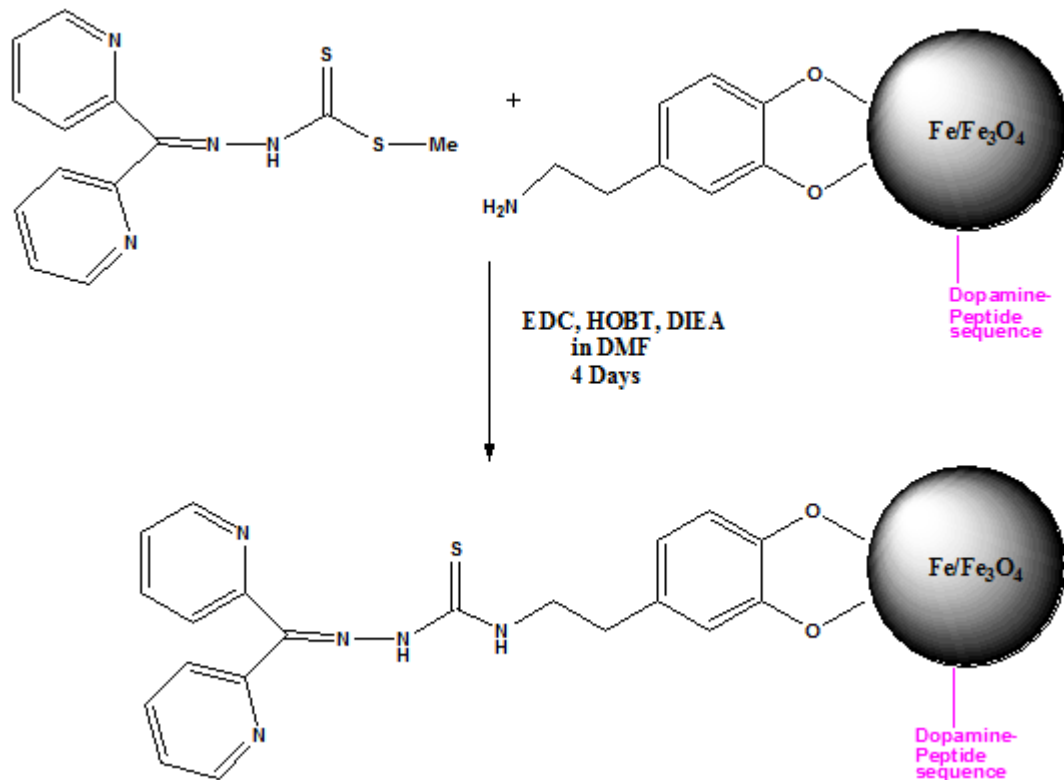
Figure A.5:- Coupling the thiosemicarbazone iron chelator to the free dopamine on the Fe/Fe$_3$O$_4$ magnetic nanoparticles.

Figure A.6:- Division of 96-well plate for MTT assay, for different concentrations of the nanosystems and times.
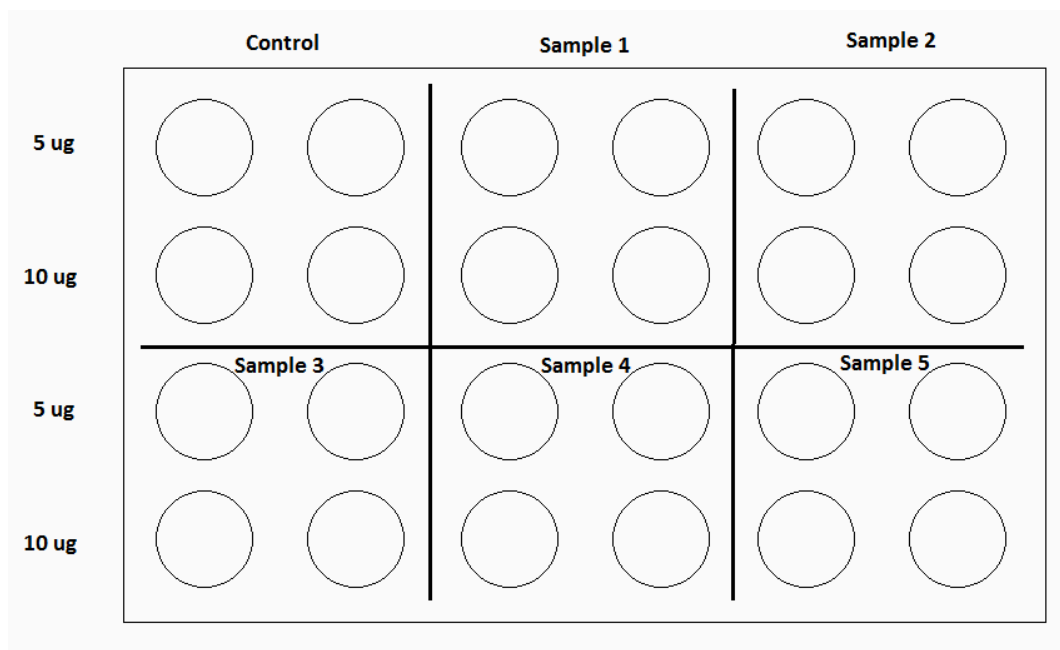
Figure A.7:- Division of the 24-well plate for Prussian blue staining to determine loading of the nanosystems into 4T1 cell line.
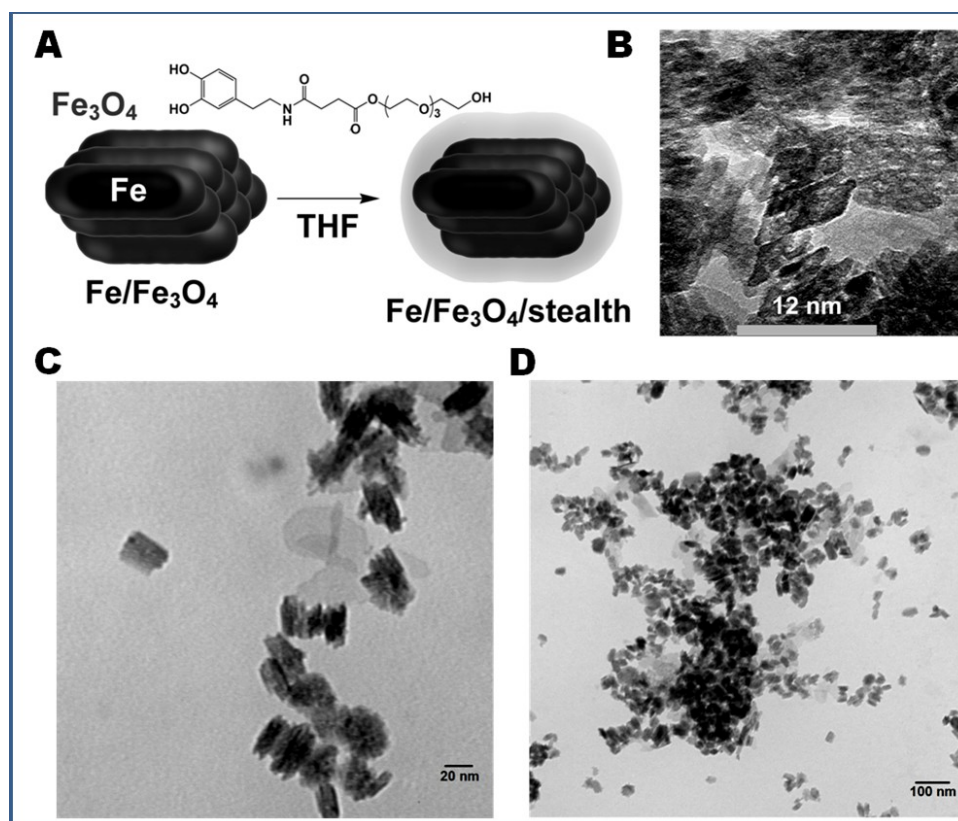
Figure A.8:- Nanoparticle synthesis.

A. Core/shell iron/iron oxide nanoparticles were synthesized and then coated in a dopamine based stealth ligand. B, C, D. (This work has already been published in; *International Journal of Nanomedicine ,2012, Vol 7, 297–306.*)
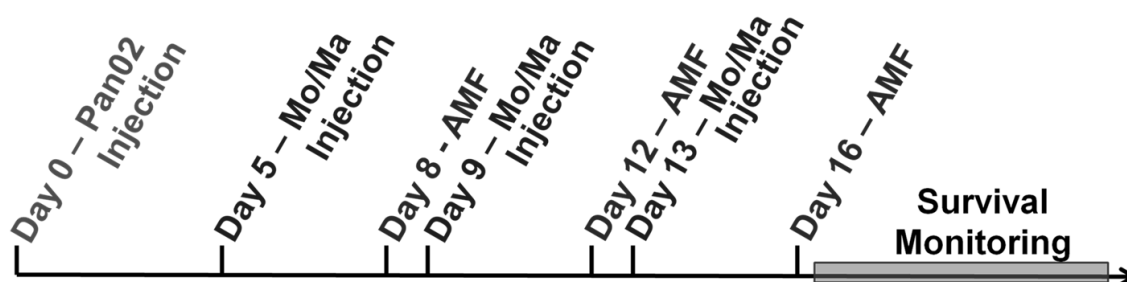
Figure A.9:- Treatment cycle for the *in vivo* study.

(This work has already been published in; *International Journal of Nanomedicine ,2012, Vol 7, 297–306*.)

Appendix B - Figures and Graphs for Results
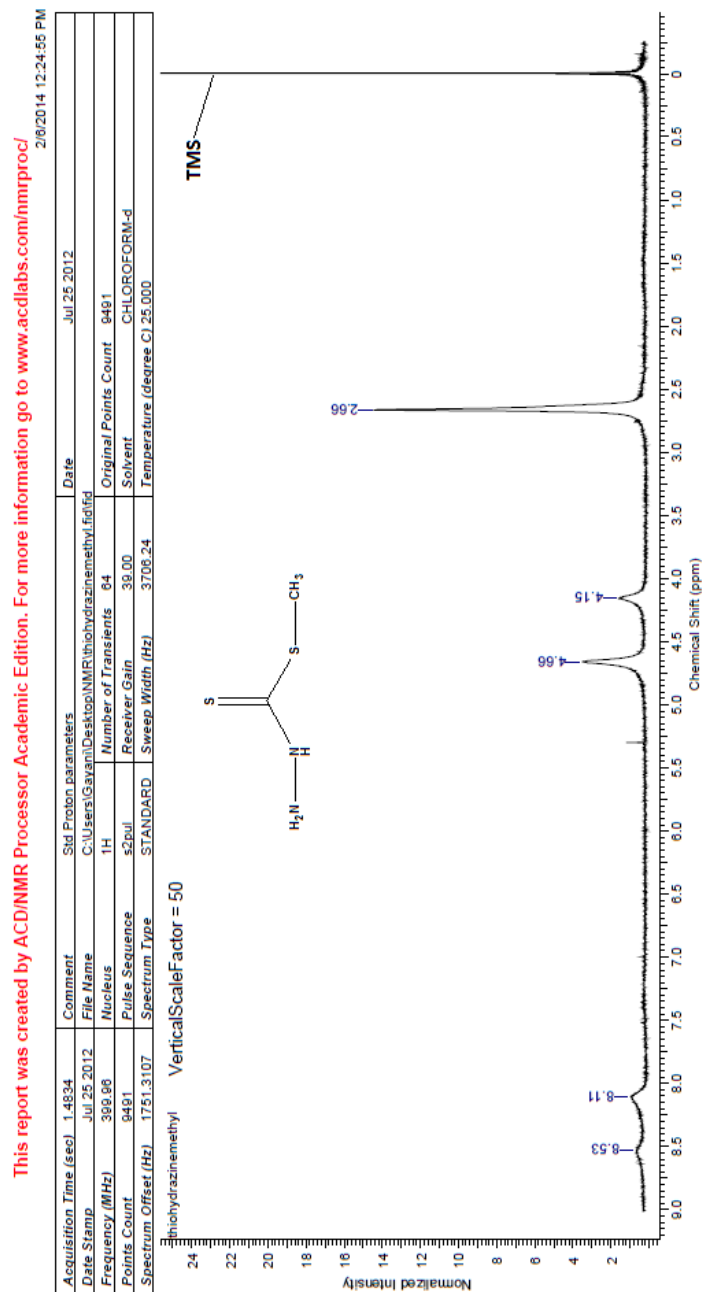
Figure B.1:- ^{1}HNMR of Hydrazinecarbodithioic acid methylester.

^{1}H NMR (CDCl$_3$-d, δ ppm) 2.66 (s, 3H, CH$_3$), 4.15(s, 2H, NH$_3^+$ (protonated nitrogen) D$_2$O exchangeable) 4.66 (s, 2H, NH$_2$, D$_2$O exchangeable), 8.11 (s, H, NH$_2^+$CS (protonated nitrogen), D$_2$O exchangeable), 8.53 (s, H, NHCS, D$_2$O exchangeable).
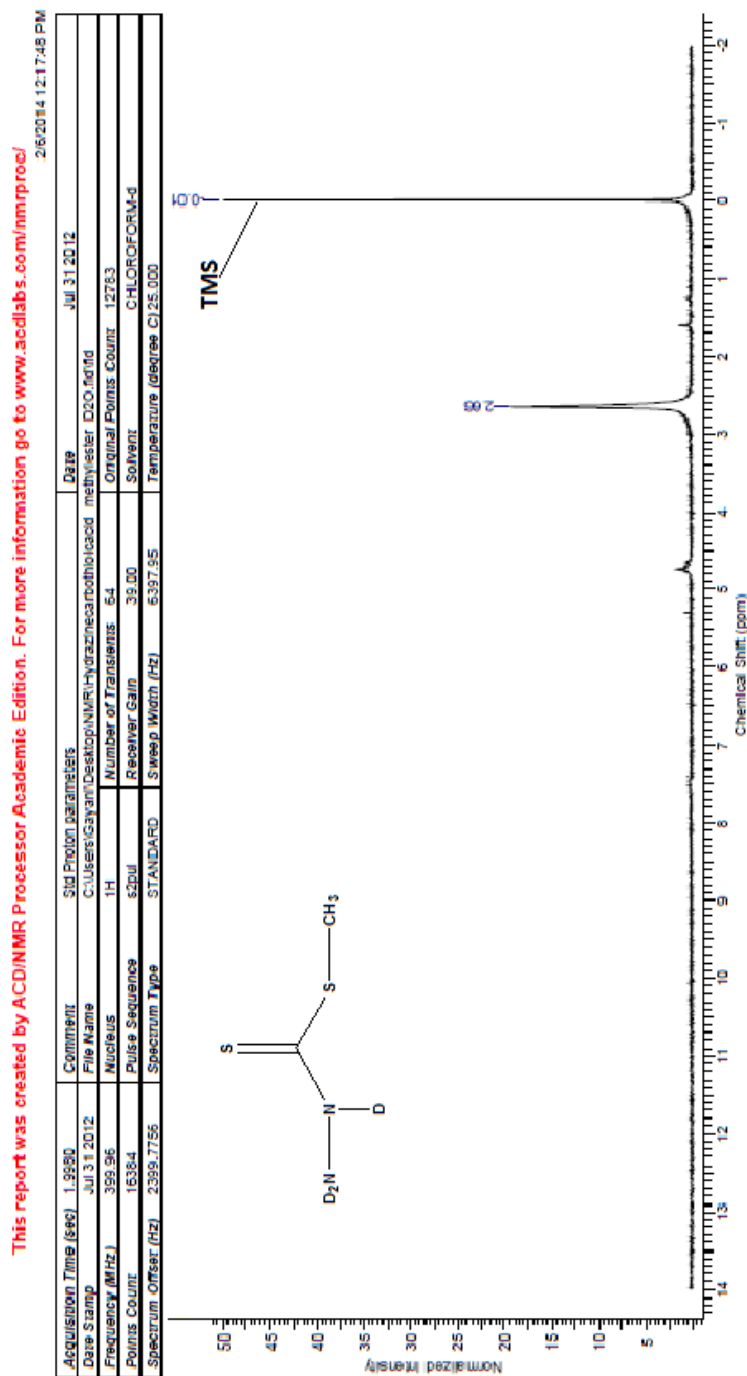
Figure B.2:- ^{1}HNMR of the D_2O exchanged of Hydrazinecarbodithioic acid methylester.
^{1}H NMR (CDCl$_3$-d, δ ppm) 2.66 (s, 3H, CH$_3$), 4.15(s, 2H, NH$_3^+$ (protonated nitrogen) D$_2$O exchangeable) 4.66 (s, 2H, NH$_2$, D$_2$O exchangeable), 8.11 (s, H, NH$_2^+$CS (protonated nitrogen), D$_2$O exchangeable), 8.53 (s, H, NHCS, D$_2$O exchangeable).
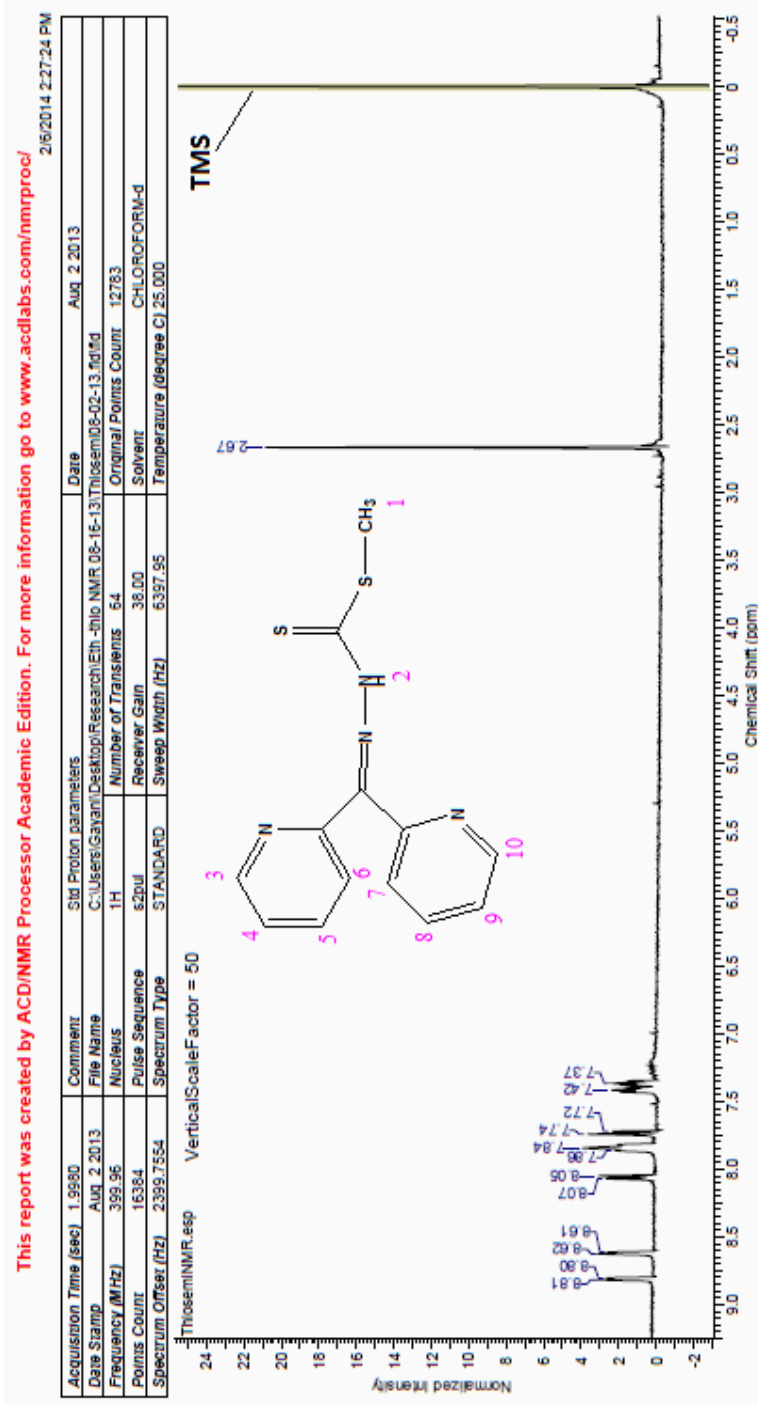
Figure B.3:- ^{1}HNMR of the thiosemicarbazone iron chelator,

N´-(Di-pyridin-2yl-methylene)- hydrazinecarbodithioic acid methylester.

^{1}H NMR (CDCl3, δ ppm) 2.67 (s, 3H, CH$_3$); 7.52 (s, H, NH); 8.81 (d, H3), 8.62 (d, H8), 8.06 (d, H6), 7.84 (m, H5 & 8), 7.73 (d, H7), 7.42 (m, H4), 7.37 (m, H9) of the Ar-H.

Figure B.4:- ^{1}HNMR of the aryl hydrogens of the thiosemicarbazone iron chelator, N´-(Di-pyridin-2yl-methylene)- hydrazinecarbodithioic acid methylester.

^{1}H NMR (CDCl3, δ ppm) 2.67 (s, 3H, CH₃); 7.52 (s, H, NH); 8.81 (d, H3), 8.62 (d, H8), 8.06 (d, H6), 7.84 (m, H5 & 8), 7.73 (d, H7), 7.42 (m, H4), 7.37 (m, H9) of the Ar-H.
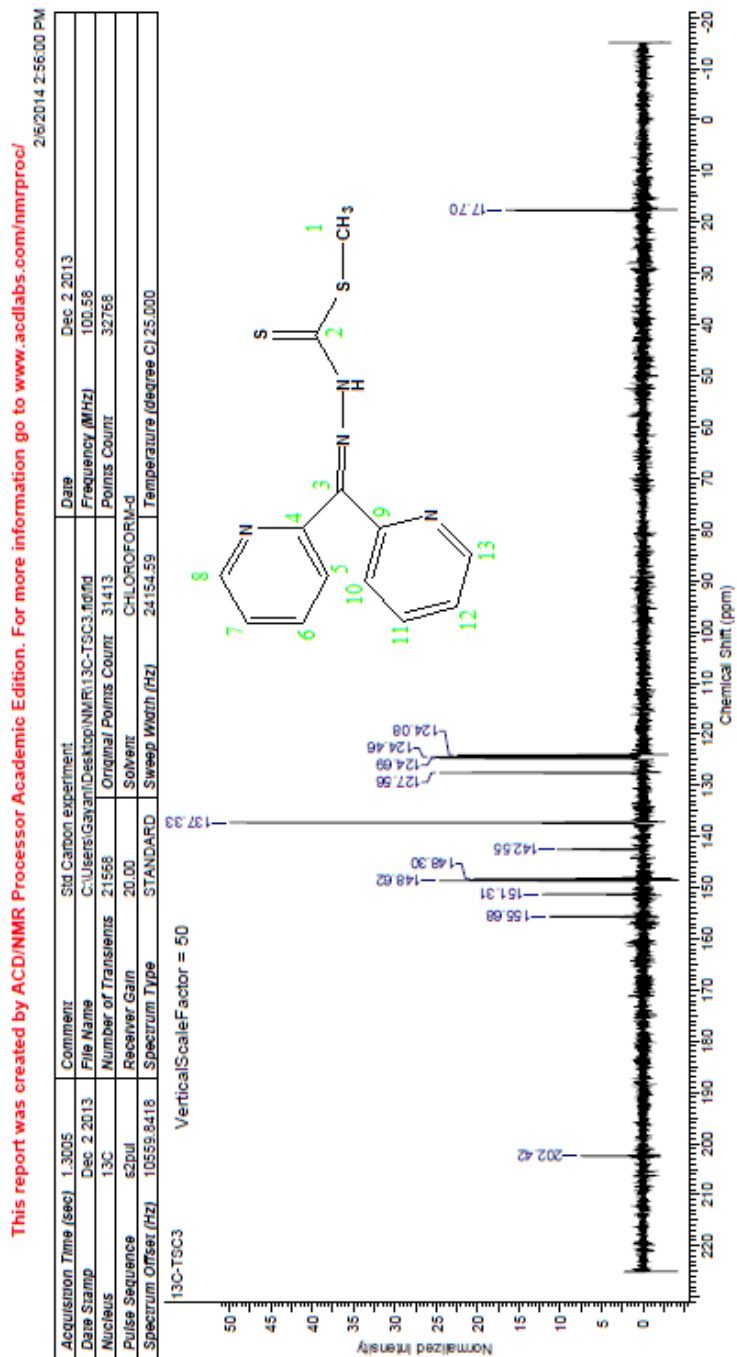
Figure B.5:- ^{13}CNMR of the thiosemicarbazone iron chelator,

N´-(Di-pyridin-2yl-methylene)- hydrazinecarbodithioic acid methylester.

^{13}C NMR (CDCl$_3$, δ ppm, J, Hz): 17.70 (CH$_3$); 124.08 (C10), 124.46 (C5), 124.69 (C12), 127.56 (C7), 137.33 (C6 & 11), 142.55 (C13), 148.30 (C8), 148.62 (C9), 151.31 (C4) of the Ar-C; 155.68 (C=N); 202.44 (C=S).
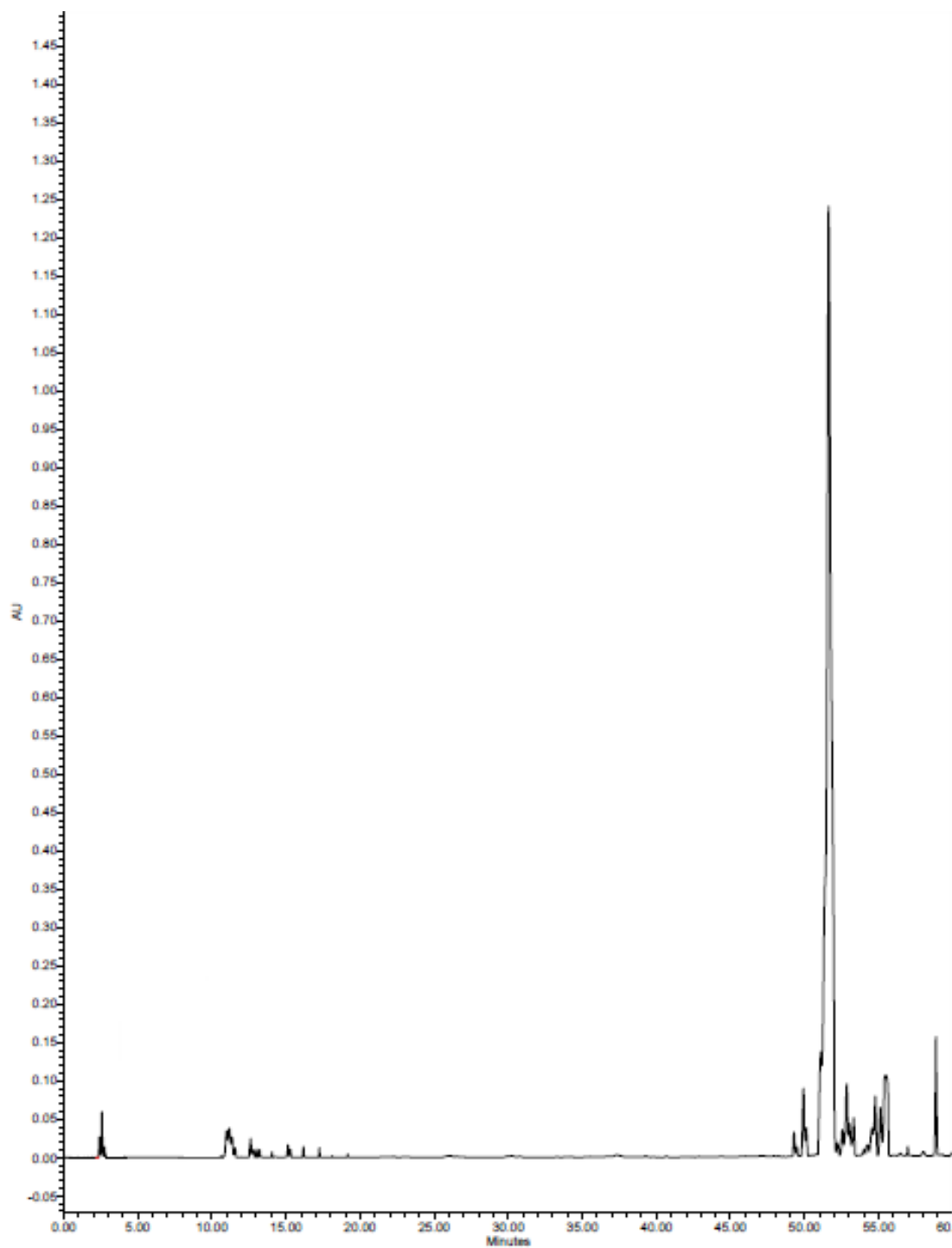
Figure B.6:- HPLC of the CGKRK(D[KLAKLAKKLAKLAK])PLFAERL peptide sequence. At time 51.62 mins the peptide was detected and shows ~ 90% purity.
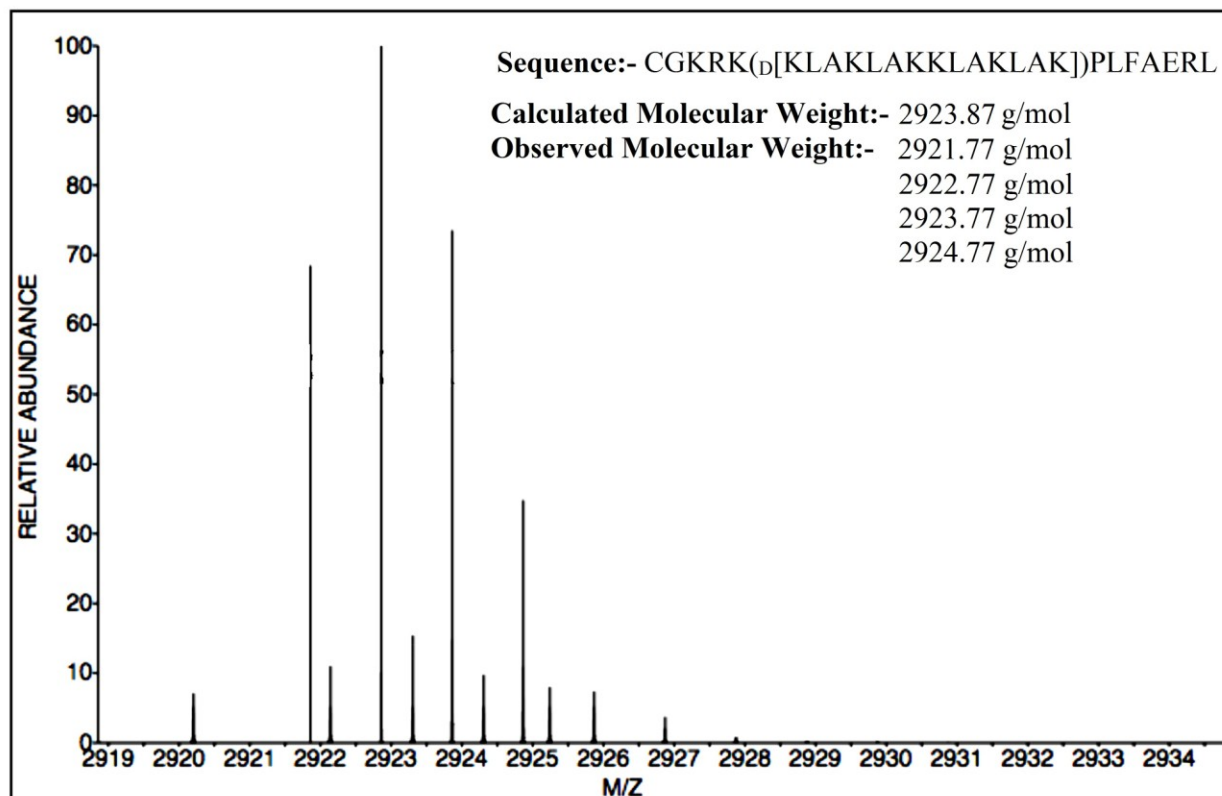
Figure B.7:- Mass spectrum of the CGKRK(D[KLAKLAKKLAKLAK])PLFAERL peptide sequence.
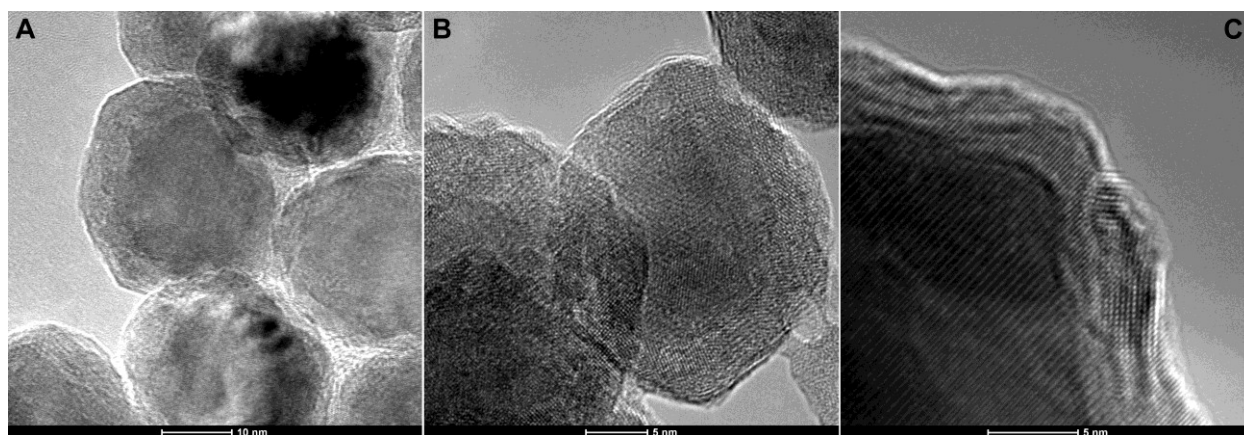
Figure B.8:- Fe/Fe$_3$O$_4$ nanoparticles
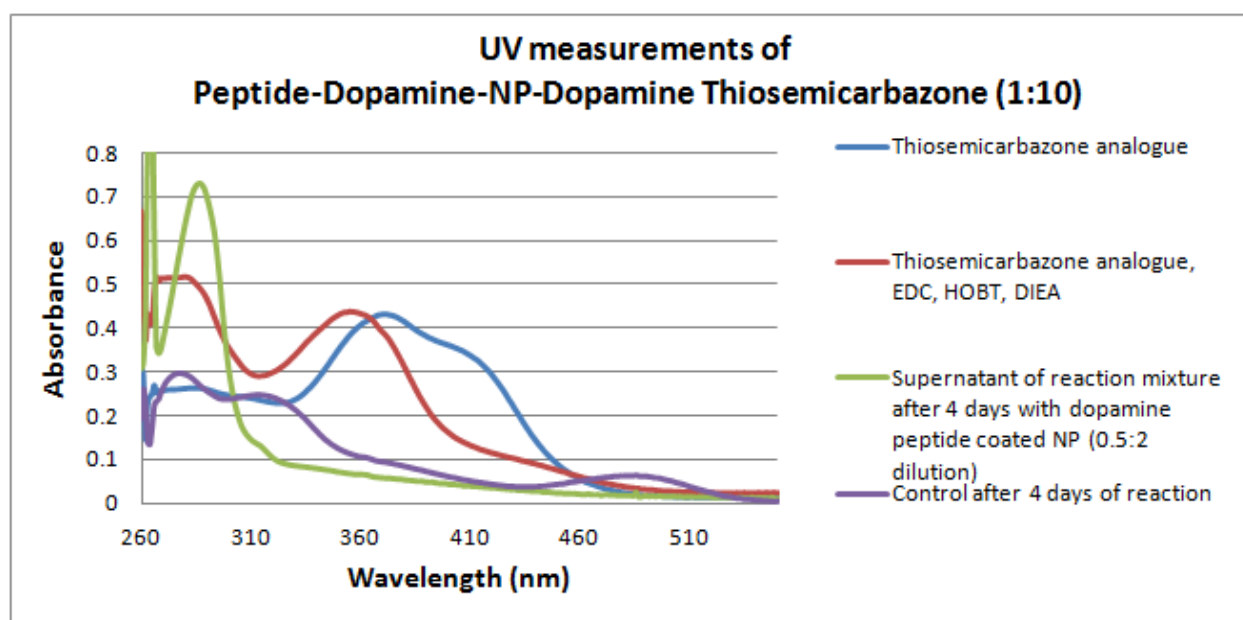
Figure B.9:- UV graph of Peptide-Dopamine-NP-Dopamine-Thiosemicarbazone (1:10) reaction.
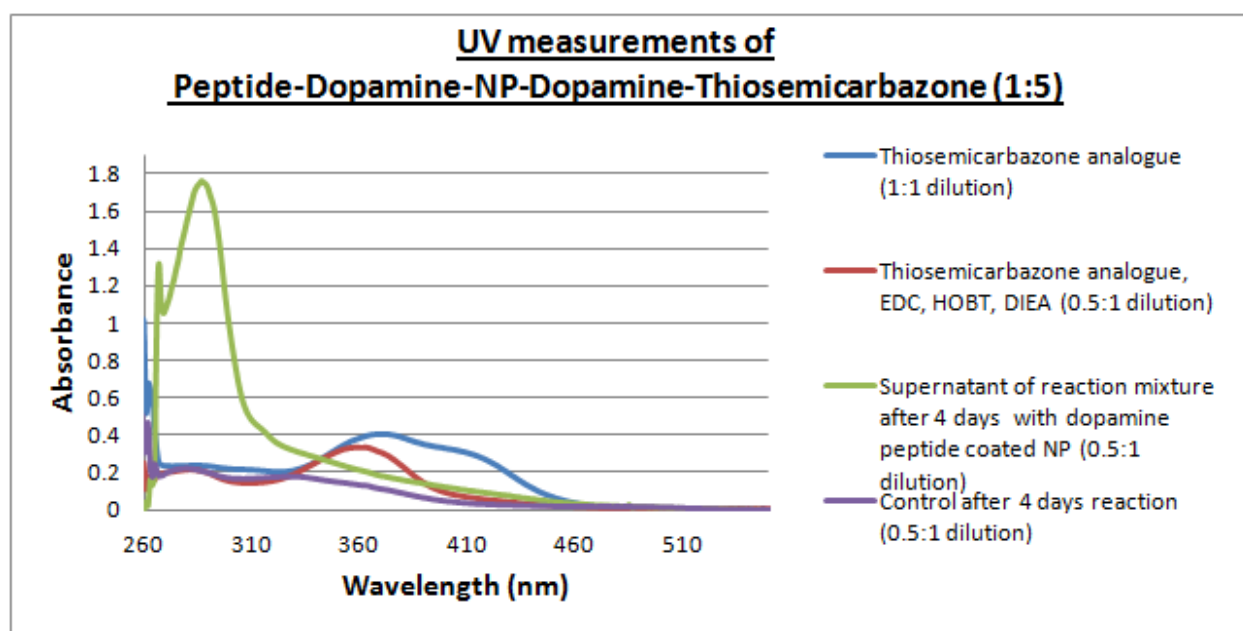
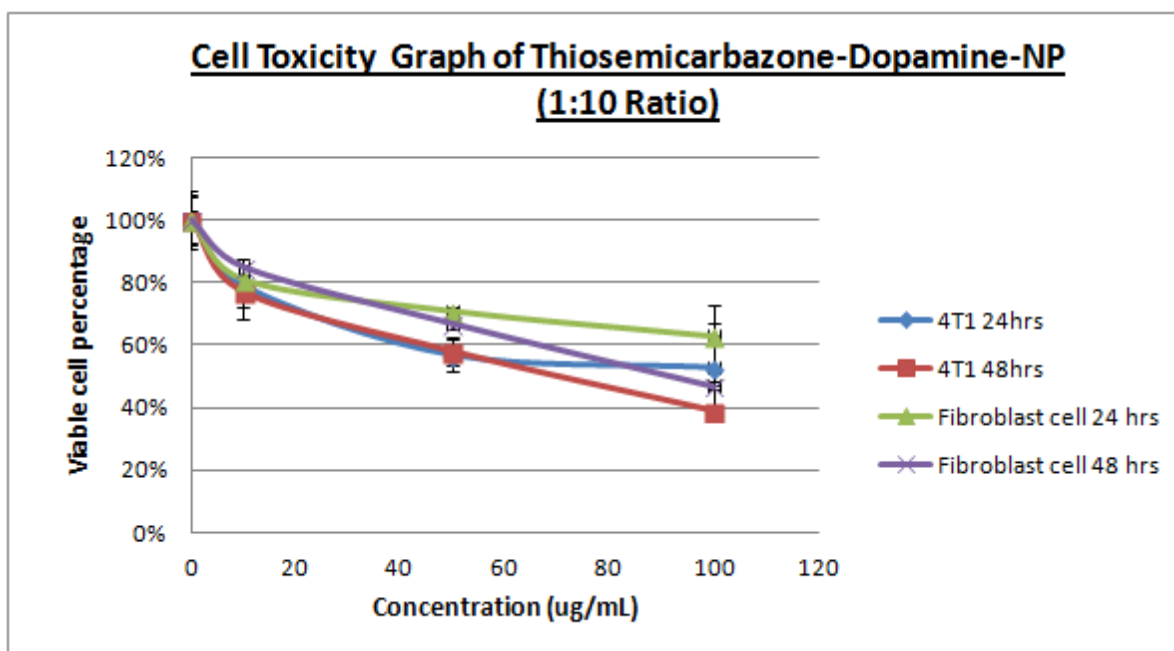**Figure B.10:-** UV graph of Peptide-Dopamine-NP-Dopamine-Thiosemicarbazone (1:5) reaction.
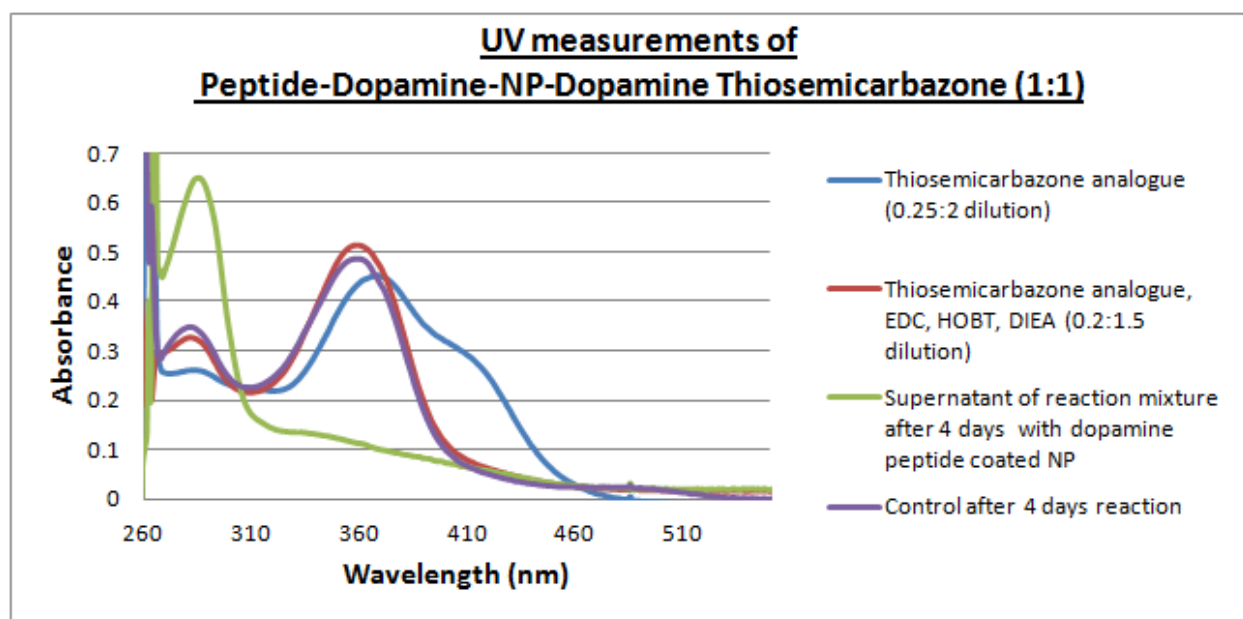
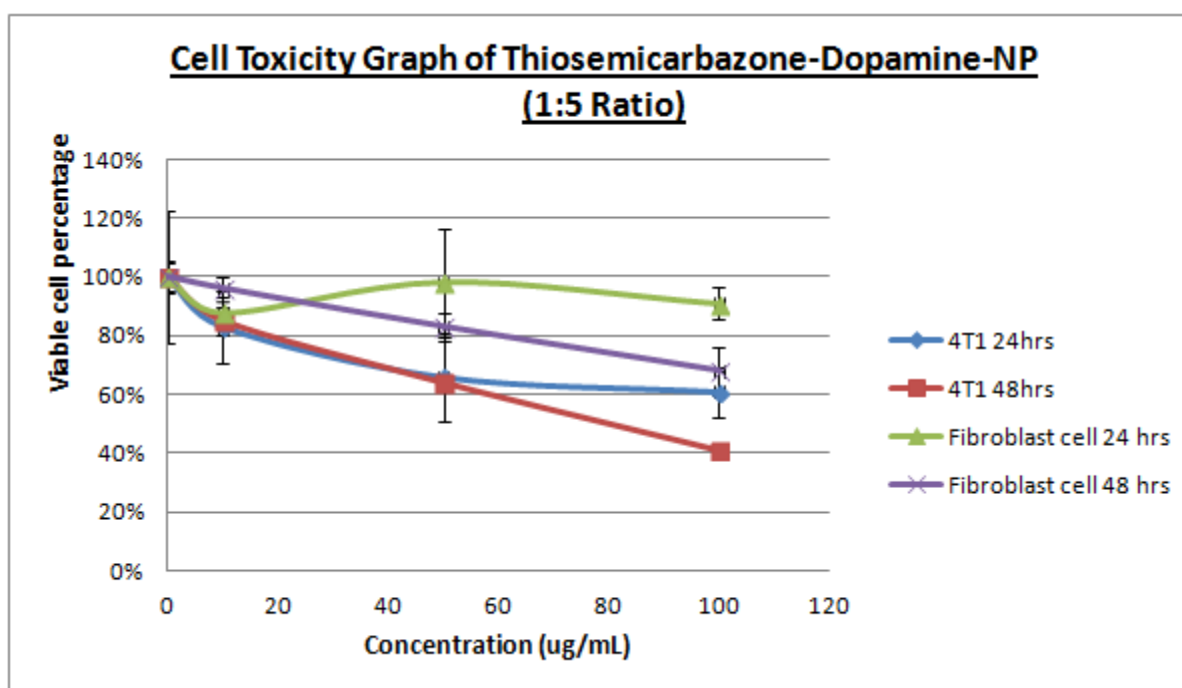**Figure B.11:-** UV graph of Peptide-Dopamine-NP-Dopamine-Thiosemicarbazone (1:1) reaction.
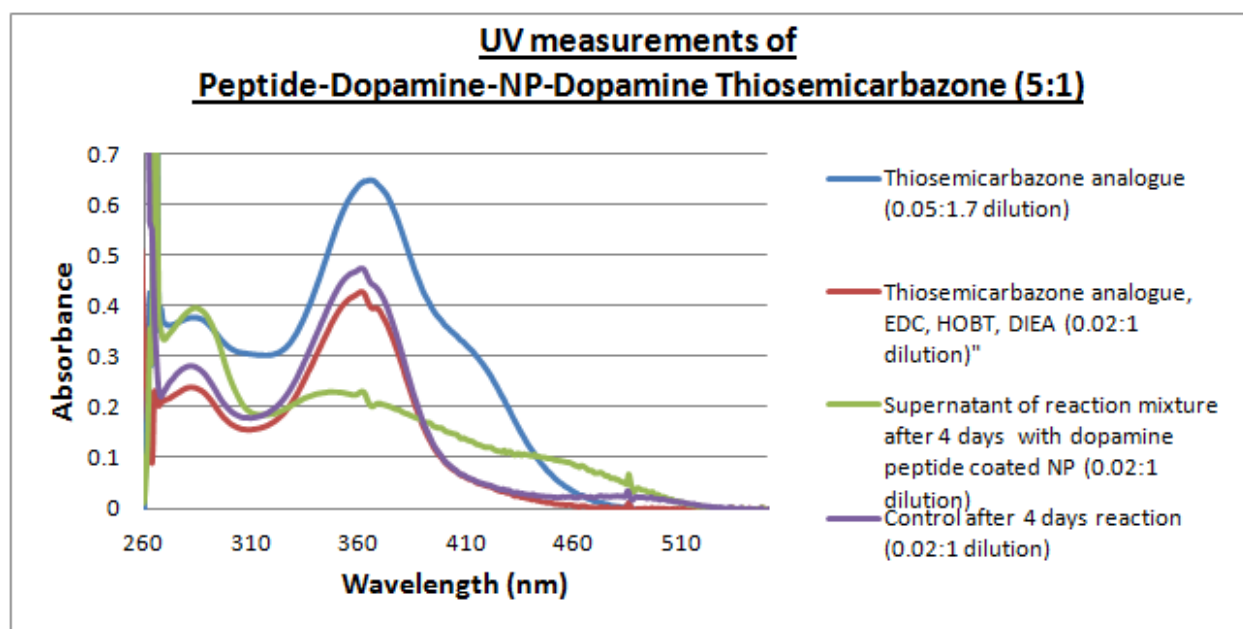
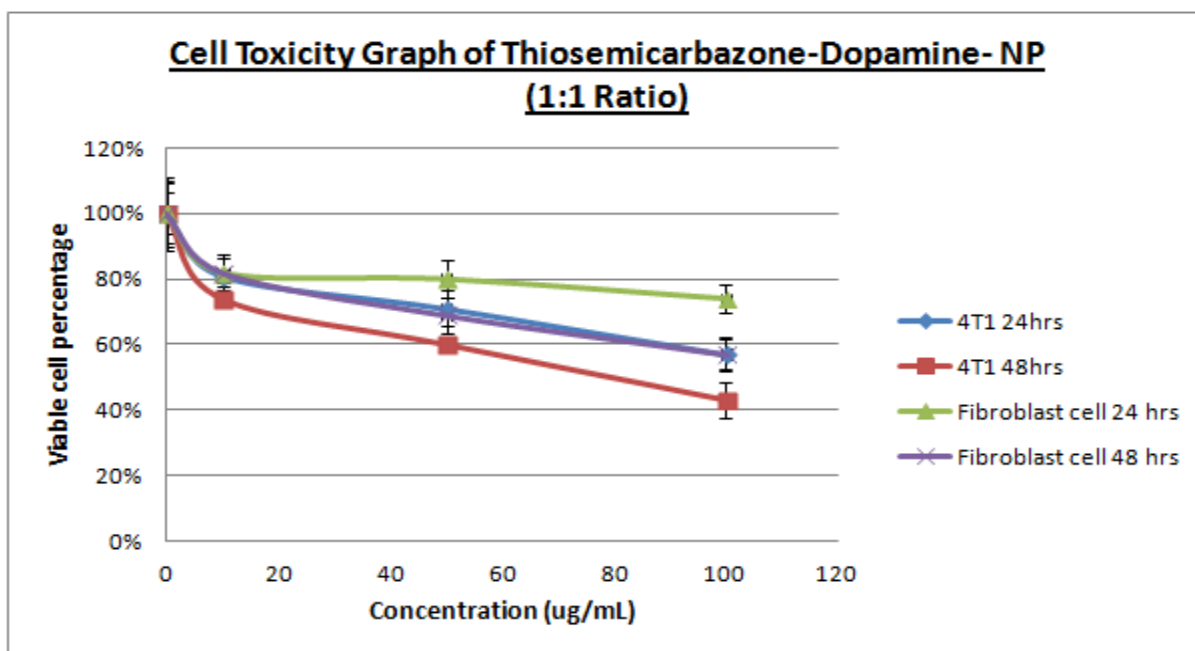**Figure B.12:-** UV graph of Peptide-Dopamine-NP-Dopamine-Thiosemicarbazone (5:1) reaction.
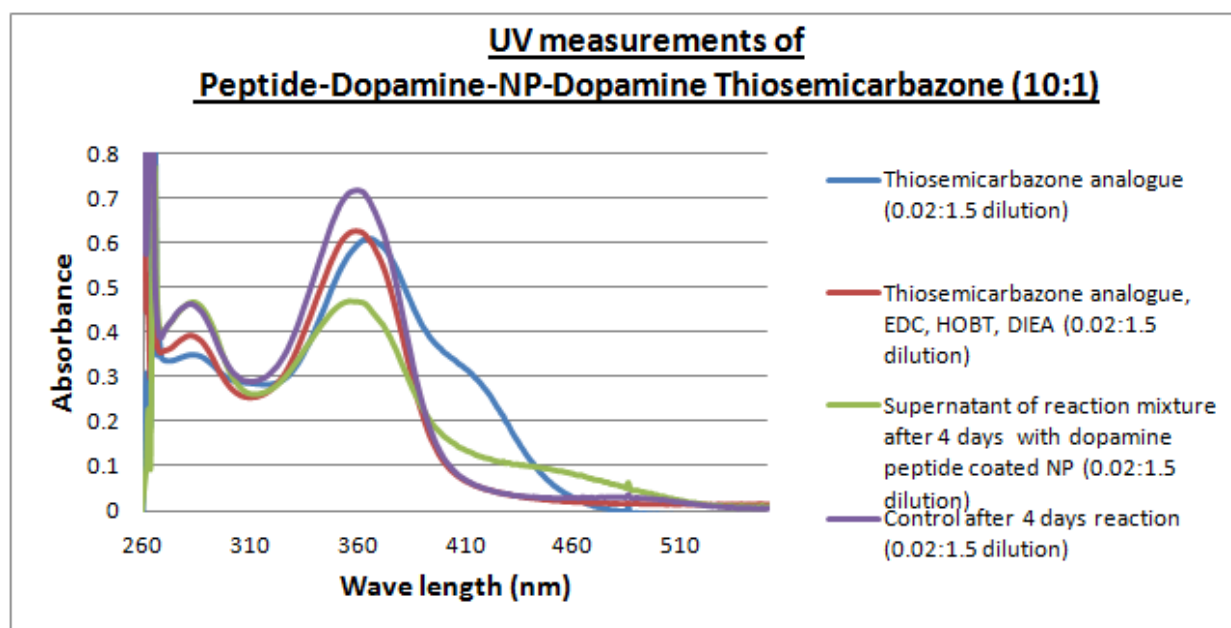
Figure B.13:- UV graph of Peptide-Dopamine-NP-Dopamine-Thiosemicarbazone (10:1) reaction.

blank2 (Combined)
Oct 7, 2013 11:48:23

Effective Diameter: 0.0 nm
Polydispersity: 0.000

Avg. Count Rate: 2.6 kcps
Baseline Index: 3.5/ 92.52%

Elapsed Time: 00:03:00

MSD

Intensity

100

75

50

25

0

5.0   5000.0

Diameter (nm)

Run	Eff. Diam. (nm)	Half Width (nm)	Polydispersity	Baseline Index
1	0.0	0.0	0.000	0.6/ 88.58%
2	0.0	0.0	0.000	9.7/ 95.52%
3	0.0	0.0	0.000	0.0/ 93.45%
Mean	0.0	0.0	0.000	3.4/ 92.52%
Std. Error	0.0	0.0	0.000	3.1/ 2.06
Combined	0.0	0.0		3.5/ 92.52%

Figure B.14:- DLS measurements of blank (distilled water).

DopNP (Combined)
Oct 7, 2013 11:55:36

Effective Diameter: **478.4 nm**
Polydispersity: **0.219**
Avg. Count Rate: **381.4 kcps**
Baseline Index: **6.4/ 97.48%**
Elapsed Time: **00:03:00**

Intensity / Diameter (nm) — MSD

Run	Eff. Diam. (nm)	Half Width (nm)	Polydispersity	Baseline Index
1	444.3	217.5	0.240	8.3/ 97.78%
2	495.0	232.4	0.220	9.8/100.00%
3	487.4	246.7	0.256	1.0/ 94.67%
Mean	475.6	232.2	0.239	6.3/ 97.48%
Std. Error	15.8	8.4	0.010	2.7/ 1.55
Combined	478.4	223.6	0.219	6.4/ 97.48%

Figure B.15:- DLS measurements of dopamine nanoparticle.
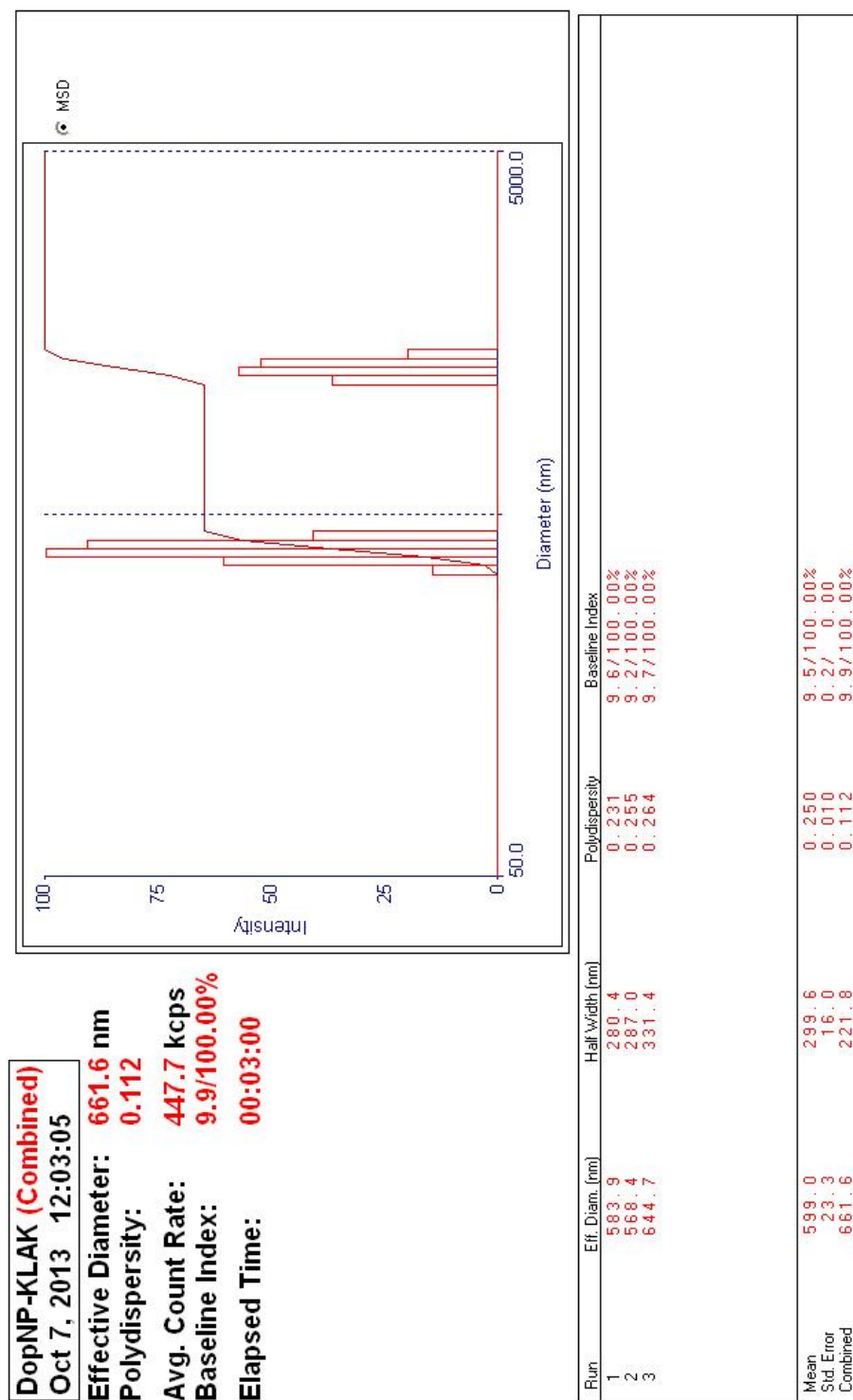
Figure B.16:-DLS measurements of Peptide-Dopamine-nanoparticle.

DopNP-KLAK(1-10) (Combined)
Oct 7, 2013   12:08:15

Effective Diameter: 459.3 nm
Polydispersity: 0.186

Avg. Count Rate: 436.5 kcps
Baseline Index: 7.2/ 98.97%

Elapsed Time: 00:03:00

Run	Eff. Diam. (nm)	Half Width (nm)	Polydispersity	Baseline Index
1	439.7	31.1	0.005	0.0/ 99.11%
2	551.0	203.2	0.136	7.1/ 97.79%
3	525.7	199.3	0.144	7.3/100.00%
Mean	505.5	144.6	0.095	4.8/ 98.97%
Std. Error	33.7	56.7	0.045	2.4/ 0.64%
Combined	459.3	198.0	0.186	7.2/ 98.97%

Intensity
100
75
50
25
0

50.0   Diameter (nm)   5000.0

MSD

Figure B.17:- DLS measurements of Peptide-Dopamine-NP-Dopamine-Thiosemicarbazone (1:10).

163
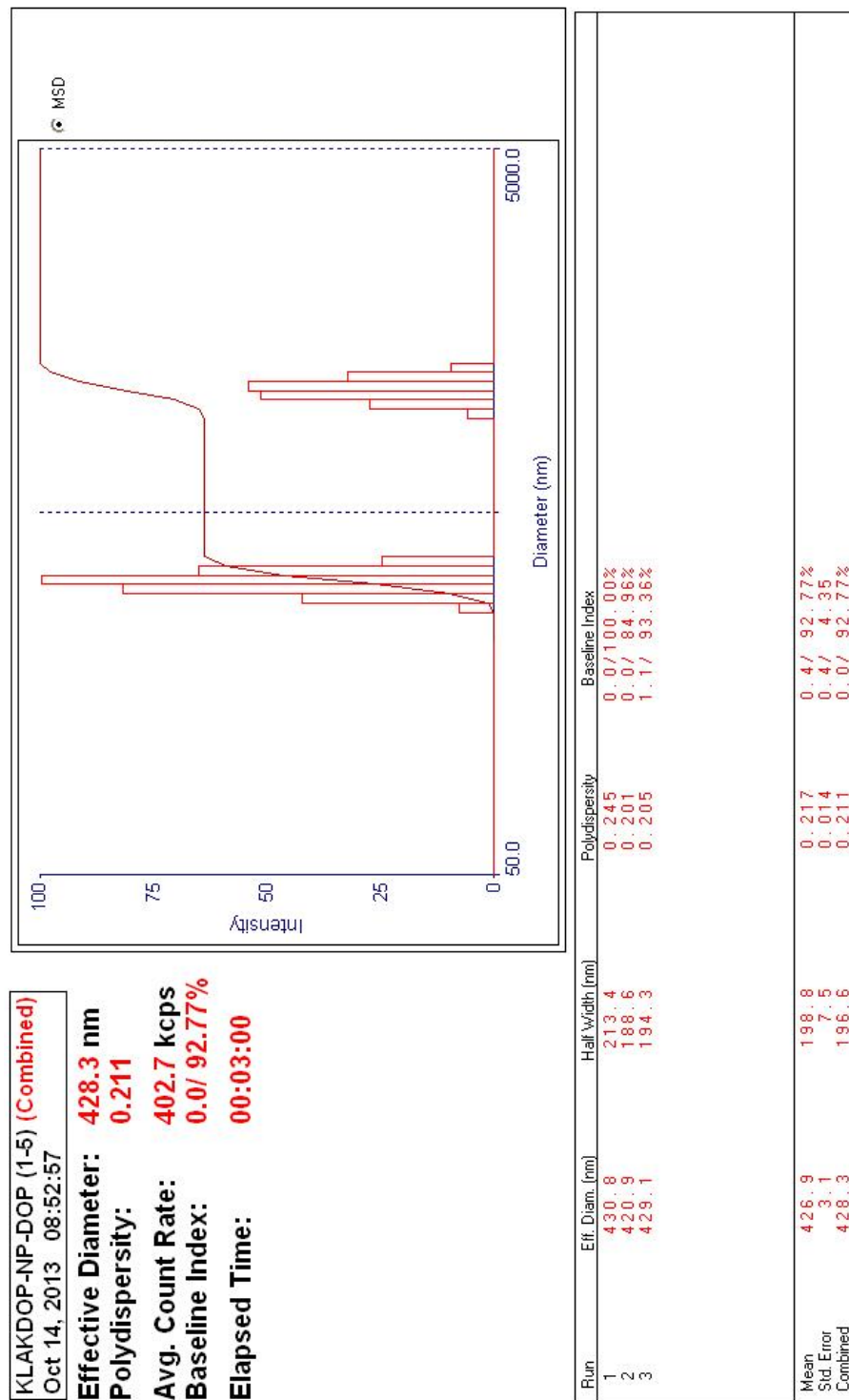
Figure B.18:- DLS measurements of Peptide-Dopamine-NP-Dopamine-Thiosemicarbazone (1:5).
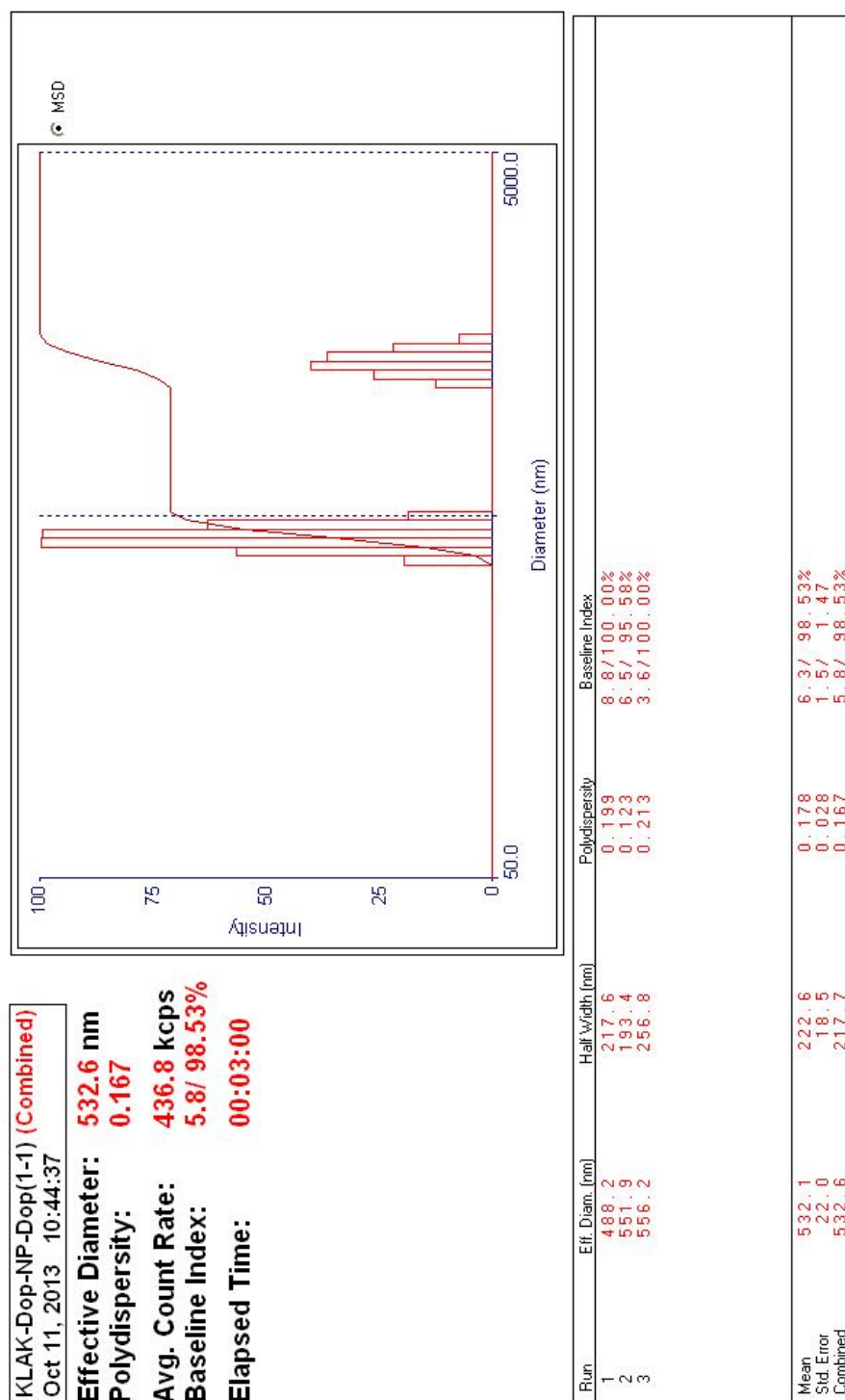
**Figure B.19:-** DLS measurements of Peptide-Dopamine-NP-Dopamine-Thiosemicarbazone (1:1).

DopNP-KLAK(5-1) (Combined)
Oct 7, 2013 12:30:50

Effective Diameter: 418.5 nm
Polydispersity: 0.181
Avg. Count Rate: 496.5 kcps
Baseline Index: 8.5/ 97.79%
Elapsed Time: 00:03:00

⊙ MSD

Diameter (nm)

Intensity
100   75   50   25   0
50.0 .... 5000.0

Run	Eff. Diam. (nm)	Half Width (nm)	Polydispersity	Baseline Index
1	385.5	154.4	0.160	9.6/100.00%
2	422.3	187.9	0.198	8.1/ 97.79%
3	461.0	186.0	0.163	8.1/ 95.58%
Mean	422.9	176.1	0.174	8.6/ 97.79%
Std. Error	21.8	10.9	0.012	0.5/ 1.28
Combined	418.5	178.2	0.181	8.5/ 97.79%

Figure B.20:- DLS measurements of Peptide-Dopamine-NP-Dopamine-Thiosemicarbazone (5:1).
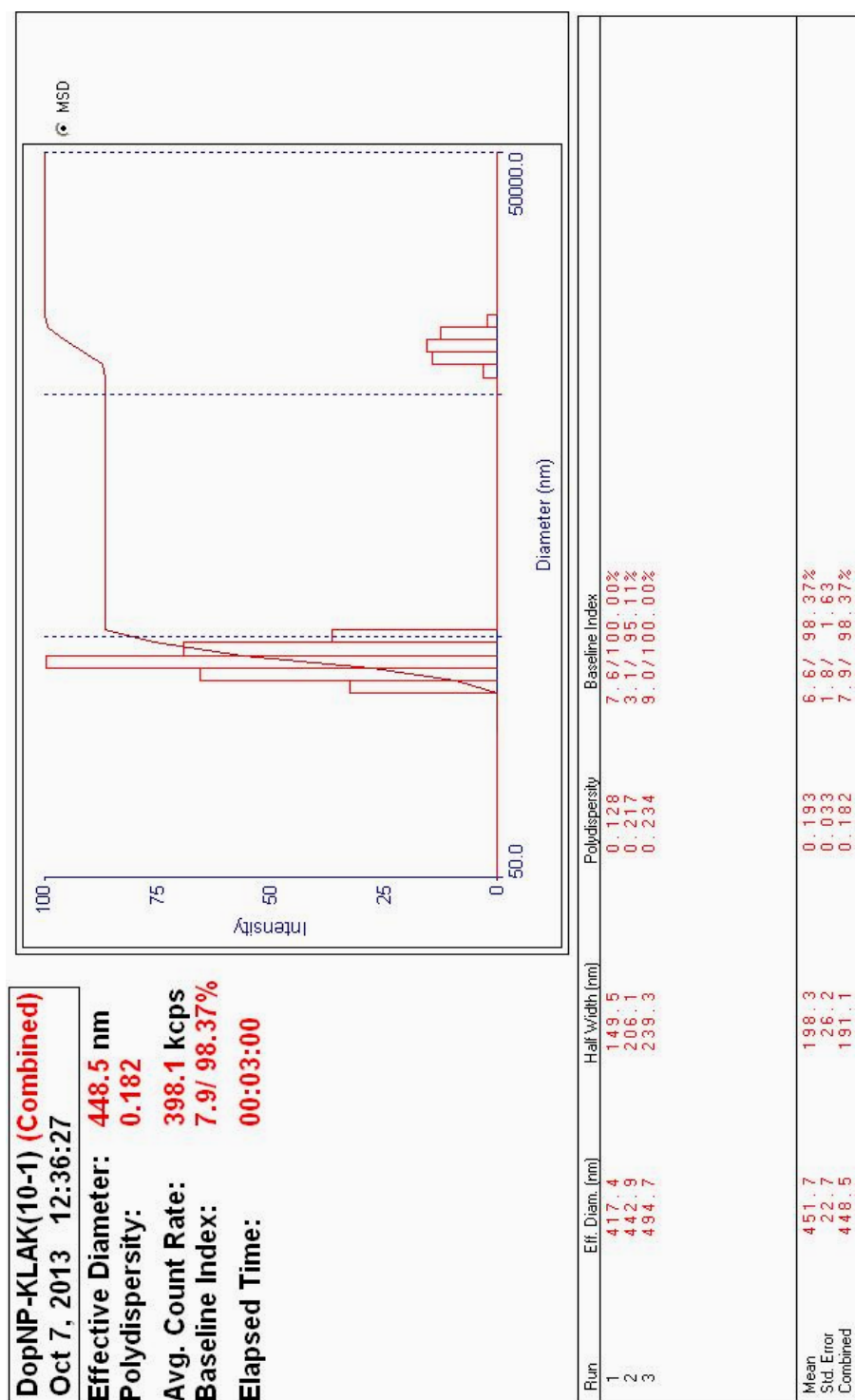
Figure B.21:- DLS measurements of Peptide-Dopamine-NP-Dopamine-Thiosemicarbazone (10:1).
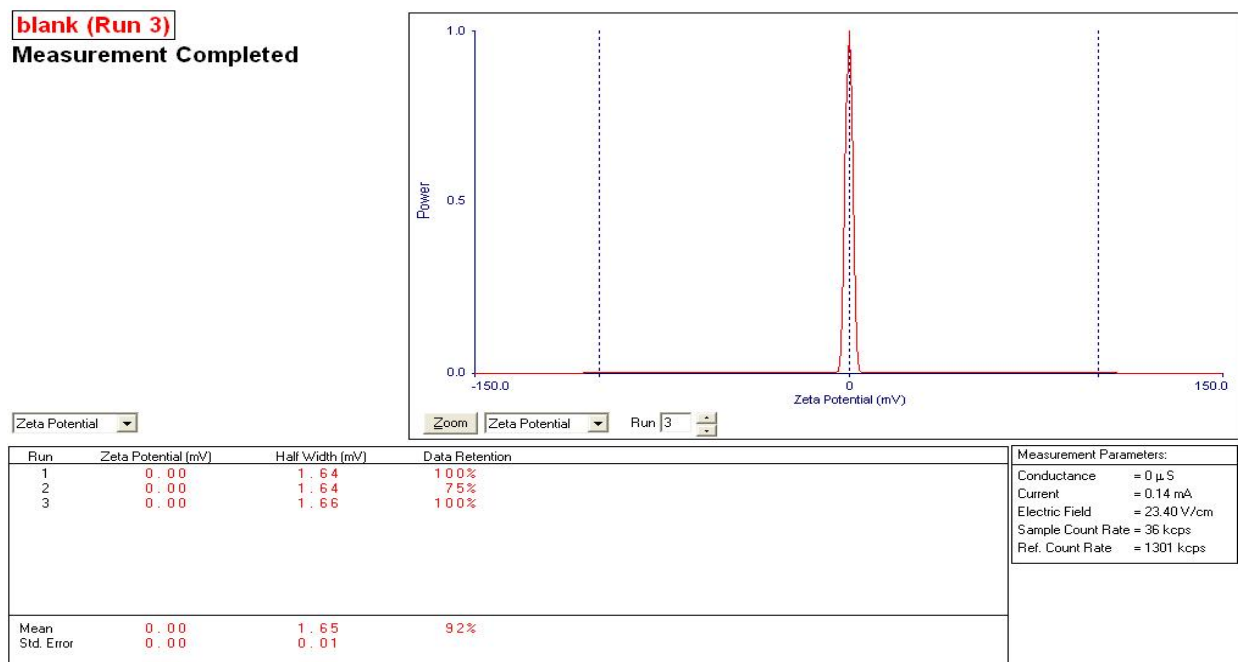
Figure B.22:- Zeta potential of Blank (distilled water).
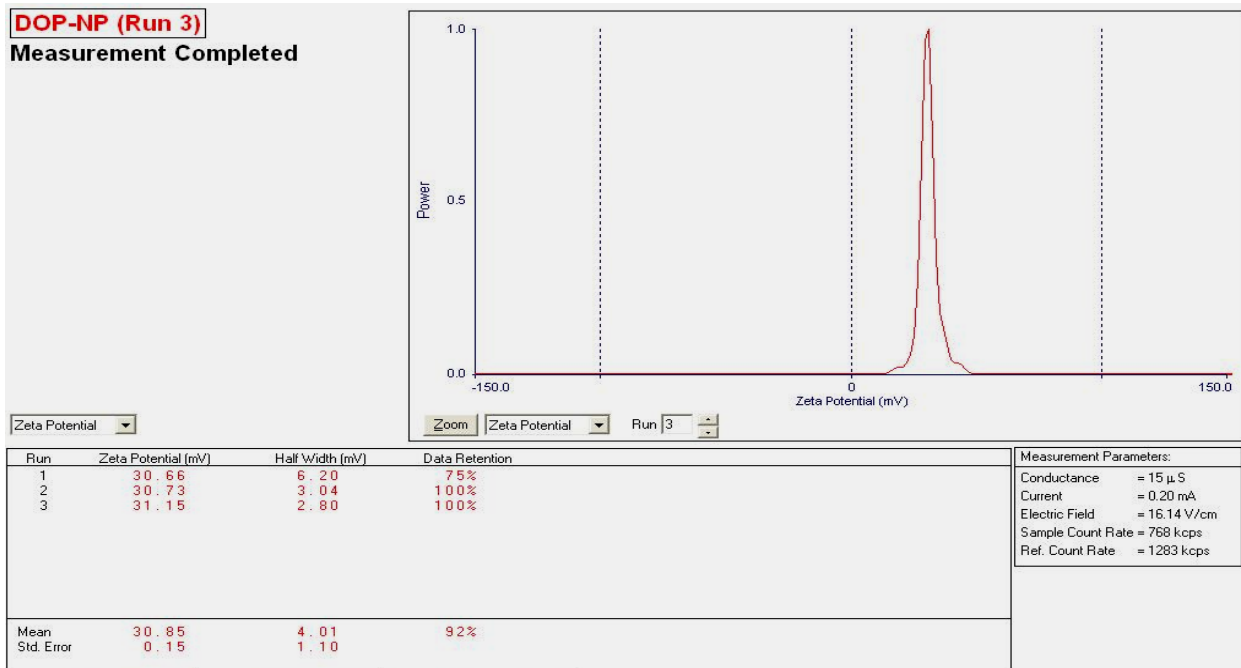
Figure B.23:- Zeta potential of dopamine coated nanoparticle.
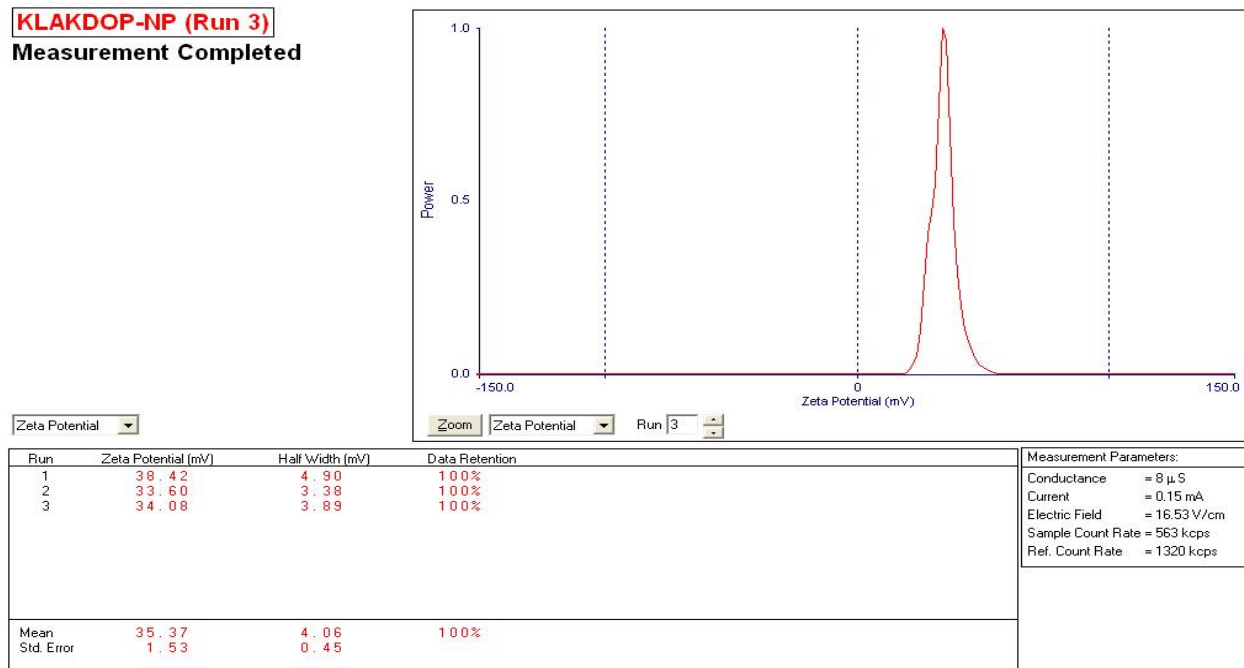
Figure B.24:- Zeta potential of Peptide-Dopamine- nanoparticle.
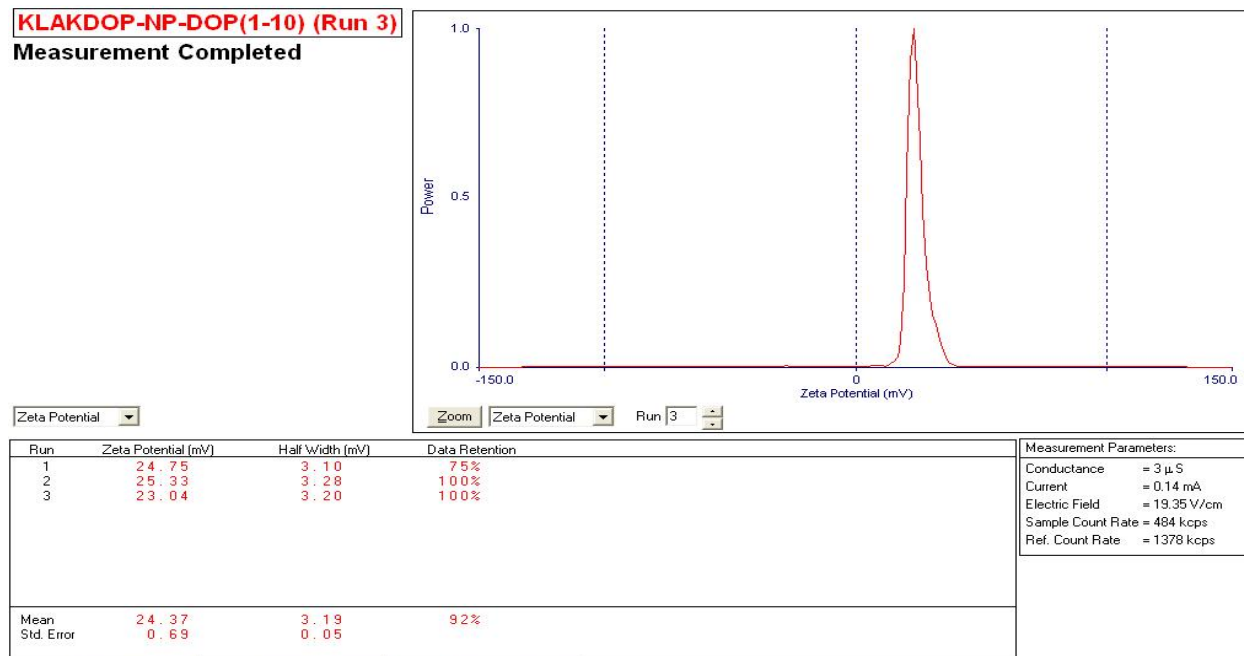
Figure B.25:- Zeta potential of Peptide-Dopamine-NP-Dopamine-Thiosemicarbazone (1:10).
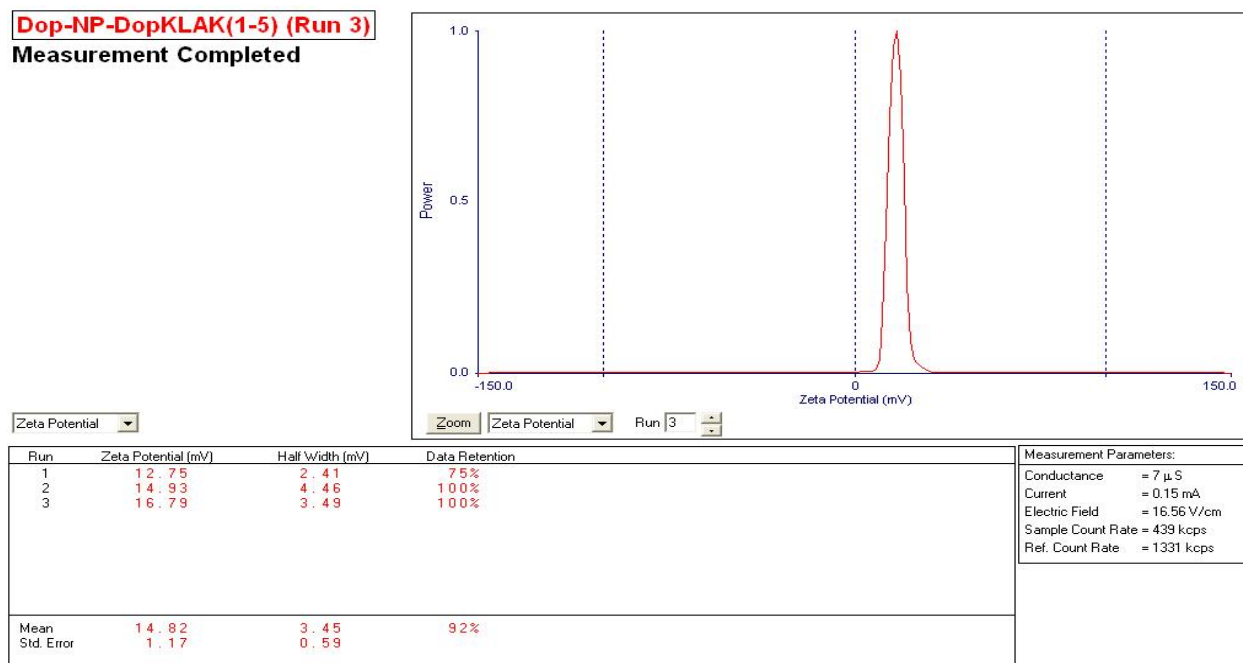
Figure B.26:- Zeta potential of Peptide-Dopamine-NP-Dopamine-Thiosemicarbazone (1:5).
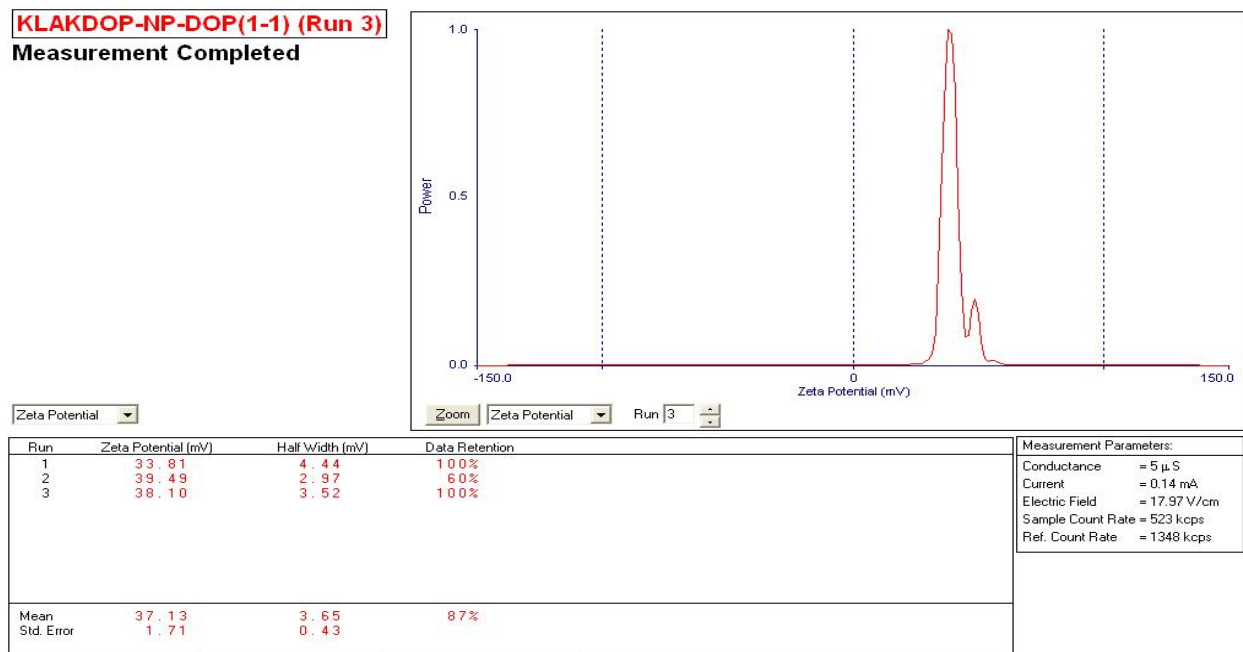
Figure B.27:- Zeta potential of Peptide-Dopamine-NP-Dopamine-Thiosemicarbazone (1:1).

KLAKDOP-NP-DOP(5-1) (Run 3)
Measurement Completed

Run	Zeta Potential (mV)	Half Width (mV)	Data Retention
1	33.65	3.29	100%
2	37.02	2.79	75%
3	45.45	4.55	100%
Mean	38.70	3.54	92%
Std. Error	3.51	0.52	

Measurement Parameters:
Conductance = 9 μS
Current = 0.16 mA
Electric Field = 15.82 V/cm
Sample Count Rate = 525 kcps
Ref. Count Rate = 1311 kcps
Uncorrected Temp. = 28.5 °C
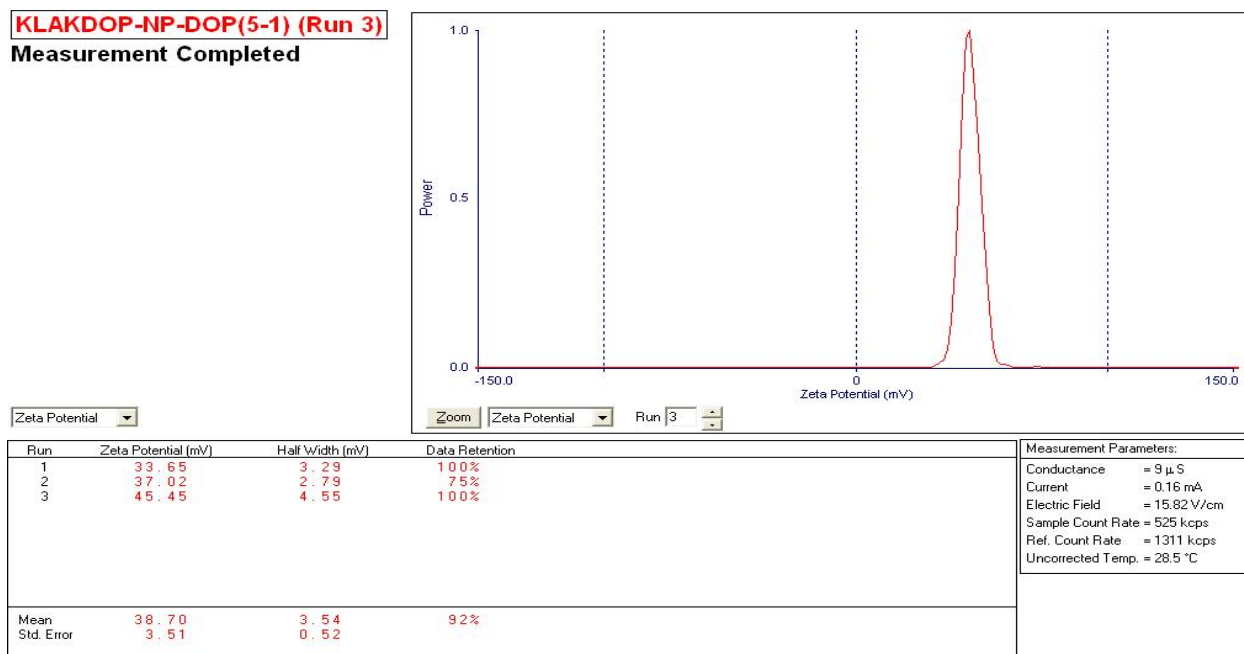
Figure B.28:- Zeta potential of Peptide-Dopamine-NP-Dopamine-Thiosemicarbazone (5:1).

KLAKDOP-NP-DOP(10-1) (Run 3)
Measurement Completed

Run	Zeta Potential (mV)	Half Width (mV)	Data Retention
1	30.09	3.51	100%
2	27.72	5.39	75%
3	38.42	4.23	75%
Mean	32.08	4.38	83%
Std. Error	3.25	0.55	

Measurement Parameters:
Conductance = 3 μS
Current = 0.14 mA
Electric Field = 19.17 V/cm
Sample Count Rate = 397 kcps
Ref. Count Rate = 1292 kcps
Uncorrected Temp. = 28.5 °C
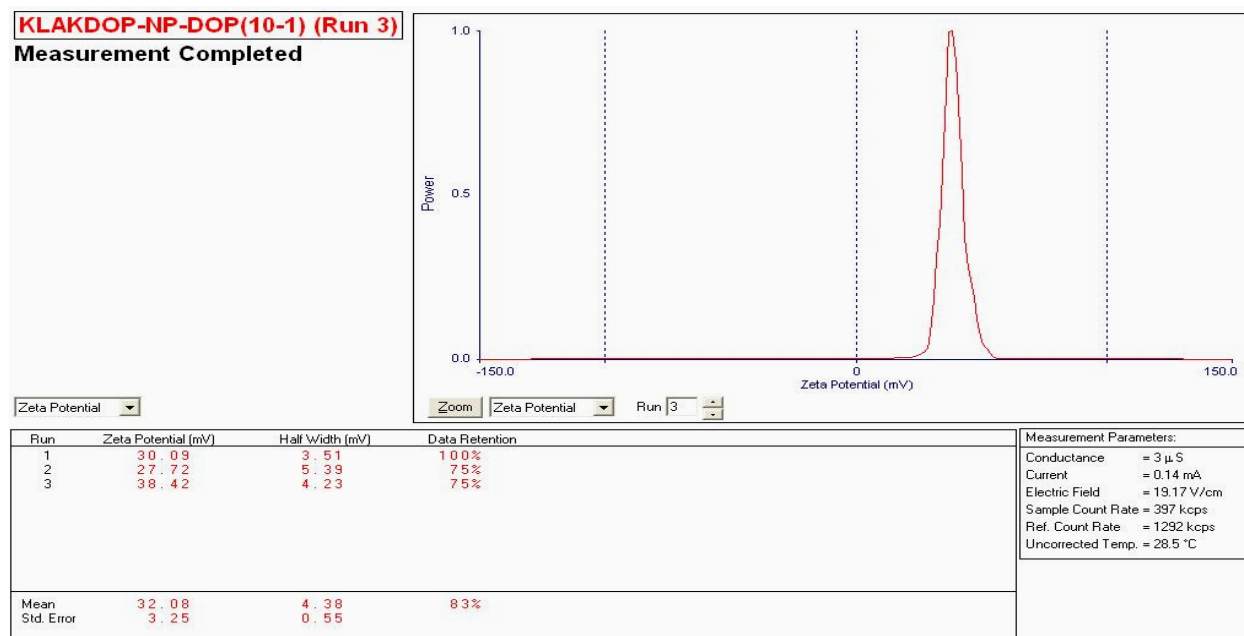
Figure B.29:- Zeta potential of Peptide-Dopamine-NP-Dopamine-Thiosemicarbazone (10:1).
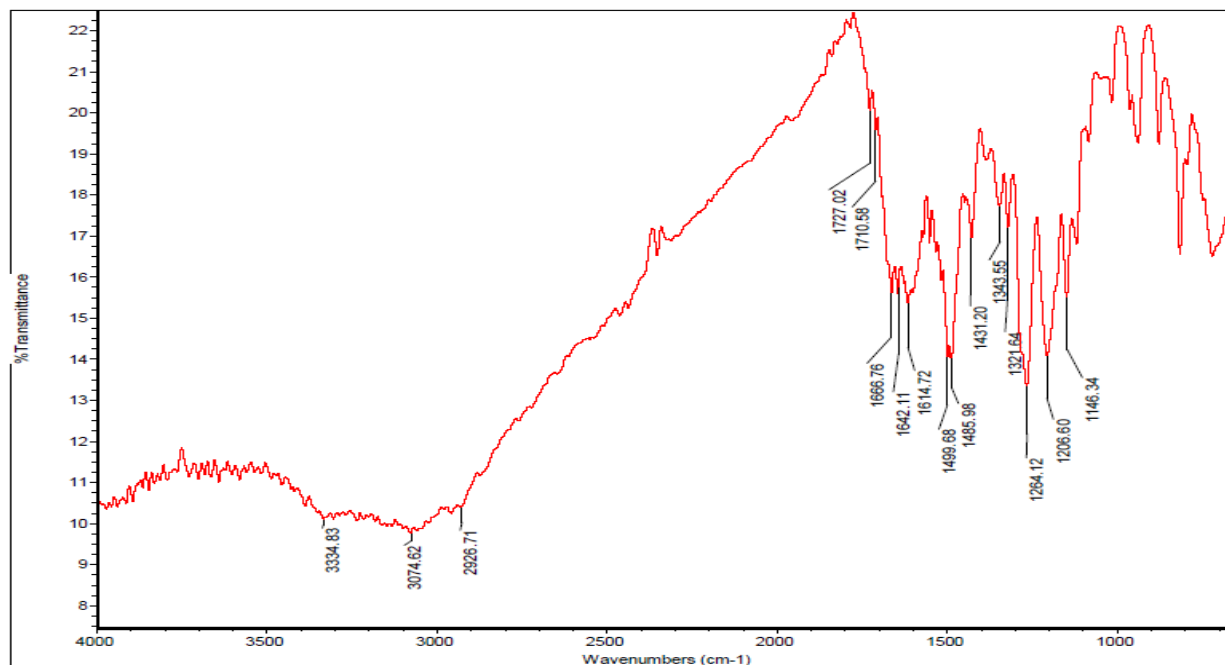
Figure B.30:- FTIR of Peptide-Dopamine-NP.
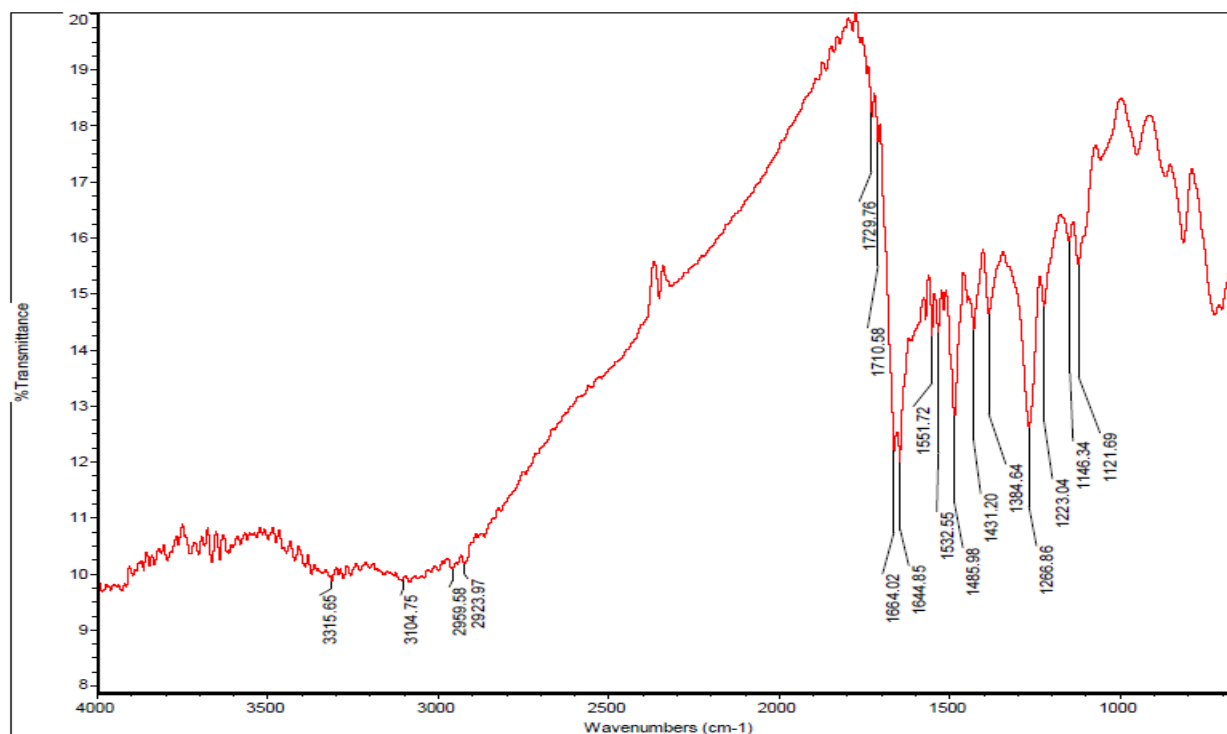
Figure B.31:- FTIR for Peptide-Dopamine-NP-Dopamine-Thiosemicarbazone (1:10).
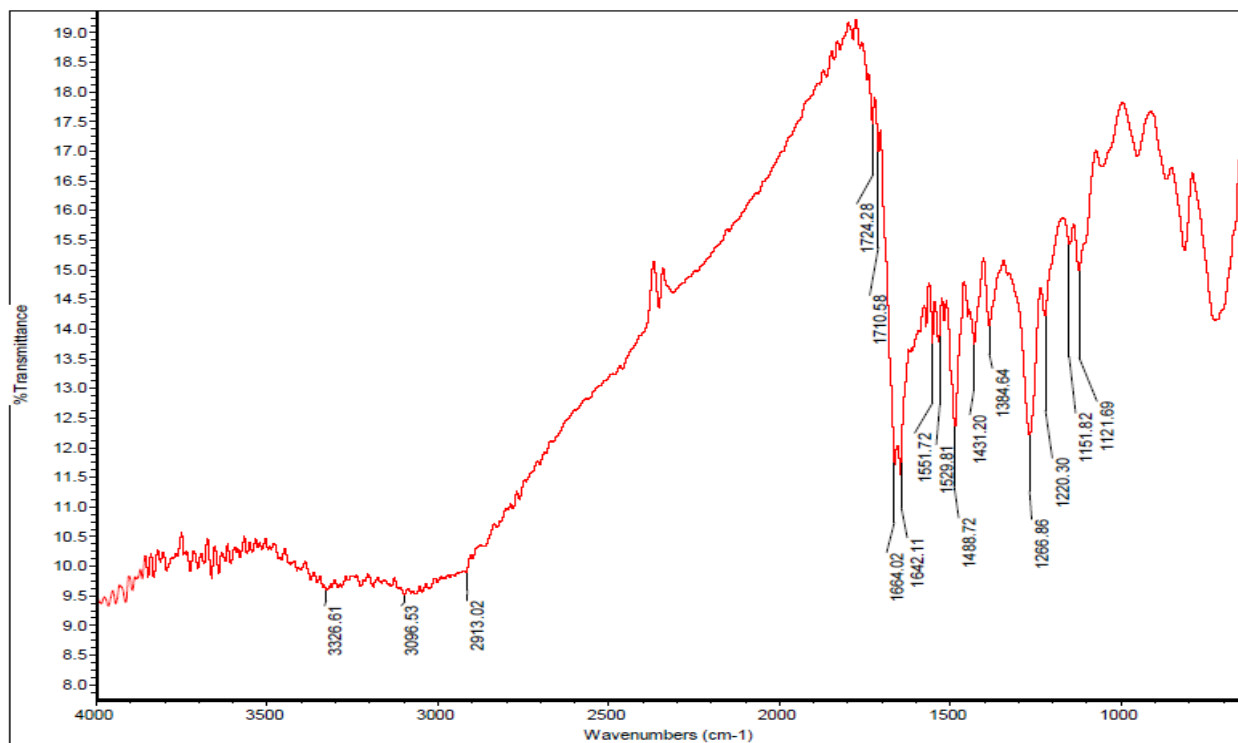
Figure B.32:- FTIR for Peptide-Dopamine-NP-Dopamine-Thiosemicarbazone 1:5.
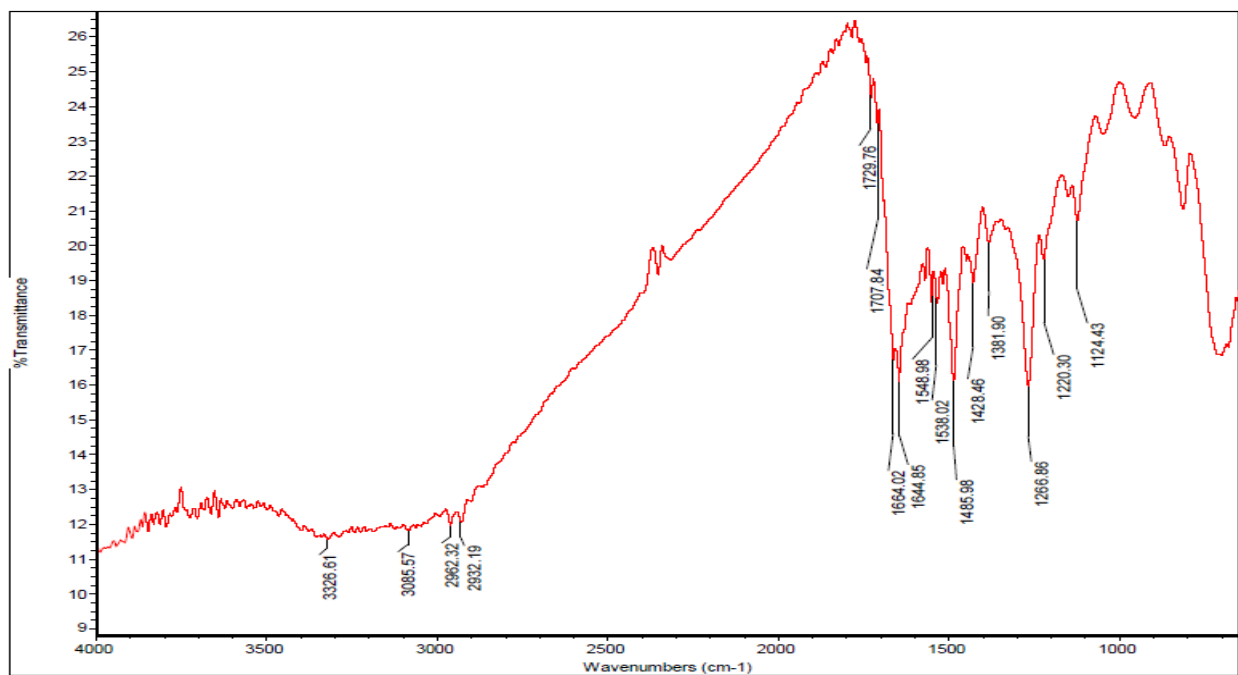
Figure B.33:- FTIR for Peptide-Dopamine-NP-Dopamine-Thiosemicarbazone 1:1.
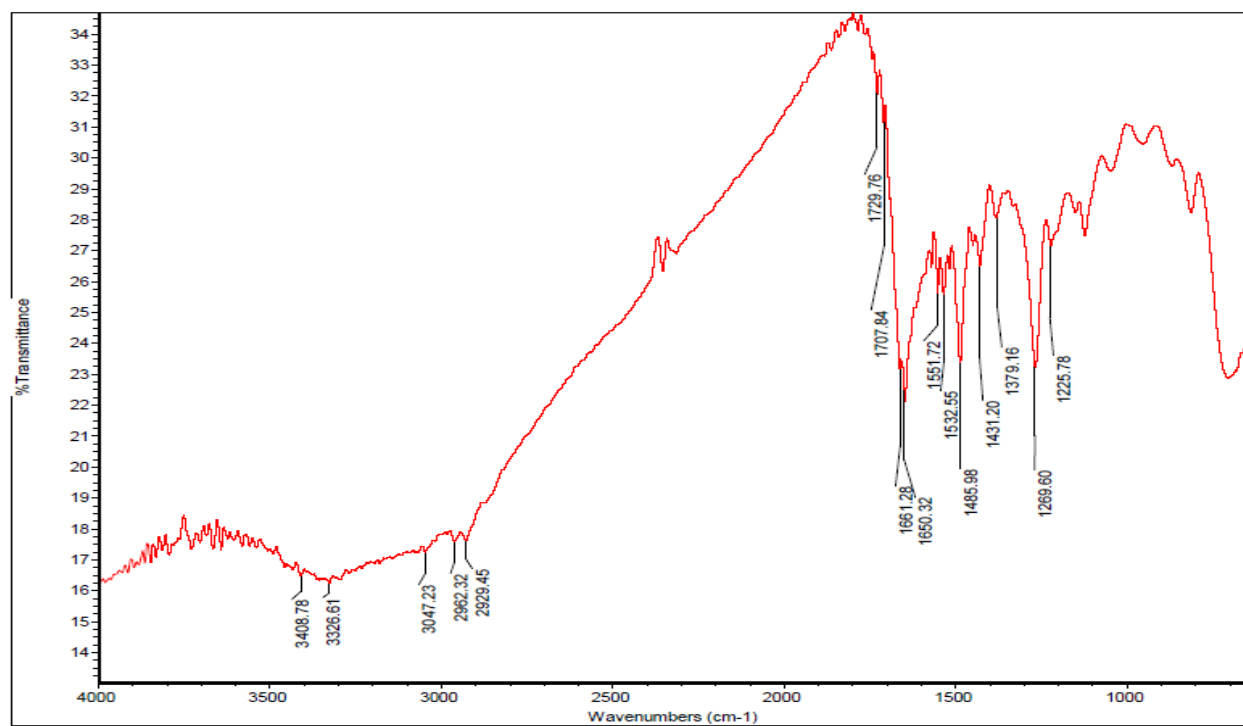
Figure B.34:- FTIR for Peptide-Dopamine-NP-Dopamine-Thiosemicarbazone 5:1.
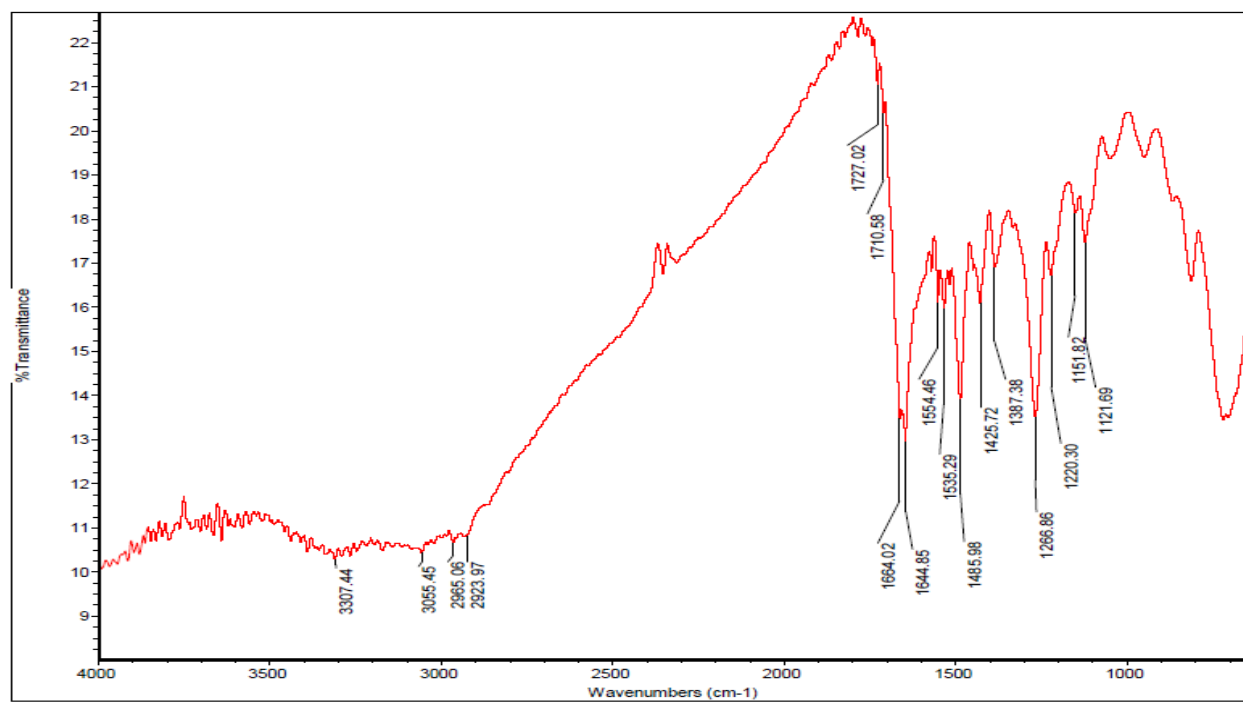
Figure B.35:- FTIR for Peptide-Dopamine-NP-Dopamine-Thiosemicarbazone 10:1.
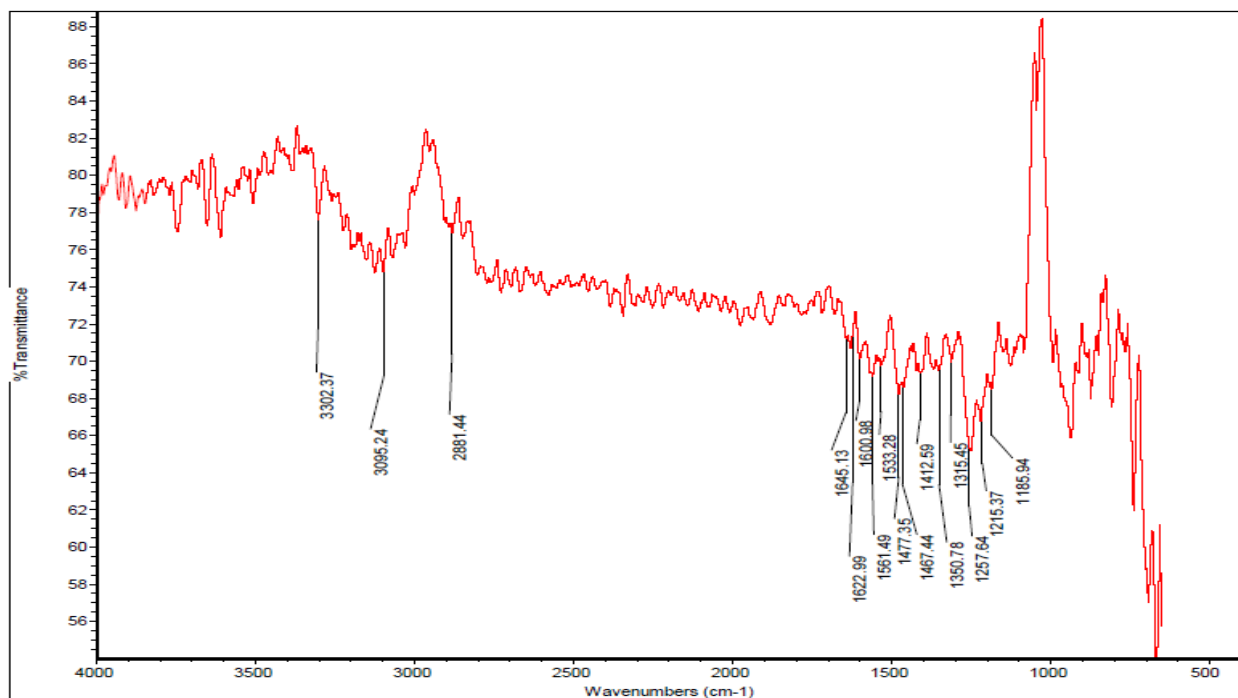
Figure B.36:- FTIR of Thiosemicarbazone-Dopamine-NP (1:10).
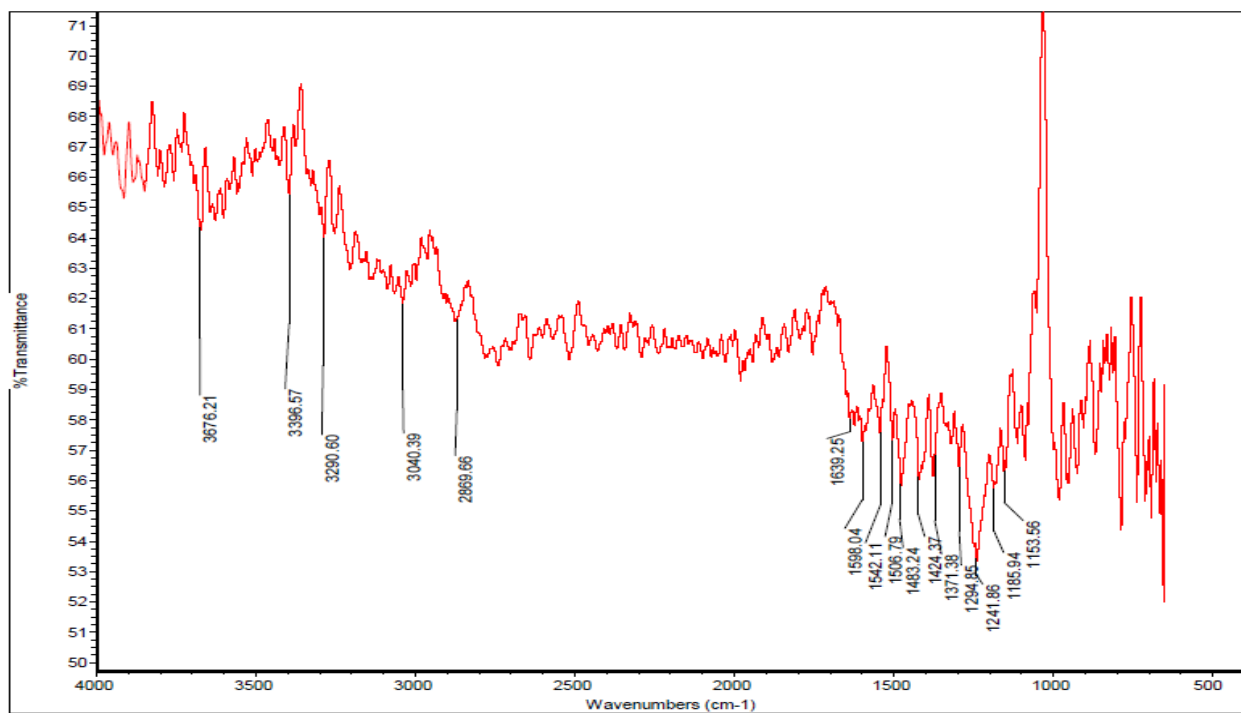
Figure B.37:- FTIR of Thiosemicarbazone-Dopamine-NP (1:5).
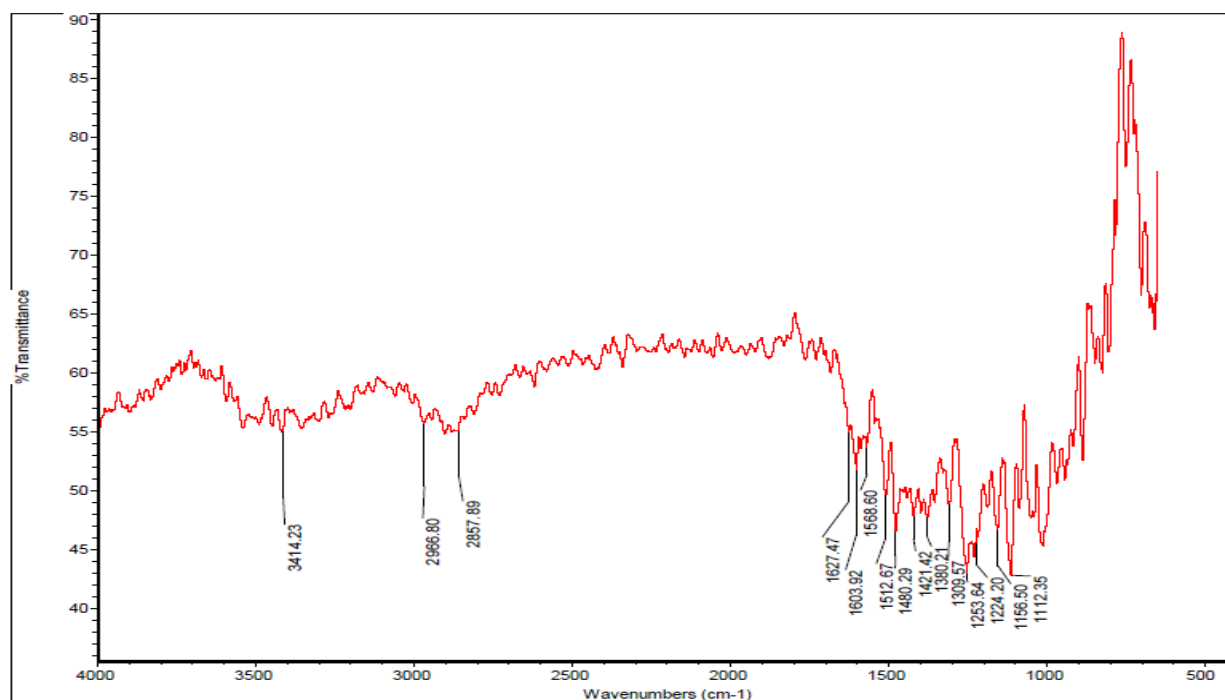
Figure B.38:- FTIR of Thiosemicarbazone-Dopamine-NP (1:1).
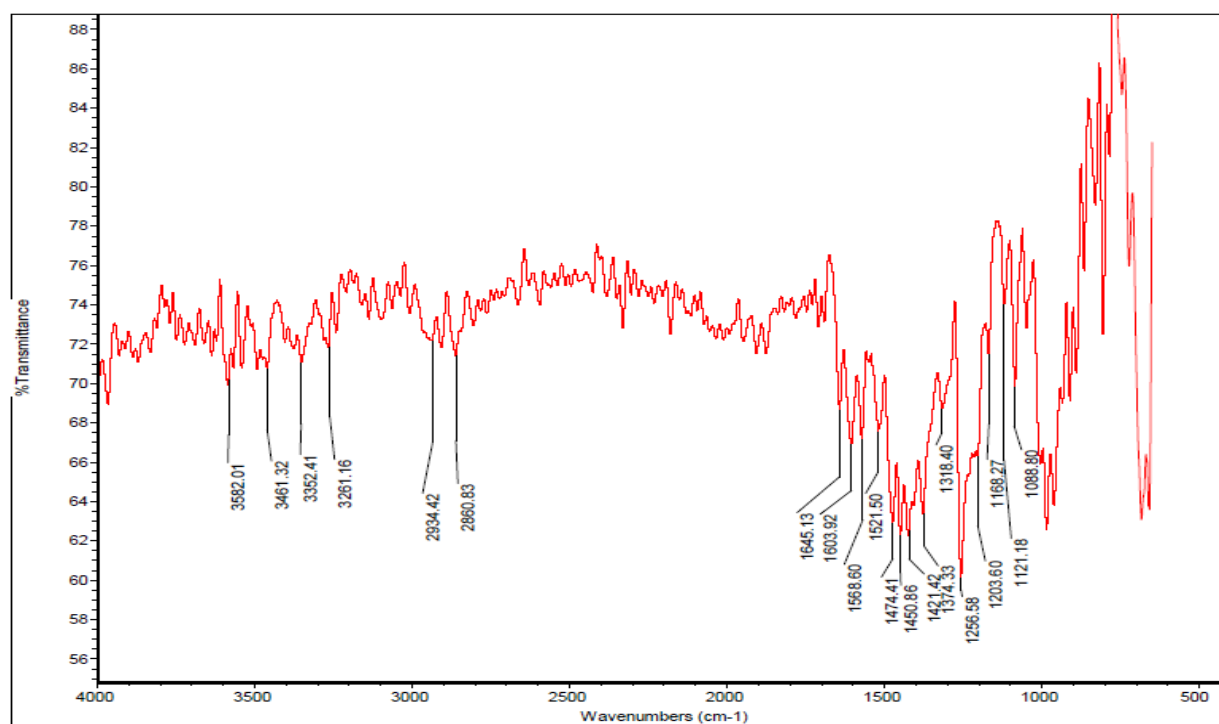
Figure B.39:- FTIR of Thiosemicarbazone-Dopamine-NP (5:1).
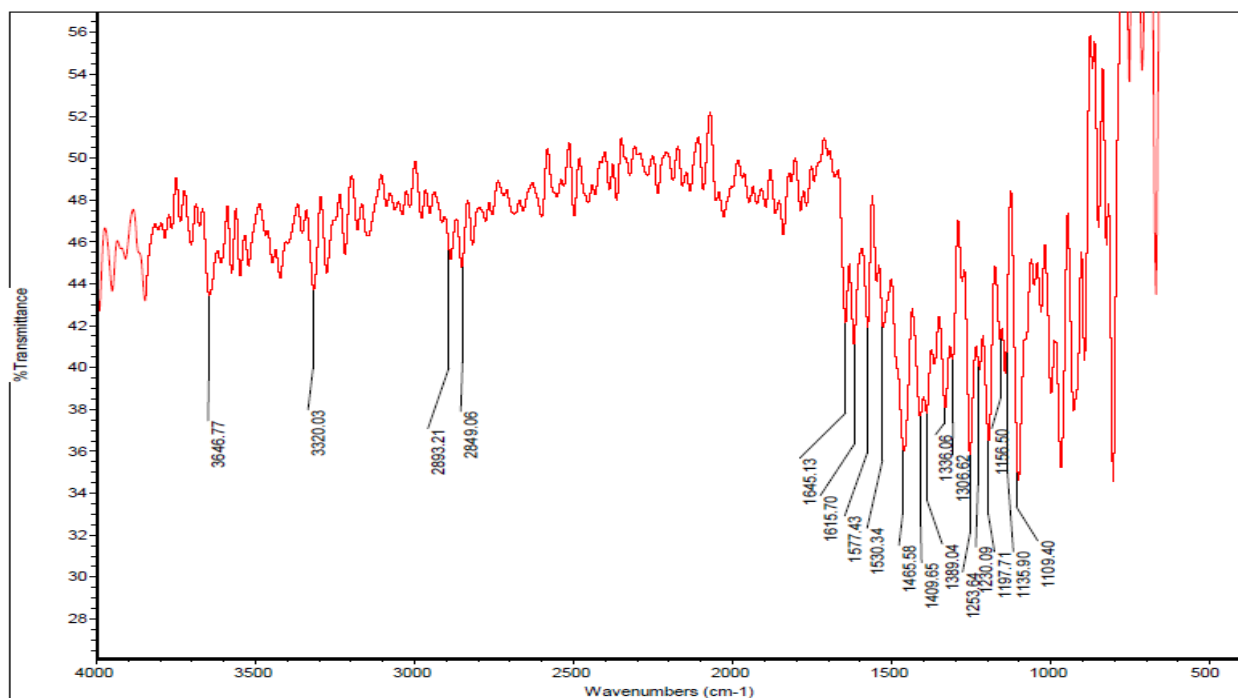
Figure B.40:- FTIR of Thiosemicarbazone-Dopamine-NP (10:1).
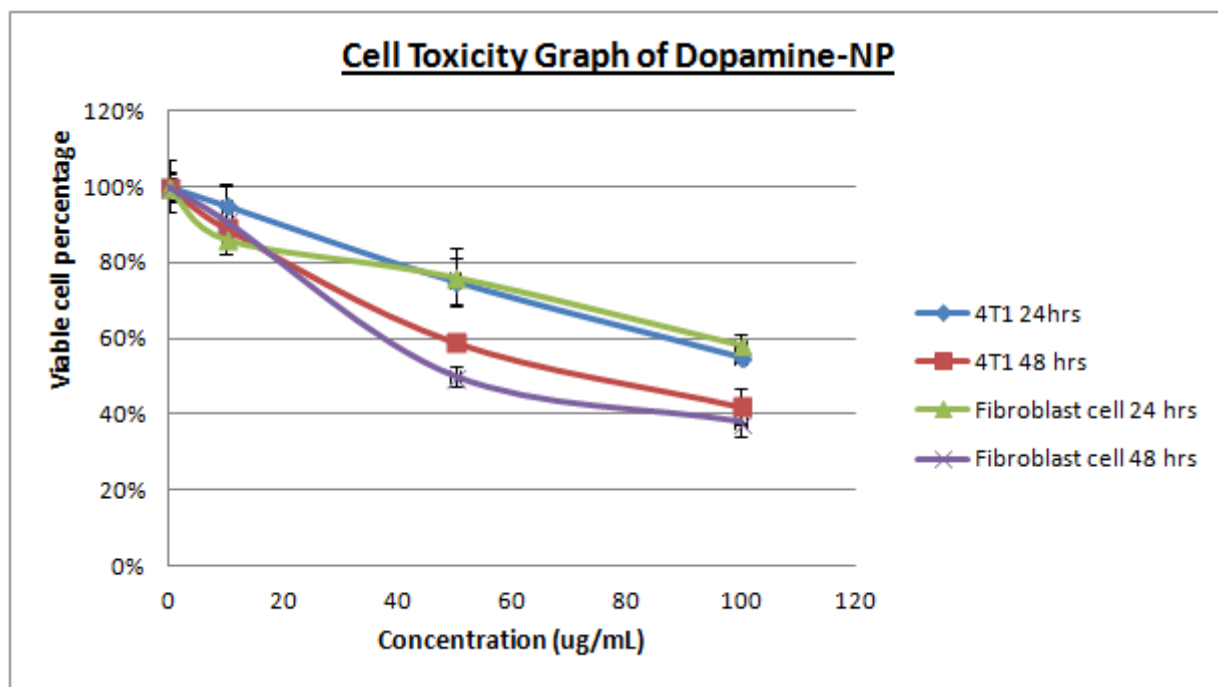
Figure B.41:- Cell toxicity graph of dopamine coated nanoparticle.

177
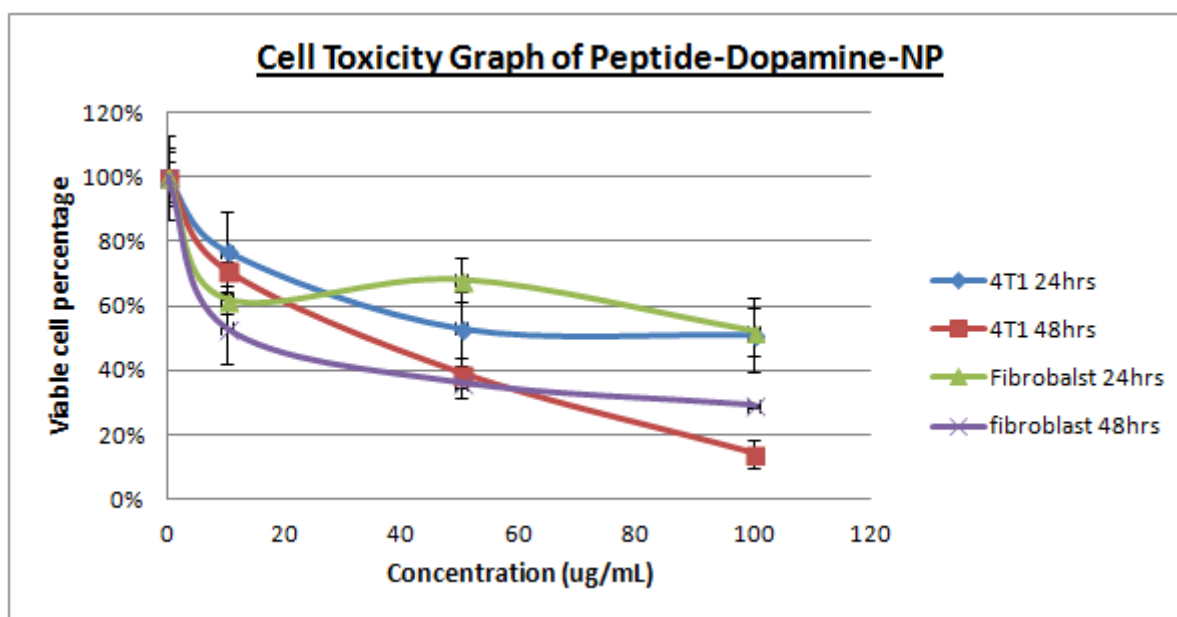
Figure B.42:- Cell toxicity graph of Peptide-Dopamine- nanoparticle.
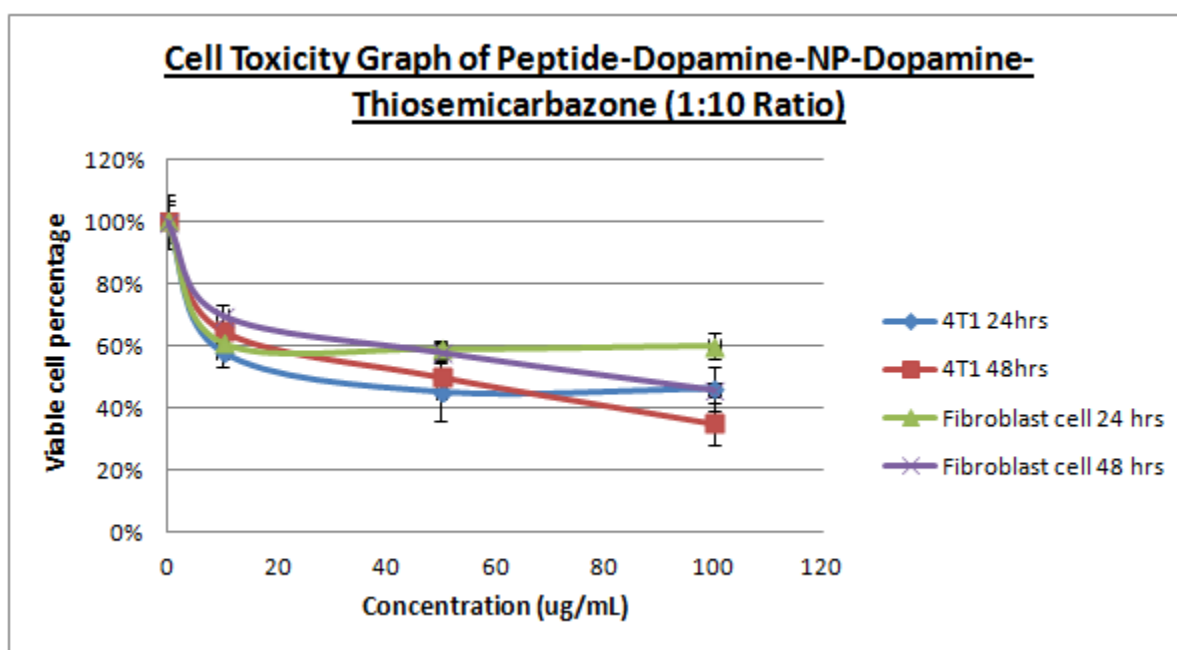
Figure B.43:- Cell toxicity graph of Peptide-Dopamine-NP-Dopamine-Thiosemicarbazone (1:10).

178
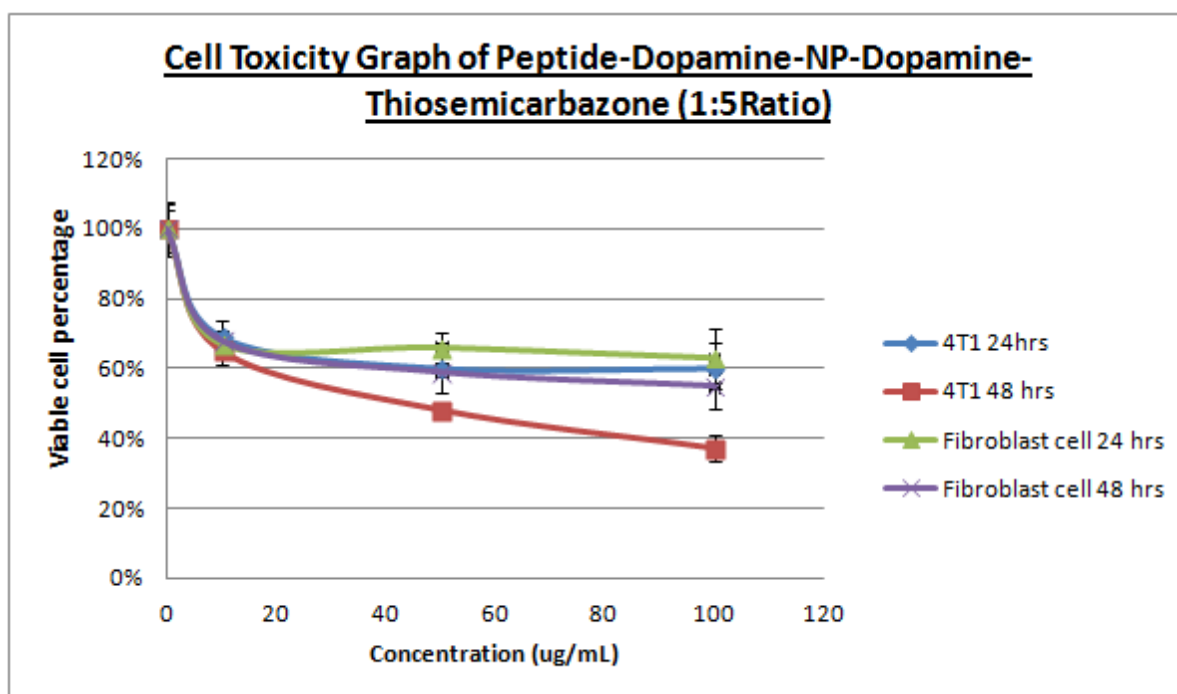
Figure B.44:- Cell toxicity graph of Peptide-Dopamine-NP-Dopamine-Thiosemicarbazone (1:5).
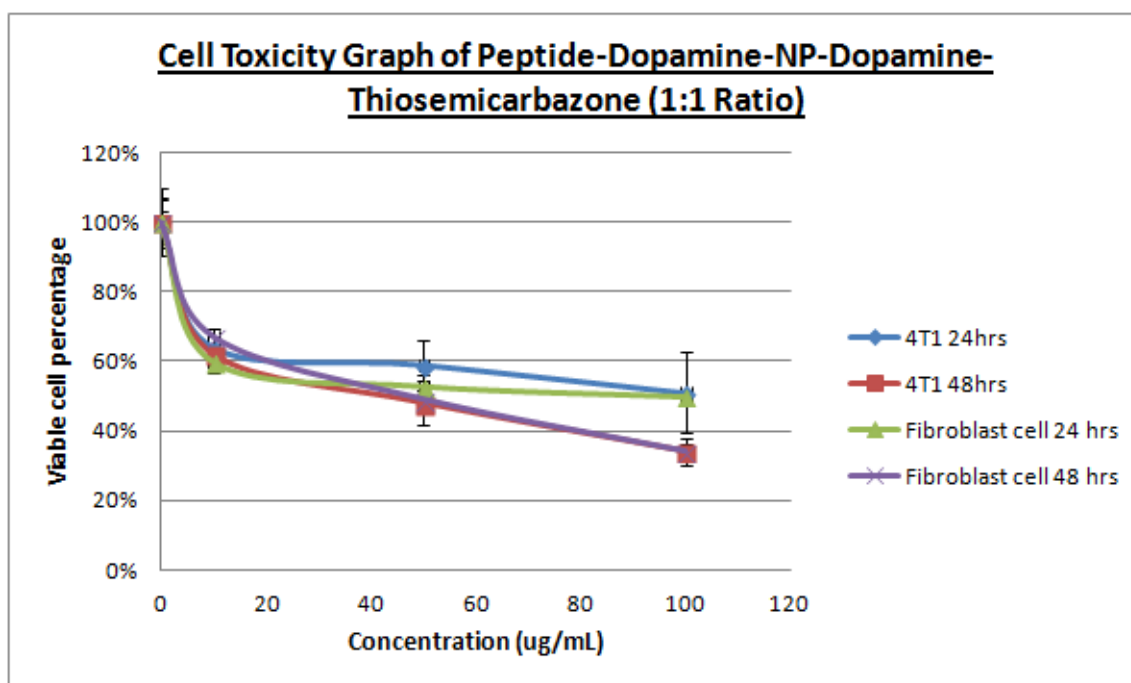
Figure B.45:- Cell toxicity graph of Peptide-Dopamine-NP-Dopamine-Thiosemicarbazone (1:1).
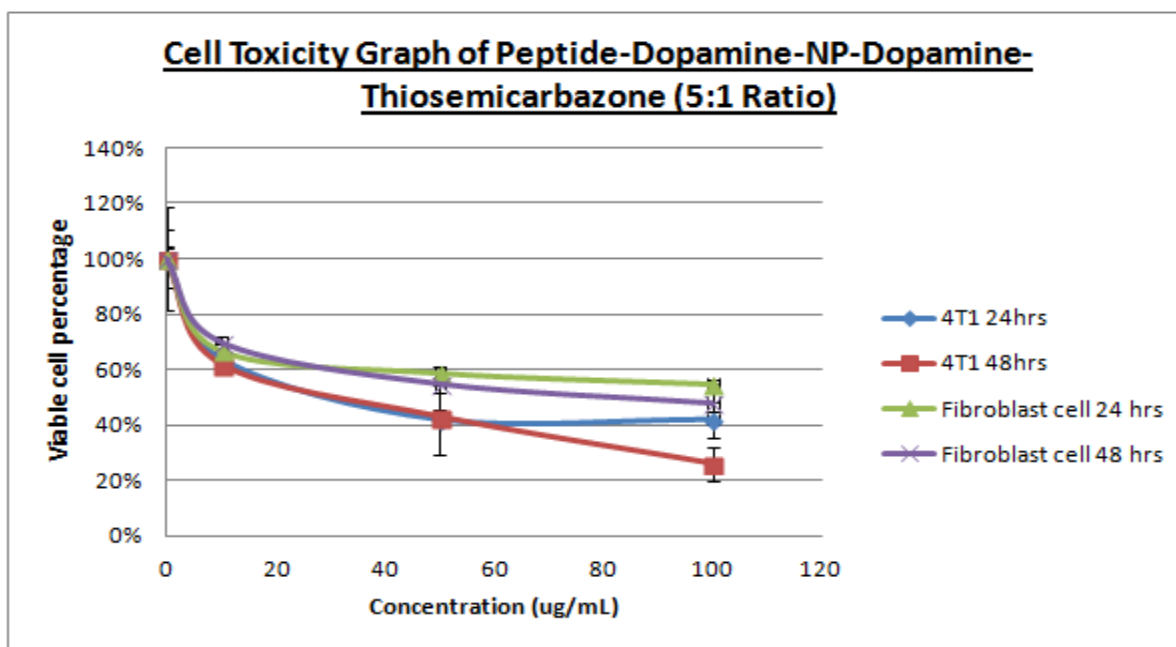
Figure B.46:- Cell toxicity graph of Peptide-Dopamine-NP-Dopamine-Thiosemicarbazone (5:1).
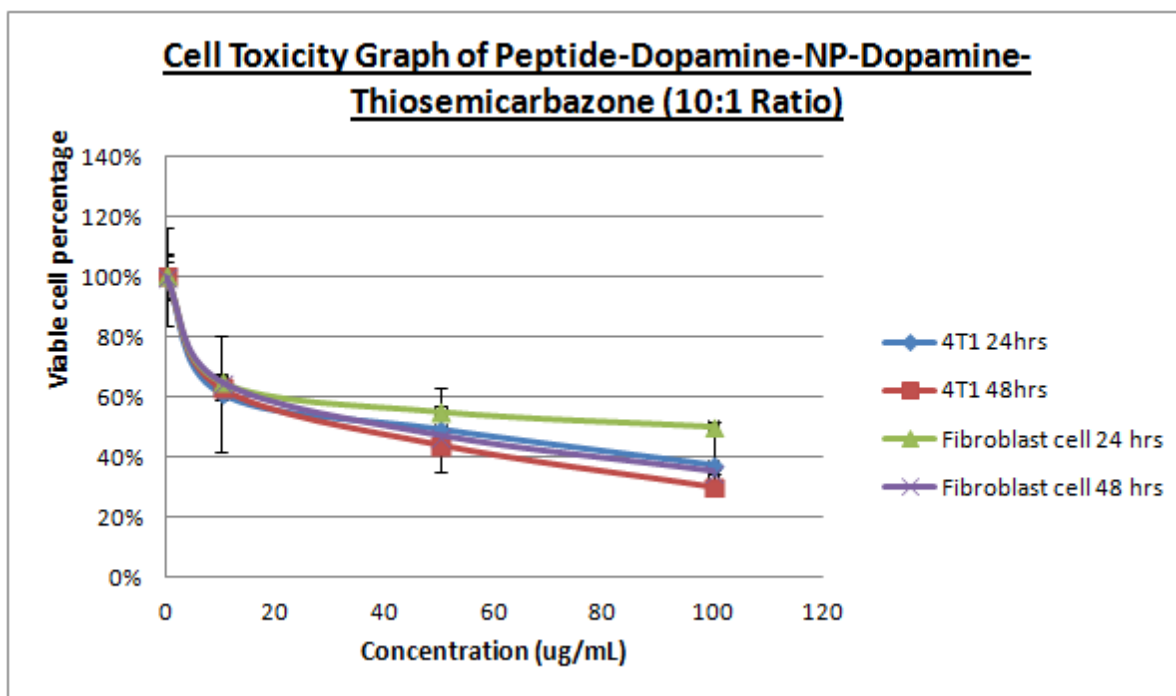
Figure B.47:- Cell toxicity graph of Peptide-Dopamine-NP-Dopamine-Thiosemicarbazone (10:1).

Figure B.48:- Cell toxicity graph of Thiosemicarbazone-Dopamine-NP (1:10).

Figure B.49:- Cell toxicity graph of Thiosemicarbazone-Dopamine-NP (1:5).

Figure B.50:- Cell toxicity graph of Thiosemicarbazone-Dopamine-NP (1:1).
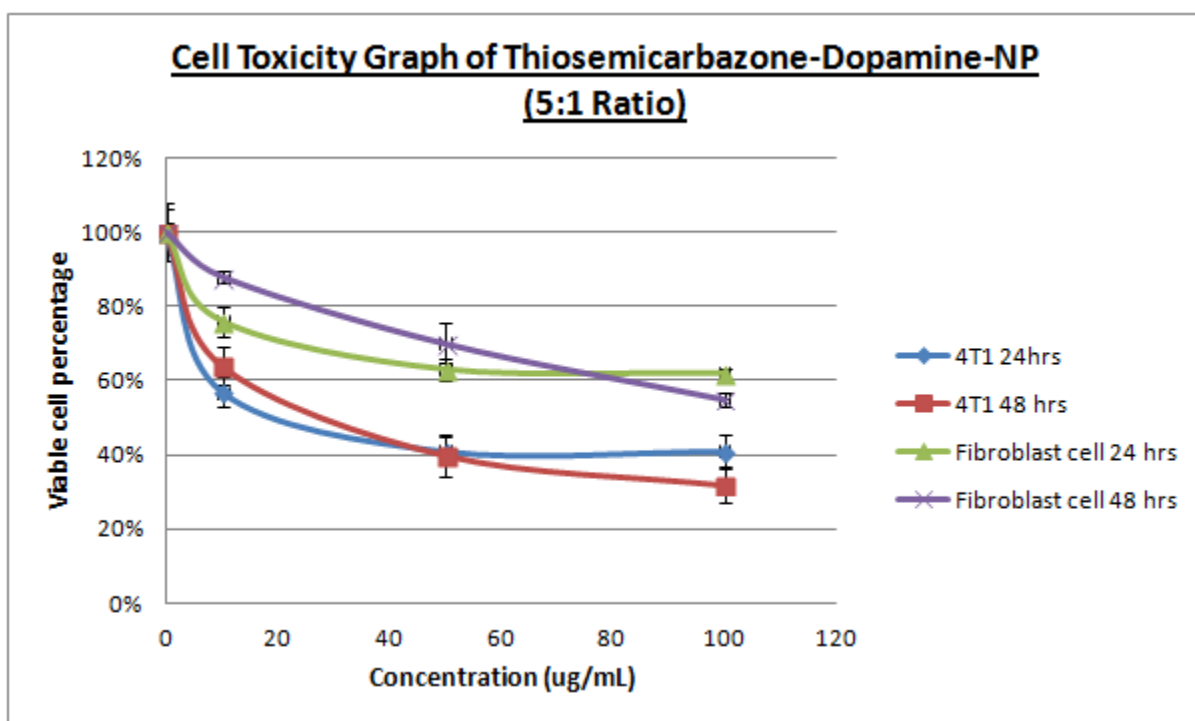
Figure B.51:- Cell toxicity graph of Thiosemicarbazone-Dopamine-NP (5:1).
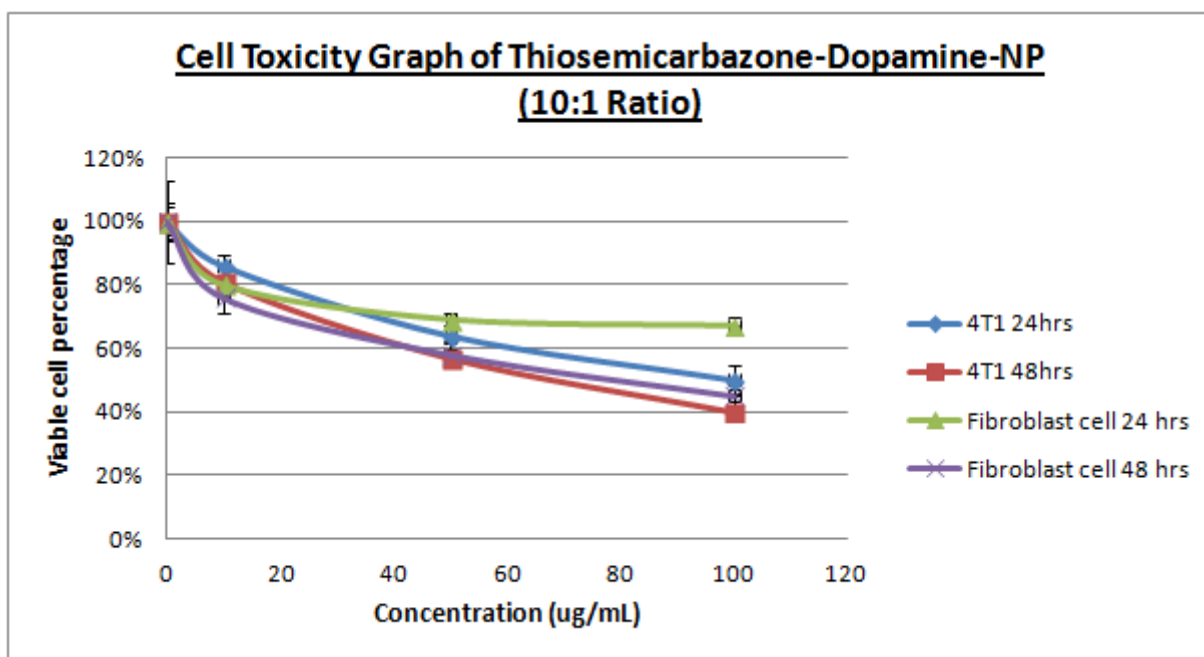
Figure B.52:- Cell toxicity graph of Thiosemicarbazone-Dopamine-NP (10:1).
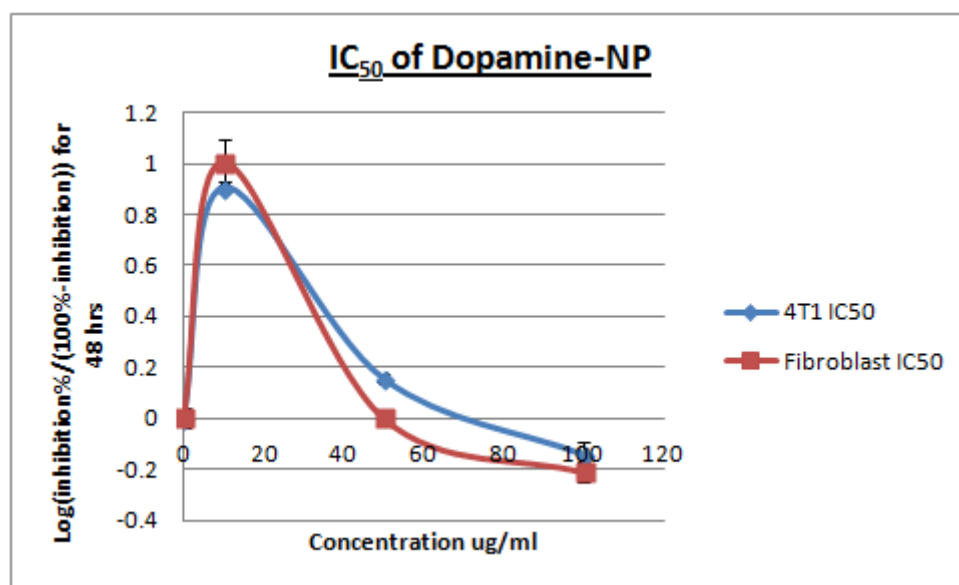
Figure B.53:- IC$_{50}$ of Dopamine-NP for 4T1 and fibroblast cell lines.
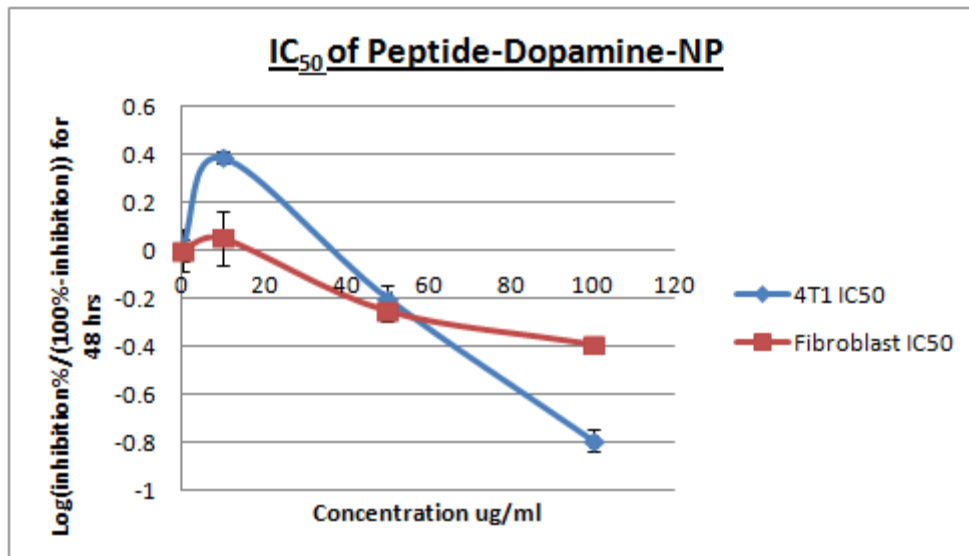
Figure B.54:- IC$_{50}$ of Peptide-Dopamine-NP for 4T1 and fibroblast cell lines.
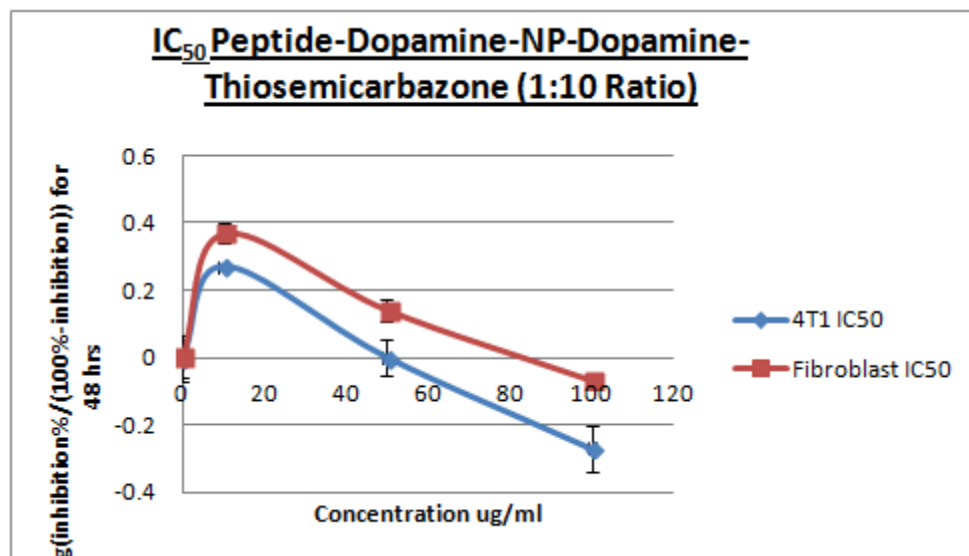
Figure B.55:- IC$_{50}$ Peptide-Dopamine-NP-Dopamine-Thiosemicarbazone (1:10).
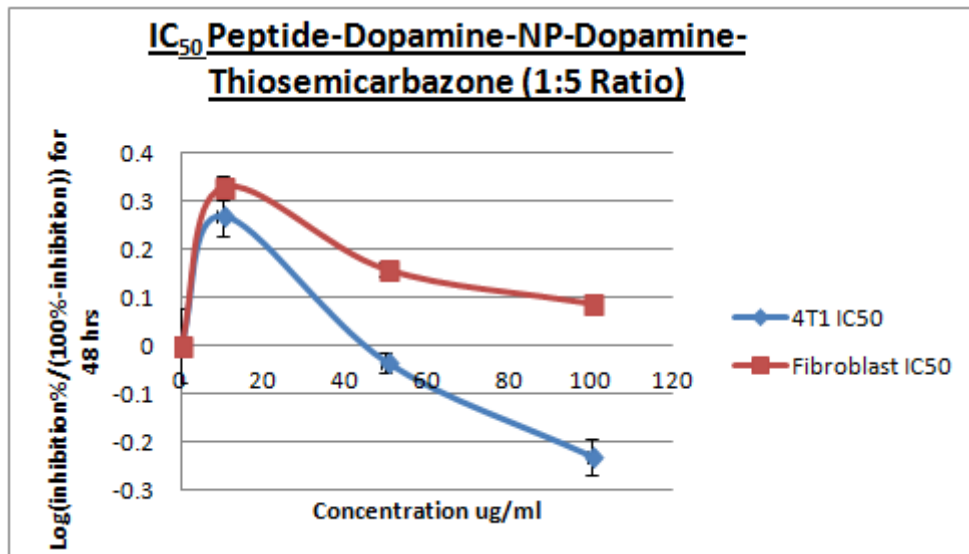
Figure B.56:- IC$_{50}$ Peptide-Dopamine-NP-Dopamine-Thiosemicarbazone (1:5).
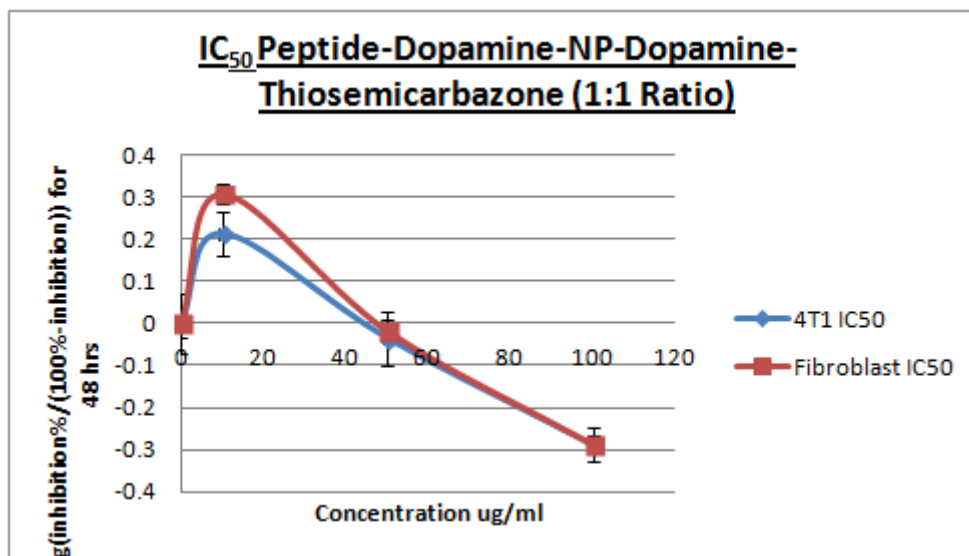
Figure B.57:- IC$_{50}$ Peptide-Dopamine-NP-Dopamine-Thiosemicarbazone (1:1).
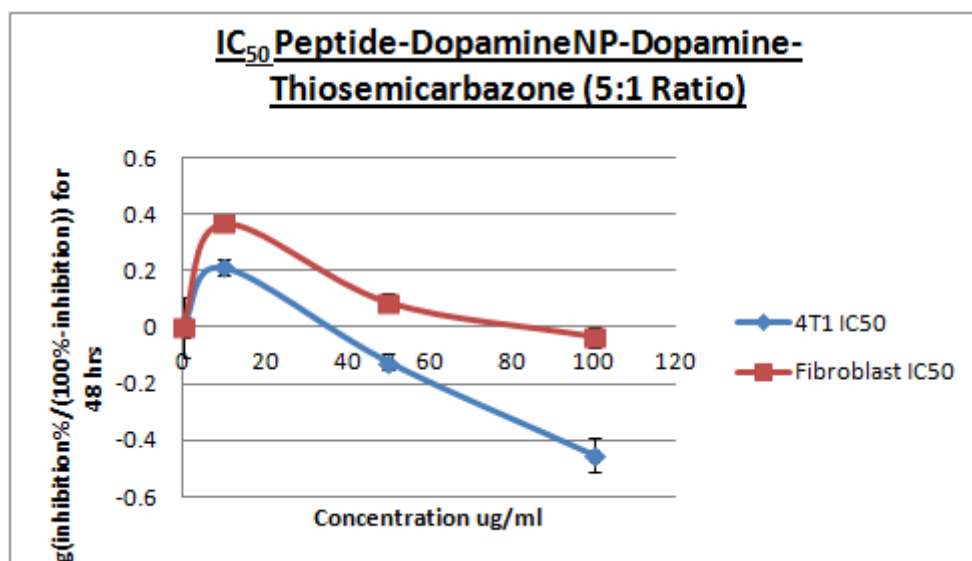
Figure B.58:- IC$_{50}$ Peptide-Dopamine-NP-Dopamine-Thiosemicarbazone (5:1).
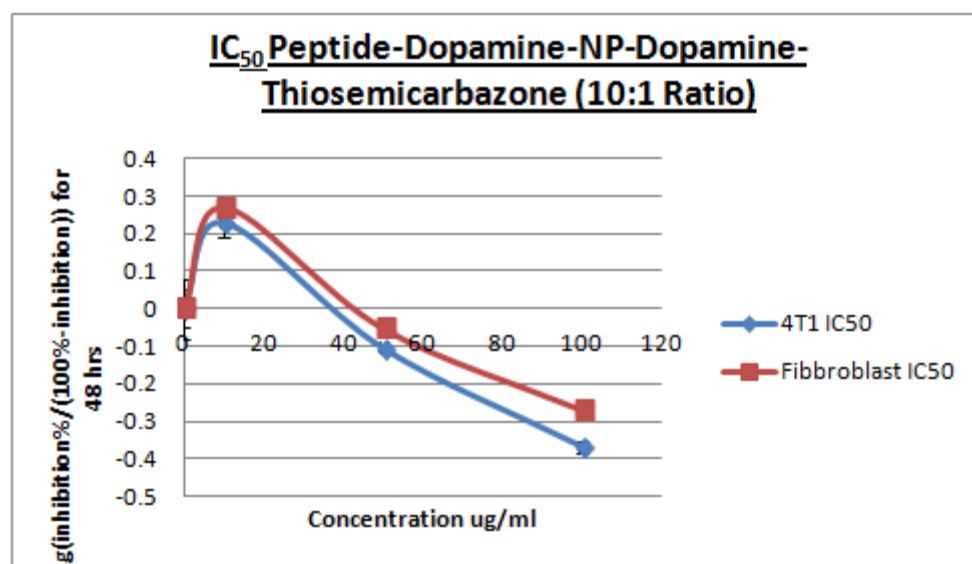
Figure B.59:- IC$_{50}$ Peptide-Dopamine-NP-Dopamine-Thiosemicarbazone (10:1).
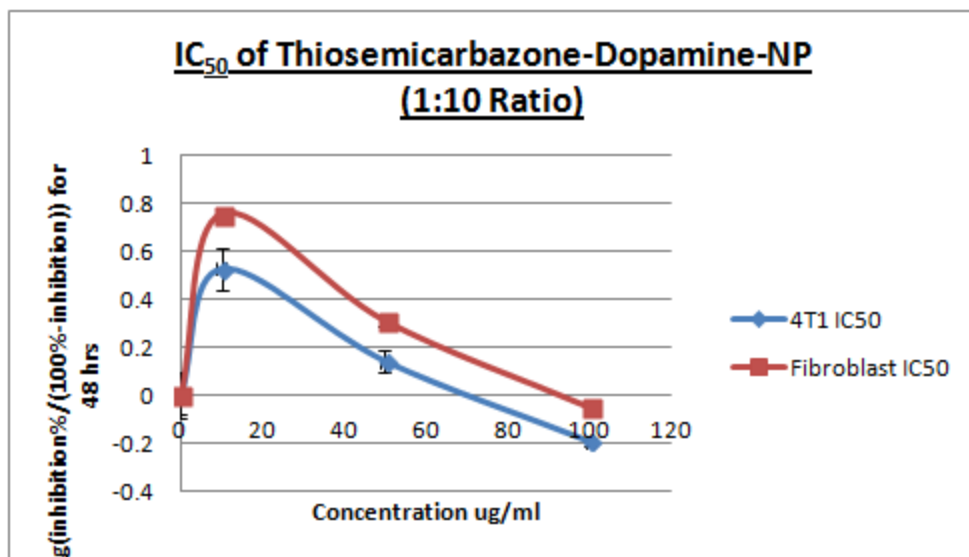
Figure B.60:- IC$_{50}$ of Thiosemicarbazone-Dopamine-NP (1:10).
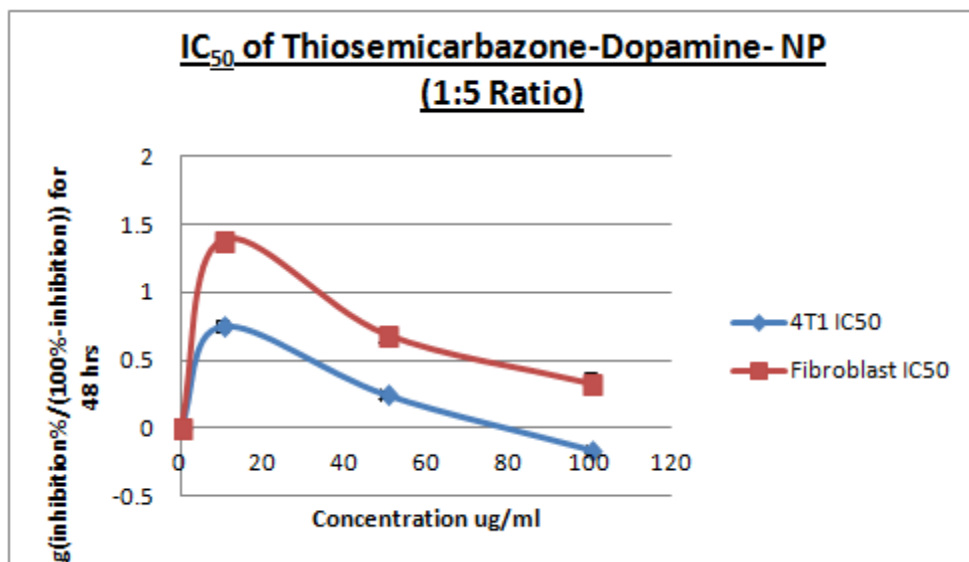
Figure B.61:- IC$_{50}$ of Thiosemicarbazone-Dopamine-NP (1:5).
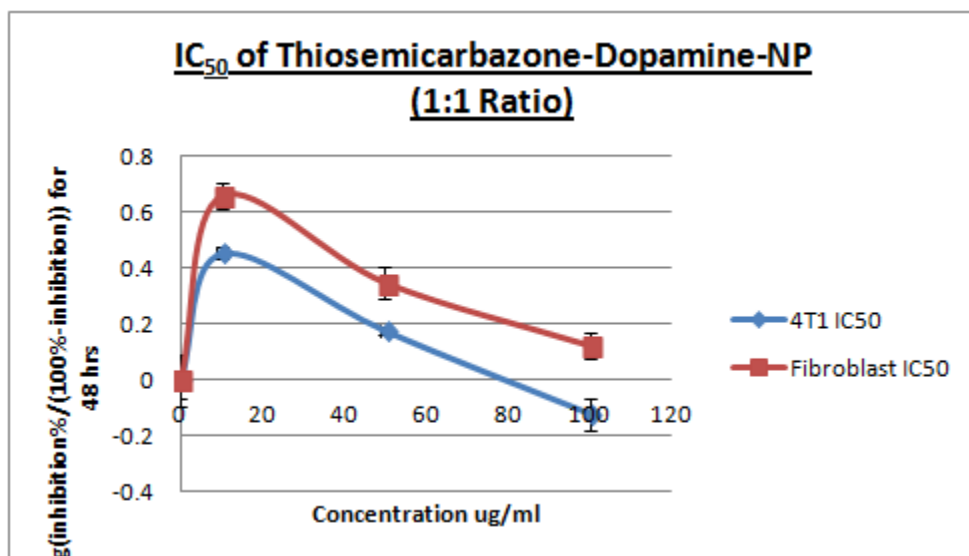
Figure B.62:- IC$_{50}$ of Thiosemicarbazone-Dopamine-NP (1:1).
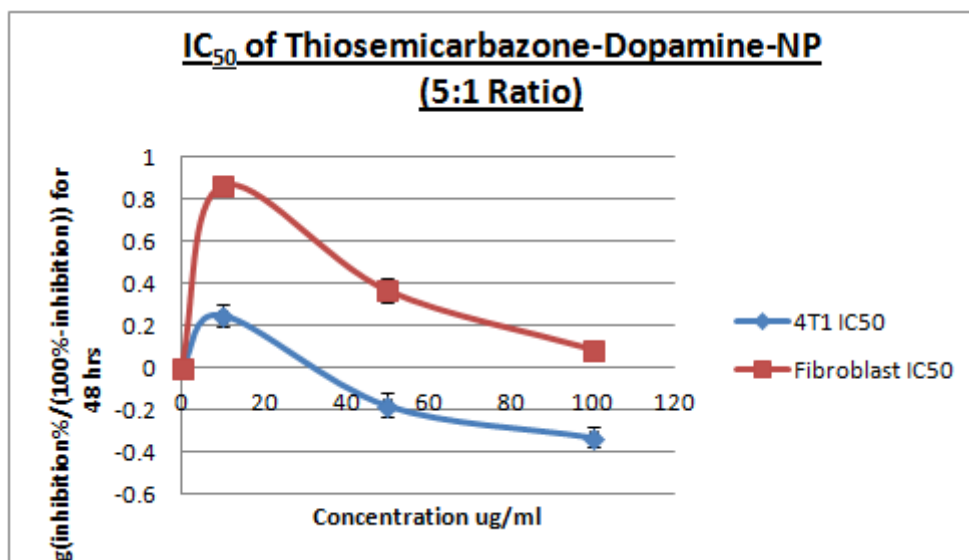
Figure B.63:- IC$_{50}$ of Thiosemicarbazone-Dopamine-NP (5:1).
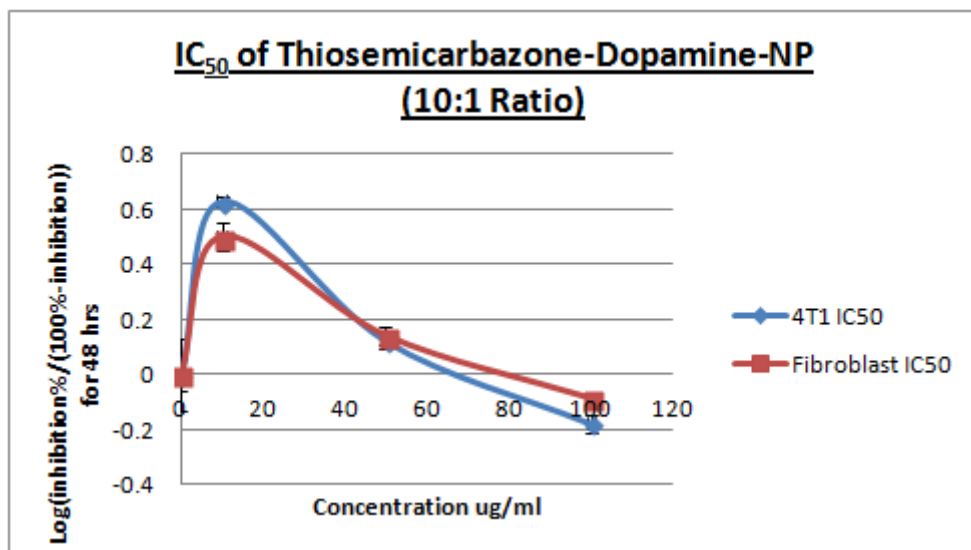
Figure B.64:- IC$_{50}$ of Thiosemicarbazone-Dopamine-NP (10:1).
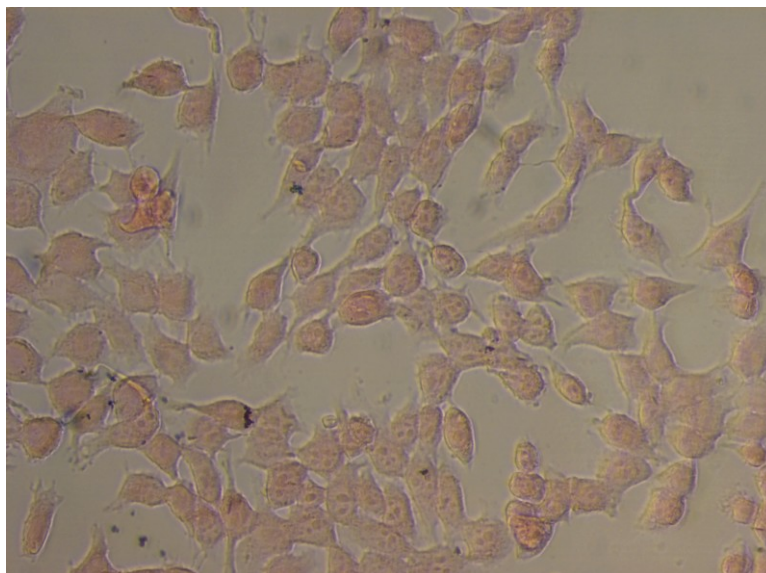
Figure B.65:- Prussian blue staining control of 4T1 cells.
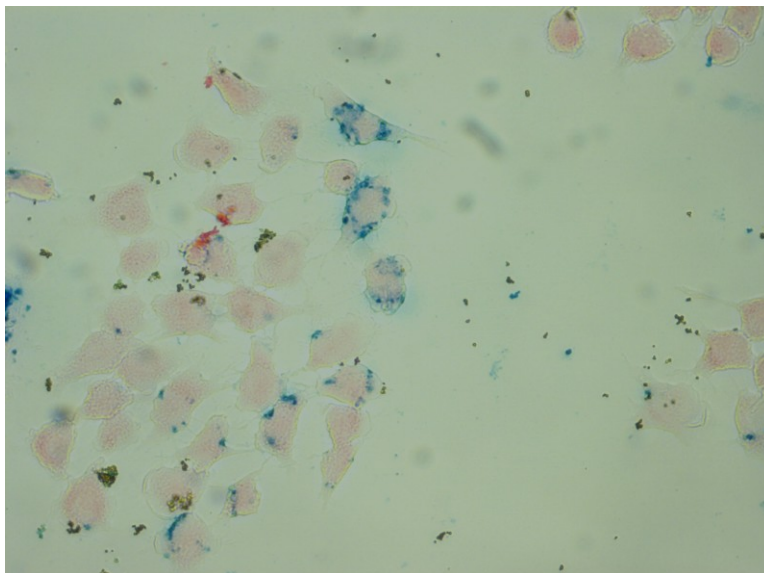
Figure B.66:- Prussian blue staining of 4T1 cells incubated with 5µg of Dopamine coated nanoparticles.
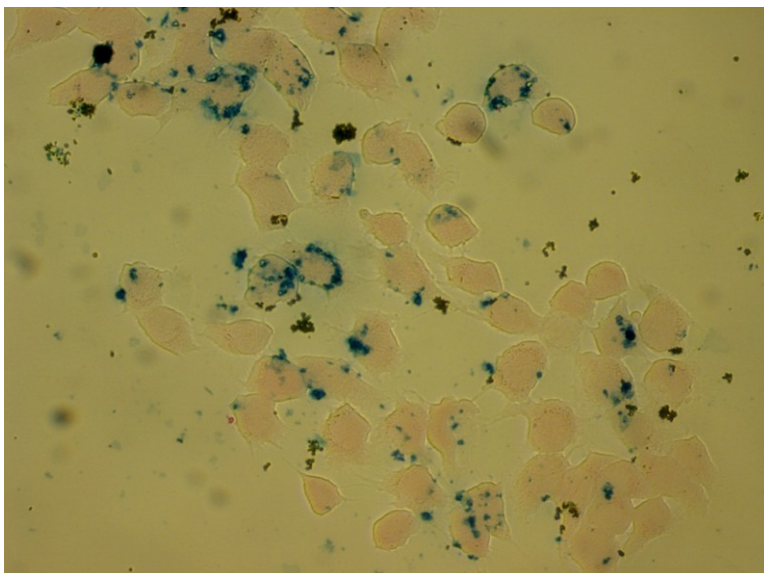
Figure B.67:- Prussian blue staining of 4T1 cells incubated with 10µg of Dopamine coated nanoparticles.
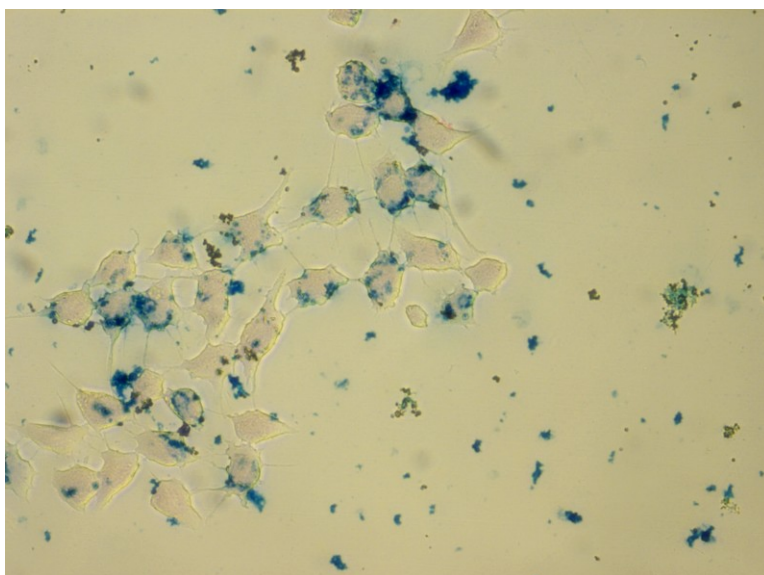
Figure B.68:- Prussian blue staining of 4T1 cells incubated with 5µg of Peptide-Dopamine coated nanoparticles.
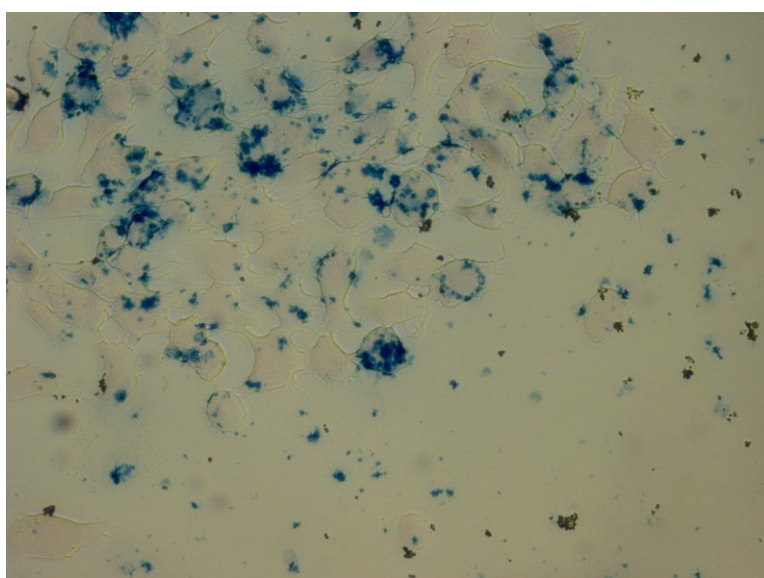
Figure B.69:- Prussian blue staining of 4T1 cells incubated with 10µg of Peptide-Dopamine coated nanoparticles.
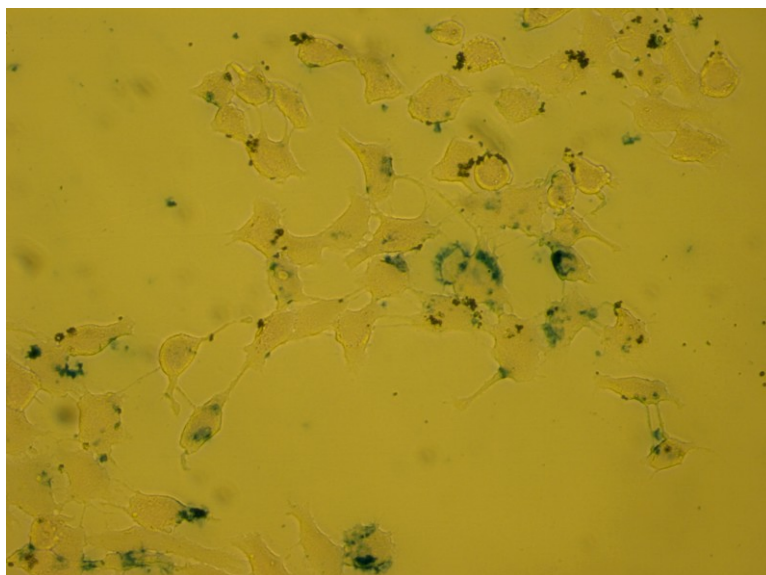
Figure B.70:- Prussian blue staining of 4T1 cells incubated with 5µg of Peptide-Dopamine-NP-Dopamine-Thiosemicarbazone (5:1).
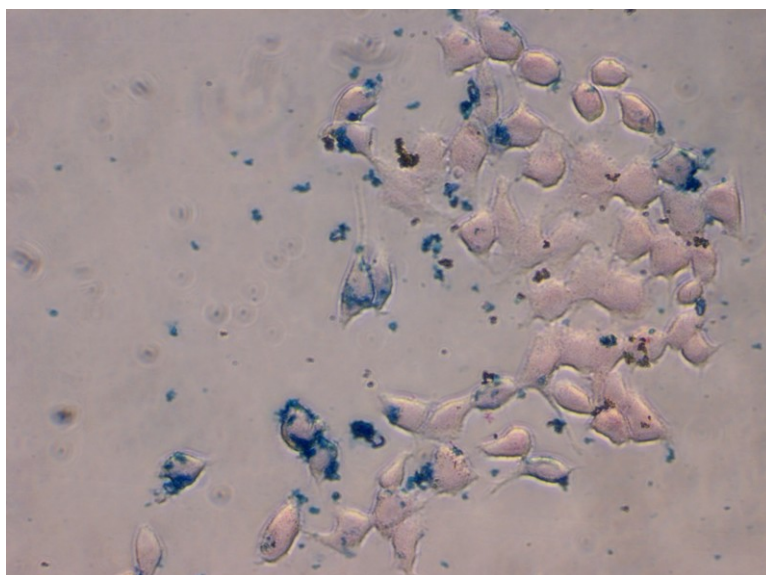
Figure B.71:- Prussian blue staining of 4T1 cells incubated with 10µg of Peptide-Dopamine-NP-Dopamine-Thiosemicarbazone (5:1).
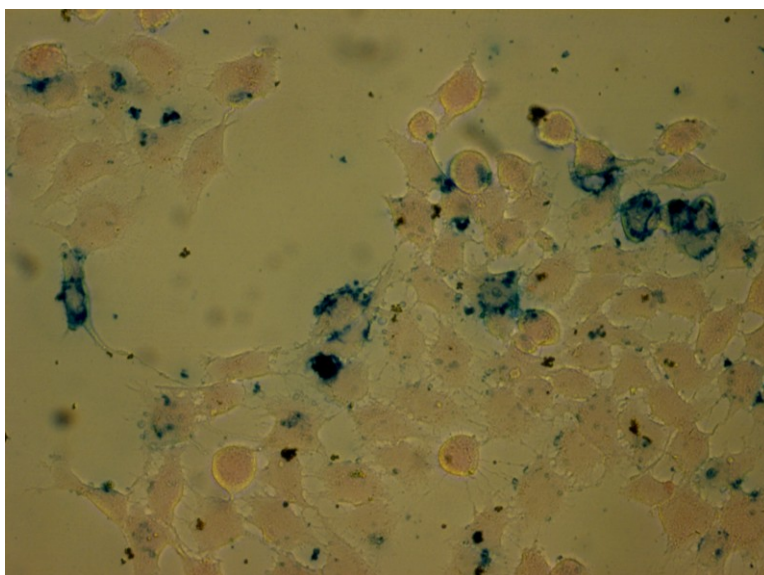
Figure B.72:- Prussian blue staining of 4T1 cells incubated with 5µg Thiosemicarbazone-Dopamine coated nanoparticles (5:1)
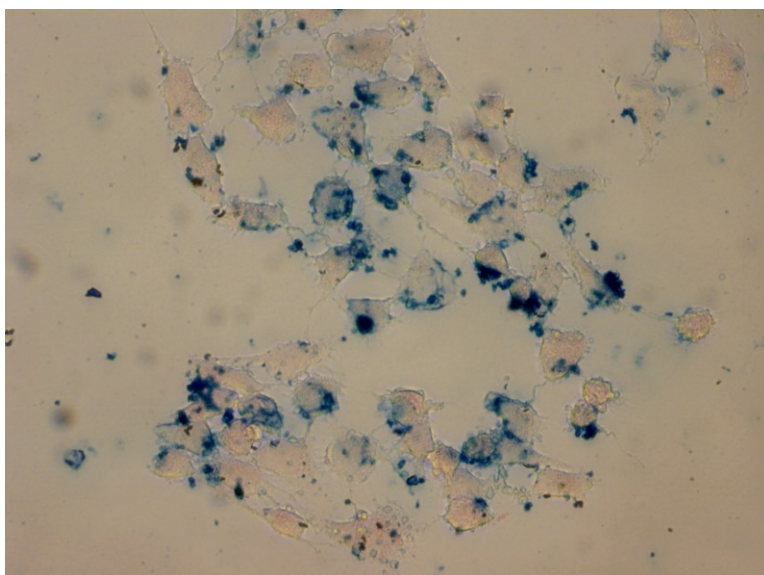
Figure B.73:- Prussian blue staining of 4T1 cells incubated with 10µg of Thiosemicarbazone-Dopamine coated nanoparticles (5:1).
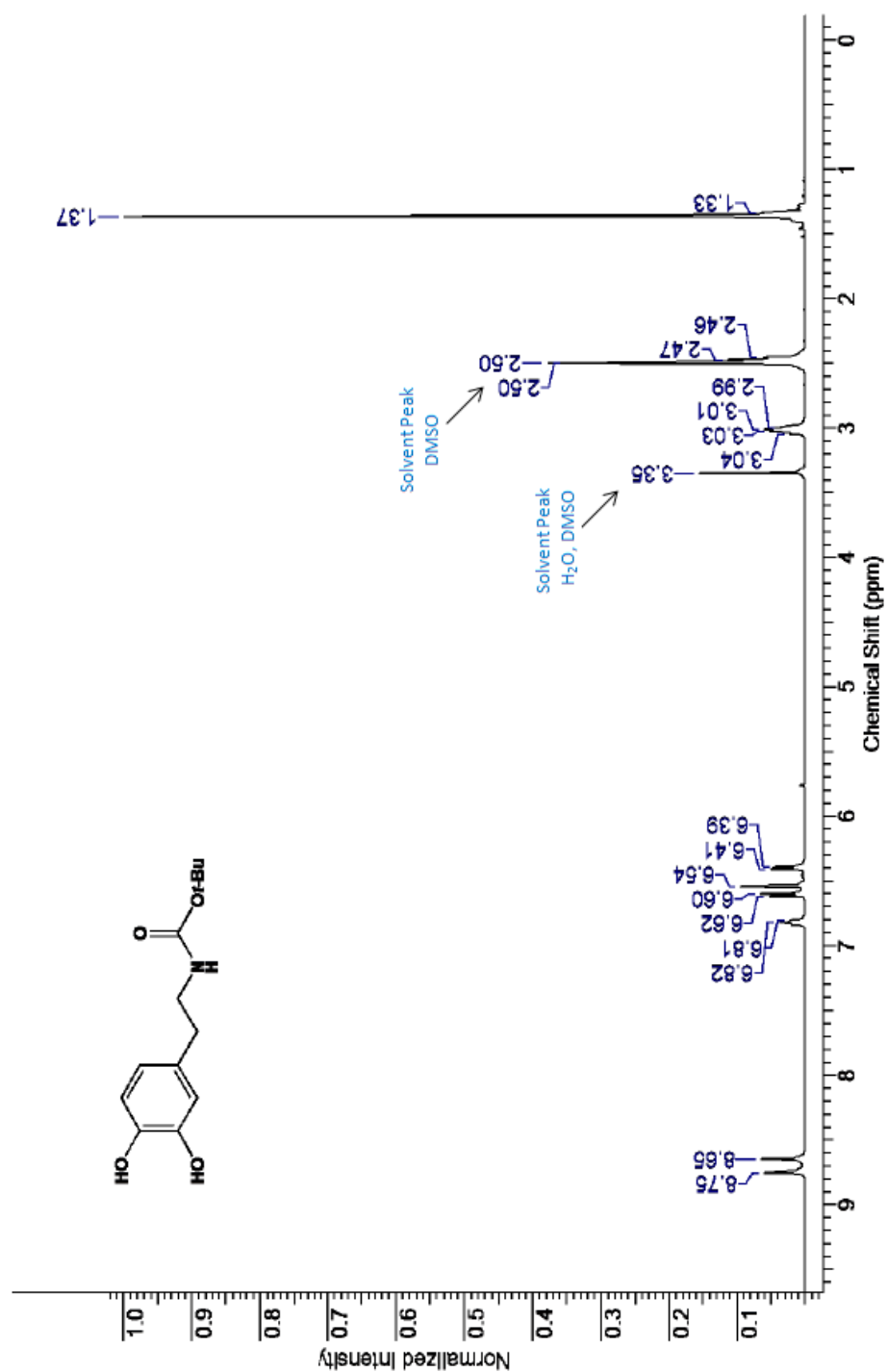
Figure B.74:- ^{1}HNMR Boc protected Dopamine
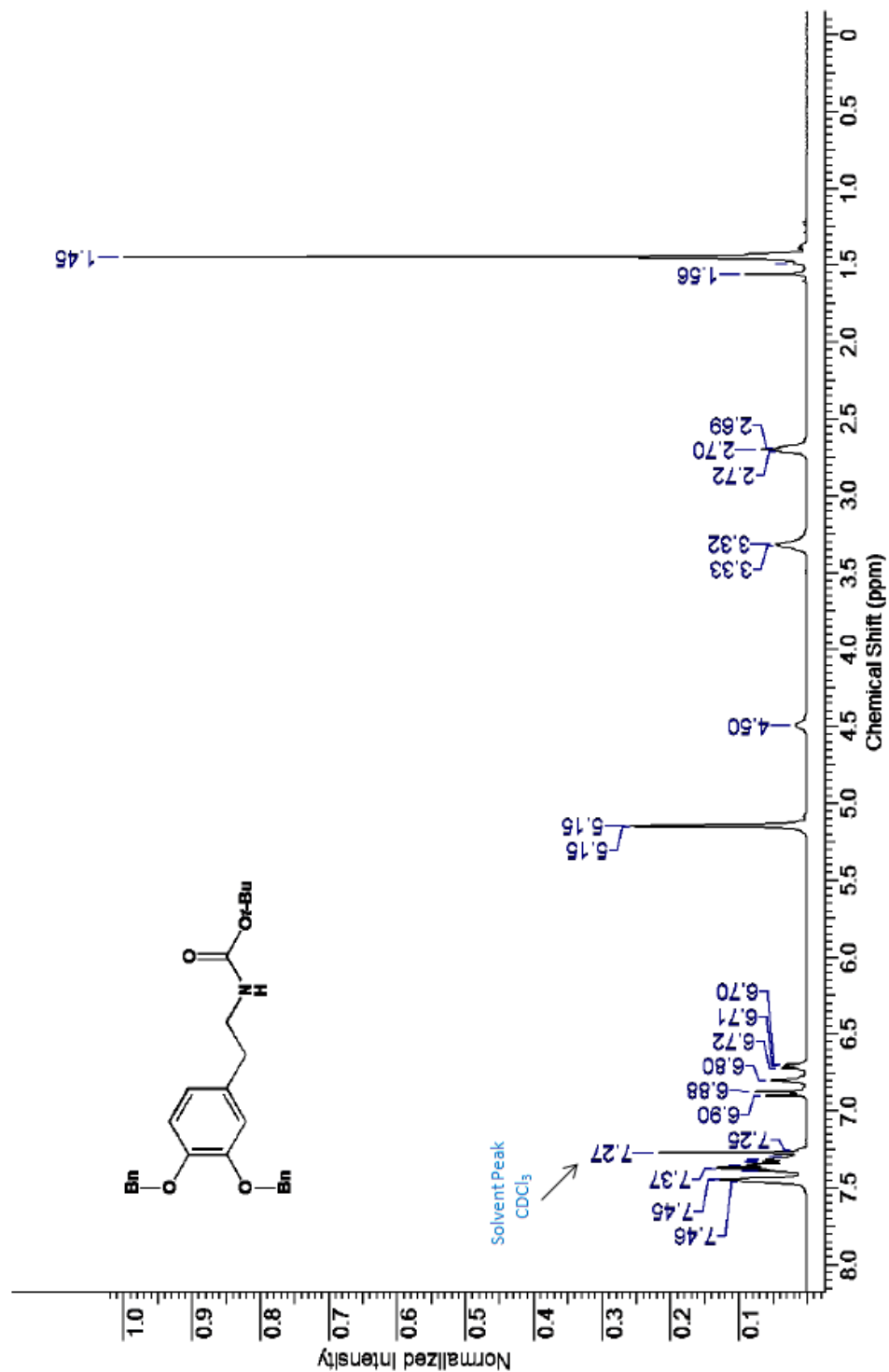
Figure B.75:- ^{1}HNMR Benzyl protected Boc-dopamine
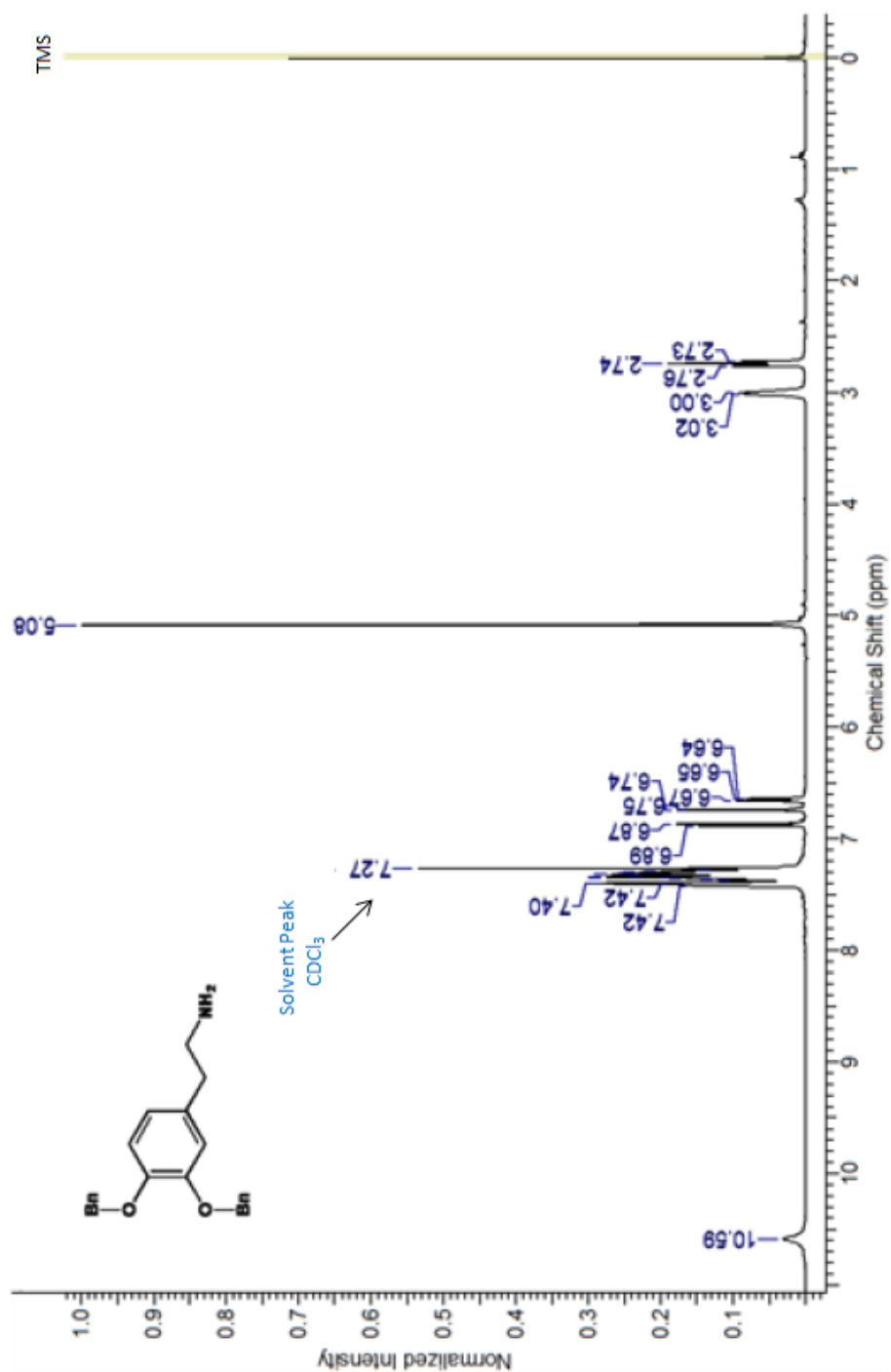
Figure B.76:- ^{1}HNMR Benzyl protected dopamine
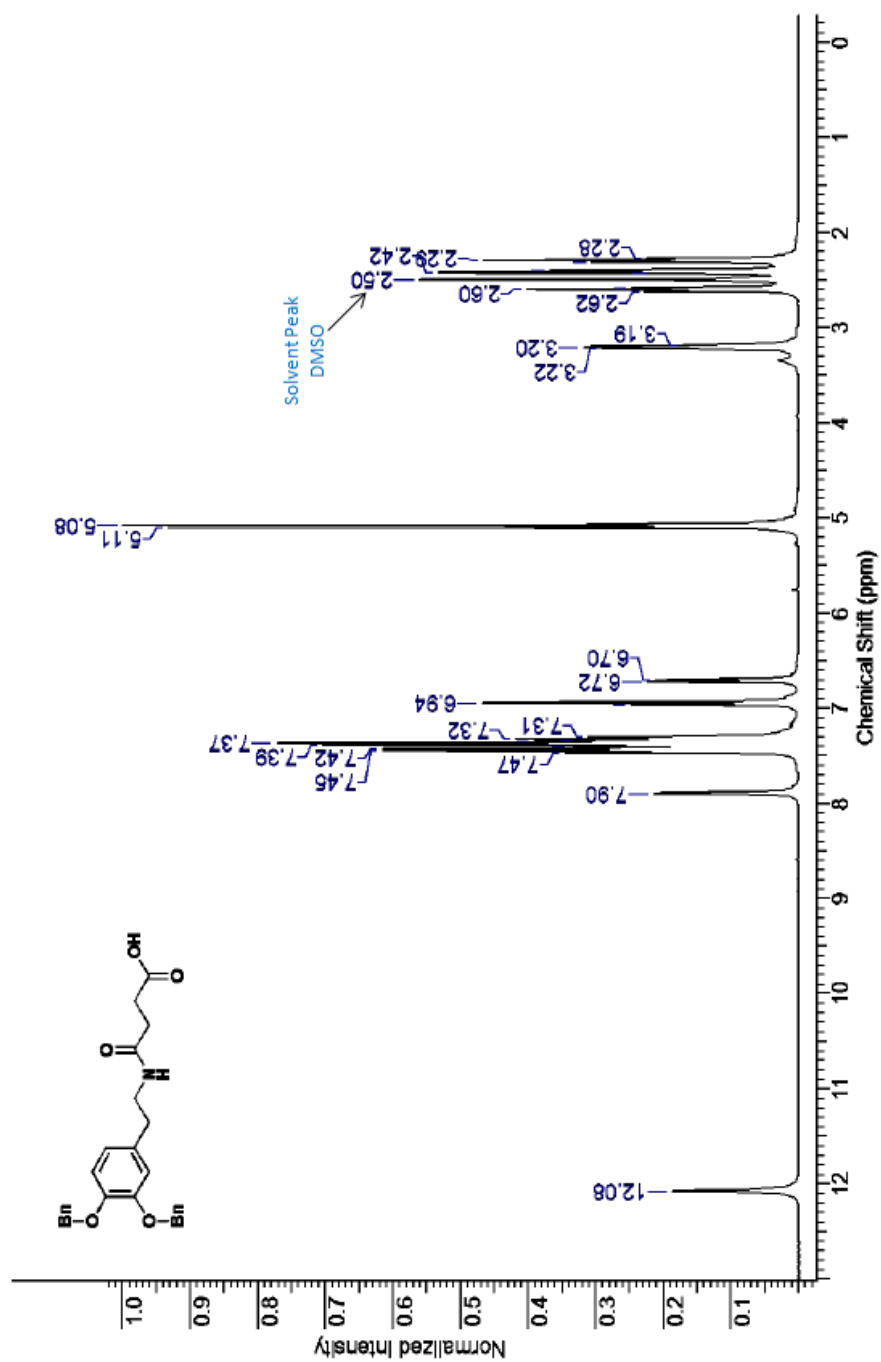
Figure B.77:- ^{1}HNMR Succinic anhydride coupled benzyl protected dopamine

197
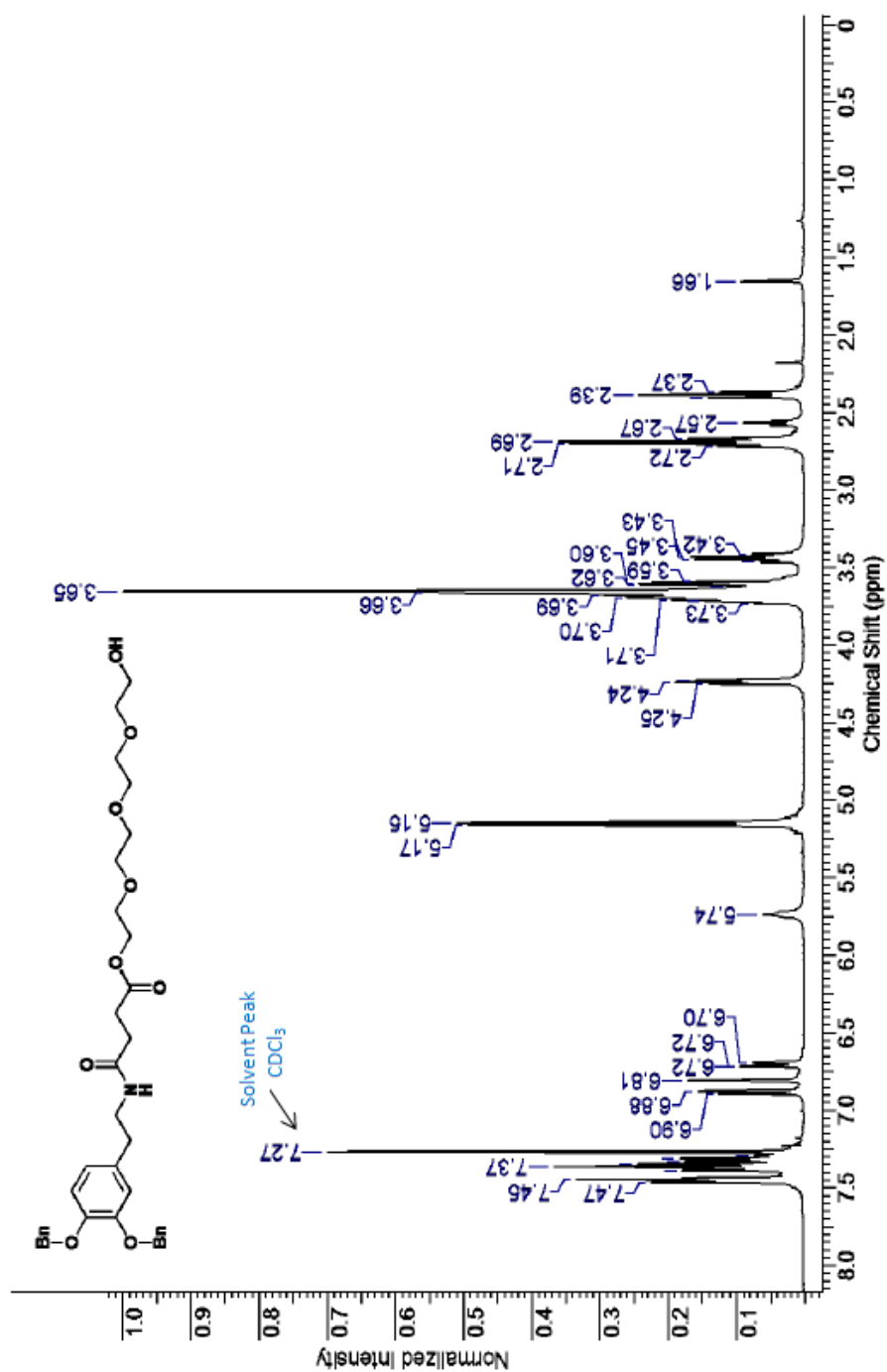
Figure B.78:- ^{1}HNMR Tetraethylene glycol coupled benzyl protected dopamine.

Figure B.79:- ^{1}HNMR Tetraethylene glycol coupled dopamine..
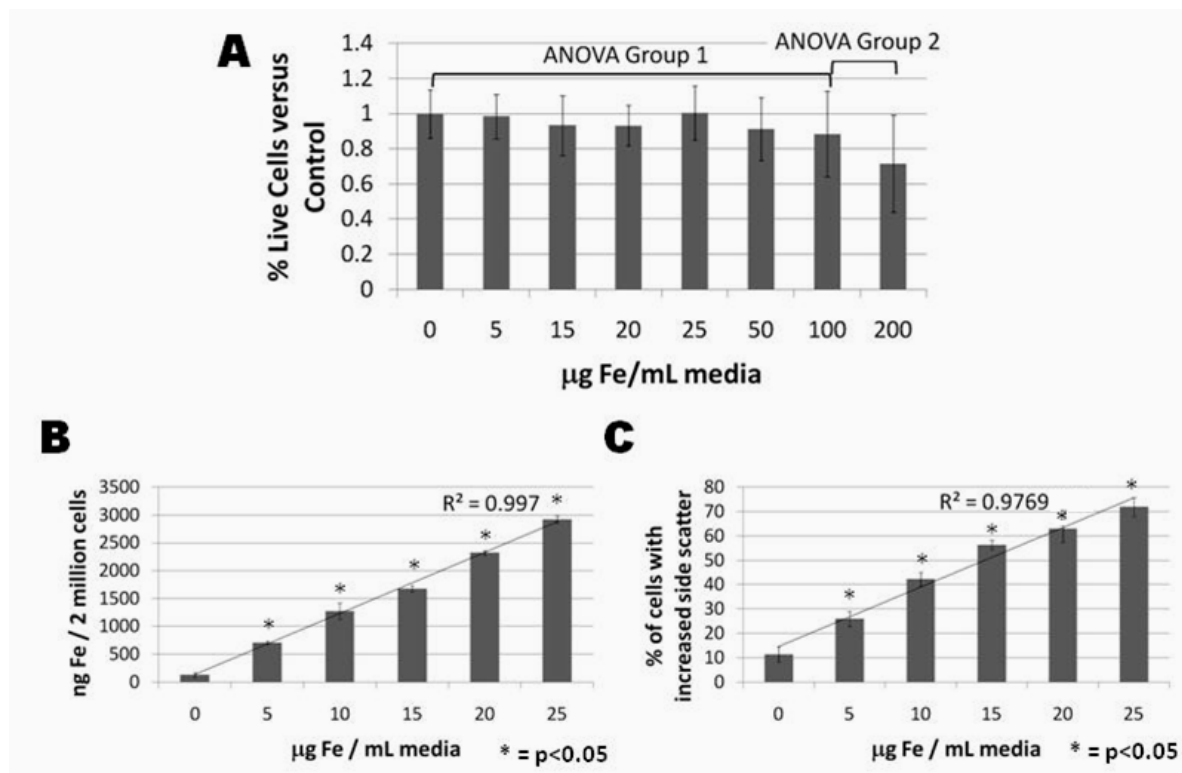
Figure B.80:- Nanoparticle Loading.

    Mo/Ma were cultured overnight in increasing concentrations of nanoparticles. The next morning cells were washed and assayed. A. Toxicity of Nanoparticles: Cells were assayed for viability using MTT. B. Loading of Nanoparticles: Cells were assayed for iron content using the ferrozine assay. C. Percent of Cells Loaded: Cells were assayed for increased side scatter using flow cytometry. Error bars are standard deviation.

       (This work has already been published in; *International Journal of Nanomedicine ,2012, Vol 7, 297–306*.)
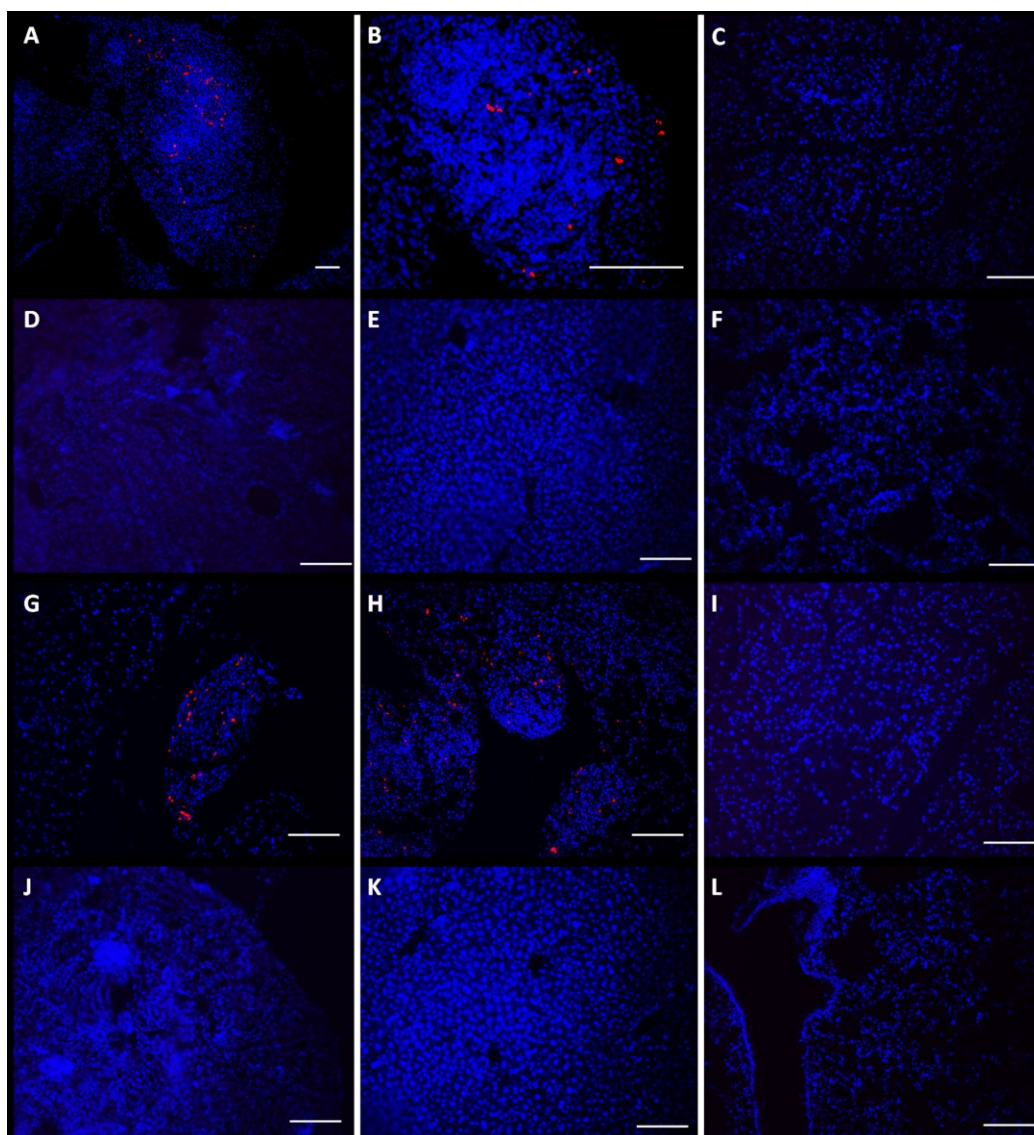
Figure B.81:- Mo/Ma Only Infiltrate Pan02 Tumors.

PKH26 labeled monocytes were injected i.p. into mice bearing i.p. Pan02 tumors. A-F. Mice were euthanized three days after monocyte injection and organs were harvested and imaged for PKH26 (monocytes). Representative images are shown. A. Tumor 10x; B. Tumor 40x; C. Pancreas; D. Kidney; E. Liver; F. Lung. G-L. Mice were euthanized six days after monocyte injection and organs were harvested and imaged for PKH26 (monocytes). Representative images are shown. G. Tumor (note healthy pancreas at the top left); H. Tumor; I. Pancreas; J. Kidney; K. Liver; L. Lung. Blue is DAPI (nuclear counterstain), Red is PKH26 (monocytes). All scale bars are 100 μm, objective is 20x unless otherwise specified. (This work has already been published in; *International Journal of Nanomedicine ,2012, Vol 7, 297–306.*)

Figure B.82:- Mo/Ma Infiltrate Pan02 Tumors.

A,B. Mo/Ma loaded with PKH26 were injected into mice bearing i.p. Pan02 tumors. Six days later mice were euthanized and tumors were harvested. A. Dapi counterstained section shows Mo/Ma labeled with PKH26 in tumor. Blue = Dapi, Red = PKH26 (Mo/Ma). B. H&E staining of serial sections shows irregular morphology demonstrating that the targeted area is a tumor. Scale bars = 100 μm. C. Mo/Ma loaded with Dapi were injected into mice bearing Pan02(fluc) tumors. Five days later mice were euthanized and tumors were harvested. Sections were stained with rabbit anti-firefly luciferase and DyLite649-goat anti rabbit. Immunohistochemistry verifies that the Mo/Ma infiltrate pancreatic tumors. Blue = Dapi (Mo/Ma), Red = DyLite 649 (Pan02 cells). Scale bar = 100 μm.

(This work has already been published in; *International Journal of Nanomedicine ,2012, Vol 7, 297–306.*)
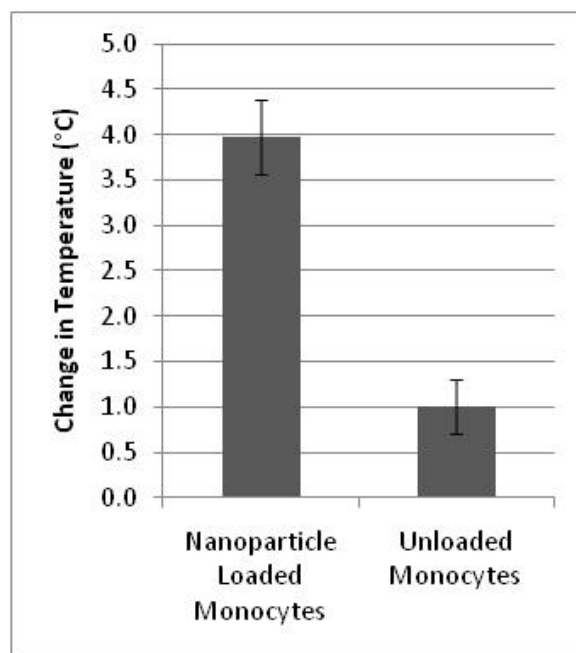
Figure B.83:- Heat generation by nanoparticle loaded Mo/Ma.

(This work has already been published in; *International Journal of Nanomedicine ,2012, Vol 7, 297–306*.)
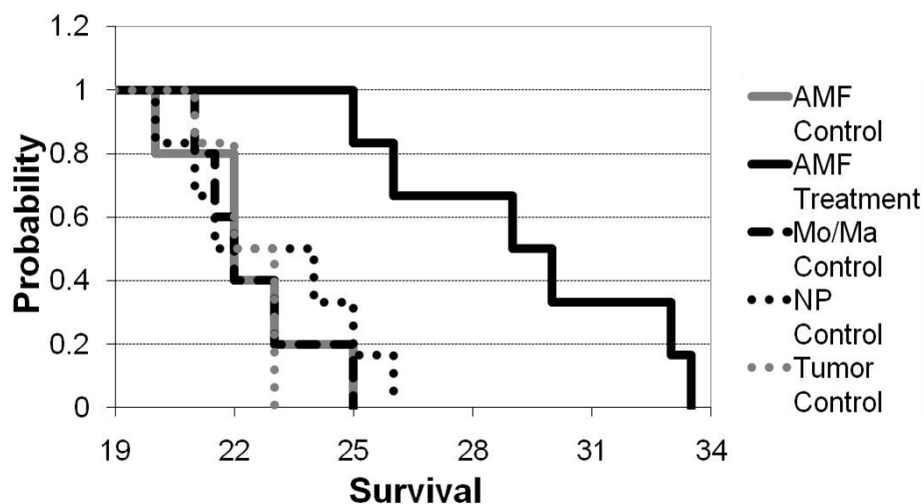
Figure B.84:- Duration to Clinical Symptoms ('Survival').

Mice were treated and monitored as described. Mice were euthanized when they displayed clinical signs of cancer and the day/time was recorded (n=5 or 6 for each group). $p < 0.005$ for AMF treatment versus all other groups. (This work has already been published in; *International Journal of Nanomedicine ,2012, Vol 7, 297–306*.)
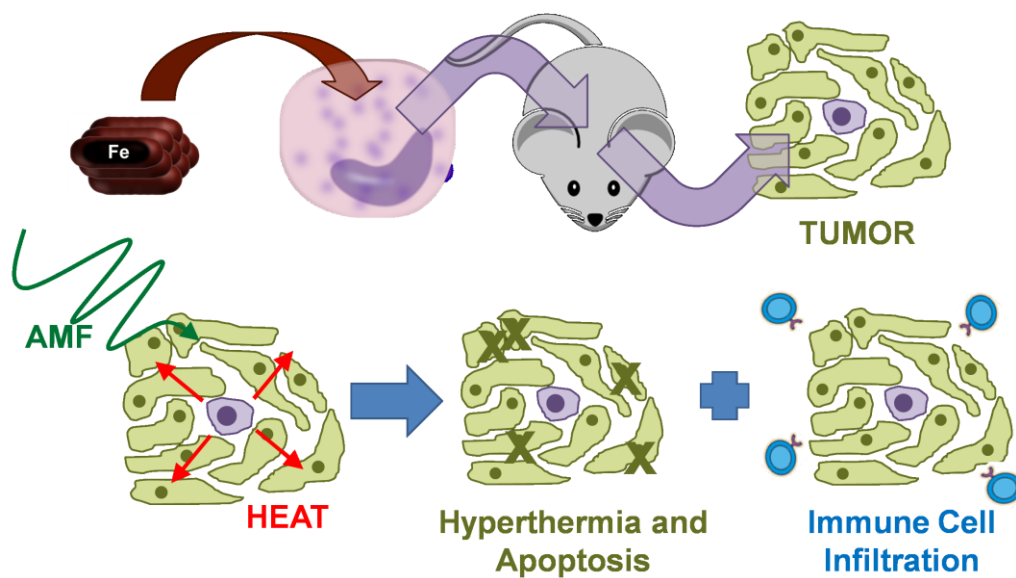
Figure B.85:- Model of the demonstrated system.

First, nanoparticles were loaded into Mo/Ma by coculture. The Mo/Ma were then injected i.p. into mice bearing i.p. Pan02 tumors and they specifically homed to the tumors. Three days after injecting the cells, the mice were exposed to AMF, which caused the nanoparticles to generate heat, leading to hyperthermia.

(This work has already been published in; *International Journal of Nanomedicine ,2012, Vol 7, 297–306.*)

Appendix C - Previous Experimental Attempts

C.1 Experimental Procedure 1

We first tried to synthesize the thiosemicarbazone analogue coupled to 4-(hydrazine carbothioamido) butonic acid. The next step was to couple the peptide sequence to the carboxylic acid of the 4-(hydrazine carbothioamido) butonic acid coupled thiosemicarbazone analogue. Next coupling of the dopamine to peptide and coating the Fe/Fe_3O_4 nanoparticle was to be done. The nanoplatform synthesis is shown in Scheme 1 and 2.

In this procedure the first step was to synthesize 4-(hydrazine carbothioamido) butonic acid by reacting 4-aminobutyric acid with carbondisulfide and hydrazine hydrate as shown in scheme 1.[1] The reaction was carried out by first dissolving 4-aminobutyric acid (1 eq) in cold ethanol (0-5°C). To this solution potassium hydroxide (1 eq) and carbon disulfide (2eq) was added and was stirred for 1 hr. Next hydrazine hydrate (1 eq) was added and was reacted at 50^0C for 2 hours. However, as stated in reference 1, we did not obtain any precipitate as a product. We took an aliquot of the clear reaction solution, removed the solvent by means of rotary evaporation, and took a ^{1}H-NMR to discern if any 4-(hydrazine carbithioamido) butonic acid was formed. ^{1}H NMR (DMSO-d_6, δ ppm) 1.82 (m, 2H, CH_2 β to COOH), 2.03 (s, 2H, NHCSNH, D_2O exchangeable), 2.23 (t, 2H, CH_2 α to COOH), 3.36 (t, 2H, CH_2 γ to COOH), 4.34 (s, 2H, NH_2, D_2O exchangeable), 12.24 (s, 1H, OH of COOH, D_2O exchangeable) as stated in reference 1 (Figure C.1).

According to ^{1}H NMR some 4-(hydrazine carbothioamido) butonic acid had formed (Figure C.2). Several attempts were carried out to purify the product 4-(hydrazine carbothioamido) butonic acid, however purification was not successful and were not able to obtain a percentage yield. Therefore, we were able to conclude that this reaction did not proceed.
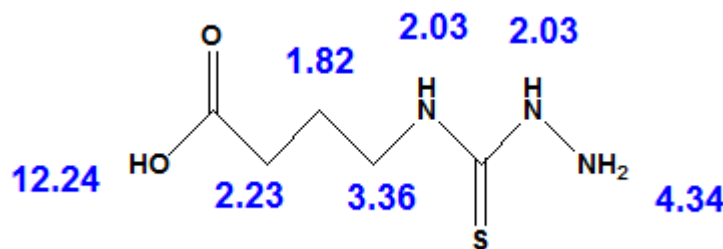
Figure C.1:- ^{1}H NMR chemical shifts for 4-(hydrazine carbothioamido) butonic acid.

Scheme 1:- Synthesis of Thiosemicarbazone Coupled Peptide.
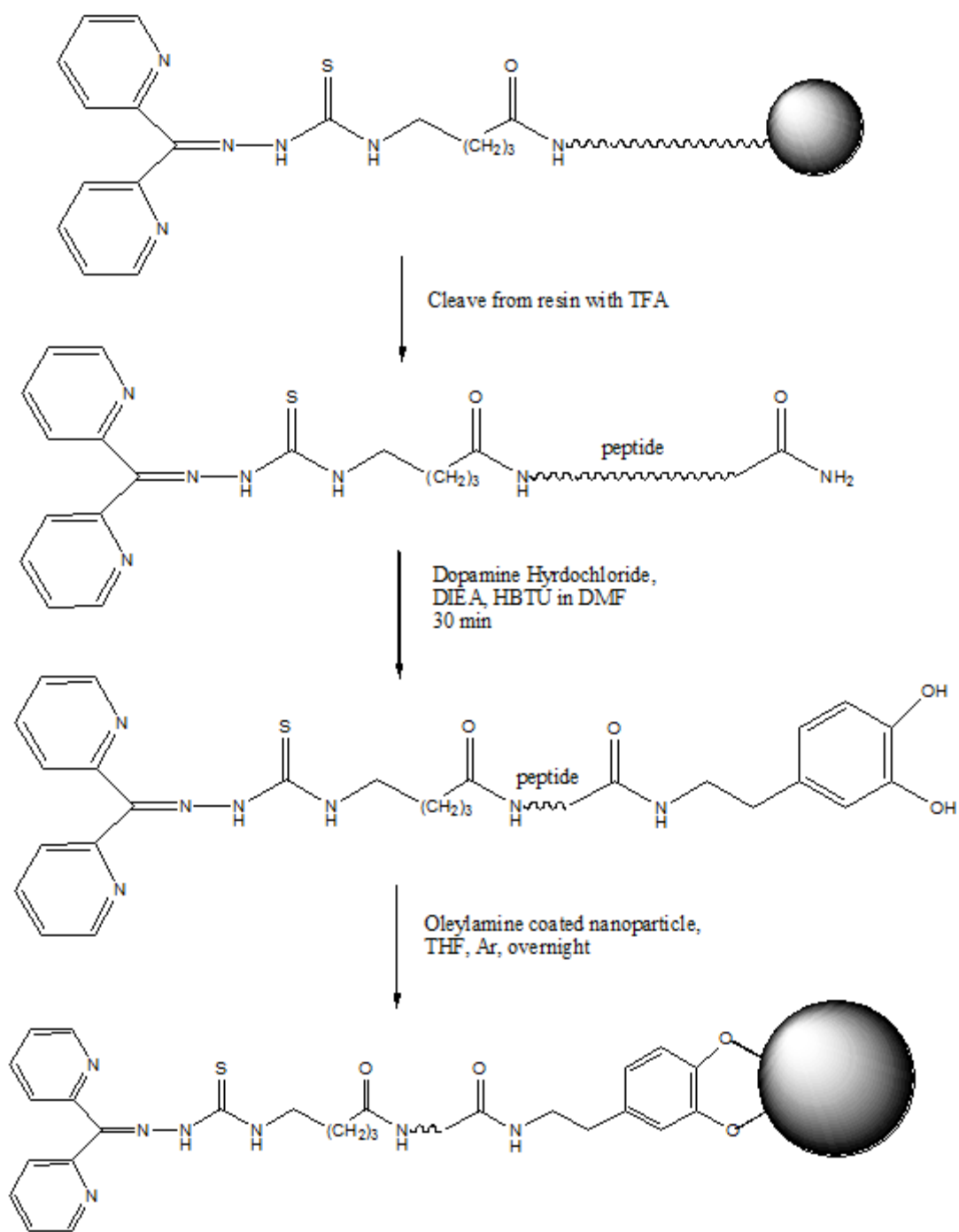
Scheme 2:- Synthesis of Thiosemicarbazone -Peptide-Dopamine coated Nanoparticle.
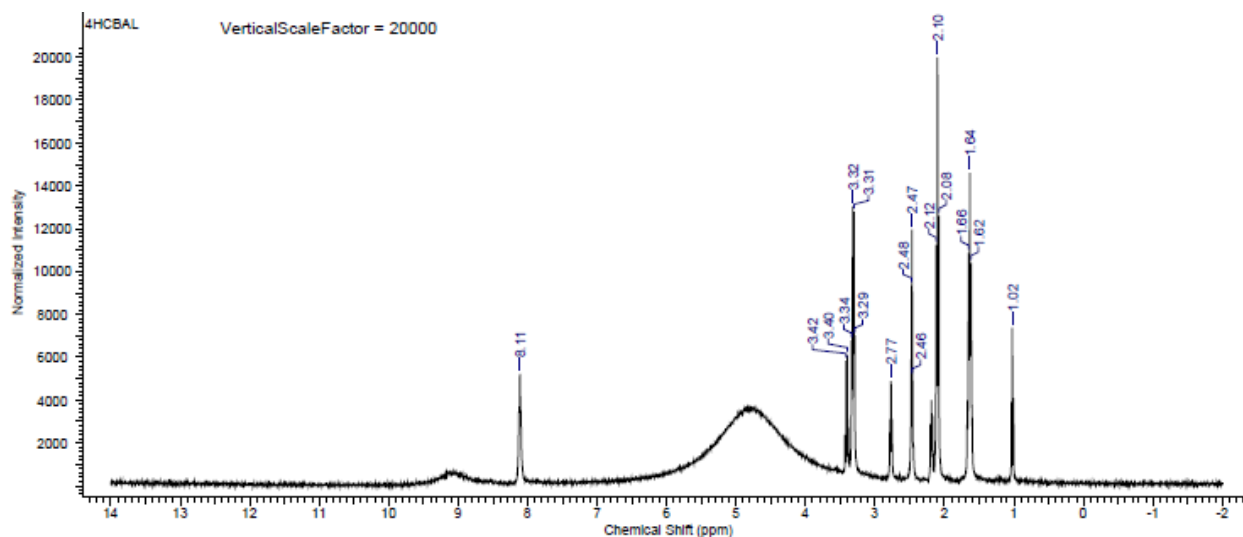
Figure C.2:- ^{1}H NMR of the 4-(hydrazine carbothioamido) butonic acid reaction mixture.

C.2 Experimental procedure 2

Next, we reacted t-butyl protected glycine with the thiosemicarbazone analogue (synthesized as in 1.7.1), as shown in Scheme 3.[1] And next to be continued from the second step as in the Scheme 1 to 2. The reaction was performed with different ratios of protected glycine (1 eq, 1.25 eq), at different temperatures (room temperature and 50°C) and at reaction different times(2 hrs, 1-6 days). A spot on a TLC plate was seen in the reaction performed at r.t for 6 days with 1.25 eq of protected glycine. The TLC was carried out on silica plates with 1:9 solvent ratio of ethanol: methylene chloride (Figure C.3). We took an aliquot of the clear reaction solution, removed the solvent by means of rotary evaporation, and took a ^{1}H-NMR to discern if any product was formed. But the ^{1}H-NMR (Figure C.5) turned out to be as same as the thiosemicarbazone analogue as seen in Figure B.3. No product was formed therefore a percentage yield was not obtained.

208
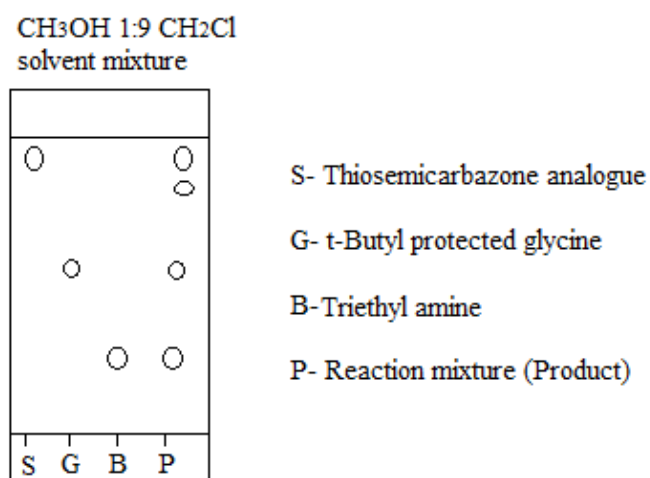
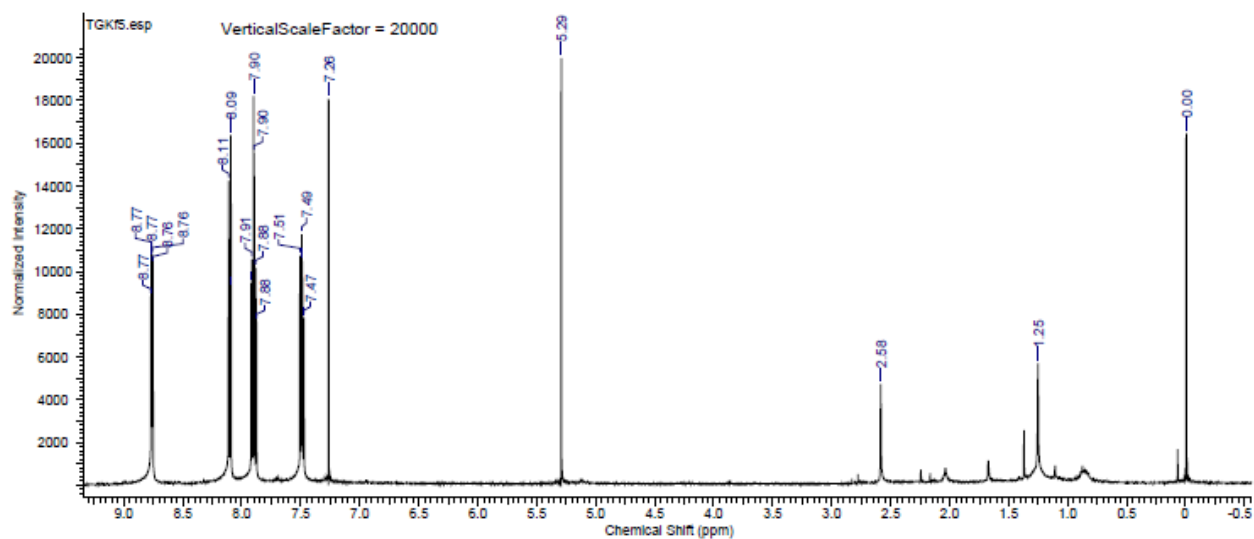**Figure C.3:-** TLC of the reaction for thiosemicarbazone coupled with t-butyl protected glycine.
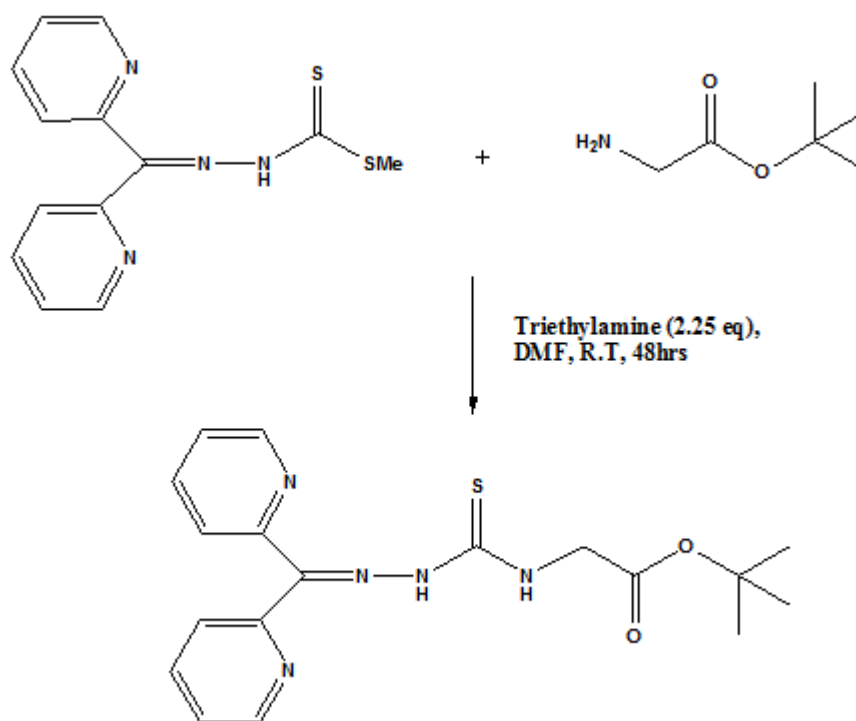
Scheme 3:- Synthesis of thiosemicarbazone coupled with t-butyl protected glycine.
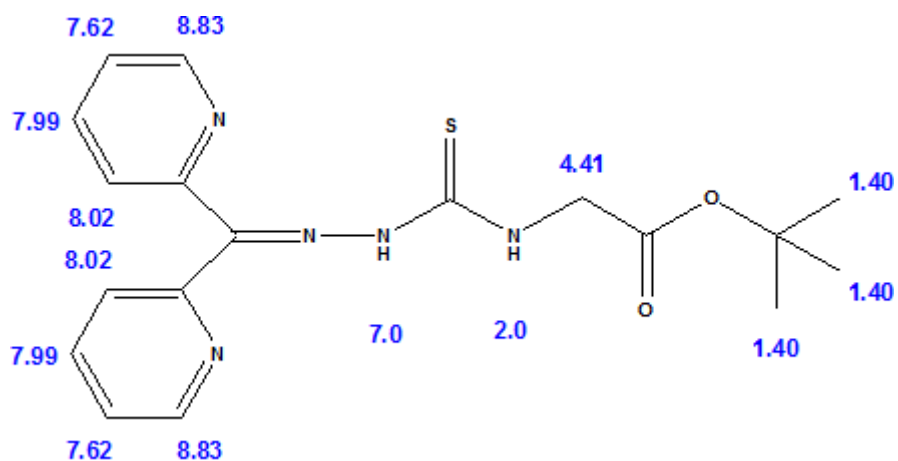
Figure C.4:- Predicted ^{1}H-NMR thiosemicarbazone coupled with t-butyl protected glycine.
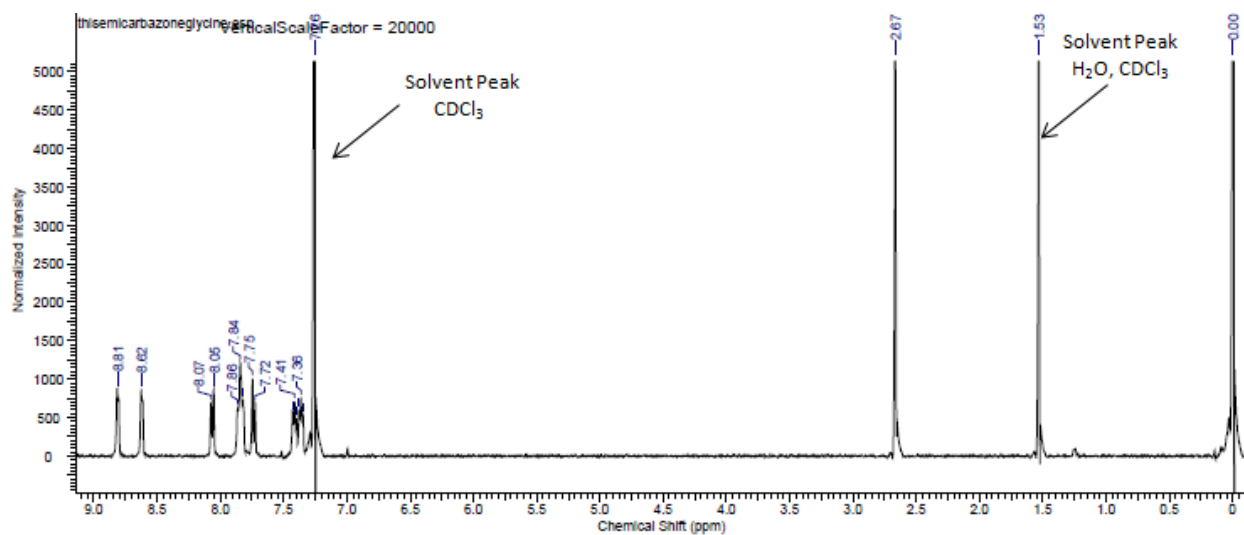
Figure C.5:- ^{1}H-NMR of the reaction mixture of thiosemicarbazone coupled with t-butyl protected glycine (crude).

210

The reaction was also carried out in DCM with coupling reagents EDC (1.2 eq), DMAP (1 eq) and was refluxed at 80°C and was monitored with TLC, presence of a product was detected (Figure C.6). The reaction mixture was washed with water to remove the coupling reagents. The organic layer removed by means of rotary evaporation, and a ^{1}H-NMR was taken to discern if any product was formed. From the ^{1}H-NMR (Figure C.7 crude) presence of coupling reagents were still observed therefore purification of the product was attempted through a silica column with 1:9 solvent ratio of ethanol: methylene chloride as the solvent. However from the ^{1}H-NMR of the purification fractions it was observed that the product was not able to be completely purified (Figure C. 8-14). Therefore a yield for the pure compound was not able to be obtained.
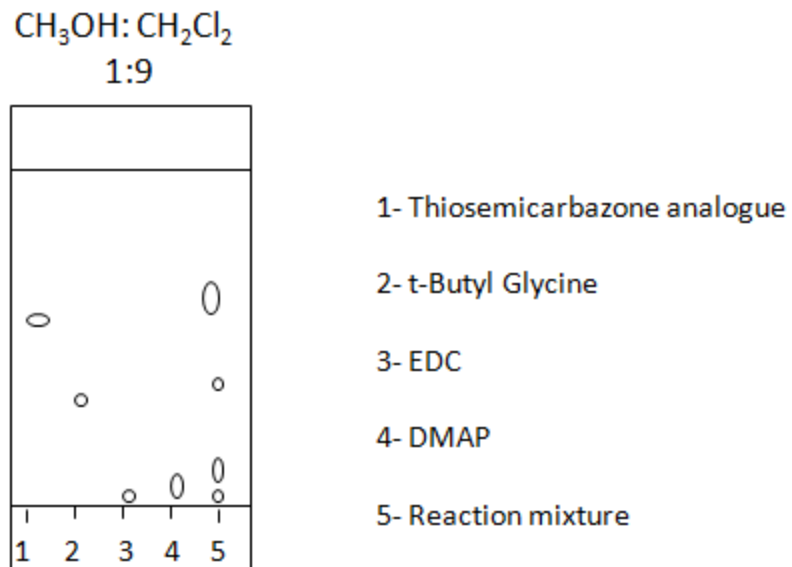
Figure C.6:- TLC of the EDC coupling reaction method for thiosemicarbazone coupled with t-butyl protected glycine.
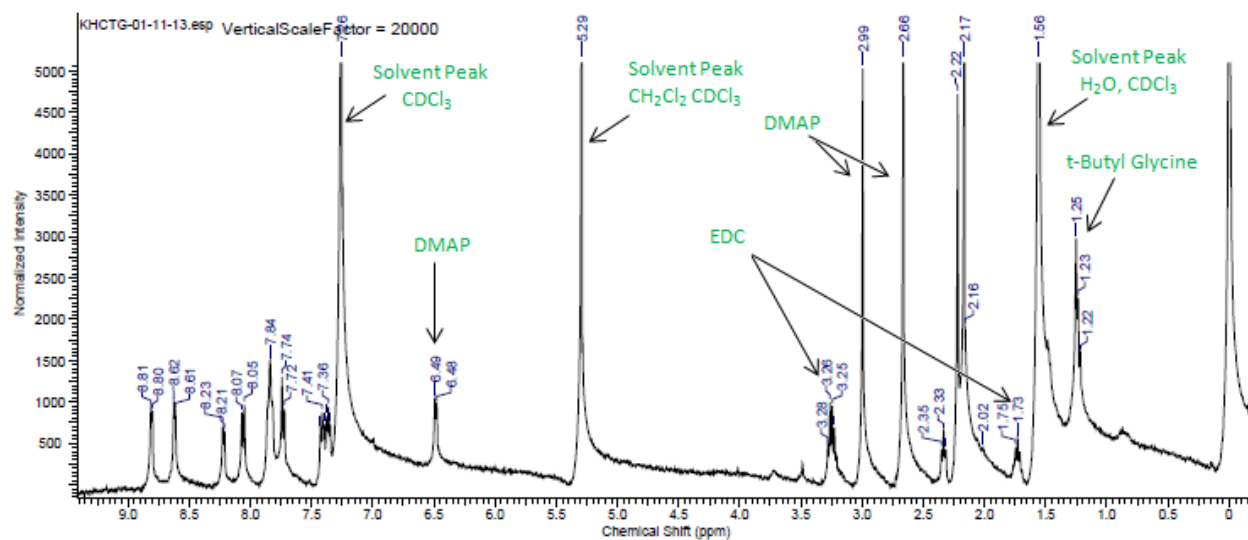
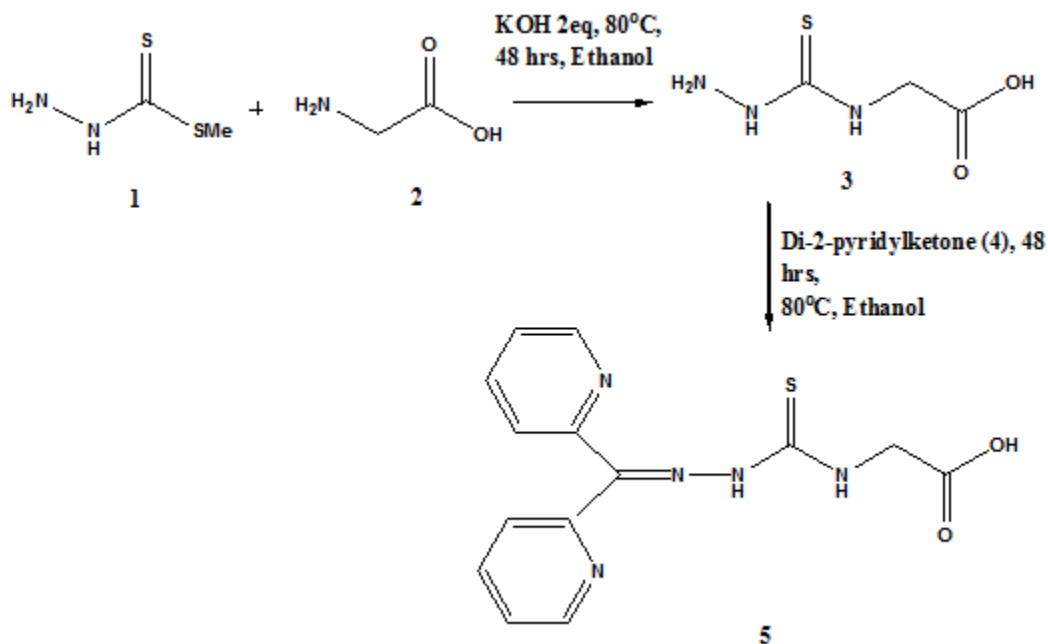**Figure C.7:-** ^{1}H-NMR of thiosemicarbazone coupled with t-butyl protected glycine using the EDC coupling method (crude).
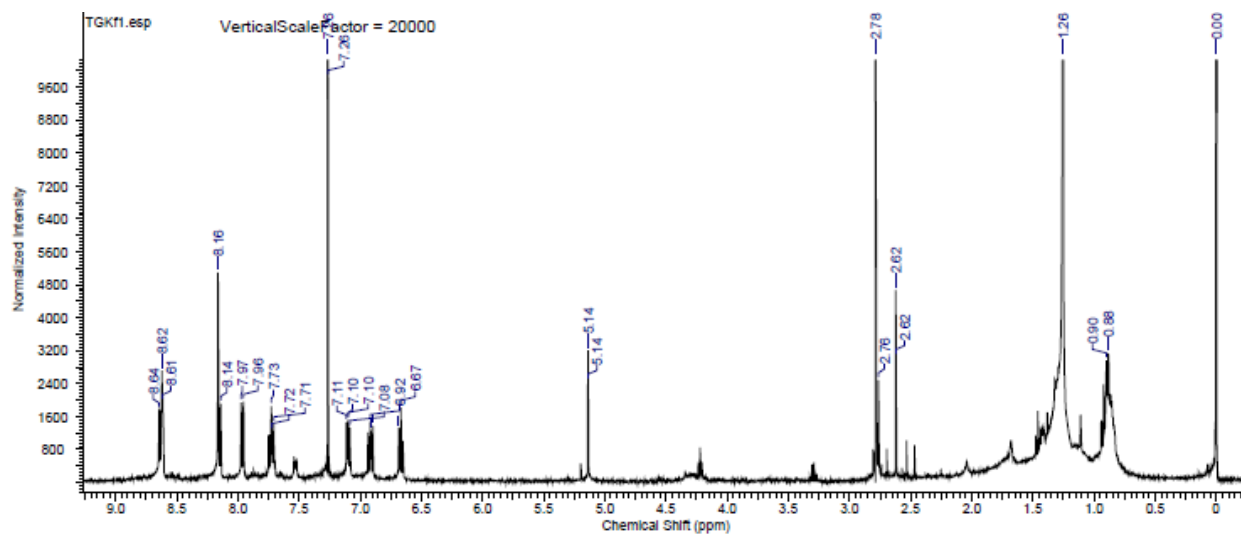
Figure C.8:- ^{1}H-NMR of fraction 1 of thiosemicarbazone coupled with t-butyl protected glycine using the EDC coupling method.
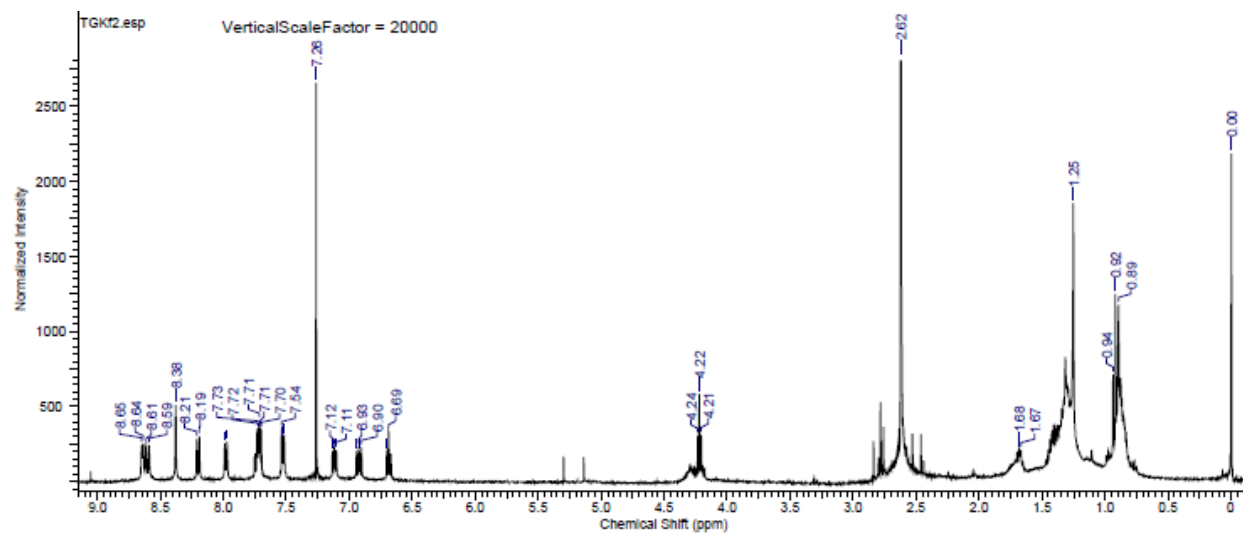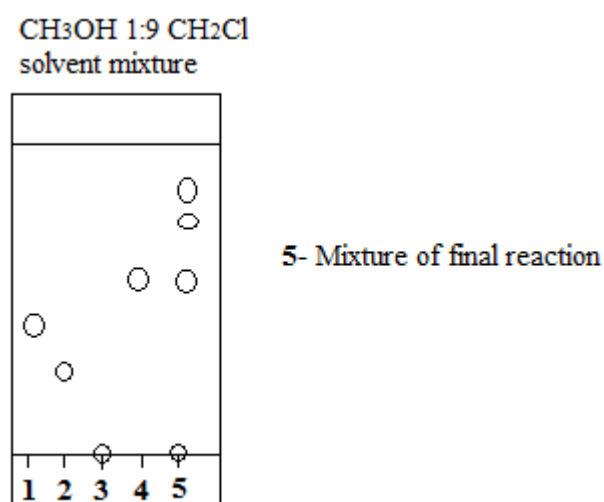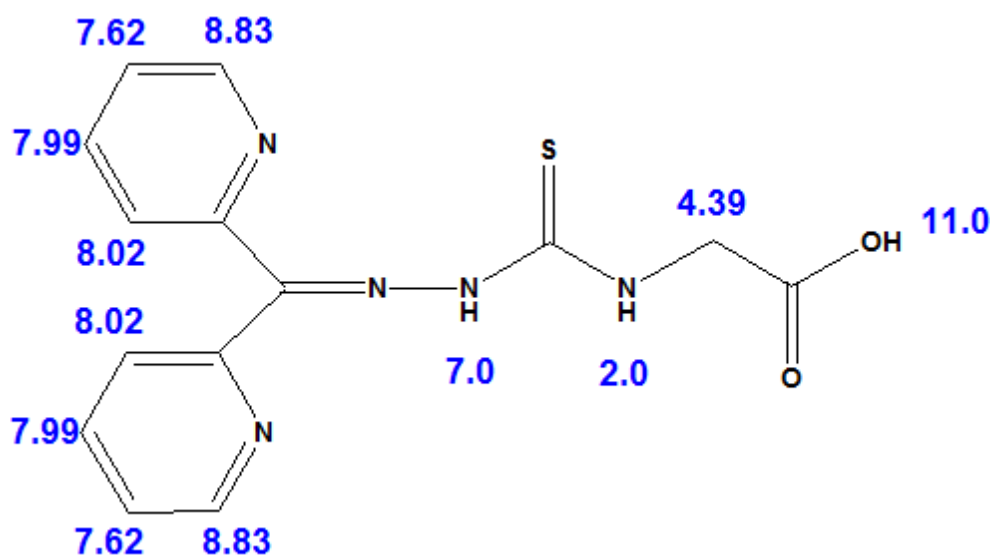
Figure C.9:- ¹H-NMR of fractions 2,3,4 of thiosemicarbazone coupled with t-butyl protected glycine using the EDC coupling method.

Figure C.10:- ¹H-NMR of fraction 5 of thiosemicarbazone coupled with t-butyl protected glycine using the EDC coupling method.
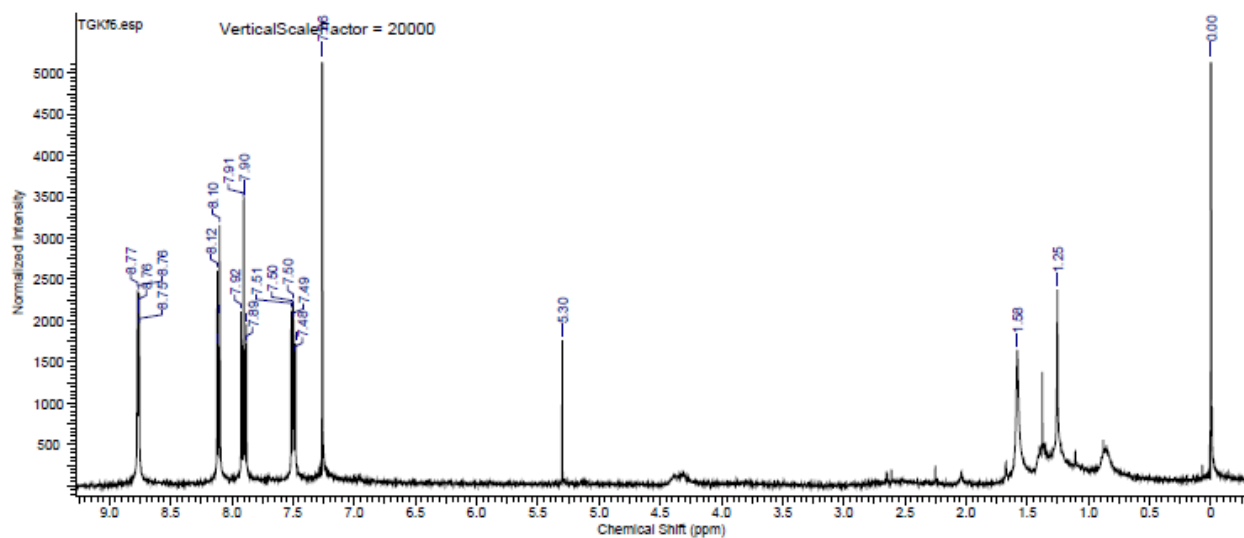
Figure C.11:- ^{1}H-NMR of fraction 6 of thiosemicarbazone coupled with t-butyl protected glycine using the EDC coupling method.
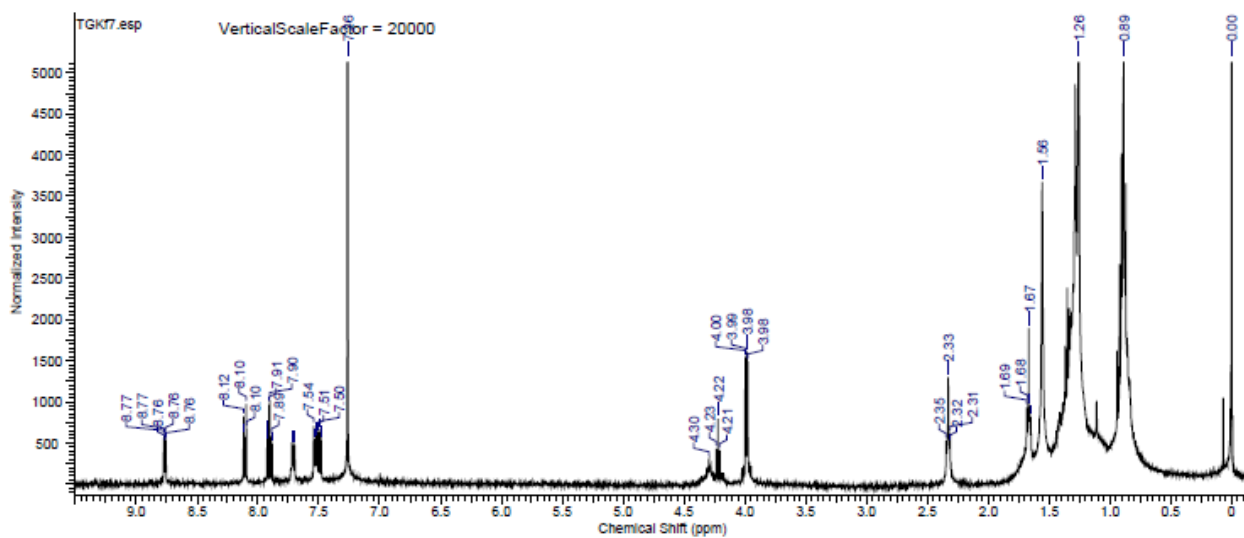
Figure C.12:- ^{1}H-NMR of fraction 7 and 8 of thiosemicarbazone coupled with t-butyl protected glycine using the EDC coupling method.
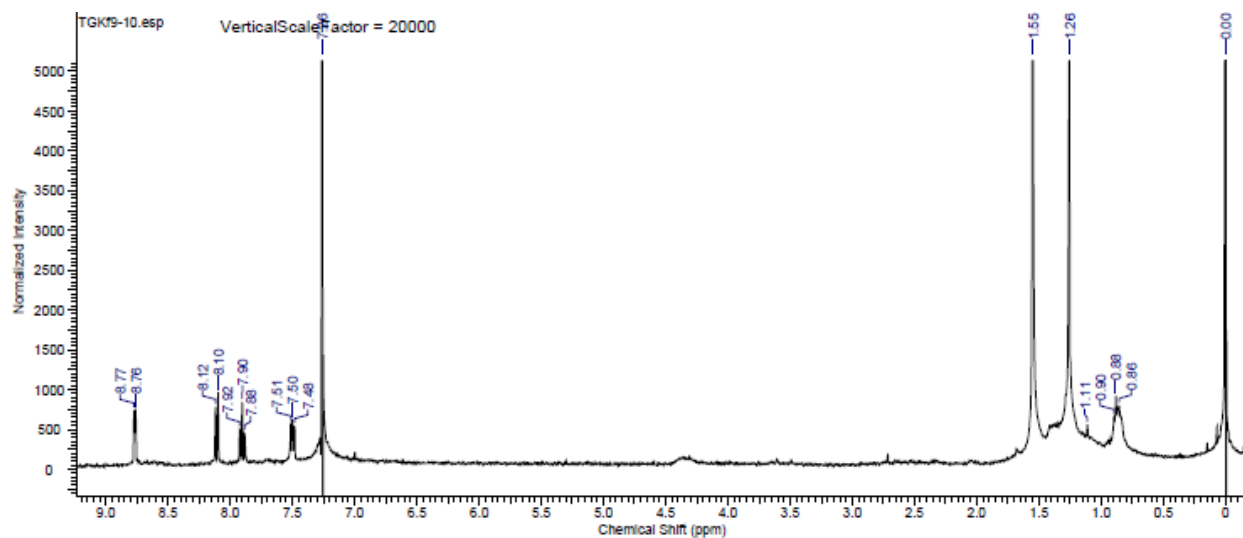
Figure C.13:- ^{1}H-NMR of fractions 9 and 10 of thiosemicarbazone coupled with t-butyl protected glycine using the EDC coupling method.
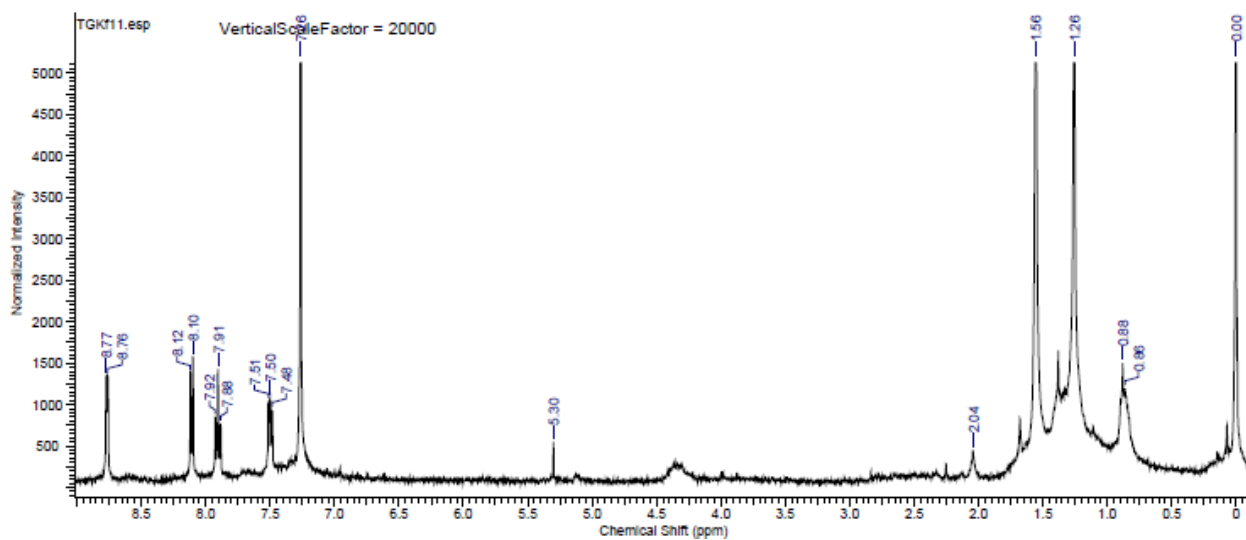
Figure C.14:- ^{1}H-NMR of fraction 11 of thiosemicarbazone coupled with t-butyl protected glycine using the EDC coupling method.

C.3 Experimental procedure 3

Next, we reacted glycine with the hydrazine carbothio methyl ester (synthesized as in 1.7.1). This was done by dissolving potassium hydroxide (2 eq) in hot ethanol (70°C) and then glycine (1 eq) was added. The solvent was removed by means of rotary evaporation. A white product was remaining. This product was added to a solution of hydrazine carbothio methyl ester (1 eq) and refluxed at 80°C for 48 hrs. After 2 hrs di -2-pyridylketone (1 eq) was added and further refluxed for 48 hrs (Scheme 4).[1,2] The solution was acidified to convert the salt product (if any formed) to the organic form. TLC was carried out on silica plates with a 1:9 solvent ratio of ethanol: methylene chloride (Figure C.15). The crude ^{1}H-NMR is shown in figure C.17. Purification of the product was attempted on a silica column and the ^{1}H-NMR's of the fractions are shown in figures C.18-21. The first 2 fractions were eluted using ethyl acetate 1:2 hexane. The other fraction were eluted with 1:20 solvent ratio of ethanol: methylene chloride. However, we were not able to completely purify the reaction product, therefore a yield was not able to be calculated. This may be due to reaction on the column or due to the formation of numerous by-products of this reaction.

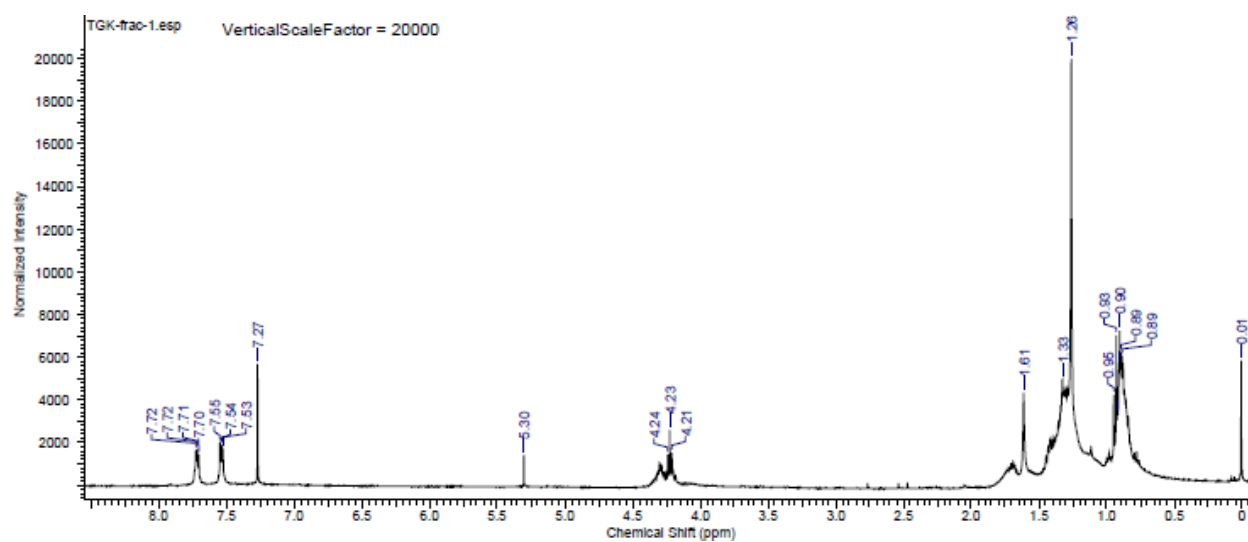**Scheme 4:-** Synthesis of glycine coupled thiosemicarbazone.

Figure C.15:- TLC of glycine coupled thiosemicarbazone reaction.

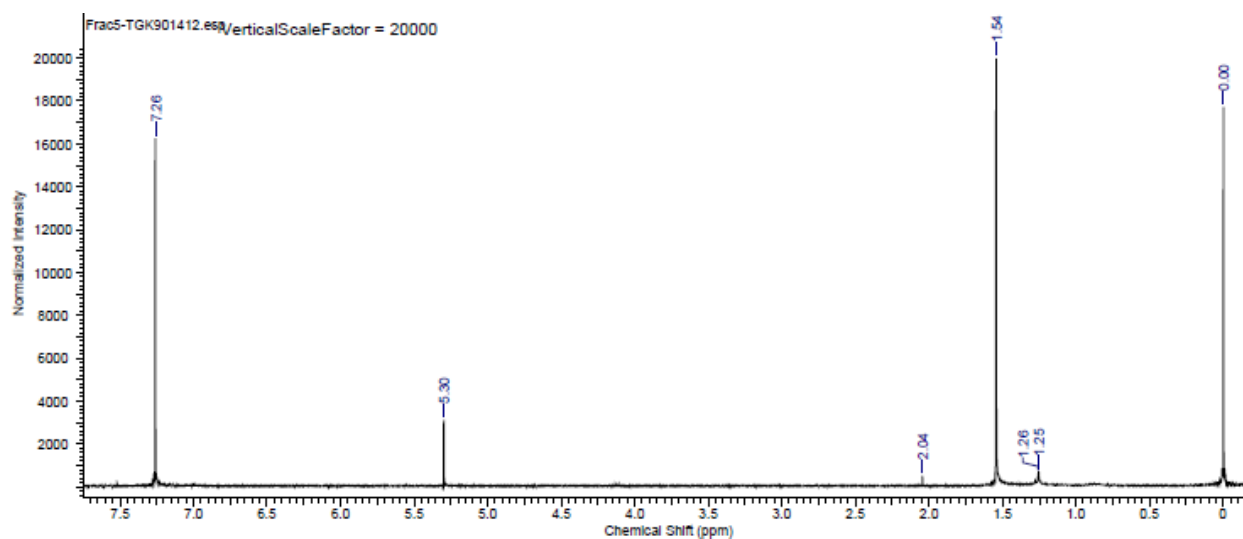**Figure C.16:-** Predicted ^{1}H-NMR thiosemicarbazone coupled with glycine.
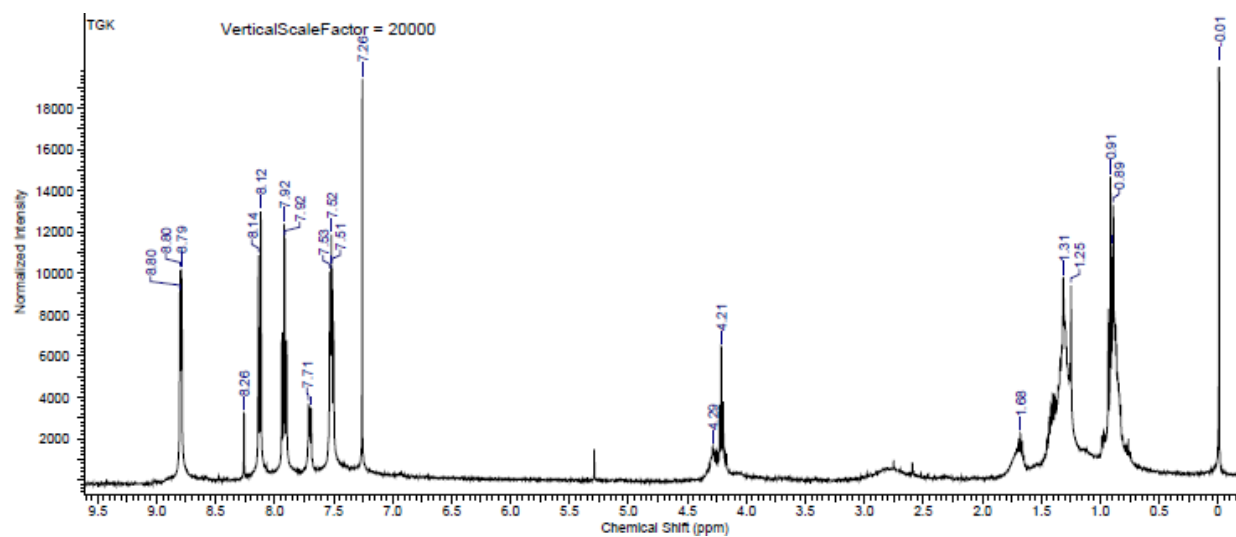
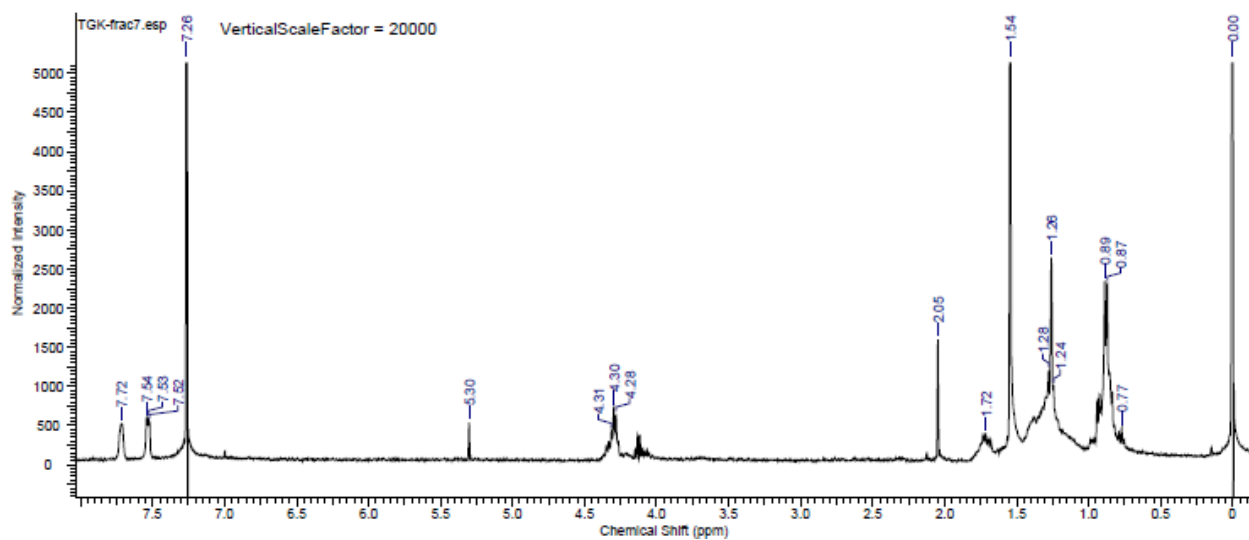**Figure C.17:-** ^{1}H-NMR of glycine coupled thiosemicarbazone reaction (crude).

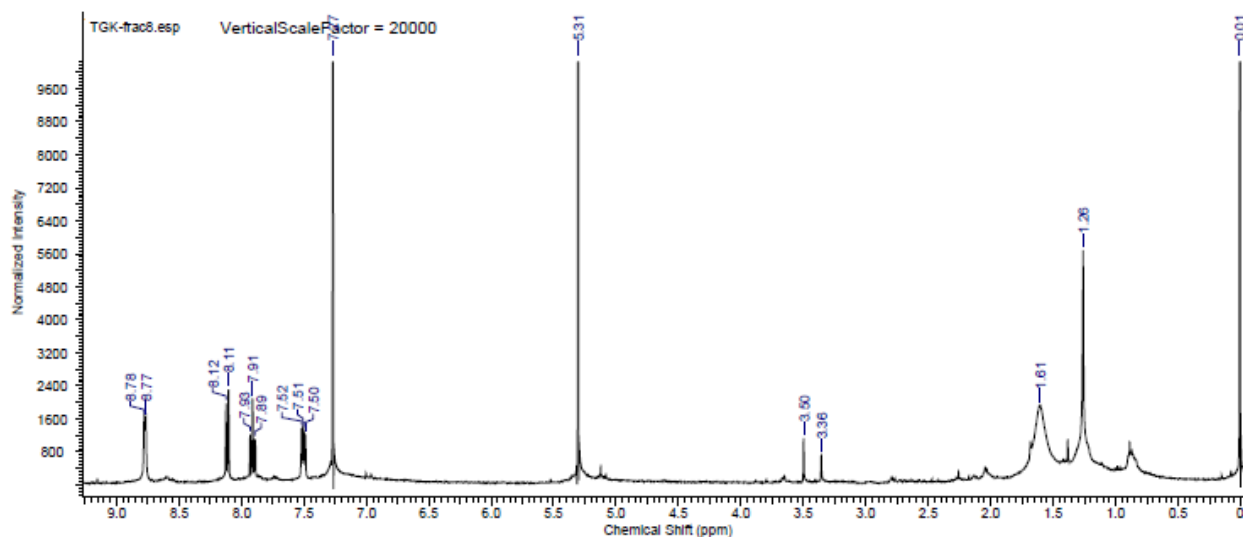**Figure C.18:-** ^{1}H-NMR of fraction 1 of glycine coupled thiosemicarbazone reaction.

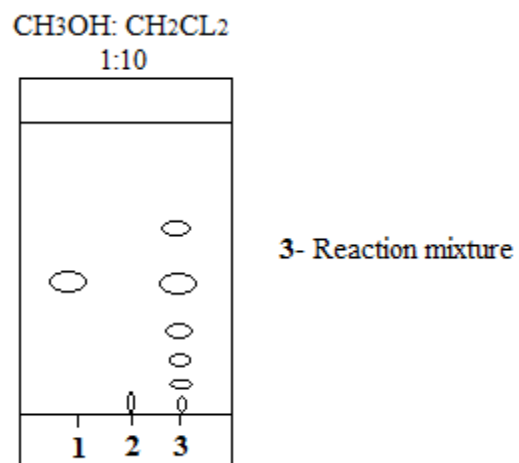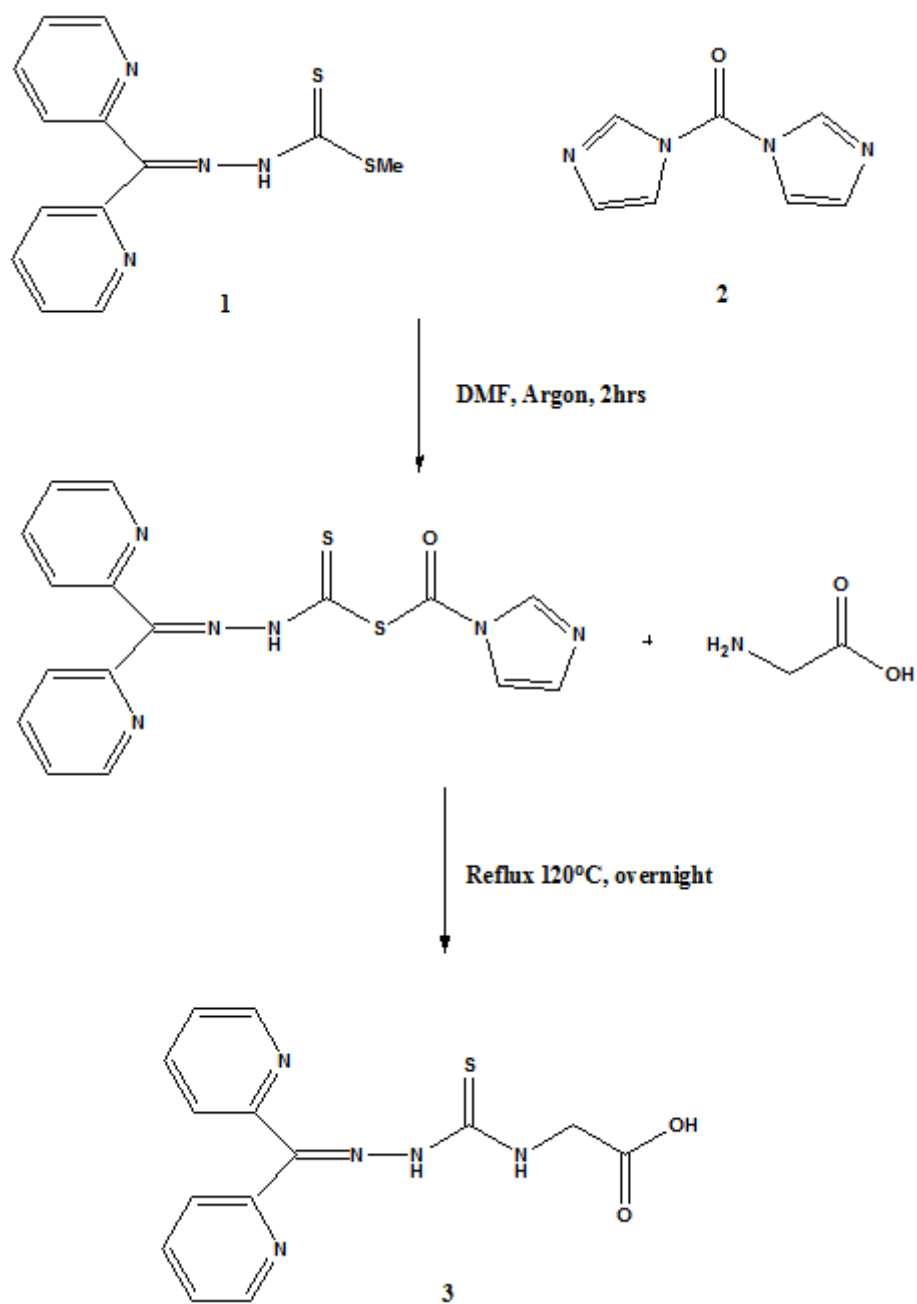**Figure C.19:-** ^{1}H-NMR of fractions 2, 3, 4 and 5 of glycine coupled thiosemicarbazone reaction.

Figure C.20:- ^{1}H-NMR of fraction 7 of glycine coupled thiosemicarbazone reaction.

Figure C.21:- ^{1}H-NMR of fraction 8 of glycine coupled thiosemicarbazone reaction.

C.4 Experimental procedure 4

The next attempt was to react the thiosemicarbazone analogue (1 eq) (synthesized as in 1.7.1) with 1,1'-carbonyldiimidazole (CDI) (1.2 eq) in DMF under argon for 2 hrs. In step 2, glycine was added to the reaction mixture and the reaction was monitored by TLC for 2 days. Since no product formed, the reaction mixture was refluxed at 120 $^{\circ}$C overnight (scheme 5). Methylene chloride was added and DMF was removed by washing with water and extracting the compound into methylene chloride. The organic layer was washed three times with saturated aqueous sodium chloride. Several spots on the TLC were seen when developed with 1:10 solvent ratio of ethanol: methylene chloride (Figure C. 22) (crude ^{1}H-NMR Figure C.23). Purification of the product was attempted on a silica column with with 1:10 solvent ratio of ethanol: methylene chloride. However the fraction obtained were shown to be not pure as seen in the ^{1}H-NMR's (Figures C.24-30) of the column fractions. Therefore percentage yield of the pure product could not be calculated.
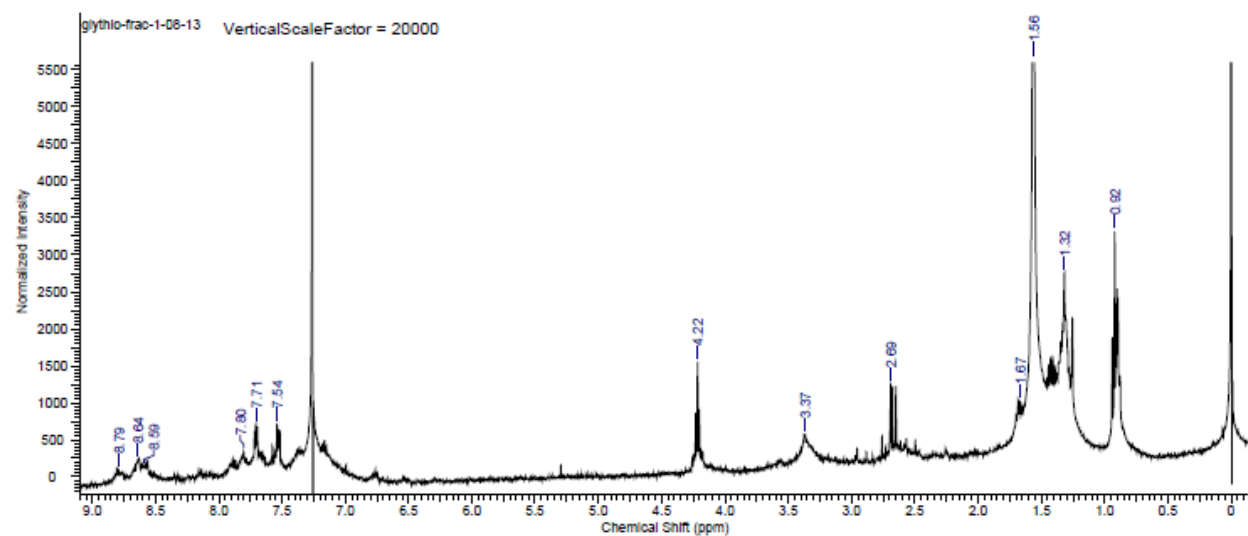
CH3OH: CH2CL2
1:10

3- Reaction mixture

1 2 3

Figure C.22:- TLC of the synthesis of glycine coupled thiosemicarbazone by CDI method.

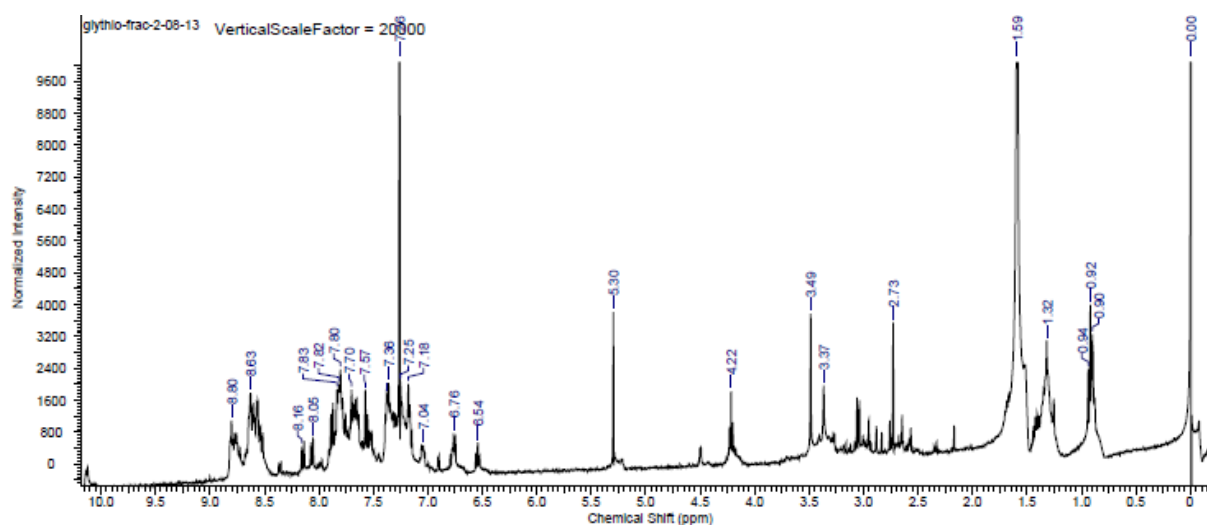**Scheme 5:-** Synthesis of glycine coupled thiosemicarbazone through CDI reaction method.
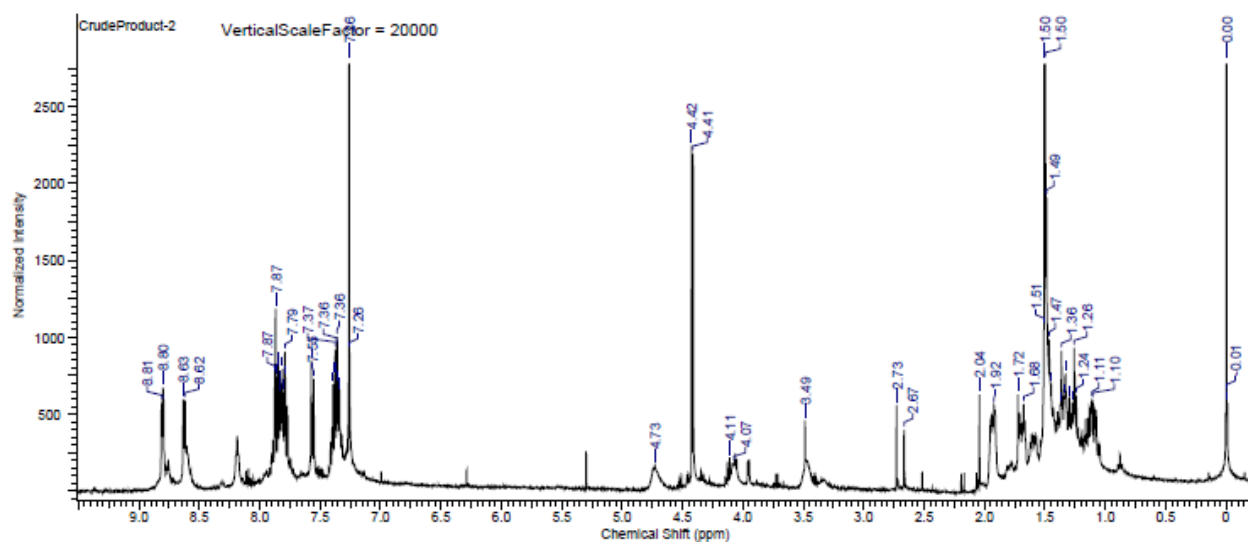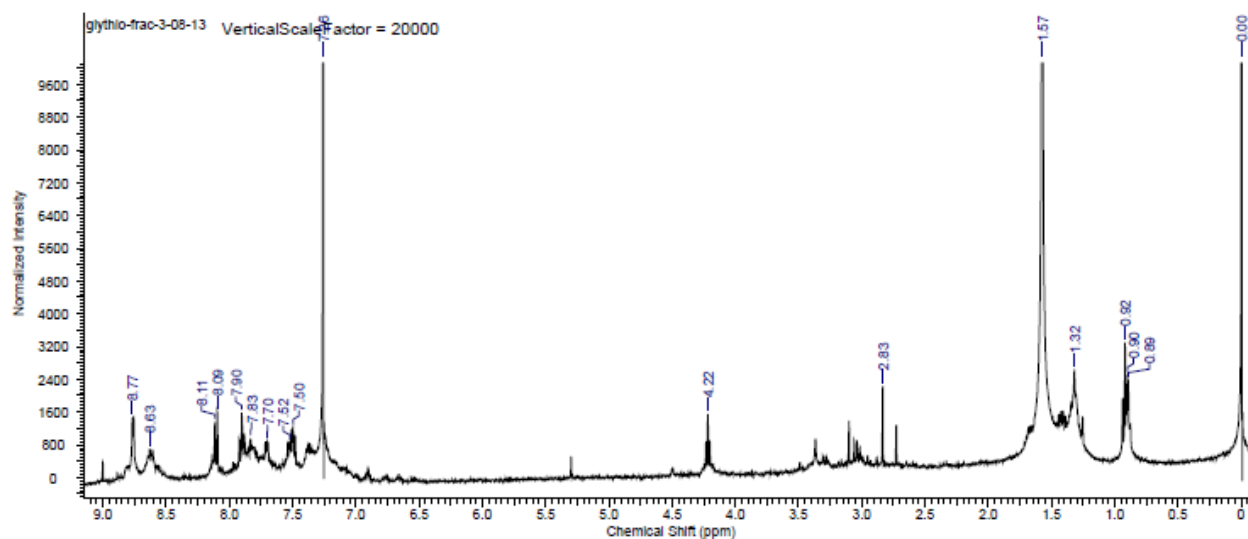
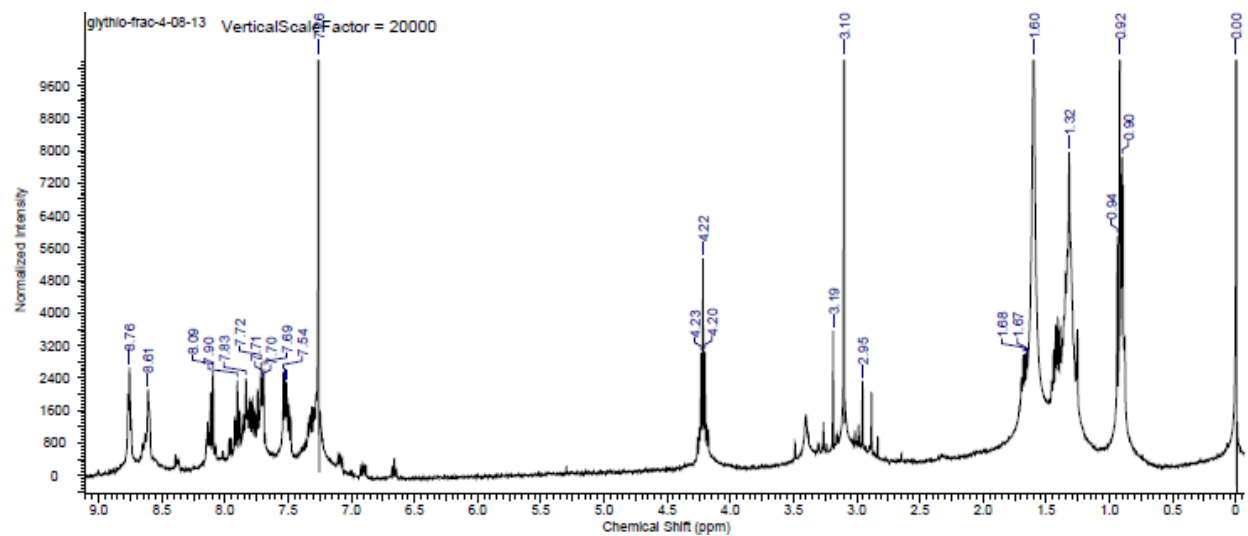**Figure C.23:-** ^{1}H-NMR of glycine coupled thiosemicarbazone reaction by CDI method (crude).

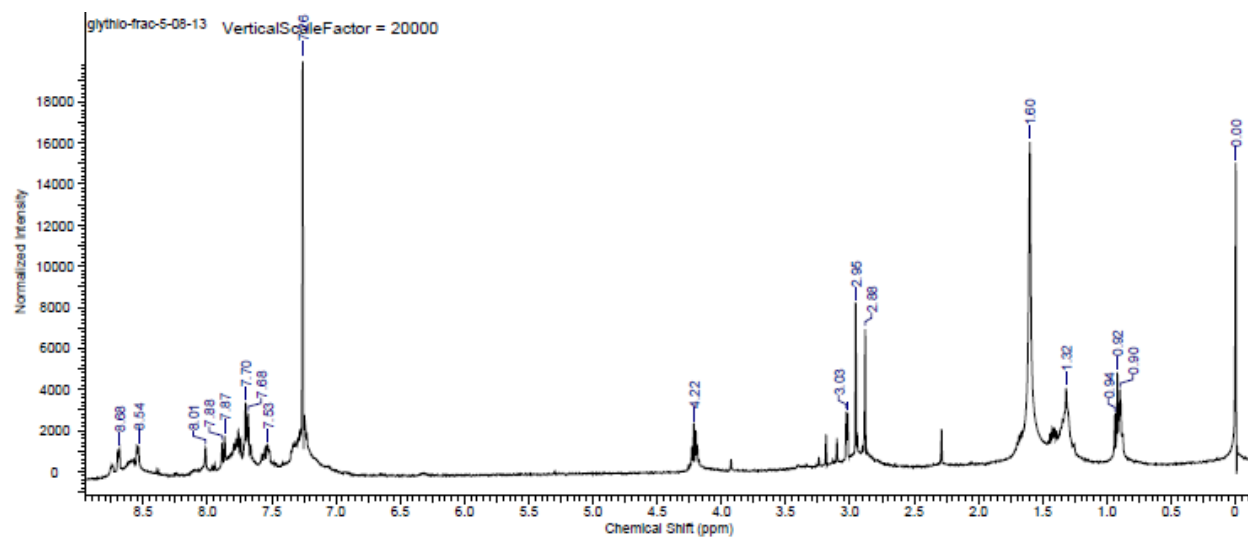**Figure C.24:-** ^{1}H-NMR of fraction 1 of glycine coupled thiosemicarbazone reaction by CDI method.

Figure C.25:- ^{1}H-NMR of fraction 2 of glycine coupled thiosemicarbazone reaction by CDI method.

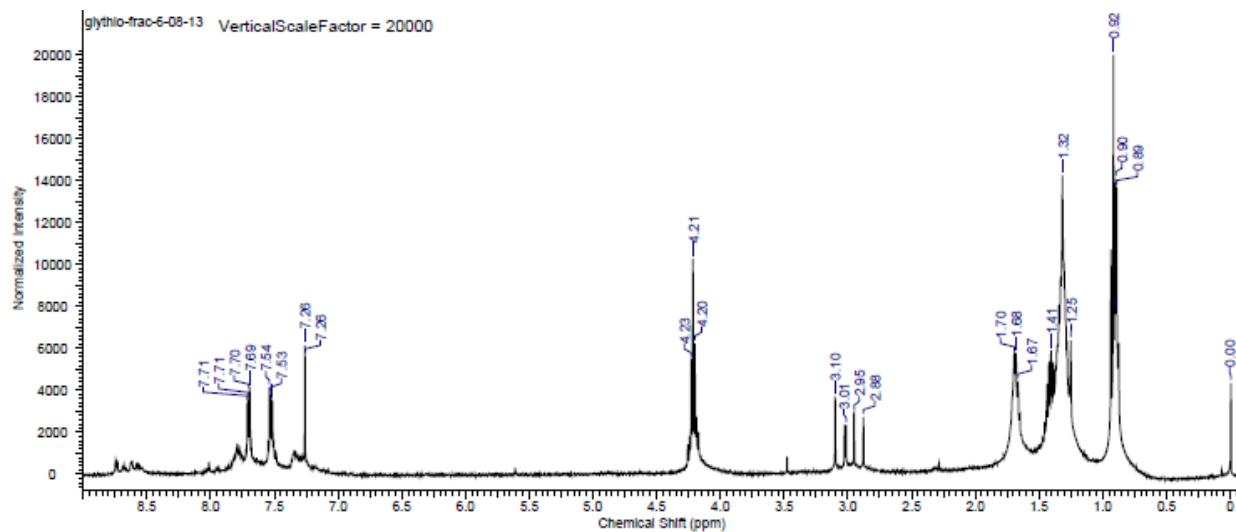**Figure C.26:-** ^{1}H-NMR of fraction 3 of glycine coupled thiosemicarbazone reaction by CDI method.

Figure C.27:- ^{1}H-NMR of fraction 4 of glycine coupled thiosemicarbazone reaction by CDI method.

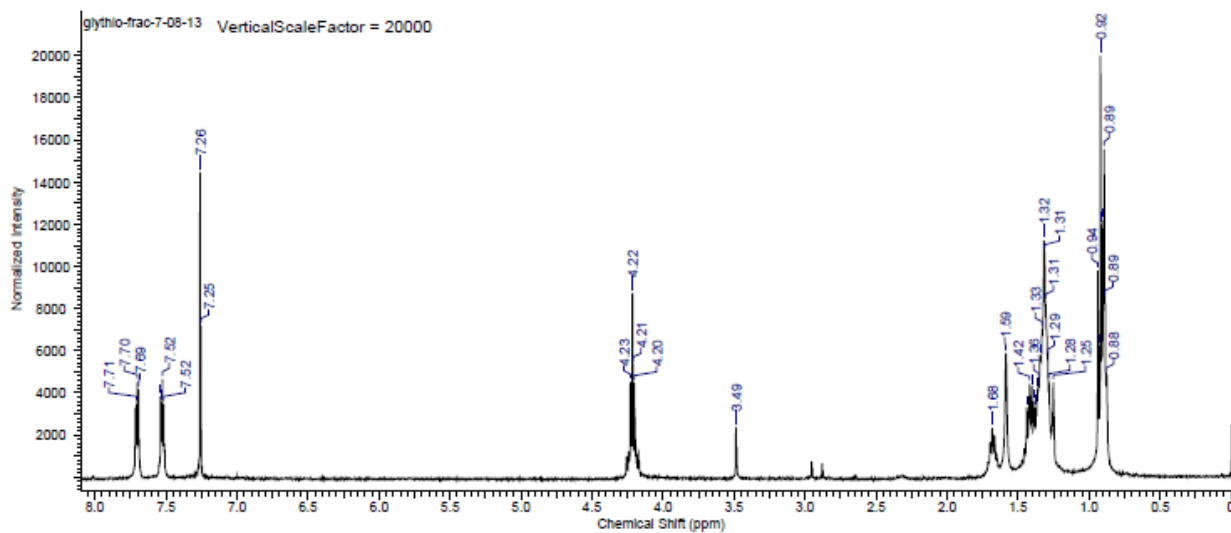**Figure C.28:-** ^{1}H-NMR of fraction 5 of glycine coupled thiosemicarbazone reaction by CDI method.

Figure C.29:- ^{1}H-NMR of fraction 6 of glycine coupled thiosemicarbazone reaction by CDI method.

Figure C.30:- ^{1}H-NMR of fraction 7 of glycine coupled thiosemicarbazone reaction by CDI method.

C.5 Reference

1. Ragavendran J. V.; Sriram D.; Kotapati S.; Stables J.; Yogeeswar P.; Newer GABA derivatives for the treatment of epilepsy including febrile seizures: A bioisosteric approach, *European Journal of Medicinal Chemistry*, *Vol. 43, Issue 12*, 2008, 2650–2655.

2. Hu K.; Yang Z.H.; Pan S.S.; Xu H. J.; Ren J.; Synthesis and antitumor activity of liquiritigenin thiosemicarbazone derivatives, *European Journal of Medicinal Chemistry*, *Vol. 45, Issue 8*, 2010, 3453–3458.